UNIVERSITÀ
DEGLI STUDI
DI PADOVA

Head Office: Università degli Studi di Padova

Department of Chemical Sciences

Ph.D. COURSE IN: Science and Engineering of Materials and Nanostructures

SERIES: XXX

Multiscale design of nanostructured materials for heterogeneous catalysis

Coordinator: Ch.mo Prof. Giovanni Mattei

Supervisor: Ch.mo Prof. Stefano Agnoli

Ph.D. student: Francesco Carraro

A Tina.

Contents

Abstract.....5

1. Introduction.....7

2. Atomic scale design of crystal structures.....17

2.1 Spinel structure.....20

2.2 Iron based spinel oxides and chemical looping processes.....24

2.3 X-Ray Absorption Spectroscopy: a powerful tool to investigate spinel structures.....26

2.4 Operando XAS investigation of reduction and oxidation processes in cobalt and iron mixed spinels during the chemical loop reforming of ethanol.....30

2.4.1 Experimental section.....31

2.4.2 Results and Discussion.....33

2.5 Conclusion.....53

3. Multiscale design of nanostructured Pd/CeO2 heterogeneous catalysts.....57

3.1 CeO2.....59

3.2 Structure and surface dependent behavior of ceria.....60

3.3 Engineering CeO2 morphology at the nanoscale.....63

3.4 Metal nanoparticles on CeO2.....70

3.5 Multi-scale design of Pd@CeO2 heterogeneous catalysts for selective methanol decomposition...72

3.5.1 Experimental section.....75

3.5.2 Results and discussion.....76

3.5 Conclusion.....89

4. Multiscale design of nanoreactors for heterogenous catalysis.....93

4.1 Metal Organic Frameworks.....96

4.2 MOFs and catalysis.....97

4.3 Post-synthetic metalation of a Mn-based MOF.....103

4.3.1 Experimental section.....104

4.3.2 Results and discussion.....106

4.4 Layer by layer growth of MnMOF for the design of nanostructured core@shell materials.....115

4.4.1 Experimental section.....117

4.4.2 Results and discussion.....118

4.5 Conclusion.....128

5. Multiscale design of nanostructured hybrid materials.....133

5.1 Aerosol process.....138

5.2 Graphene.....141

5.2.1 Crumpling of graphene.....143

5.3 Graphene-based nanohybrids and Hydrogen Evolution Reaction.....147

5.4 Fast One-Pot Synthesis of MoS2/Crumpled Graphene p-n Nanonjunctions for Enhanced Photoelectrochemical Hydrogen Production.....153

5.4.1 Experimental Section.....153

5.4.2 Results and Discussion.....160

5.5 Conclusion.....173

6. Conclusion.....177

List of acronyms and abbreviations.....183

List of publications.....185

List of oral/poster presentations.....186

List of Collaborations.....186

Acknowledgments.....187

Abstract

In this thesis, by means of different case studies, we explore the design from the micro to the atomic scale of different nanostructured heterogeneous catalysts that can be applied in the field of energy conversion and chemicals synthesis. We highlight the importance of the rational design of the materials to improve significantly the efficiency and performances of novel heterogeneous catalysts. The chemical nature and the morphology of the catalysts are correlated with their catalytic activities in order to tailor their physicochemical properties for each specific application. To do this, we have employed a large set of tools offered by Materials Science, exploring advanced synthetic methods and *operando* and *in situ* characterization techniques.

This thesis is divided into four main chapters where we presented four exemplary systems in which we focused our attention on different aspects of materials design. Each chapter comprises an introduction and a conclusion section, in which we tried to go into the details of each targeted application and of the specific design strategy employed. However, at the beginning and at the end of the thesis, the reader can find an Introduction and a Conclusion section where we tried to collocate the goals and challenges of this work within a broader context of materials science and catalysis.

In Chapter 2, we have focused our attention on the design at the atomic scale of spinel oxide structures that were used as redox catalysts for the production of pure H_2 through Chemical Loop Reforming of ethanol. In fact, we have investigated the correlation between the role of chemical nature (Co vs Fe), geometrical site (tetrahedral vs octahedral site) and crystal phase (spinel vs wüstite) on spinel redox chemistry. This could lay the basis for a rational design of spinel oxide based materials with specific chemical and functional properties.

In Chapter 3, we have focused our attention on the design at the micro, nano and atomic scale of nanostructured catalysts based on Pd and $CeO_2$for the selective methanol decomposition to syngas (H_2+CO). The multiscale design of the materials passed through the synthesis of CeO_2 nanostructures with different size/morphology and with well-defined exposed facets and their decoration with Pd nanoparticles.

In Chapter 4, we investigated the design at the atomic scale of nanoreactors: the micropores of Metal Organic Frameworks (MOFs). In fact, by exploiting the intrinsic modularity of MOFs, we have obtained an array of interconnected nanoreactors that possess the same chemical and sterical environment. We have studied the introduction in the micropores of different metal cations that could impart different catalytic activities. The obtained materials were studied as catalysts for hydroformylation reactions. Moreover, we have studied the design of an innovative core@shell composite material based on MOF thin film shell and on Pd/CeO_2 core. The final goal of this project will be the use of this multifunctional system as a tandem catalyst, possibly for ethylene hydroformylation, using methanol as *in situ* source of syngas.

In Chapter 5, we have investigated a fascinating synthesis method of nanostructured multifunctional composite materials from micro to atomic scale: the aerosol process. In this process, each aerosol droplet can be considered as a microreactor. Using this strategy, we have synthesize hybrid materials based on crumpled heteroatoms doped graphene oxide and MoS_2 nanoparticles and we tested their catalytic activity toward the electro- and photoelectro-chemical hydrogen production.

Chapter 1

Introduction

1. Introduction

Nowadays the reduction of the world energy consumption is one of the main challenge for our society. The world population is continuously increasing and consequently the energy demand is destined to grow more and more. In this scenario, actions taken in order to reduce global warming and pollution must be the main concerns of the scientific and industrial world.[1] If we really want to tackle these problems, we need to reduce the energy consumption without affecting the well-being of our society. Therefore, it is mandatory to develop more efficient and greener (i.e. carbon neutral) processes for the conversion of the energy at all levels, from the automotive field to the electric energy production. One of the largest energy demands of our society is related to the production of chemicals, which accounts for approximately 25% of industrial energy consumption.[2] Within the production of chemicals, the most energy consuming processes are based on heterogeneous catalysis.[3] These numbers highlight the urgency for the development of new-generation, more efficient (i.e. increasing selectivity and lowering operative temperature) catalysts in some key processes such as hydrogen production, water splitting, biofuel production and conversion to fine chemicals, etc. The empirical optimization of industrial catalysts by empirically tuning the elemental composition or changing the supports of the active phase to achieve greater activity and selectivity could be efficient, but the process is in general quite lengthy and characterized by incremental improvements, whereas the urgency of modern society and environmental challenges requires more disruptive innovational approach. Materials science plays a fundamental role in this scenario, since the only way to improve significantly the efficiency and performances of heterogeneous catalysts goes through a rational design of materials that need to be tailored from the macro to the atomic scale for specific applications. Already in 1995, the concept of rational catalysts design was mentioned as one of the "holy grails" in the field of catalysis by Breslow[4], and nowadays this topic needs to be tackled at different levels with even greater resolution.

For example, the morphology and size control of metal oxides as catalysts support or as nanocatalysts were proven to be useful strategies for the tuning of the catalytic activity and showed a great potential for innovative catalyst design.[5,6] The crystal shape of metal oxide particles can influenced the redox properties of the material: at the atomic scale, different exposed crystal facets can affect catalytic activity, selectivity and durability.[5] When employed as support for another catalyst, in the simplest case a metal nanoparticle, the choice of different crystallographic surfaces of the substrate may lead to the stabilization of rather different phases of the supported catalysts and to different size of these nanoparticles.[7] Reducing the size of the support, for example from micrometric to nanometric crystals, could have several effects on the final material: there could be an increase of the reducibility of the oxide support with the reduction of the particle size, or new size dependent properties can emerge.[8] The increase of the surface area provides a higher number of active sites per gram of catalyst or could increase the density of defects that could heavily influence the deposition of the supported phase. Moreover, as surface-science studies have clearly demonstrated in recent decades, in the case of supported catalysts, the interface (the boundary between two phases) plays a critical role since many of the physicochemical properties of materials are profoundly modified and some new phenomena such as electronic hybridization effects, encapsulation and spillover can take place.[9] Therefore, a fundamental understanding of catalyst interfaces is another keystone for the rational design of high-performance catalysts.[10]

Obviously, these considerations are not limited to the case of metal and metal oxide nanoparticles. In the field of catalysis, new materials stepped into the limelight in the last years.[11] For example, graphene based materials are nowadays widely studied for several different applications in the energy field, from electro to photo catalysis.[12] Graphene could be a useful platform for the design of composite materials, for example permitting the dispersion of nanoparticles over its surface in order to limit their size and to exploit its electrical conductivity.

Metal Organic Frameworks (MOFs) constitute a class of materials that is brightly emerging in the last years.[13] Briefly, MOFs are constituted by size-selected inorganic clusters joined together by organic linkers in 3D crystalline microporous structures with excellent thermal and chemical stability. One of the main interesting aspects of MOFs is their modularity: by changing the nature of MOF's components it is possible to finely tune the physicochemical properties of these materials. A second pivotal aspect is the presence of microporosity, which in catalysis can be exploited to design inside the MOF themselves a series of nanoreactors. These two qualities combined open the way to the possibility of finely tune the chemical environment of these nanoreactors at the atomic scale by changing the nature of organic ligand/metal node or by the coordination of metal cations or complexes in order to introduce new active sites. Moreover, these microporous materials can be coupled with different materials (i.e. metal NPs) with the aim of designing novel multifunctional materials.[14]

As future perspective, the results of the rational design of multifunctional catalysts that we will be discussed in this thesis could be exploited for a radically new approach in catalysis that goes under the name of *tandem* or *synergistic* catalysis. It refers to the possibility of coupling different chemical reactions in a single reaction environment (*one-pot*) by exploiting the several catalytic centers present in a multifunctional material.[15,16,17] In this way the consumption of energy, production of wastes and especially the chemical workout are strongly reduced due to the elimination of intermediate purification and separation steps. The ability to produce *in situ* the reactants for a multi-step reaction also allows great logistics advantages, especially if some of the chemicals necessary at some point of the synthesis, are unsafe to handle (i.e. highly pressurized gases such H_2) or potentially toxic (i.e. CO, HCl etc). The study of *rationally designed systems,* (i.e. ordered and perfectly reproduced structural units designed with atomic scale precision), could permit to investigate by a reductionist approach even highly complicated chemical reactions.[18] In fact, in some fields (i.e. metal/metal oxide interface), the results of such an approach were able to transform catalysis from an empiric practice based on *trial and error* to a sophisticated discipline based on rational understanding and capable of *ab initio* tailor-made design.

In this thesis, we investigated the multiscale design of different nanostructured heterogeneous catalysts (schematically summarized in Figure 1) that can be applied in the field of energy conversion and chemical synthesis. In our studies, we wanted to emphasize the fundamental role of the design of the chemical nature and of the morphology of the catalysts and their correlation with the catalytic activity. We focused on materials design at the atomic scale investigating a wide range of aspects such as the control of the cation site occupancy in a crystal structure, the introduction of single atom catalytic sites in nanoreactors or of dopants and specific defects into the bulk or the surface of a material. All these efforts had has final goal the induction of a precise catalytic activity in our materials. In a second step, we have enlarged our approach and tried to expand the materials design to the nano and micro scale. At these length-scales, several factors can influence the catalytic activity of the materials: very small (few nm) NPs could have improved performances (i.e. higher density of active sites, stronger electronic interaction with the support); the control of crystal morphology can lead to the exposure of well-defined highly active surfaces; the reactants diffusion to the active sites could be dramatically influenced by the morphology of the material (i.e. microporous size and chemical/sterical environment, spatial distribution of different active sites in composite materials). Moreover, we employed different *operando* and *in-situ* characterization techniques, to gain a deeper understanding of the behavior of our catalytic materials in realistic working conditions.

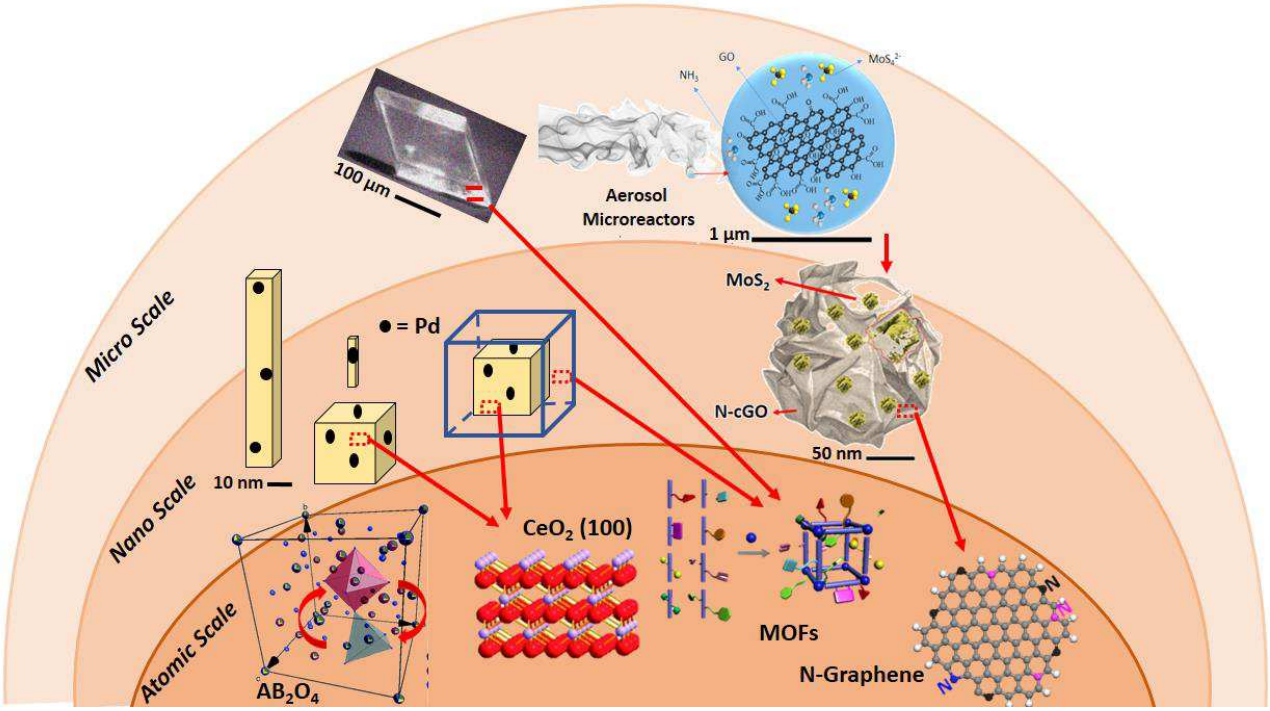

Figure 1: Schematic view of the different materials investigated in our case studies, highlighting the different length of scales at which we designed the catalysts.

The thesis is divided in four main chapters. In Chapter 2, we investigated the design at the atomic scale of spinel oxides based redox catalysts. We have investigated $FeCo_2O_4$ and $CoFe_2O_4$ nanoparticles as oxygen carriers for the Chemical Loop Reforming (CLR) of ethanol. [19] CLR redox catalytic process is aimed to the production of clean H_2. Hydrogen is considered as one of the most promising clean energy source for the future. However, hydrogen is a secondary energy source. This means that its environmental impact and price depends on its production and purification processes. Nowadays the principle production process is based on non-renewable sources with high CO_2 impact (fossil hydrocarbons or coal). There are also more environmentally friendly processes such as electrolysis (from solar or wind produced electron energy) and reforming of bio-hydrocarbons, but their cost is not yet competitive for large-scale development.[20] In the last years, a new approach that can employ renewable sources and offers an efficient CO_2 sequestration capability was proposed, the CLR. In fact, compared to classical reforming, this process is separated into two steps that allows obtaining highly pure hydrogen.[21] Briefly, the oxygen and electron carrier, in general an oxide, is exposed firstly to a reducing stream (i.e. ethanol, methanol, syngas, CO). In the second step, it is exposed to steam in order to produce H_2 and the redox catalyst is oxidized to its initial state. Hydrogen and C-containing products will be produced in two separated steps, eliminating the expensive hydrogen purification step. The viability of the cycling process is determined by the reaction conditions and by the nature of the oxide employed as redox catalyst. In our study, we combined the investigations by means of *operando* (Quick Extended X-ray Absorption Fine Structure) and ex-situ (X-ray Diffraction (XRD), Raman and Mössbauer Spectroscopies) techniques, of the correlation between the design of the crystal structures at the atomic scale and the catalytic activity. In fact, modifying the cation sites occupancy of the spinel structure we modified the redox properties of the materials and therefore their catalytic activity towards the CLR process. We followed the kinetics of the phase transformations induced by the reaction with ethanol, during which the ferrites are transformed to more reduced oxides and eventually metal phases. Similarly, we investigated the oxidation process of the reduced form of the catalysts operated by water steam. Thanks to this study, we correlated the cation nature and its occupation site in the spinel structure (tetrahedral or octahedral sites) with the redox properties of this kind of binary oxides.[22] Moreover, by combining the structural information provided

by X-ray absorption spectroscopy with the analysis of the byproducts of ethanol decomposition (Gas Chromatography (GC)) we could associate different selectivity with cation chemical nature and occupancy in the spinel structure. This knowledge could allow a precise calibration of these redox materials and therefore may allow designing a new generation of catalysts whose properties are perfectly tuned for a precise application.

In Chapter 3, we studied Pd/CeO_2 based materials for the synthesis of syngas ($CO + H_2$) through the selective decomposition of methanol.[23] This reaction could be exploited in several different catalytic processes, ranging from energy recovery of waste heat (from various industrial activities or from methanol fuel cells) to the synthesis of fine chemicals. Moreover, methanol could be obtained from renewable sources (i.e. bio-fuels), making this reaction appealing from an environmental point of view. Palladium is an active catalyst for the decomposition of methanol to syngas, whose chemical activity is largely affected by the interaction with the support. Nanostructured Cerium oxide plays a fundamental role in this kind of catalysts, since it can establish strong electronic interactions with finely dispersed palladium nanoparticles (NPs) leading to a substantial enhancement of their catalytic performance. Ceria acid–base properties, and thus its catalytic activity and interaction with metal NPs, are closely related to the surface structure. This synergistic effect is dependent on structural factors such as the nanoparticle size and the crystallographic orientation of the facets because they control the coordination and chemical environment of oxygen anions and cerium cations. To study these structure/activity relationships, we deposited Pd NPs on nanostructured cerium oxides powders exposing mainly the same {100} faces, but with different morphology and average dimension, and we have investigated their activity toward methanol decomposition. The catalytic activity of the catalysts was evaluated in a fixed-bed flow reactor and the reaction products were analyzed by GC. The physicochemical properties of the materials were investigated combining different techniques such as Raman Spectroscopy, High-Resolution Transmission Electron Microscopy (HR-TEM), Energy-Dispersive X-ray Spectroscopy (EDX), N_2 adsorption-desorption isotherms and Brunauer–Emmett–Teller (BET) analysis and X-ray Photoemission Spectroscopy (XPS). Since the active sites for methanol decomposition in Pd/CeO_2 catalysts are at the interface between metal and oxide, the characterization of the surface of the catalyst in realistic working condition is fundamental for a deep understanding of the catalytic process. Therefore, we investigated through *in situ* XPS the surface of our materials during the different steps of the catalytic process (i.e. as-prepared, activated, and post mortem catalyst) in order to correlate the oxide nanocrystals shape with surface reducibility, interaction with metal NPs and eventually catalytic activity. Consequently, the catalytic activity of Pd/CeO_2 catalysts can be tuned by design at the nanoscale the morphology of the oxide support. With this study, we wanted to highlight the importance of the engineering at the micro and nano scale of the size, morphology, and exposed facets of individual particles, as fundamental steps to control the surface chemistry of both oxide and metal nanoparticles and eventually to tune the catalytic activity and synergistically integrate different catalytic sites in a unique composite. In fact, it should be noticed that if a catalyst used for syngas synthesis is rationally integrated in a multifunctional material, the *in situ* produced CO and H_2 could be exploited to carry out a second catalytic reaction (i.e. tandem reactions).[5] We have studied the integration of these Pd/CeO_2 catalysts in a multifunctional material in Chapter 4, but we will introduce this topic in the next paragraph.

In Chapter 4, we investigated the design at the atomic and nano scale of MOFs and their possible integration in a multifunctional material based on MOFs and on one of the Pd/CeO_2 catalysts investigated in the first chapter. In particular, we studied MOFs with organic linkers bearing sites that are poised for post-synthetic metalation (PSM). In catalysis, MOFs micropores can be seen as nanoreactors. This paves the way to the possibility of finely tune the chemical environment of these nanoreactors by changing the nature of organic ligand/metal node or by the coordination of metal cations (through PSM) in order to have new active sites. In fact, looking with the eyes of the molecules, each MOF crystal could be considered as an ordered array of interconnected nanoreactors

where, thanks to the modularity of MOFs, the chemical and steric environment that the reactants will encounter, could be suited for specific chemical conversion steps or other functional activities such as detection and separation. We focused our attention on a Mn(II)-based MOF (hereafter MnMOF).[24] The MnMOF linkers are constituted by flexible di-pyrazole chelating units poised for post-synthetic metal binding. We quantitatively metalated MnMOF by a variety of transition metal ions (i.e. Co(II), Cu(II), Rh(I), Fe(II), Ni(II) and mixture of them) and we tested the catalytic activity of Rh metalated MnMOF as catalyst for hydroformylation reactions. The reaction products were analyzed by GC, whereas the physicochemical properties of the materials were characterized by XRD, Raman Spectroscopy, BET analyses, SEM and EDX.

Finally, combining the knowledge acquired with these investigations and the studies about Pd/CeO_2 catalysts, we explored the synthesis of multifunctional catalysts based on core@shell structure of Pd/CeO_2 (core) and post-synthethic metalated MOFs (shell). The materials were synthesized using different methods as solvothermal synthesis, layer-by-layer growth,[25] impregnation and precipitation methods. The goal was to combine MOFs with the metal/oxide systems, which were the object of our previous investigations, and eventually to design nanostructured multifunctional catalysts.[26] In this kind of system, we plan to study the possibility of exploiting the *in situ* production of CO and H_2 (through methanol decomposition catalyzed by Pd/CeO_2) to carry out a second catalytic reaction in the shell of the material (i.e. hydroformylation reactions). [26] Potentially, this kind of composite materials could have a ground breaking impact in the catalysis field. In fact, MOFs can host additional functional units (i.e. metal nanoparticles, polyoxometallates, guest molecules and ions) becoming therefore an integrated platform for advanced chemical conversions possibly associated with chemical detection, storage and separation.[27] The unique properties of MOFs as support materials are obviously connected to their huge surface area and microporosity that can have a profound effect on the hosted entity, being able to impart enhanced activity and better selectivity. It has to be highlighted that the activity of a multifunctional catalyst stems from a synergic effect of the different material components and it is not simply the sum of properties of the single components. Therefore, in our case study, the MOF growth must be rationally designed: it should permit the supply of methanol at the Pd/ceria interface (so the shell must be thin enough) and its active catalytic sites should be in a position favorable to work synergistically with the metal/oxide interface. The growth of thin layers of MnMOF has not been reported yet in the literature and this synthesis work resulted to be extremely challenging. Nonetheless, we obtained good results with the layer-by-layer growth of MnMOF on CeO_2 nanocubes. The physicochemical properties of the composite materials were characterized by XRD, BET analyses, Raman Spectroscopy, XPS, HR-TEM and EDX. At the time of writing, the characterization of the catalytic activity of these multifunctional materials is not concluded yet and therefore these results are not included in this thesis. However, with this study we wanted to highlight the importance of a rational multiscale design of such as complex multifunctional material. At its base, there was the design from micro to atomic scale of Pd/CeO_2 material (ceria crystals morphology and exposed facets, size and interaction with ceria of Pd NPs). Moreover, we had to consider the design at nano and atomic scale of the MOF shell (fine control of shell thickness at the nanoscale and functionalization of micropores at the atomic scale).

In Chapter 5, we investigated the preparation and functional characterization of some novel hybrid composites based on 2D materials (graphene and MoS_2). The central scope of this study was the synthesis of nanostructured composite materials through a fast and simple one-pot synthesis taking place in a “travelling microreactors”. In fact, we exploited the aerosol process for the synthesis of these materials, whereeach aerosol droplet containing the material precursors can be considered as a true microreactor.[28] Aerosol process is an extremely versatile method to synthesize nanostructured materials because by changing the composition of the starting solution it is possible to obtain materials with an increasing level of complexity. Using the modular insertion of suitable precursors in the starting solution, it is possible to synthesize different types of graphene-based materials ranging from heteroatom-doped graphene nanoballs to hierarchical nanohybrids made up by nitrogen-doped crumpled

graphene nanosacks that wrap finely dispersed MoS_2 nanoparticles. These materials were carefully investigated by microscopic (SEM, standard and HR TEM), diffraction (grazing incidence X-ray diffraction (GIXRD)) and spectroscopic (high resolution XPS, Raman and UV−visible spectroscopy) techniques, evidencing that nitrogen dopants provide anchoring sites for MoS_2 nanoparticles, whereas the crumpling of graphene sheets drastically limits their aggregation. The activity of these materials was tested toward the photoelectrochemical production of hydrogen.[29] This hybrid material can actually be considered a multifunctional catalyst since it is based on the interaction between two moieties that are responsible for the creation of a p-n nanojunction and have two synergistic roles (imparting good electric conduction the Nitrogen doped graphene, and lowering the overpotential the MoS_2) inside a unique catalytic reaction that is the photoinduced hydrogen evolution reaction. From a general point of view, the *in situ* hydrogen production is an important reaction in the field of tandem catalysis, because H_2 could be immediately employed in a successive reaction after the *in situ* production, therefore a more complex synthesis can become safer and more sustainable. The sustainability of this process is highlighted also by the role of the solar light that significantly reduces of the overpotential necessary to start the hydrogen production and by the absence of noble metals in the catalyst. Moreover, the structure of this hybrid could be considered a model for the synthesis of other catalysts based on 2D nanosheets and the experience acquired with this synthesis will be very important for the synthesis of other nanostructured materials. The control over the NPs dispersion is fundamental for the synthesis of a tandem catalyst, in which the formation of spatially controlled heterointerfaces is exploited to control and orchestrate the catalytic activity.

References

[1] J. M. Thomas,W. J. Thomas, Principles and Practice of Heterogeneous Catalysis 2nd Edition, **2014**, 656-658.
[2] ExxonMobil. Outlook for Energy: A View to 2040, **2015**, 1−80.
[3] C. M. Friend, X.Bingjun *Acc. Chem. Res.* **2017**, 50, 517−521.
[4] R. Breslow, *Acc. Chem. Res.* **1995**, 28 (3), 146−153.
[5] R. Si, , M. Flytzani-Stephanopoulos, *Angew. Chem. Int. Ed.***2008**, 47, 2884–2887.
[6] X.W. Xie, Y. Li, Z. Q. Liu, M. Haruta, , W. J. Shen, *Nature* **2009,** 458, 746–749.
[7] M. Cargnello, V. V. T. Doan-Nguyen, T. R. Gordon, R. E. Diaz, E. A. Stach, R. J. Gorte, P. Fornasiero, C. B. Murra, Science **2013** , 341(6147), 771-773.
[8] I. Ilgaz Soykal, H. Sohn, D. Singh, J. T. Miller, U. S. Ozkan, *ACS Catal.*, **2014**, 4 (2), 585–592.
[9] G. A. Somorjai, Y. Li, Introduction to Surface Chemistry and Catalysis, 2nd Edition, ISBN: 978-0-470-50823-7, Wiley.
[10] A. T. Bell, *Science* **2003**, 299(5613), 1688-1691.
[11] A. K. Geim, K. S. Novoselov, *Nature Materials* **2007,** 6, 183 – 191.
[12] X. Fan, G. Zhang , F. Zhang, *Chem. Soc. Rev.*, **2015**, 44, 3023-3035
[13] J. R. Long, O. M. Yaghi, *Chem. Soc. Rev.,* **2009**, 38, 1213-1214.
[14] C. M. Doherty, D. Buso, A. J. Hill, S. Furukawa, S. Kitagawa, P. Falcaro, *Acc. Chem. Res.*, **2014**, 47 (2), 396–405.
[15] J. A. Mata, F. E. Hahnd, E. Peris, *Chem. Sci.*, **2014**, 5, 1723-1732
[16] J. C. Wasilke, S. J. Obrey, R. T. Baker, G. C. Bazan, *Chemical reviews*, **2005,** *105*, 1001-1020.
[17] F.-X. Felpin, E. Fouquet *ChemSusChem* **2008**, 1, 718 – 724.
[18] G. Ertl, "Reactions at surfaces: from atoms to complexity", *Nobel Lecture*, **2007.**
[19] J. Adanez, A. Abad, F. Garcia-Labiano, P. Gayan, L. F. De Diego, *Prog. Energy Combust. Sci.*, **2012**, 38, 215–282.
[20] S. K. Ngoh, D. Njomo, *Renewable Sustainable Energy Rev*., **2012**, 16, 6782–6792.
[21] C. Trevisanut, O. Vozniuk, M. Mari, S. Yurena, A. Urrea, C. Lorentz, J.-M. M. Millet, F. Cavani, *Top Catal* ,**2016**, 59, 1600–1613.
[22] F. Carraro, O. Vozniuk, L. Calvillo, L. Nodari, C. La Fontaine, F. Cavani, S. Agnoli, *J. Mater. Chem. A*, **2017**, 5, 20808-20817.
[23] W.-J. Shen, Y. Matsumura, *Journal of Molecular Catalysis A: Chemical* **2000,** 153, 165-168.
[24] W. M. Bloch, A. Burgun, C. J. Coghlan, R. Lee, M. L. Coote, C. J. Doonan, C. J. Sumby, *Nat. Chem*., **2014**, 6
[25] M. C. So, S. Jin, H. Son, G. P. Wiederrecht, O. K. Farha, J. T. Hupp, *J. Am. Chem. Soc.*, **2013**, 135 (42), 15698–15701.
[26] Y. Yamada, C.K. Tsung, W. Huang, Z. Huo, T. Soejima, C.E. Aliaga, G.A. Somorjai, P. Yang, *Nat. Chem.,* **2011**, 3(5), 372-6.
[27] Q.-L. Zhu, Q. Xu *Chem. Soc. Rev.*, **2014**, 43, 5468.
[28] Y. Chen, F. Guo, A. Jachak, S.-P. Kim, D. Datta, J. Liu, I. Kulaots, C. Vaslet, H. D. Jang, J. Huang, A. Kane, V. B. Shenoy, R. H. Hurt, *Nano Lett*. **2012** , 12(4),1996–2002.
[29] F. Carraro, L. Calvillo, M. Cattelan, M. Favaro, M. Righetto, S. Nappini, I. Píš, V. Celorrio, D. J. Fermín, A. Martucci, S. Agnoli, G. Granozzi, *ACS Appl. Mater. Interfaces*, **2015**, 7 (46), 25685–25692.

Chapter 2

Atomic scale design of crystal structures

2. Atomic scale design of crystal structures

In this chapter, we will discuss the design at the atomic scale of spinel oxides based catalysts for the hydrogen production through the chemical loop reforming of ethanol. This study is focused on the investigation by means of an *operando* technique (Quick-EXAFS) of the correlation between the atomic scale design of crystal structures and catalytic activity. For the first time, we have investigated the redox properties in real catalytic conditions of a series of archetypal spinel structures identifying what are the most active reaction sites and how the cation environment is changing during chemical reduction.[1] Quite notably, we were able to demonstrate that the redox properties of the materials, and therefore their catalytic activity can be modified by controlling the cation sites occupancy inside the spinel structure. This study was carried out in collaboration with Prof. Cavani's group at the University of Bologna, a leading group in the field of chemical looping processes. We deeply investigated, in *operando* conditions, the chemical and structural changes occurring during the steam reforming of ethanol on nanocatalysts based on Fe, and Co mixed oxides with spinel structure. (i.e. $CoFe_2O_4$ and $FeCo_2O_4$). In particular, the steam reforming is achieved using a thermochemical loop that consists of the sequential dosing of ethanol and water, which therefore determine reduction and oxidation cycles in the materials. By performing QuickEXAFS experiments at the Fe and Co K edges, we have followed the kinetics of the phase transformations induced by ethanol, during which the ferrites are transformed to more reduced oxides (i.e. excess cation spinels and the wustite-like phases) and eventually metal phases. Similarly, we have investigated the oxidation process of the reduced form of the catalysts operated by water. This study has allowed correlating the cation nature and the occupation site in the spinel structure (tetrahedral or octahedral sites) with the redox properties in this wide family of binary and ternary oxides. This fundamental knowledge represents a stepping stone for a surgical preparation of functional materials, where the environment of every single cations is specifically designed to achieve a specific a specifically calibrated chemical activity. Moreover, this study highlights the importance of advanced characterization technique in operando conditions in the field of catalysis and in the design at the atomic scale of the materials. Only with a deep and precise knowledge of the structure of the catalyst, both as-prepared and in working condition, is possible to developed a rational design of new materials tailored for specific catalytic processes.

2.1 Spinel structure

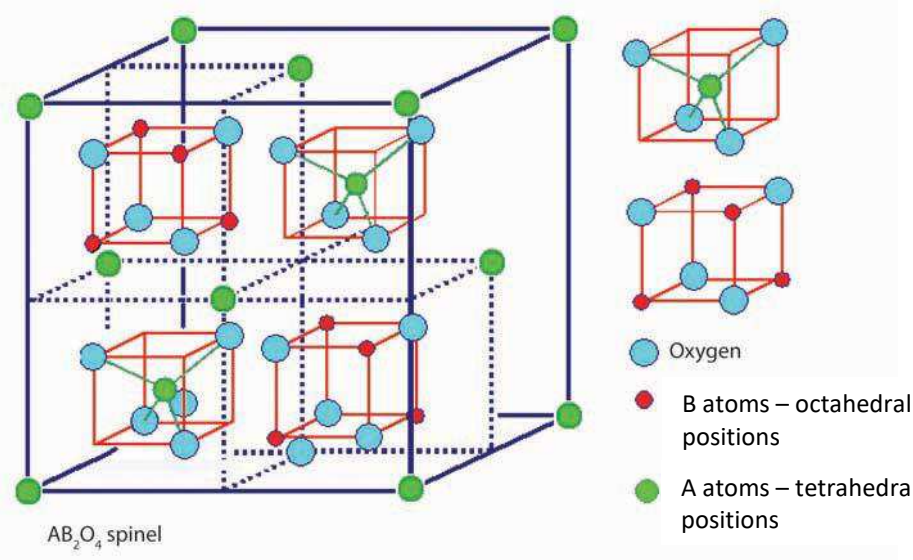

Figure 1: schemtatic view of the spinel structure of a spinel oxide with general composition AB_2O_4. Image adapted from: http://www.tf.uni-kiel.de/matwis/amat/def_en/kap_2/basics/b2_1_6.html.

Spinel structure is based on the cubic close packed arrangement of anions whose tetrahedral and octahedral interstices are occupied by metal cations.[2] An array of n close packed anions, produces 2n tetrahedral holes and n octahedral holes. One-eighth of tetrahedral and one-half of octahedral holes are occupied. Usually, i.e. in normal spinels, A cations occupy tetrahedral sites and B cations occupy octahedral sites (Figure 1).

Therefore, the AB_2X_4 stoichiometry can be expressed as $A_{2n/8}B_{n/2}X_n$. Alternatively, the spinel structure and can be also described as an fcc array of A cations into which are present smaller cubes with stoichiometry B_4X_4 and AX_4. Cations A and B can be arranged in different ways over the different coordination sites of the spinel structure. There are two limit cases of cation sites occupancy. If A and B cations occupy respectively only tetrahedral and octahedral sites, the structure is known as “normal” spinel. Conversely, if B cations occupy all the tetrahedral sites, and therefore octahedral sites are occupied by A and B, the structure is known as “inverse” spinel. Usually the parameter γ, known as inversion parameter, is used to describe the cation sites occupancy in spinels. The inversion parameter (or degree of inversion) corresponds to the fraction of tetrahedral sites occupied by B cations. The two limit cases are γ=0 and γ=1 that corresponds to normal and inverse spinel structures, respectively. Spinels redox properties, and more generally their catalytic activity, are strongly influenced by the nature of cations A and B and by their distribution among the octahedral and tetrahedral sites. In fact, spinels with general formula AB_2O_4 could be variably filled by metal cations in such a way that the overall electroneutrality of the system is maintained. In general, A is a divalent and B is trivalent. However, any combination of A and 2B that lead to a total charge of +8 can be fit into a spinel structure. Depending on the nature of cations, the degree of inversion of a spinel is determined in a complex way by several parameters such as covalent bonding effects, crystal field stabilization energies (CFSE), cation geometric size and thermal history of the material (Figure 2). For example, according to crystal field theory, the octahedral site preference energy (OSPE) of cations is defined as the difference in the crystal field stabilization energy between octahedral and tetrahedral fields. A greater absolute OSPE value means that the cations will preferably occupy the octahedral interstices.

Table 1: Crystal Field Stabilization Energies (CFSE) and Octahedral Site Preference Energies (OPSE) of different cations. Table adapted from "Burns, R. G. Mineralogical Applications of Crystal Field Theory; Cambridge University Press: Cambridge, U.K., 1993; p 249".

Ion	No. of 3d electrons	CFSE (kJ mol^{-1})		OSPE (kJ mol^{-1})
		Octahedral field	Tetrahedral field	
Sc^{3+}	0	0	0	0
Ca^{2+}	0	0	0	0
Ti^{4+}	0	0	0	0
Ti^{3+}	1	-87.4	-58.6	-28.8
V^{3+}	2	-160.2	-106.7	-53.5
Cr^{3+}	3	-224.7	-29.3	-157.8
Cr^{2+}	4	-100.4	-29.3	-71.1
Mn^{3+}	4	-135.6	-40.2	-95.4
Mn^{2+}	5	0	0	0
Fe^{3+}	5	0	0	0
Fe^{2+}	6	-49.8	-33.1	-16.7
Co^{3+}	6	-188.3	-108.8	-79.5
Co^{2+}	7	-92.9	-61.9	-31.0
Ni^{2+}	8	-122.2	-36.0	-86.2
Cu^{2+}	9	-90.4	-26.8	-63.7
Zn^{2+}	10	0	0	0
Ga^{3+}	10	0	0	0
Ge^{3+}	10	0	0	0

As summarized in table 1, the absolute OPSE value of Co^{3+} (79.5 kJ mol^{-1}) is higher than that of Co^{2+} (31 kJ mol^{-1}), indicating that Co^{3+} prefers to occupy the octahedral interstices, while Co^{2+} tends to occupy the tetrahedral interstices. As a result, Co_3O_4 tends to be a normal spinel with a formula of $Co^{2+}(Co^{3+})_2O_4$. In contrast, the inverse spinel Fe_3O_4 can be expressed as $Fe^{3+}(Fe^{3+}Fe^{2+})O_4$ because the absolute OPSE value of Fe^{2+} (16.7 kJ mol^{-1}) is higher than that of Fe^{3+} (0 kJ mol^{-1}). However, these thermodynamic parameters are only the starting point for the rational design of a catalyst based on mixed spinel oxides. In fact, the thermal history of the material plays a key-role in the final structure of the spinel, highlighting the high-degree of complexity of the design at the atomic level of the site occupancy of spinel structures.

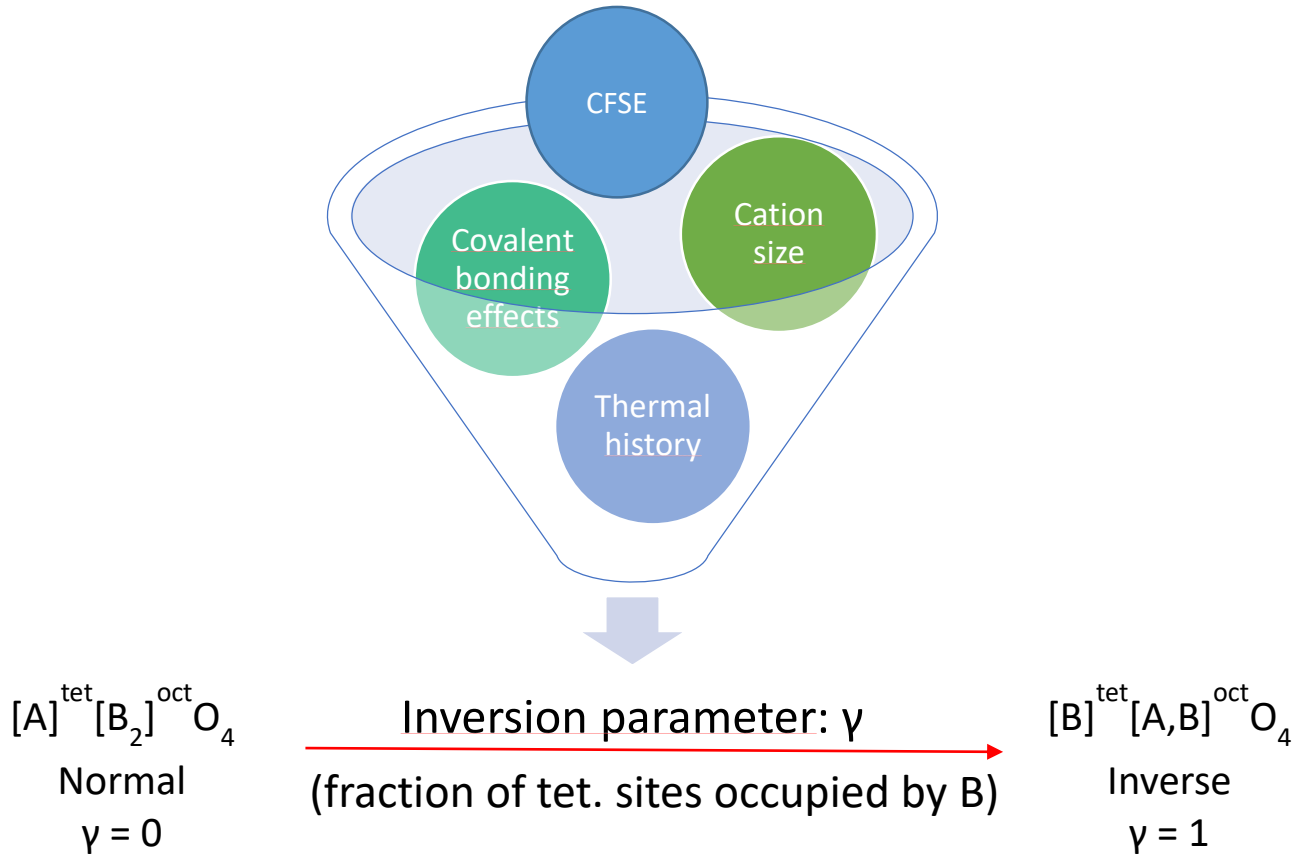

Figure 2: Schematic view of the factors that determined the inversion parameter of a spinel.

Therefore, by precisely tuning the composition and the synthesis protocols of spinel oxides is possible to obtain a wide variety of compounds with similar mechanical and thermal stabilities, but rather different chemical activity. Oxides with spinel structure are widely investigated in the literature as ionic oxygen and electron carrier materials for heterogeneous catalysis[3], gas-sensors[4], anodes for Li-ion batteries[5], electrocatalysis[6], etc (Figure 3). From the chemical point of view, spinels exhibit a quite fascinating acid-base and redox activity that are keystones of several catalytic reactions. As a matter of fact, these oxides may present Brønsted or Lewis acid (i.e. undercoordinated surface cations) and basic sites (i.e. surface hydroxyls and oxygen species). Moreover, according to the nature of the cations, they can host a variety of redox couples (e.g. Fe(II)/Fe(III) or Co(II)/Co(III)).

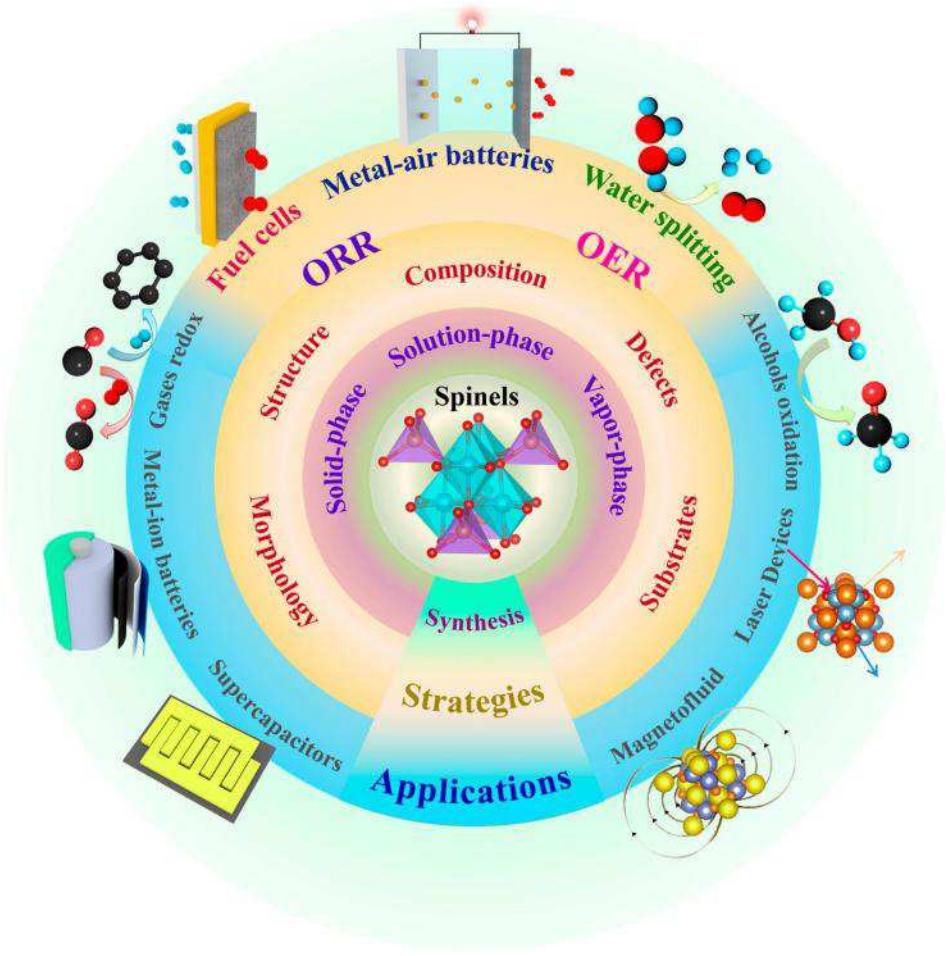

Figure 3: Illustration of the structures, synthesis, strategies, and applications of spinels. Reprinted with permission from "Qing Zhao, Zhenhua Yan, Chengcheng Chen, and Jun Chen, Chem. Rev. 2017, 117, 10121−10211". Copyright © 2017, American Chemical Society.

2.2 Iron based spinel oxides and chemical looping processes

Metal oxides have always held a strong position in catalysis given their wide use as supports, promoters, and active phases.[7,8] Quite recently though, the interest for these materials have increased even more because they perfectly satisfy the stringent requirements enforced by the new standards of sustainability and environmental "greenness"[9] of modern chemistry.[10] This has stimulated the scientific community to look for new oxides with special structural and chemical properties that are optimized for specific catalytic applications.[11] In this context, complex oxides i.e. compounds containing several types of metal cations in different structural environments, represent ideal candidates for the development of advanced materials with easily tunable multifunctional properties.[8,12] Among these, a central spot is occupied by the large family of spinels, which are crystalline oxides characterized by excellent stability associated with high structural flexibility.[13,14]

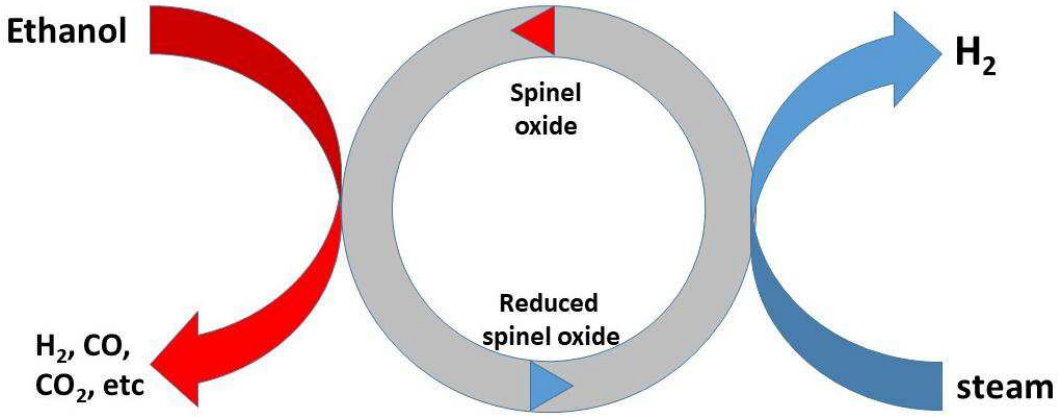

Figure 4: Schematic view of the two steps of the chemical loop reforming of ethanol catalyzed by a spinel oxide.

Hereafter, we will focus the attention on the catalytic properties of iron based spinel oxides. More precisely, we have investigated iron-cobalt mixed spinels as oxygen ion and electron carrier materials for the chemical-loop reforming (CLR) of ethanol (Figure 4). This work was carried out in collaboration with the group of Prof. Cavani (University of Bologna), one of the most expert research group in the field of CLR process. CLR redox catalytic process is aimed to the production of clean H_2. Hydrogen is considered one of the most promising energy source for the future. However, hydrogen is a secondary energy source. This means that its environmental impact and price depend on the production and purification processes. Nowadays the principle production process is the reforming of fossil hydrocarbons or coal. The drawbacks are the employment of non-renewable sources and the high CO_2 emissions. Environmentally friendly processes currently employed are based on electrolysis (from solar or wind produced electron energy) and reforming of bio-hydrocarbons. However, the hydrogen production cost is still not competitive for large-scale development.[15] Chemical looping hydrogen systems were extensively studied in the last years because they can employ renewable sources and offers an efficient CO_2 sequestration capability.[16] In fact, compared to classical reforming, the process is split into two steps.[3] In the first step, the oxygen and electron carrier is exposed to a reducing stream. Ethanol, methanol, syngas and CO are some example of possible reductants for chemical looping processes.[17] Successively, in the second step is exposed to steam in order to produce H_2 and the redox catalyst is oxidized to its initial state. Hydrogen and C-containing products are therefore produced in two separated steps. The viability of the cycling process is determined by reaction conditions and by the nature of the oxide employed as redox catalyst. In the last couple of years, spinel structured ferrites have been widely investigated in this field.[3] In fact, it was demonstrated that modifying cations nature it is possible to tailor the physical and chemical properties of spinels in order to prepare specific oxygen

and electrons carriers for a precise application, including chemical looping processes.[18] Substitution of Fe centers with other transition metals leads to the formation of an inverse, normal, or mixed spinels with different degree of inversion. Besides this, such an introduction may strongly modify the redox properties of the resultant ferrospinels.[19] Several research groups have investigated the effect of various M-additives on the stability and redox behavior of iron oxide for chemical hydrogen storage using, amongst others, Pd, Pt, Rh, Ru, Al, Ce, Ti, Zr[20] and Al, Cr, Zr, Ga, V , Mo[21]. For example, it was found out that Pd, Pt, Rh and Ru additives have an effect of promoting the reduction and lowering the re-oxidation temperature of iron oxide. At the same time, Al, Ce, Ti, Zr, Cr, Ga and V additives prevent deactivation and sintering of iron oxide during repeated redox cycles. However, according to our knowledge, a systematic study on the role of dopants and their effect on the chemical-physical properties of the resulting mixed M-modified ferrites as future perspective materials for chemical-loop reforming of ethanol has not been done until now. Thus, the aim of this work is to investigate the behavior of these new materials in the two-step chemical-loop reforming of ethanol.

2.3 X-Ray Absorption Spectroscopy: a powerful tool to investigate spinel structures

One of the most powerful probes for the structural characterization of matter is represented by the electromagnetic radiation in the x-ray region (λ between 0.1 Å and 50 Å). In this energy range, the electromagnetic radiation interacts with the electrons tightly bound to the atoms of the investigated material. The x-ray radiation could be scattered by these electrons or there could be absorption and excitation phenomena through photoelectric processes. When a monochromatic x-ray beam of intensity I_0 and energy E is passing through a sample of thickness x, it is possible to detect a decrease in the transmitted beam intensity I_1. This reduction, in analogy to the Lambert-Beer law, can be described as:

$$\ln(I_0/I_1) = \mu(E)x$$

where μ is the linear absorption coefficient and describes the probability that an x-ray photon is absorbed by the target material. Usually, μ decreases as the x-ray photons energy is increased. Only when the photon energy is equal to the bonding energy of a core-electron of an element of the material we can observe a sudden increase of the absorption coefficient. In this condition, there is an excitation of a core electron of the absorbing atom to a continuum state, so a photoelectron is produced. In an absorption spectrum, these kinds of steps are called absorption edges. The threshold energy (E_0) of an absorption edge is defined as the minimum energy needed for the emission of a photoelectron and experimentally is measured as the first inflection point of the absorption edge. Therefore, E_0 value is related to the oxidation state of the absorbing atom. Following Sommerfeld's notation, increasing the photon energy the absorption edges are labelled in the order K, L_I, L_{II}, L_{III}, M_I, etc., and correspond respectively to the emission of a photoelectron from the 1s, 2s, $2p_{1/2}$, $2p_{3/2}$, 3s, etc., orbitals.

In condensed matter, the high-energy side of the absorption edge is characterized by an oscillating trend that is called x-ray absorption fine structure (XAFS). This is due to the constructive-destructive interactions of the emitted photoelectron with the photoelectrons backscattered after interaction with the electronic density of neighbor atoms placed at a specified distance from the emitting atom. Constructive interactions between outgoing and backscattered photoelectron waves lead to an increase of the electron density and therefore to an increase of the probability of photon absorption (μ). Conversely, destructive interactions lead to a decrease of μ. Together these maxima and minima of μ lead to the oscillating trend of x-ray absorption spectra. Therefore, this fine structure oscillation is described as the modulation of the absorbance:

$$\chi(E) = (\mu(E) - \mu_0(E))/\mu_0(E)$$

where $\mu_0(E)$ is the absorption coefficent of the isolated absorbing atom and $\mu(E)$ is the measured absorbance.

Usually, the energy range between 50 and 1000 eV after E_0 is called Extended X-ray Absorption Fine Structure (EXAFS) region and the scattering processes of photoelectrons, considering the validity of sudden approximation in this energy range, can be described with the so-called EXAFS equation (in *k*-space):

$$\chi_i(k) = \sum_j \frac{N_j \cdot S_0^2(k)}{k \cdot R_j^2} \underbrace{\left|f_{eff}(k)\right|_j}_{\text{Effective amplitude function}} \underbrace{\exp(-2k^2\sigma_j^2)}_{\text{Debye-Waller factor}} \underbrace{\exp[-2R_j/\Lambda(k)]}_{\text{Mean free path factor}} \underbrace{\sin[2kR_j + \phi_{ij}(k)]}_{\text{Total phase}}$$

N_j=n° of atoms in shell j
R_j=radius of shell j
S_o^2=amplitude factor

In this equation, considering the absorbing atom *i*, EXAFS oscillations are described as a sum of modified sine waves $\chi_i(k)$ with different frequency and phase for each backscattering coordination shell *j*. For the complete theoretical background of EXAFS equation, the reader is referred to several text books, for example "EXAFS: Basic Principles and Data Analysis" by B. K. Teo (Springer, 1986). Here, we will focus our attention on the parameters that influence the EXAFS equation and consequently on the information that can be obtained from EXAFS analysis. The dumping of EXAFS oscillation $\chi_i(k)$ is due to several factors such as the disorder of the local structure or the disorder induced by thermal effects (Debye-Waller factor), the distance between absorbing and backscattering atoms (Mean free path factor) and the increase of the energy of incident photons with the respect of E_0.

Summarizing, the structure of the absorption edge of an absorbing atom is usually divided in three regions, depending on the energy E of the X-ray beam:

- Pre-edge region ($E<E_0$): low probability of x-ray absorption. Sharp pre-peaks before the edge are related to electronic transitions within the atom to empty or partially filled energy levels.
- Edge region ($E\approx E_0$): high probability of electronic transition toward unoccupied bound states or to continuum states.
- Near-edge and EXAFS regions ($E>E_0$): emission of photoelectrons with kinetic energy $E_k=E-E_0$.

In order to analyze XAS spectra, usually the spectrum is divided in two regions. The energy range $-50<E_0<50$ eV, is called X-ray Absorption Near Edge Structure (XANES), whereas the region 50-1000 eV above the edge is called EXAFS. XANES spectra can provide information about oxidation state of the absorbing atom (E_0) and bonding geometry effects (edge shape, due to the possibility of the excitation to unoccupied bound states). EXAFS can provide information on the nature and number of atoms surrounding the absorbing atom. Therefore, XAS is a powerful tool for the characterization of the local coordination environment of the absorber atom.

With a conventional laboratory x-ray source, it is in principle possible to observe these kind of features, but the low brilliance and the limited energy range that can be investigated are huge limitations for the study of these phenomena. Only with the development of synchrotron-based radiation, the X-ray Absorption Spectroscopy (XAS) became a very powerful and versatile characterization technique for the local structure and the oxidation state of most elements ($Z>16$). In the last years, many synchrotron XAS beamlines developed different systems that permit to measure XAS *in operando* conditions in different reaction environments (i.e. gas-solid reactions, electrochemistry environment, vacuum, etc.). Moreover, one of the latest development of synchrotron based XAS is the so called QuickEXAFS. With this technique, it is possible to acquire time-resolved XAS spectra (up to 100 spectra per second) and this enables the possibility to monitor fast kinetic processes in applied materials used in catalysis and energy sciences.

Experimentally, in a typical experiment in transmission mode, the sample is aligned perpendicularly to the synchrotron x-ray beam (Figure 5). There are three different detectors (ion chambers) that can measure the intensity of the x-ray beam. One is placed before the sample, in order to measure the intensity I_0 of the incoming beam. One is placed after the sample, in order to measure the intensity of the transmitted beam I_1. Finally, the last detector is usually placed after a foil composed of the same element that is investigated. Measuring the XAS spectra of this reference foil (therefore measuring $\ln(I_1/I_2)$) is possible to calibrate the energy of the x-ray beam.

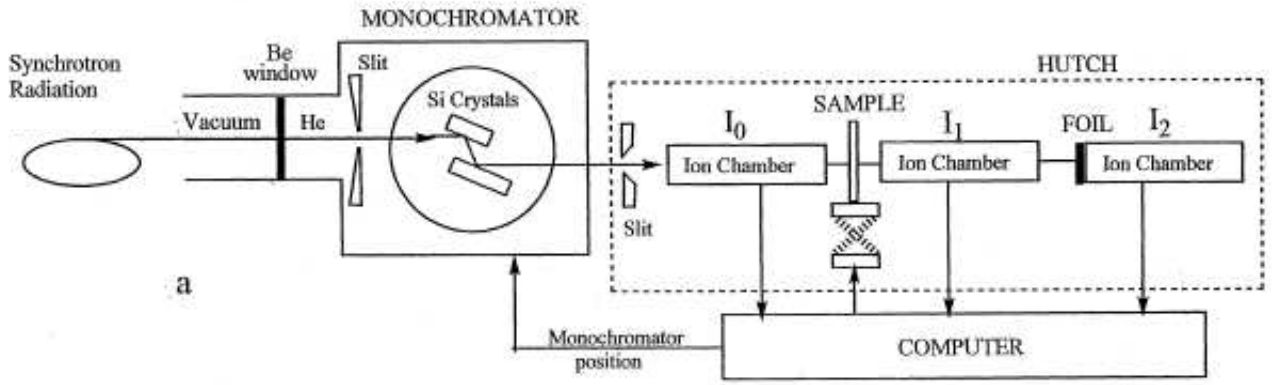

Figure 5: Experimental arrangement for XAS measurements in transmission mode (with a metal foil for the energy calibration). Image adapted from "Farideh Jalilehvand, Structure of hydrated ions and cyanide Complexes by X-ray Absorption Spectroscopy, PhD thesis, 2000"

The goal of this chapter is the discussion of the design of a catalyst at the atomic level, modifying the site occupancy of spinel structures in order to induce different catalytic activities. In order to perform this extremely sophisticated materials design, the characterization of the structure of the as-prepared catalyst and of the catalyst in real working condition is fundamental. Thanks to XAS, it is possible to have a deep insight on the local coordination environment of the atoms that composed the structure. In the literature, there are several examples of XAS studies of spinel structures. The possibility of characterizing the oxidation state and the local coordination environment (tetrahedral or octahedral) of transition metals that compose the spinel structure, combined with the possibility of performing XAS experiments in different catalytic relevant environments paves the way to several studies. However, to the best of our knowledge, in the literature there are not studies focused on mixed spinels reduction processes followed in real time (monitoring the formation of reduced phases) or studies in CLR working conditions. These kind of studies are fundamental for our purposes. In our work, we precisely investigated the local structure and were able to identify what are the most chemically active cations inside the spinel structure and what are the parameters that control the chemical activity toward ethanol.

In order to highlight the information that can be extracted from XAS studies, the XANES spectra of different oxides containing Fe and Co, measured at the Co and Fe K-edges are reported in figure 6. $CoFe_2O_4$ and $FeCo_2O_4$ are the spinels that were investigated as CLR catalysts, Co_3O_4, Fe_3O_4, Fe_2O_3 and CoO were measured as reference material. In transition metals K-edges, XANES transitions involve the excitation of a 1*s* photoelectron into a mainly 4*p* derived continuum of states. The peak of the absorption edge, located 5-10 eV after the threshold energy, is called with-line and is related to these transitions. In general, when the valence of the absorbing metal atom is increased (i.e the metal is present in a higher oxidation state), a shift of the absorption edge toward higher energy is observed. Comparing the energy position of the absorption edge in the XANES spectra with that of the reference samples, it is possible to determine with great accuracy the oxidation state of each element in the spinel structure. From these XANES spectra we can therefore determine the oxidation state of Co and Fe in the two investigated mixed-spinels by comparing their edge position with that of reference compounds. From the shape of the edge, it is possible to infer that these materials have different local coordination geometry and the analysis the XANES spectra allows quantifying the contribution of different species in an unknown phase (XANES fits will be discussed in the "results and discussion" section of this chapter). Moreover, in these spectra it is possible to appreciate the contribution of the tetrahedral coordination of absorbing atom in the pre-peak feature. Tetrahedral coordination is non-centrosymmetric whereas octahedral coordination in highly centrosymmetric. If Fe, or Co, have a highly non-centrosymmetric coordination environment, the transition from

1*s* to 3*d* states (with 3*d*-4*p* mixing) is enabled. This loss of inversion symmetry in the environment of the absorbing atom causes an increase in the intensity of the pre-peak located at about 15-20 eV before the threshold energy. Therefore, from the analysis of XANES spectra it is possible to determine accurately the mean oxidation state of the absorbing atom in the investigated material and to obtain information about its local coordination environment (tetrahedral or octahedral). EXAFS spectra analysis may give us even more precise information about local coordination (i.e. nature of backscattering atoms, ratio between octahedral and tetrahedral coordinated atoms), but this analysis will be discussed later in this chapter.

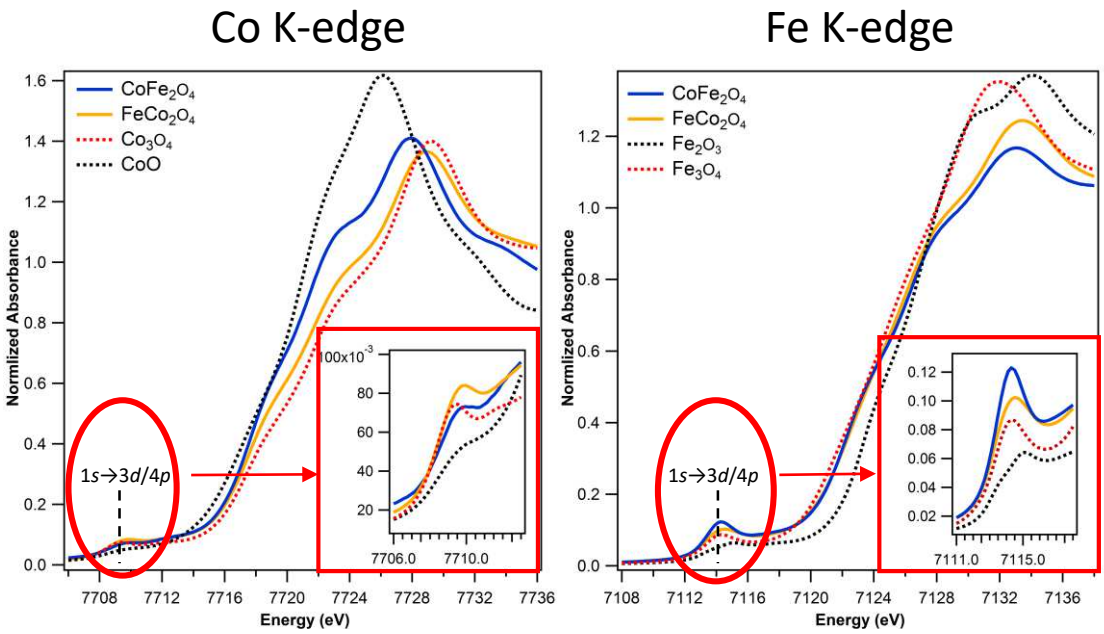

Figure 6: X-ray Absorption Near-Edge Structure (XANES) spectra at Co and Fe K-edges of references and of as-prepared investigated materials. The spectra were collected in transmission mode.

2.4 *Operando* XAS investigation of reduction and oxidation processes in cobalt and iron mixed spinels during the chemical loop reforming of ethanol

As already mentioned, spinels, in their simplest and most typical form, are formed by divalent and trivalent cations in a 1:2 ratio. However, almost any type of cation combination, encompassing also monovalent and tetravalent ions in the right stoichiometry, can be fitted into the structure. This gives access to the preparation of a wide range of oxide materials that exhibit a large gamut of different physicochemical properties. Nonetheless, the huge potential of spinels, inherent to their structural and chemical versatility, has been only partially exploited in practical applications because of a limited understanding of very fundamental processes such as their oxidation/reduction or phase transitions and their dynamic behavior *in operando* conditions.[22]

Unfortunately, the high versatility and flexibility of spinel structures design come at a price of high complexity, so a high level of empiricism characterizes this field. A substantial gap of knowledge still prevents a rational design of spinel materials for specific catalytic applications.

Recently however, due to the development of advanced *in operando* techniques, it has been possible to obtain an exceptionally detailed understanding about the structure/activity correlation in these materials. As an example, it has been shown by X-ray absorption spectroscopy (XAS), that the high chemical reactivity observed in Mn based spinel catalysts in the oxygen evolution reaction and oxygen evolution reaction can be traced back to Mn in octahedral sites.[23] On the other hand, in the field of gas-phase heterogeneous catalysis, it has been demonstrated by *in situ* Diffuse Reflectance Infrared Fourier Transform Spectroscopy (DRIFTS) combined with x-ray absorption spectroscopy (XAS) and Raman spectroscopy, that octahedral coordinated Co(II) sites are more easily oxidized to Co(III) in comparison with Co(II) in tetrahedral site, and Co(III) species are the active centers for the oxidation of organic volatile compounds.[24]

These results highlight the great interest for understanding the interplay between geometrical (e.g. tetrahedral vs octahedral occupancy) and chemical factors (e.g. oxidation state) to determine the final reactivity of materials.

In our study, we decided to investigate two exemplary mixed Co-Fe spinels, the cobalt rich iron cobaltite ($FeCo_2O_4$) and the iron rich cobalt ferrite ($CoFe_2O_4$). This latter has demonstrated to be an extremely interesting material for electrocatalysis,[25,26] oxidation reactions,[27,28] and as oxygen or electron carriers[29] for a two steps Chemical Loop Reforming (CLR).[3,30,31,32] On the contrary, very few works are focused on $FeCo_2O_4$ and its potential in catalysis still is largely untapped.[33,34,35]

As discussed in the previous section, CLR represents a potentially carbon neutral process for the production of high purity hydrogen. It is based on a dual thermal redox cycle. At first the oxide material is exposed to reducing atmosphere to obtain highly reduced phases and then to steam for its reoxidation and consequent formation of H_2.[36]

We have focused our attention on the use of ethanol as reducing agent.[37] This choice is quite appealing because ethanol is a not toxic, low cost, fuel that can be easily obtained from renewable sources and on the other hand Co-Fe mixed spinel are abundant and cheap materials with a low environmental impact. CLR of ethanol on spinels therefore has a great potential for the sustainable production of hydrogen.

By a combination of different *in situ* characterization techniques and catalytic measurements we have investigated the structural and chemical properties of these mixed Co-Fe spinels during each step of the CLR of ethanol. For the first time, we were able to follow in real time, the reduction process of mixed spinels, monitoring the formation of a series of reduced phases. We were also able to identify which are the most chemically active

cations inside the spinel structure and what are the parameters that control the chemical activity toward ethanol (Figure 7).

The fundamental knowledge acquired in this study may be a stepping stone for the design of new improved materials to be used as solid oxygen carriers and novel catalysts for the selective oxidation of alcohols.

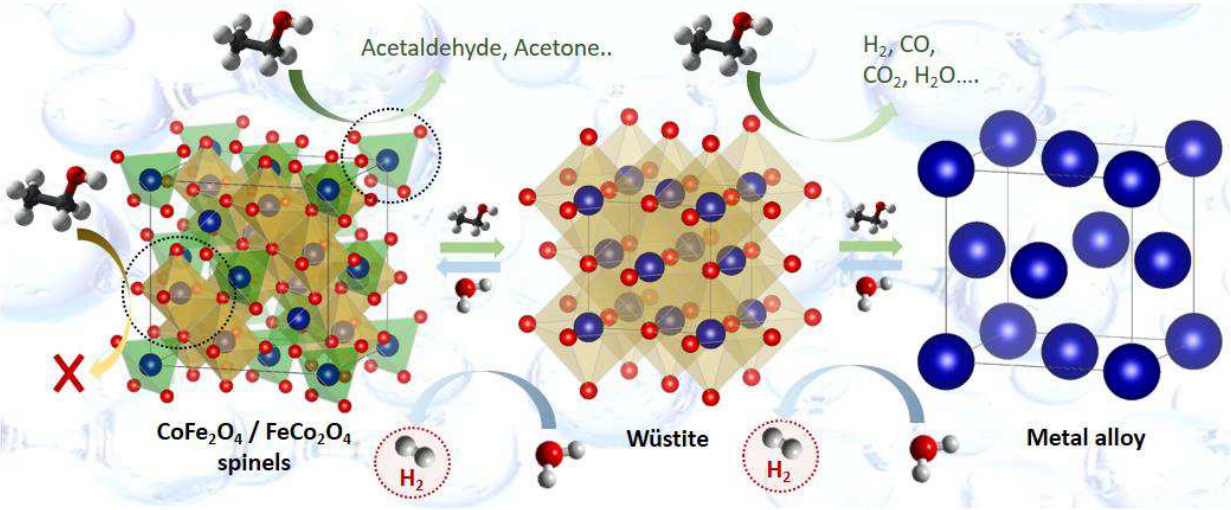

Figure 7: Schematic view structural changes investigated by XAS occurred during the chemical loop reforming of ethanol and of the reaction products. Reproduced from Ref. 1 with permission from the Royal Society of Chemistry.

2.4.1 Experimental section

Synthesis of spinel oxides

$CoFe_2O_4$ (cobalt ferrite) and $FeCo_2O_4$ (iron cobaltite) that were prepared by a simple precipitation route from aqueous solutions. $CoFe_2O_4$ was synthesized by Prof. Cavani group (University of Bologna), using the co-precipitation method reported by Vozniuk et al.[42] Briefly, a solution containing metal nitrate precursors in the desired molar ratios was drop-by-drop added into the reaction vessel containing 0.5 L of 2 M NaOH (Sigma-Aldrich) aqueous solution at 50°C under vigorous stirring. The suspension was stirred for 2 h at 50°C keeping the pH above 13 by adding a 3M NaOH solution if necessary. The precipitate was separated by vacuum filtration, washed with distilled water and dried at 120°C. Finally, the solid material was calcined in static air at 450°C for 8h with the heating rate of 10°C min^{-1}. $FeCo_2O_4$ was synthesized following a recipe previously reported in literature.[43] Briefly, iron chloride ($FeCl_3 \cdot 6H_2O$, Sigma-Aldrich) and cobalt chloride ($CoCl_2 \cdot 6H_2O$, Sigma-Aldrich), with a Co:Fe molar ratio of 2:1 , were dissolved in distilled water and poured into a boiling 2M KOH solution under vigorous stirring at 80°C for 1 hour. After repeated filtering and washing with boiling distilled water, the resulting power was dried at 120°C and then calcined at 900°C for 17h with a heating rate of 5°C min^{-1}.

Materials characterization

Operando Quick EXAFS measurements were carried out in transmission mode at the Fe K and Co K edges at the ROCK beamline (SOLEIL synchrotron, France). The Quick-EXAFS monochromator (equipped with a Si(111) channel-cut crystal) operated at an oscillation velocity of 2 Hz. The detectors were ionization chambers. The samples in powder form were diluted with boron nitride (mass ratio=1:1.2) and inserted into quartz capillaries (diameter=1.5 mm, wall thickness=0.03 mm). The capillaries were centered perpendicularly to the X-ray beam

and connected to a heated gas line. The samples were heated at the desired temperature (from RT to 500°C) by a heating gun. During the annealing in reductive atmosphere (from RT to 500°C, 5°C min-1), ethanol was dosed using a syringe pump and nitrogen as carrier gas (0.69% of ethanol in N_2). During chemical loop reforming (CLR) of ethanol the samples were heated at the desired temperature (350 or 450°C) in inert atmosphere. Then ethanol and water were dosed alternatively (20 or 40 minutes steps) using syringe pumps and nitrogen as carrier gas. EXAFS spectra were continuously acquired during these processes. The corresponding metal foils were measured simultaneously and used to calibrate and align the spectra. Pellets of the various oxide standards were measured in transmission mode at RT.

XAS data were analyzed using the software based on the IFEFFIT library, ATHENA and ARTEMIS.[38] The XANES spectra were separated into different chemical species using the Linear Combination Fitting (LCF) analysis. Normalized spectra of the corresponding metallic Fe,Co, FeO, CoO, Fe_3O_4, Co_3O_4, Fe_2O_3, fresh ferrite and cobaltite were used as predictor components. EXAFS fits were performed employing two clusters of atoms, one having the absorbing atom in tetrahedral site (A site, considering the general formula of a normal spinel AB_2O_4) and one having the absorbing atom in octahedral site (B site, considering the general formula of a normal spinel AB_2O_4).[39] Within this model, the parameter x_b(M) is the fraction of A (Fe in $FeCo_2O_4$ or Co in $CoFe_2O_4$) cations in octahedral sites. Consequently, the occupation of tetrahedral sites by B cations, which also corresponds to the inversion parameter *γ,* is defined by the parameter x_a(M)=1- x_b(M). It has to be noticed that the fraction of M^{3+} in B sites must satisfy the requirement $x_b(Fe^{3+})=(2-x_b(Co^{2+}))/2$ in the case of $CoFe_2O_4$ and $x_b(Co^{3+})=(2-x_b(Fe^{3+}))/2$ in the case of $FeCo_2O_4$. In the two clusters used for simulating EXAFS spectra, the coordination numbers N_i were kept fixed, whereas R_i (interatomic distance of the i^{th} shell), $2\sigma_i^2$ (mean square displacement about the half-path length of the i^{th} path) and E_0 (energy shift) were free to vary.

Powders were characterized by P-XRD in a Philips X'Pert X'Celerator, with Cu-kα radiation in a 2θ range between 5-80° with step of 0.1°. These measurements were acquired by Prof. Cavani group.

Characterization by Raman spectroscopy was performed using a ThermoFisher DXR Raman microscope. The spectra were recorded using a laser with an excitation wavelength of 532 nm (5 mW), focused on the sample with a 10× objective (Olympus).

The specific surface area was measured applying the single-point BET method, using a Carlo Erba Sorpty 1700.

Energy Dispersive X-ray Spectroscopy of the as prepared materials were acquired using a field emission electron source equipped with a GEMINI column (Zeiss Supra VP35), and confirmed the expected chemical composition of the two fresh catalysts.

Mössbauer spectroscopy studies were performed by Dr. Nodari (CNR-ICMATE, Padova) on a conventional constant acceleration spectrometer, with a room-temperature (hereafter RT) Rh matrix ^{57}Co source, nominal strength 1850 MBq. The hyperfine parameters isomer shift (δ), quadrupole shift (ε), full linewidth at half maximum (Γ), were expressed in mms^{-1} while internal magnetic field (B) in Tesla and the relative area (A) in %. The parameters were obtained by means of standard least-squares minimization techniques. In order to allow the ordering of all the magnetic components and to obtain a good estimation of the sites population, 80 K measurements were performed by using liquid nitrogen static cryostat. 80 K spectra were fitted using the following procedure. Firstly, the spectra were fitted with the minimum number of sextet, whose parameters are indicative of the octahedral and tetrahedral population.[40] Once estimated the degree of inversion, defined as the Fe(III) population in the tetrahedral sites, γ the spinel stoichiometry was determined. Then the fitting procedure was improved considering the effect of tetrahedral next-nearest (NN) neighbour on the octahedral sites, as

suggested in literature. Assuming a statistical occupation of tetrahedral sites by Fe(III) and Co, the magnetic pattern of the octahedral sites was fitted with the proper number of sextet obtained by applying a binomial distribution:

$$P(m) = \frac{6!}{m!\,(6-m)!}\gamma^{m}(1-\gamma)^{6-m}$$

P(m) represents the probability of finding *m* Fe atoms in a shell of NN neighbor tetrahedral sites, depending on the degree of inversion, γ. The obtained results were used to determinate the numbers of sub-components of the octahedral sites and their relative area.

Reactivity experiments were carried out by Dr. O. Vozniuk (Prof. Cavani Group) by loading 400 mg of the pelletized sample (with particles diameter ≈0.25 to 0.6 mm) in the fixed-bed quartz flow reactor with an internal diameter of 12 mm and a length of 30 cm. The products were monitored on-line by an Agilent 3000A micro-GC with 3 parallel columns: (A) a PlotQ column, with He carrier, for the separation of CH_4, CO_2, H_2O, ethylene, ethane, propane, etc.; (B) a OV1 column, with He carrier, for the separation of ethanol, CO_2, acetaldehyde, H_2O, acetone, acetic acid, ethyl acetate, diethyl ether, 2-pentanone, toluene, etc.; (C) a Molecular Sieve 5A column, Ar carrier, for the separation of H_2, O_2, N_2, CH_4, and CO. A Plot U back flash column was installed in order to avoid CO_2 and H_2O poisoning in the third column. Anaerobic oxidation tests were carried out at 450°C (for 20 min) by feeding continuously a stream of ethanol vapors (app.15 mol%) in N_2; the latter was also used as a standard. Yields of each product were calculated by the same method as described in a previous publication of Cavani et ali.[41]

2.4.2 Results and Discussion

Characterization of as-prepared catalysts

Combining X-ray Diffraction (XRD), Raman spectroscopy, Energy Dispersive X-ray spectroscopy (EDX), Mössbauer and X-ray Absorption Spectroscopy (XAS), we have determined the structure and the chemical composition of the two samples.

Figure 8b shows the XRD data for the two Co-Fe oxides. The pattern of $CoFe_2O_4$ shows the typical reflections of magnetite (Fe_3O_4), as reported in our previous papers[42] Similarly, the diffraction data of $FeCo_2O_4$ indicate the formation of a spinel structure.[43,44] No other phases are observed, confirming that a homogeneous and highly crystalline $FeCo_2O_4$ phase is formed at the synthesis temperature (i.e. 450°C for $CoFe_2O_4$ and 900ºC $FeCo_2O_4$). As a consequence of the elevated calcination temperature, the iron cobaltite exhibits lower specific surface area (4 $m^2\ g^{-1}$) and larger crystallite size (32 nm) than cobalt ferrites (12 nm crystallite size, 69 $m^2\ g^{-1}$ surface area) (see Table 2). The spinel structure of both samples is also confirmed by the Raman spectra reported in Figure 8a. Vibrational spectroscopy is a powerful technique for the structural analysis of spinel oxides, since their spectroscopic fingerprint is highly specific, and strongly affected by stoichiometry, cation distribution, and defects. The Raman spectra of spinels are generally complex and show more Raman-active modes than those predicted by group theory: $F_{2g}(1)$, E_g, $F_{2g}(2)$, $F_{2g}(3)$ and A_{1g}. The additional vibrations may appear because of local distortions of the crystal lattice. These defects do not affect the long range order of the system, and often cannot be directly detected by XRD. The strong intensity and sharpness of the bands in the $FeCo_2O_4$ spectrum confirm the high crystallinity of the sample. Five main vibration modes are observed at 192, 479, 507, 598 and 673 cm^{-1}, the latter showing a shoulder at about 645 cm^{-1}. The most intense vibration modes are related to MO_4 (the peak at 673 cm^{-1} and its shoulder) and MO_6 stretching (at 192 cm^{-1}). The $CoFe_2O_4$ spectrum presents six vibration modes, as already reported in the literature.[45] The five first order Raman modes can be observed at about 182,

306, 476, 562, 636 and 690 cm^{-1}. The intense vibration modes at 636 and 690 cm^{-1} are the $A_{1g}(2)$ and $A_{1g}(1)$, respectively, which can be assigned to the MO_4 stretching vibrations and to the disorder effect of Co(II) and Fe(III) over the T_d and O_h sites.[45,46]

Table 2: Summary of materials properties: degree of inversion surface area, crystallite size and particle size.

Sample	**γ (EXAFS)**	**γ (Mössbauer 80K)**	**SSA, m^2/g (N_2 adsorption)**	**Crystallite size, nm (XRD)**	**Particle size, nm (N_2 adsorption)**
$CoFe_2O_4$	0,8	0,74	69	12	16,2
$FeCo_2O_4$	0,6	0,56	4	32	275

The oxidation state and site occupancy of the metal species in the spinel structure were determined by ex-situ XAS.[47,48,49] In transition metals K-edges, XANES transitions involve the excitation of a 1s photoelectron into a mainly 4p derived continuum of states. In general, when the valence of the absorbing metal atom is increased (i.e the metal is present in a higher oxidation state), a shift of the absorption edge toward higher energy is observed. XANES and Fourier Transform (FT) EXAFS spectra for the Co-Fe spinels are shown in Figure 8 c,d,e,f. Comparing the energy position of the absorption edge in the XANES spectra with that of the reference samples, it is possible to determine with great accuracy the oxidation state of each element in the spinel structure (Figure 8 c,d,e,f). In $CoFe_2O_4$, the oxidation state of Fe and Co is close to +3 and +2, respectively, as expected;[47] whereas in $FeCo_2O_4$, the oxidation state for Fe and Co are +3 and +2/+3, respectively. Moreover, the fine structure of the pre-edge can provide further information about the structure of spinels.[47,48,49] At K-edges in fact, pre-edge peaks, which correspond to 1s $\rightarrow$ 3d transitions (with 3d-4p mixing), may occur at about 15-20 eV before the white line. An increase of the intensity of these features corresponds to the removal of the inversion symmetry in the environment of the absorbing atom. Therefore, the pre-edge feature can provide a direct indication whether a metal center is located in a tetrahedral or octahedral site. At the Co K-edge, the pre-edge peak intensity of cobaltite is higher than that of ferrite, indicating that the cobaltite contains a higher amount of tetrahedrally coordinated Co ions. Conversely, the Fe K-edge pre-peak intensity is higher in the $CoFe_2O_4$ sample. The cation distribution was determined by EXAFS data of the starting materials.[47,49] The crystallographic site occupancy in spinels is defined by the inversion parameter γ, i.e. the fraction of tetrahedral sites occupied by majority ions.

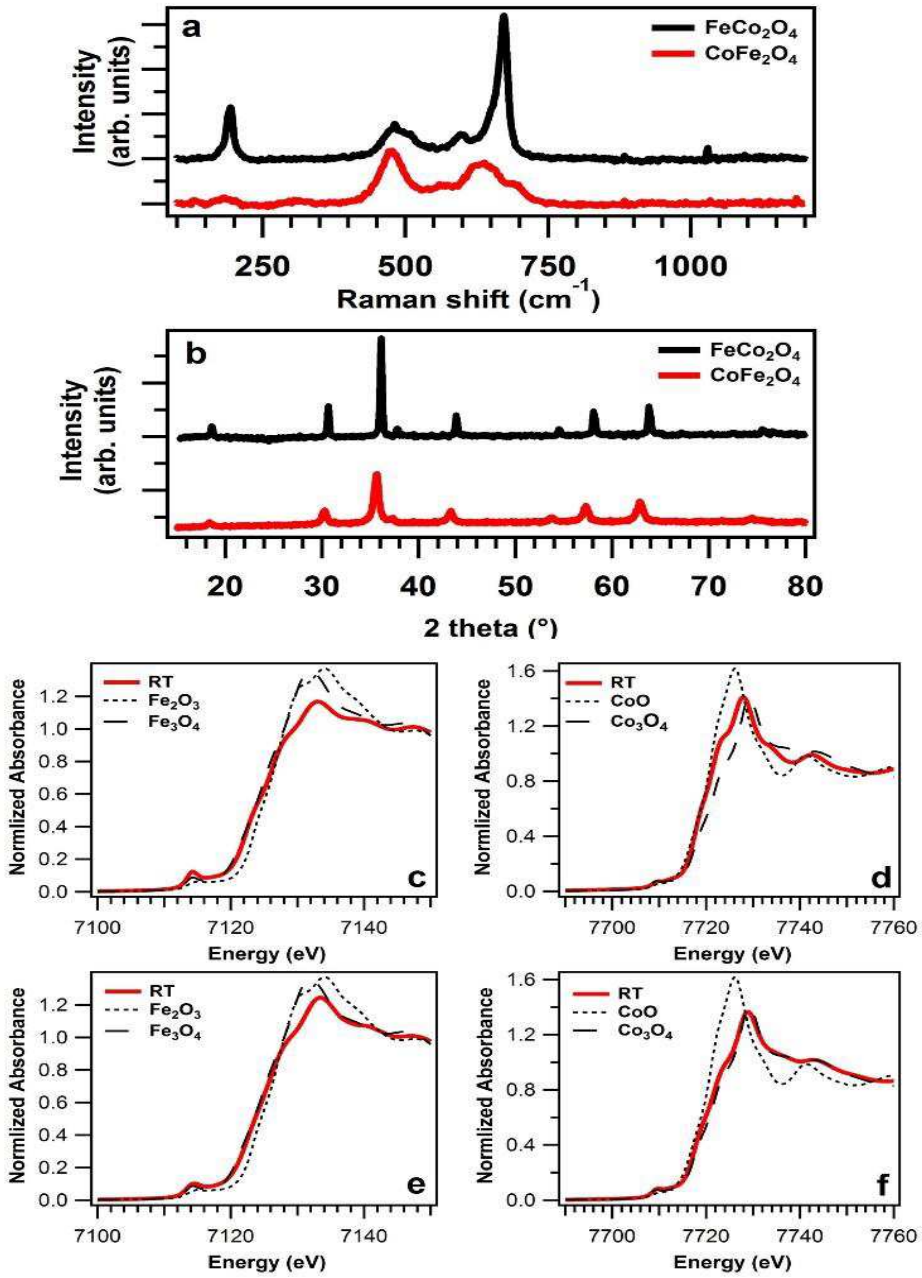

Figure 8: Raman spectra (a) and XRD patterns (b) of as prepared materials; XANES spectra at Fe(c,e) and Co (d,f) K-edge for as prepared CoFe2O4 (c,d), FeCo2O4 (e,f) and reference compounds. Reproduced from Ref. 1 with permission from the Royal Society of Chemistry.

The best fits of the FT EXAFS data are reported in Figures 9 and 10 and the corresponding parameters are reported in Tables 3 and 4. At Fe K-edge, the first peak at about 2 Å (not phase-corrected) is due to the contribution of two Fe-O single scattering paths: Fe_{Tetra}-O and Fe_{Octa}-O, which correspond to the interatomic distances between the two first coordination shells of oxygen ions, respectively. In the region between 2.0 and 3.5 Å, two contributions are observed, one at around 2.5 Å is related to Fe_{Octa}-M_{Octa} (M=Fe, Co) scattering paths and another one at about 3.5 Å to Fe_{Tetra}-M_{Tetra} or Fe_{Tetra}-M_{Octa} interactions. In fact, due to the similar cross sections, from EXAFS spectra it is not possible to distinguish between Fe and Co as backscattering atom. The EXAFS spectra at Co K-edge can be interpreted along the same line as well. An inversion degree of 0.8 and 0.6

was calculated for $CoFe_2O_4$ and $FeCo_2O_4$, respectively. These values are in agreement with previously reported data.[43] Therefore, the cation distribution can be summarized as:

$FeCo_2O_4$: $[Co(II)_{0.6}Fe(III)_{0.4}]^{Tet}[Co(II)_{0.4}Fe(III)_{0.6}Co(III)_1]^{Oct}O_4$

$CoFe_2O_4$: $[Co(II)_{0.2}Fe(III)_{0.8}]^{Tet}[Co(II)_{0.8}Fe(III)_{1.2}]^{Oct}O_4$

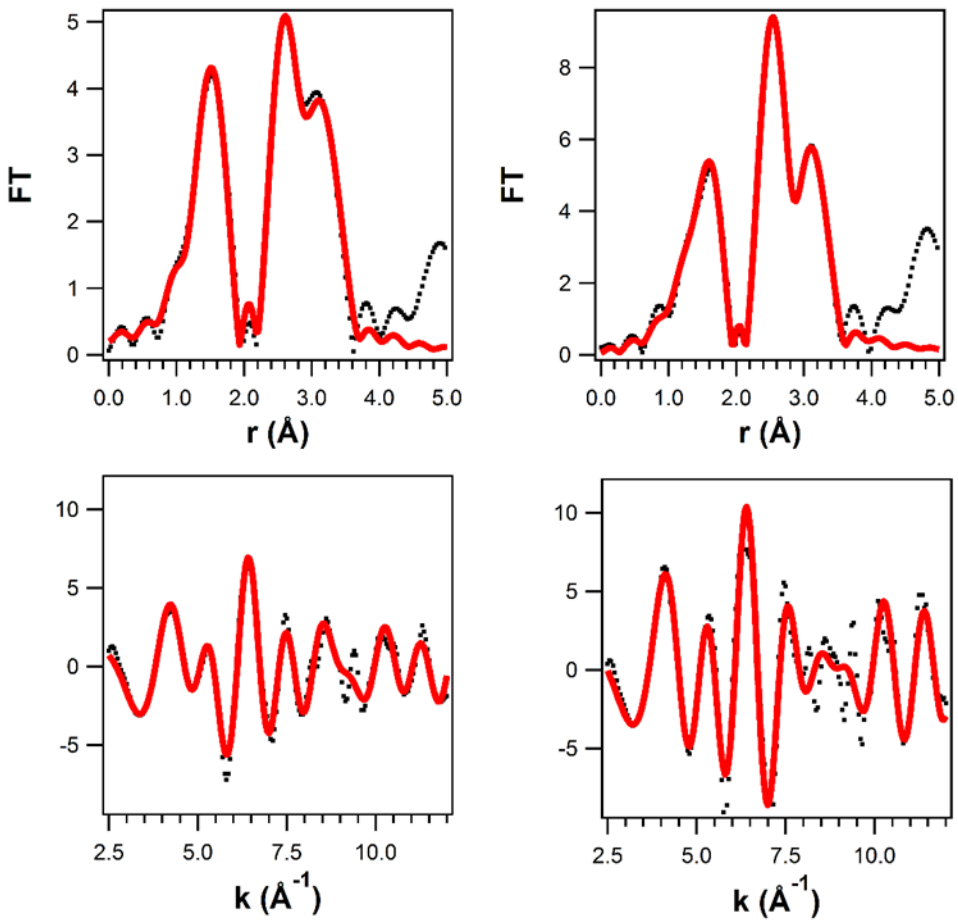

Figure 9: k^3 weighted (bottom) experimental data (black) and fit (red) with the corresponding Fourier transform (top) for the $CoFe_2O_4$ spinel recorded at the Fe K (left) and Co K (right) edges. Reproduced from Ref. 1 with permission from the Royal Society of Chemistry.

Table 3: fit parameters of $CoFe_2O_4$, R-factor=0.007. Reproduced from Ref. 1 with permission from the Royal Society of Chemistry.

Fe K edge (E_0= 1.27)				**Co K edge (E_0= 1.31)**			
Shell	N	R/Å	σ^2 / Å^2	Shell	N	R/Å	σ^2 / Å^2
x_B = 0.58				x_B = 0.83			
Fe_{Oh}-O_1	6	2.02 ± 0.01	0.005 ± 0.002	Co_{Oh}-O_1	6	2.01 ± 0.02	0.007 ± 0.002

Fe_{Oh}-M_{Oh}	6	2.90 ± 0.01	0.007 ± 0.002	Co_{Oh}-M_{Oh}	6	2.94 ± 0.02	0.008 ± 0.002
Fe_{Oh}-M_{Th}	6	3.49 ± 0.01	0.006 ± 0.002	Co_{Oh}-M_{Th}	6	3.445± 0.02	0.008 ± 0.002
x_A = 0.42				x_A = 0.17			
Fe_{Th}-O_1	4	1.952 ± 0.009	0.006 ± 0.002	Co_{Th}-O_1	4	1.98 ± 0.03	0.01 ± 0.004
Fe_{Th}-M_{Oh}	12	3.445 ± 0.009	0.009 ± 0.004	Co_{Th}-M_{Oh}	12	3.48 ± 0.02	0.006 ± 0.002
Fe_{Th}-M_{Th}	4	3.478 ± 0.009	0.030 ± 0.009	Co_{Th}-M_{Th}	4	3.51 ± 0.03	0.008 ± 0.003
				Co_{Th}-O_2	4	3.63 ± 0.03	0.006 ± 0.003

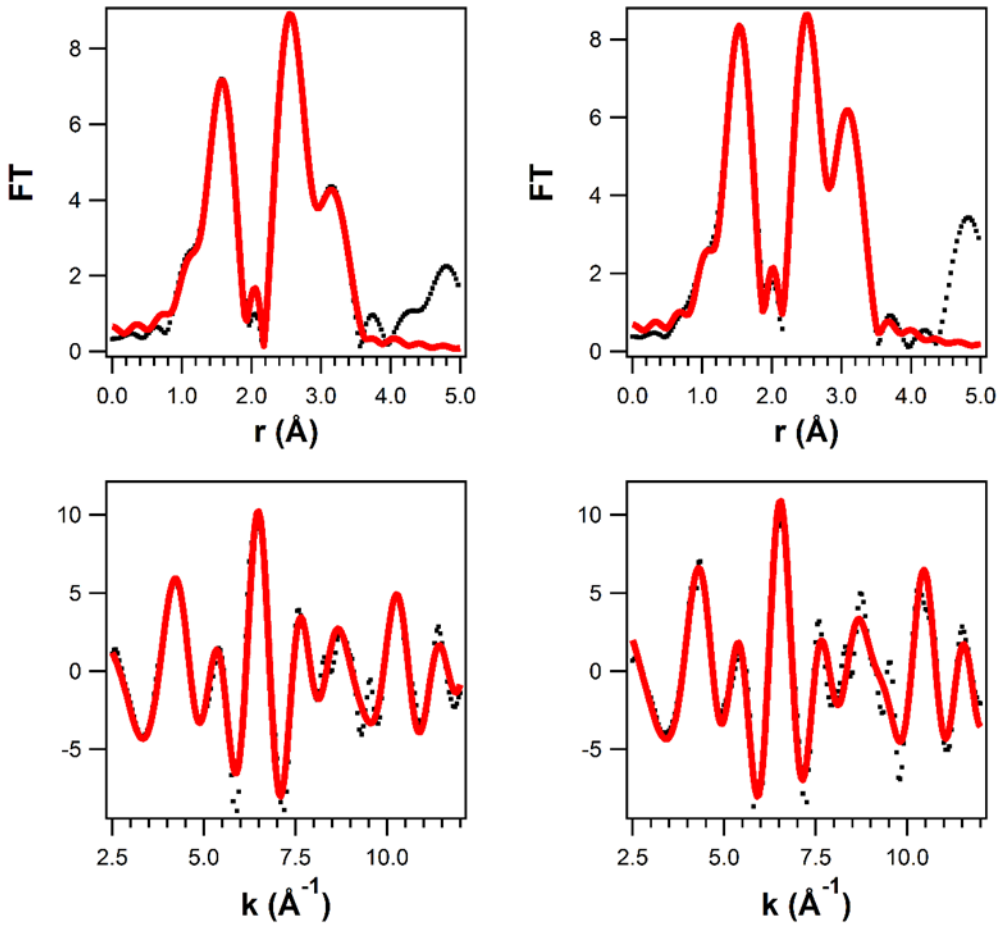

Figure 10: k^3 weighted (bottom) experimental data (black) and fit (red) with the corresponding Fourier transform (top) for the $FeCo_2O_4$ spinel recorded at the Fe K (left) and Co K (right) edges. Reproduced from Ref. 1 with permission from the Royal Society of Chemistry.

Table 4: fit parameters of $FeCo_2O_4$, R-factor=0.007. Reproduced from Ref. 1 with permission from the Royal Society of Chemistry.

Fe K edge (E_0=2.86)				**Co K edge (E_0=4.24)**			
Shell	N	R/Å	σ^2 / Å^2	Shell	N	R/Å	σ^2 / Å^2
x_B = 0.64				x_B = 0.68			
Fe_{Oh}-O_1	6	1,993 ± 0.006	0.008 ± 0.002	Co_{Oh}-O_1	6	1.97 ± 0.02	0.009 ± 0.007
Fe_{Oh}-M_{Oh}	6	2.951 ± 0.006	0.006 ± 0.001	Co_{Oh}-M_{Oh}	6	2.91 ± 0.02	0.006 ± 0.002
Fe_{Oh}-M_{Th}	6	3.474 ± 0.006	0.008 ± 0.003	Co_{Oh}-M_{Th}	6	3.43 ± 0.02	0.005 ± 0.004
x_A = 0.36				x_A = 0.32			
Fe_{Th}-O_1	4	1.98 ± 0.03	0.002 ± 0.001	Co_{Th}-O_1	4	1.93 ± 0.03	0.006 ± 0.003
Fe_{Th}-M_{Oh}	12	3.49 ± 0.01	0.008 ± 0.003	Co_{Th}-M_{Oh}	12	3.52 ± 0.01	0.011 ± 0.006
Fe_{Th}-O_2	4	3.49 ± 0.01	0.009 ± 0.003	Co_{Th}-M_{th}	4	3.70 ± 0.02	0.009 ± 0.003

The results obtained by EXAFS were further verified by Mössbauer spectroscopy measurements, which were taken both at RT and 80 K.

Concerning $FeCo_2O_4$, RT spectra shows a broad magnetic pattern (Figure 11a) as results of the magnetic relaxation due to high ordering temperature. [43] On the contrary, $CoFe_2O_4$, shows a fully magnetically ordered RT spectrum. (Figure 11b). No traces of superparamagnetic components are detectable. A preliminary fit excluded the presence of pure Fe(III) oxides, such as hematite. After cooling down the $FeCo_2O_4$ sample to 80 K, the spectrum transforms into a well-defined magnetic pattern (figure 11c), typical of Fe species in a spinel structure. As explained in the Experimental Section, the spectrum was fitted by using only two broad sextets. The so-obtained parameters were attributable to Fe(III) in tetrahedral and octahedral environment, whose relative areas are 44 and 56 respectively. Therefore, cation distribution within the spinel structure is similar to that suggested by EXAFS data, and the cobaltite can be written as: $[Co_{0.56}Fe(III)_{0.44}]^{Tet}[Co_{1.44}Fe(III)_{0.56}]^{Oct}O_4$.

Concerning the $CoFe_2O_4$ sample, the spectrum acquired at 80 K (figure 11d) was firstly fitted by using two sextets, relative to the octahedral and tetrahedral site. The tetrahedral and octahedral populations were estimated respectively in 37 and 63 of the total Fe. Once again, assuming γ= 0.37, the stoichiometry of the spinels is in good agreement with the EXAFS data, in fact the proposed formula is $[Co_{0.26}Fe(III)_{0.74}]^{Tet}[Co_{0.74}Fe(III)_{1.26}]^{Oct}O_4$. The small discrepancy in the so calculated stoichiometry can be ascribed either to small errors in the area calculation or to small differences in the recoilless fraction of the two different sites.

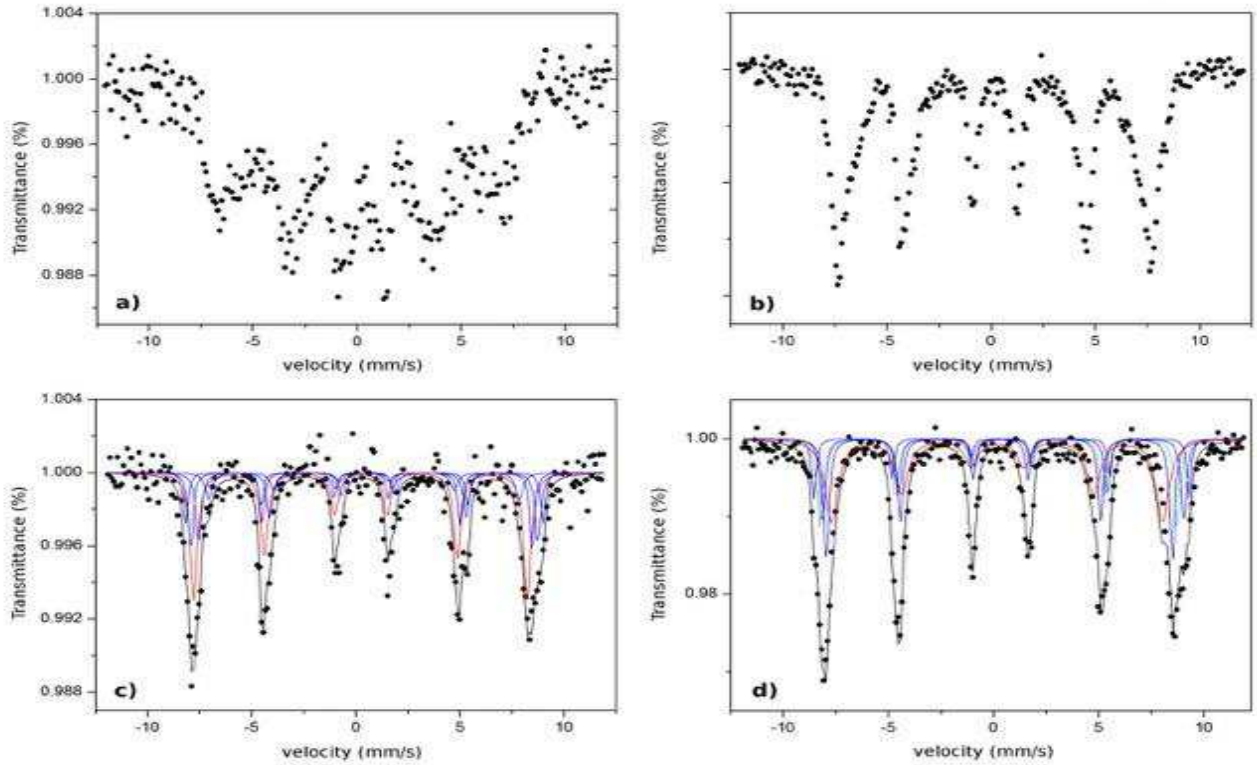

Figure 11: Mössbauer spectra of $FeCo_2O_4$ and Co_2FeO_4, collected at RT, a) and b), and at 80 K, c) and d). Black dots represent the experimental data, black lines the calculated spectra, red line the Fe(III) tetrahedral site and blue lines the sub-components of the octahedral site. Reproduced from Ref. 1 with permission from the Royal Society of Chemistry.

Table 5: 80 K Mössbauer parameters for iron cobaltite and cobalt ferrite. P(1), P(2), P(3), P(4) represent the different NN neighbour configurations. δ is quoted to α-Fe, using a 6-lines calibration. Reproduced from Ref. 1 with permission from the Royal Society of Chemistry.

$FeCo_2O_4$	δ (mm/s)	ε (mm/s)	Γ (mm/s)	B (T)	A (%)
Tetrahedral Site	0.33	-0.02	0.42	49.7	44
Octahedral Site, P(4)	0.41	0.003	0.26	53.2	11
Octahedral Site, P(3)	0.49	0.01	0.32	50.5	18
Octahedral Site, P(2)	0.39	-0.02	0.27	50.8	18
Octahedral Site, P(1)	0.42	0.019	0.40	46.2	9
$CoFe_2O_4$					
Tetrahedral Site	0.29	-0.03	0.74	48.8	37
Octahedral Site, P(4)	0.47	0.02	0.26	53.0	9
Octahedral Site, P(3)	0.37	-0.03	0.33	52.7	17
Octahedral Site, P(2)	0.41	-0.05	0.29	51.02	22
Octahedral Site, P(1)	0.44	0.03	0.30	52.25	15

In both cases, the proposed fitting highlights the linewidth broadening due to the effect of a multiplicity of hyperfine magnetic fields on the Fe(III) nuclei. If the contribution of the Near Next Neighbors (NNN) on the tetrahedral site can be neglected,[50] on the contrary on the octahedral sites it needs to be taken in account.

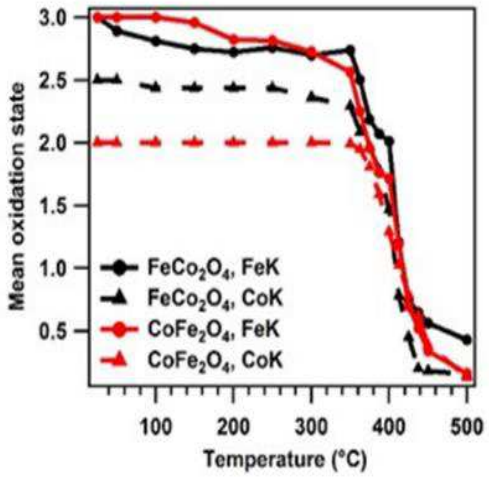

Figure 12: Oxidation states calculated from the edge position in the XANES spectra collected during the annealing treatment in reductive atmosphere (0.69 % ethanol in N_2). Reproduced from Ref. 1 with permission from the Royal Society of Chemistry.

Therefore, by using the binomial distribution described in the Experimental Section, the proper number of subcomponents and their relative areas can be obtained. Considering negligible the areas smaller than 5% of the total iron, the binomial distribution on the octahedral sites in iron cobaltite predicts the presence of four sextets, whose relative areas are given by P(4):P(3):P(2):P(1)=18:30:29:16. Also in cobalt ferrite, the binomial distribution predicts four sextets, with an intensity ratio of P(4):P(3):P(2):P(1)=11:25:33:22. The intensity of the sextets were recalculated on the basis of the total area of the octahedral site and fixed during the fitting procedure. The parameters are reported in Table 5. These differences in NNN configuration reflect the different γ in the two spinels, which is the different statistic distributions of Co atoms in the cobaltite and ferrite structures.

In operando XAS: annealing in reductive atmosphere

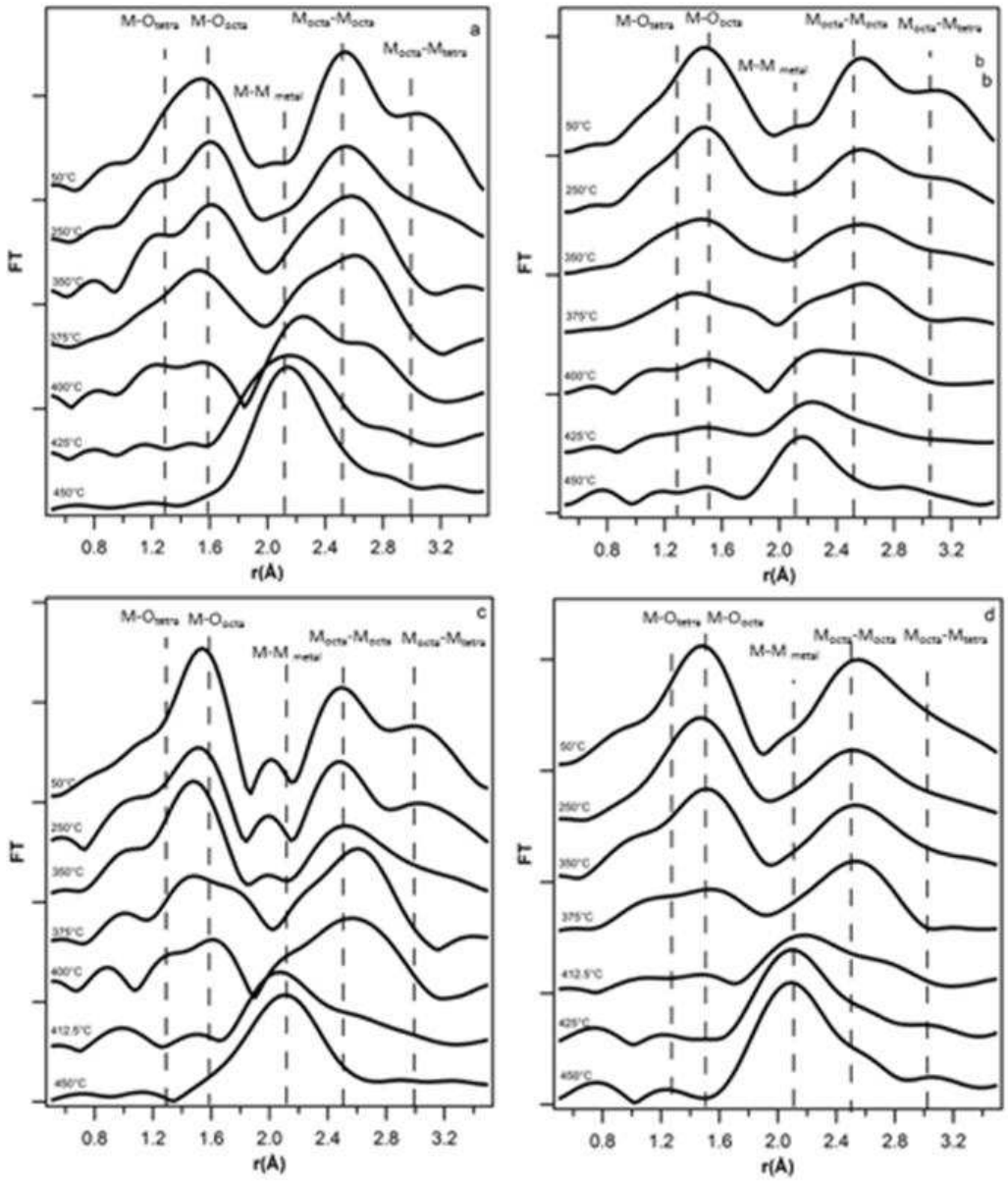

Figure 13: Fourier transform EXAFS spectra at Co K(a,c) and Fe K (b,d) edge for $CoFe_2O_4$ (a,b), $FeCo_2O_4$ (c,d) during the annealing treatment in reductive atmosphere (0.69 % ethanol in N_2). Reproduced from Ref. 1 with permission from the Royal Society of Chemistry.

Freshly prepared $FeCo_2O_4$ and $CoFe_2O_4$ spinel oxides were evaluated as electrons/O^{2-} carrier materials for hydrogen production via CLR of ethanol. The changes of the materials during the redox cycle were followed *in real time* by XAS measurements in order to determine the reactivity of the two metal ions in the different geometrical-sites. As first step, we investigated the reaction of the materials toward ethanol as a function of temperature. *In operando* XAS was performed during the annealing of the samples from RT to 500°C in reducing atmosphere (0.69% vol of ethanol in N_2). Figure 12 reports the variation of the mean oxidation state of Fe and Co determined from the edge position as a function of temperature. The change of the average oxidation state of the cations was calculated by XANES spectra (Figure 18), whereas modifications in the geometric site were deduced by the EXAFS data (Figure 13). The body of our experimental data outlines a marked difference of

reducibility in the two spinels. $FeCo_2O_4$ is stable up to 350°C, above this temperature it starts to reduce quickly, and at 425°C the material is mainly made up by the corresponding body centered cubic (bcc) metal alloy phases, as suggested by the spectral fingerprint of FT EXAFS spectra (Figure 16) and by the XRD patterns of the reduced samples (Figure 17).[51] Moreover, several works indicate that alloys are the most stable phases formed under reducing condition for mixed ferrites.[52,53] $CoFe_2O_4$ shows a similar behavior, although the reduction is more gradual: Fe starts to reduce at 150°C and becomes metal Fe at 500ºC, whereas Co is stable up to 250 ºC and then it is gradually reduced to metal Co. It has to be noted however, that the higher reducibility of $CoFe_2O_4$ can be also due to the higher surface area and defectivity of this material. In order to investigate the effect of cation site occupancy in the two spinels, we carefully analyzed the intensity trends of the EXAFS peaks (Figure 13) and of the LCF of XANES spectra (Figure 14) in $CoFe_2O_4$ and $FeCo_2O_4$ during the thermal treatment in presence of ethanol. From these data a general behavior of the reduction mechanism is deduced, which appears to be largely controlled by the type of cation coordination. The cations in tetrahedral sites (A) are more prone to reduction than those in octahedral sites (B). This is evidenced by the decrease of the peak corresponding to M_{Octa}-M_{Tetra} bonds until its complete suppression at about 350°C, whereas the M_{Octa}-M_{Octa} peak intensity decreases only slightly. Combining the EXAFS data with the LCF analysis at the Fe K and Co K edges (Figure 14), it can be concluded that the disappearance of the M_{Octa}-M_{Tetra} peak is related to the formation of M(II) oxide phases, probably a mixed $(Fe,Co)O_{1-x}$, wüstite (as suggested also by the XRD patterns acquired on the reduced samples, Figure 16). In the case of $FeCo_2O_4$, the maximum conversion to M(II) oxides is reached at 400°C, whereas in the case of $CoFe_2O_4$ at 375°C. These M(II) oxides are highly disordered, also in the short range order, since no clear EXAFS peaks can be identified. Only in the case of majority cations of the spinels (B cations, i.e. Fe in ferrite and Co in cobaltite), the growth of a shoulder related to M-O bonds typical of wüstite structures is identified at 1.7 Å, starting from 375-400°C. The higher activity of tetrahedral sites is somehow in contrast with a previous report about the reactivity of mixed ferrites toward methanol, where by ex situ characterization it was suggested a higher activity of octahedral sites,[18] however it is in agreement with other investigations on the reaction mechanism of spinel.[54,55] As a matter of fact, Mössbauer experiments suggest that during the thermal or chemical reduction of ferrites, the removal of oxygen induces a change in the oxidation state of cations that therefore adjust their site occupancy, by populating interstitial sites:[55] i.e. sites that are not normally occupied in the parent structures, however the structural details of such processes are strongly dependent on the specific oxide structures. Our XAS data therefore, for the first time capture time resolved snapshots of tetrahedral cations diffusion into normally unoccupied octahedral sites forming cation excessive[54] spinels, which at the limit of high reduction are eventually converted to wüstite type oxides. Comparing the two oxides, $FeCo_2O_4$ seems to be more stable toward reduction than $CoFe_2O_4$, as evidenced by the higher temperature needed to reduce the signals coming from the spinel.

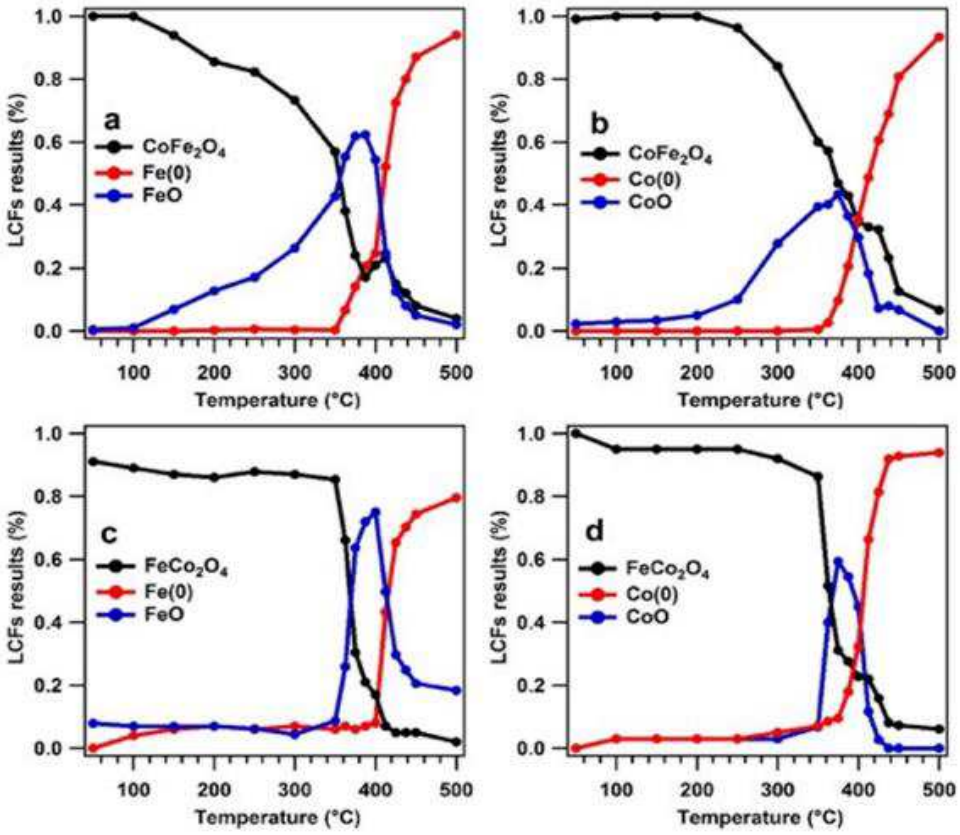

Figure 14: LCFs (% of composition vs temperature) of Fe(a,c) and Co (b,d) K-edge for $CoFe_2O_4$ (a,b) and $FeCo_2O_4$ (c,d) during the annealing treatment in reducing atmosphere (0.69 % ethanol in N_2). Reproduced from Ref. 1 with permission from the Royal Society of Chemistry.

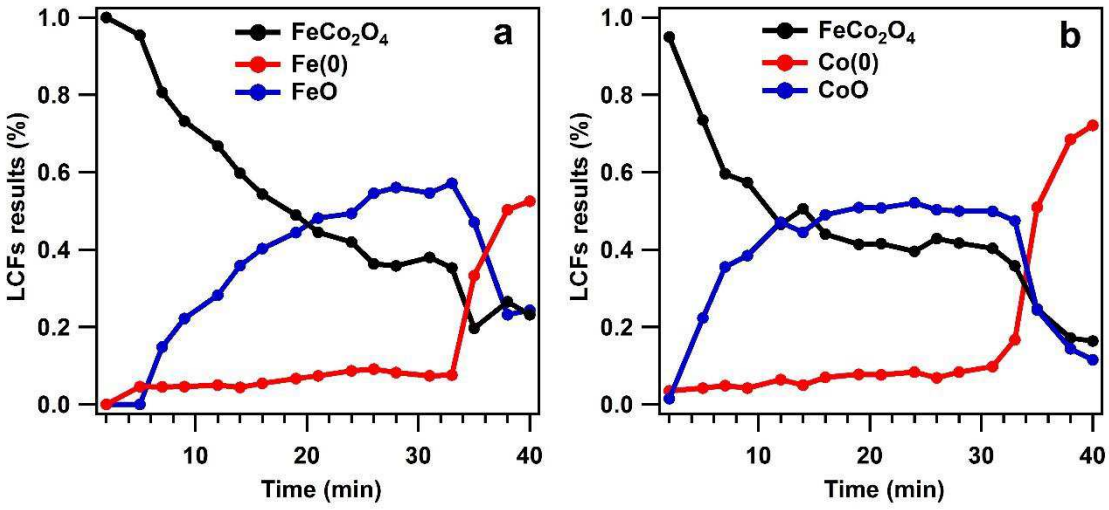

Figure 15: LCFs (% of composition vs temperature) of Fe(b) and Co (a) K-edge for $FeCo_2O_4$ (a,b) during the treatment in reducing atmosphere (0.69 % ethanol in N_2) at 450°C. Reproduced from Ref. 1 with permission from the Royal Society of Chemistry.

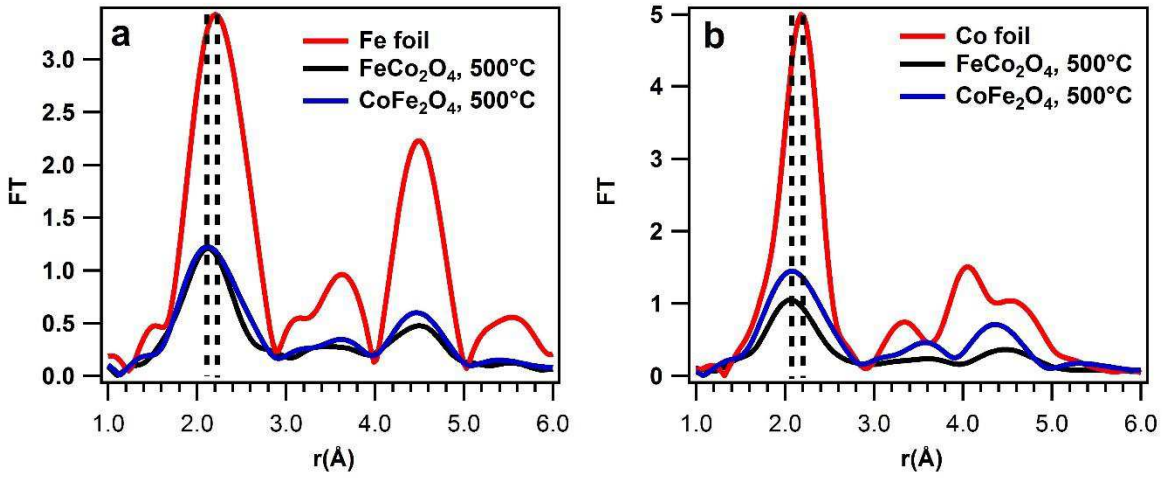

Figure 16: Fourier transform EXAFS of the $CoFe_2O_4$ and of $FeCo_2O_4$ at the end of the annealing in ethanol atmosphere (500°C) recorded at the Fe K (a) and Co K (b) edges. The FT EXAFS spectra of the reduced samples are compared with the FT EXAFS of Fe and Co metal foils. Reproduced from Ref. 1 with permission from the Royal Society of Chemistry.

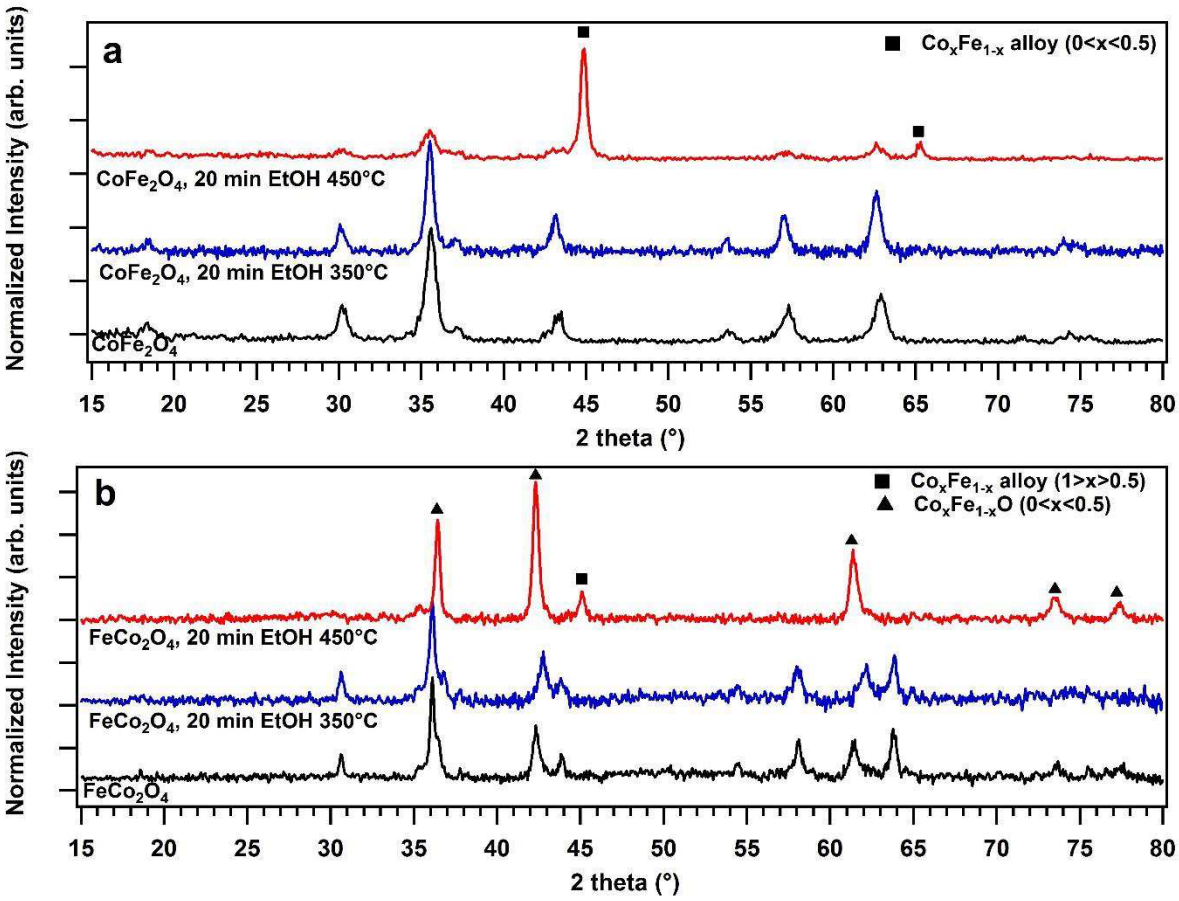

Figure 17: XRD patterns of a) $CoFe_2O_4$ and b) $FeCo_2O_4$ of as prepared samples and after 20 minutes at 350°C and 450°C in reductive atmopshere (15 mol % of ethanol in N_2). Reproduced from Ref. 1 with permission from the Royal Society of Chemistry.

However, the higher stability may be due to the larger size and low surface area of iron cobaltite nanoparticles that prevent a fast surface reaction. On the other hand, $CoFe_2O_4$ shows an almost immediate conversion to the wüstite phases. The fast reaction, characterized by an almost linear kinetics as a function of time, suggests that intrinsic defects play a key role in the reduction. At high temperatures (> 350°C), the wüstite phases and the residual ferrite/cobaltite are mostly converted to metal phases. From the LCF analysis, it is clear that the formation of the metal phases starts only when a relatively large amount of (Co, Fe) mixed wüstite is formed; therefore, a direct decomposition of the spinel to the metal seems unlikely. In general, the reduction of ferrites follows a path that is strongly dependent on the type of reducing agent (H_2, CO, alcohols), temperature, but also morphological factors.[56] In the case of the Fe_3O_4 it has been determined by thermodynamic data,[57] that a triple point exist at 1121 K where Fe_3O_4, FeO, Fe coexist, whereas for lower temperature Fe_3O_4 is directly converted to metal Fe. This prediction has been later verified experimentally in the experimental work of Bohn et al.[58] On other hand, for several spinel ferrites it has been reported an easy and direct formation of metal phases: for example, $NiFe_2O_4$ is directly reduced at 850°C by simulated biomass pyrolysis gas to a metal Nickel phase and Fe_3O_4.[59] Similarly, accurate experimental and theoretical investigations suggest that during the reduction with syngas, only in the limit of very low (<0.03) CO/CO_2 and H_2/H_2O ratios, CoO and NiO are formed from Co,Ni mixed ferrites, otherwise a direct decomposition to metal Ni and Co and iron enriched spinel is observed.[32] More recently, in the case of the reduction of cobalt ferrites, at 600°C by a mixture of syngas and CO_2 no trace of wüstite phase was observed by *in situ* XRD, but only a direct conversion of mixed spinel to a Co-Fe metal alloy.[30] Anyway all the reports in the literature suggest that the introduction of Co, Ni, and other first row transition metal cations facilitates the reduction of both the parent spinel Co_3O_4 and Fe_3O_4.[3,60] Our *in operando* results therefore outline a different scenario that clearly points to the formation of a large fraction of intermediate wüstite phases even at very modest temperature. It is also interesting to note that the presence of metal Fe in $FeCo_2O_4$ is observed only at temperatures higher than 400°C, which is a much higher temperature than that required for the formation of metal Co in the same material or metal Fe in $CoFe_2O_4$. As a matter of fact, the strength of Co-O bonds is smaller than Fe-O and one of the lowest among first row transition metal oxides,[13] and in general the introduction of Co in iron spinel has the effect to promote reducibility. This is in agreement with previous TPR measurements and reactivity studies toward methanol[3] and suggest that not only the chemical composition, but also structural factors are very important to understand the reactivity of mixed oxides. Finally, the analysis of the M-O peak intensity (1.2-1.6 Å) indicates that the A cations are fully reduced at temperature lower than that for the B cations in both samples (Fe in $FeCo_2O_4$ and Co in $CoFe_2O_4$). Notably, the LCF analysis suggests that single metal spinels (Co_3O_4 or Fe_3O_4) are not formed in any of the materials during the annealing in ethanol.

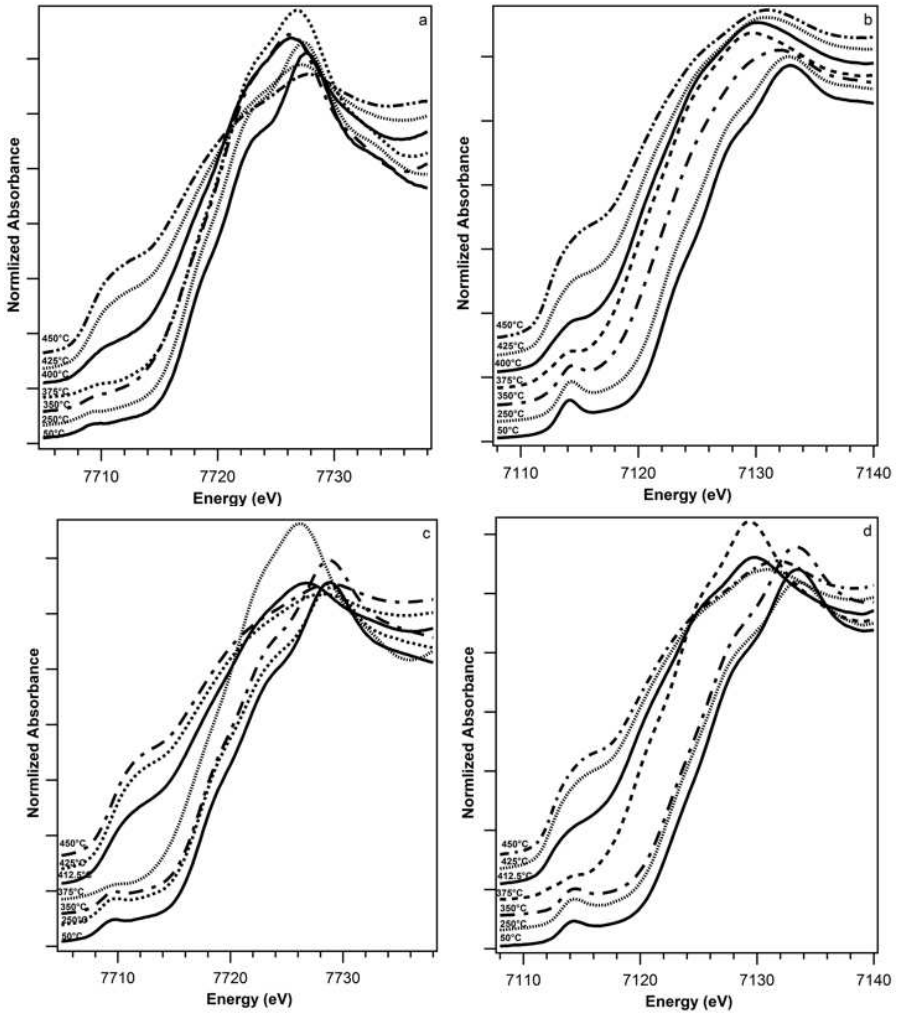

Figure 18: XANES spectra at Co (a,c) and Fe(b,d) K-edge for $CoFe_2O_4$ (a,b) and $FeCo_2O_4$ (c,d) during the annealing treatment in reducing atmosphere (0.69 % ethanol in N_2). Reproduced from Ref. 1 with permission from the Royal Society of Chemistry.

CLR of ethanol: catalytic tests

Bearing in mind these results, we tested the redox and catalytic properties of these materials with respect to the two-step CLR of ethanol at two different temperatures: at 350°C, because this is the threshold for the reduction of the catalysts; and at 450°C, because at this temperature both spinels are mostly reduced to a metal phase. Previously, the catalytic properties of $M_xFe_yO_4$ spinels as catalyst for CLR at 450°C were investigated by Vozniuk et al.[17] In the CLR process, the first step is the aerobic oxidation of ethanol, whereas the second one is the reoxidation of the catalyst by water vapor exposure.

Considering that the anaerobic oxidation is a stoichiometric process, the reduction state of the material is pivotal in determining the selectivity of the reaction path. Therefore, the temperature has a major role in this reaction. The amount of each reaction product is affected by the extent of the metal oxide reduction, which is a general statement valid for all oxygen carrier materials.

During the reduction step performed at 350°C for 20 min, the ethanol conversion and the selectivity to the main products were determined by gas chromatography (on-line micro-GC). The ethanol conversion over $FeCo_2O_4$ (Figure 19) and $CoFe_2O_4$ (Figure 20) is 18% and 20%, respectively. The main products formed during the reaction

were identified as follows: acetaldehyde, ethyl acetate, acetone, H_2O, CO_2, H_2, ethylene and ethane. Acetaldehyde is the predominant product for $FeCo_2O_4$ with an initial selectivity of about 69 %, (which decreases to 57% at the end of the cycle). On the other hand, acetaldehyde selectivity over $CoFe_2O_4$ is significantly lower and with an opposite trend as a function of time, ranging from 17 to 28% at the beginning and after 20 min of ethanol exposure, respectively. The formation of acetaldehyde is likely due to the ethanol dehydrogenation/oxydehydrogenation reactions. Ethyl acetate represents the second most important reaction product, and the two spinels show similar selectivities (19% in cobaltite and 28% in ferrite at the end of the cycle). Notably, the selectivity to acetone over $CoFe_2O_4$ is in the range from 17 to 11%, while its selectivity over $FeCo_2O_4$ is much lower (<2%).

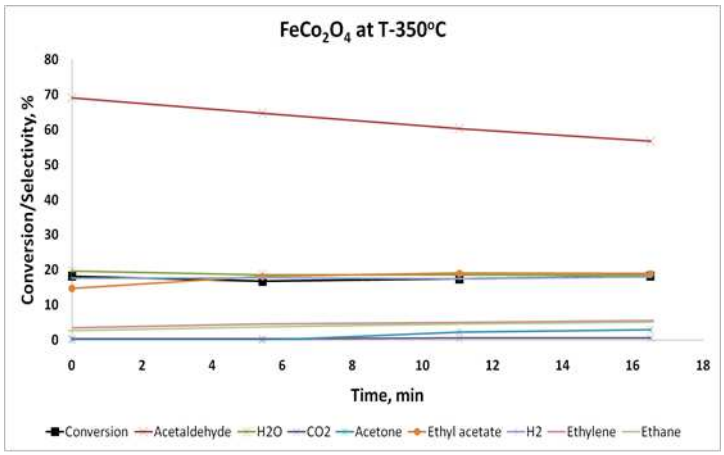

Figure 19: Conversion and Selectivities to the main products obtained for $FeCo_2O_4$ during 20 min reduction at T-350°C. Reproduced from Ref. 1 with permission from the Royal Society of Chemistry.

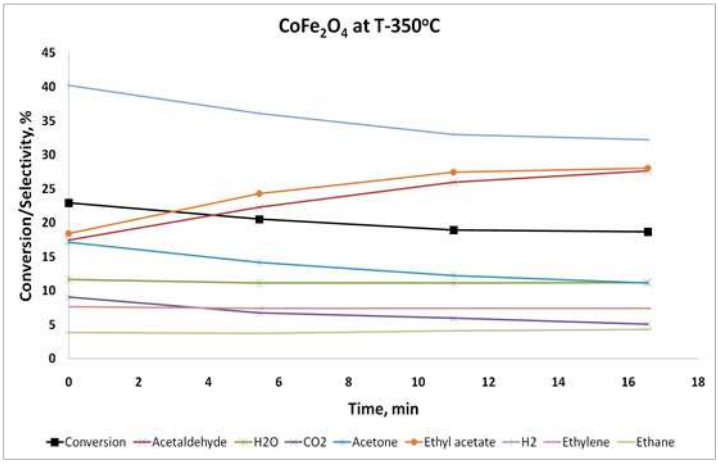

Figure 20: Conversion and Selectivities to the main products obtained for $CoFe_2O_4$ during 20 min reduction at T-350°C. Reproduced from Ref. 1 with permission from the Royal Society of Chemistry.

Figures 21 and 22 show the conversion and the selectivity to the main products, obtained during the reduction step performed at 450°C for 20 min. Already at the beginning of the reaction, the ethanol conversion is quantitative and is stable during the reduction time for both oxides. One of the main products is hydrogen, with an initial selectivity of about 30% ($FeCo_2O_4$) and 51% ($CoFe_2O_4$), which increases up to 73 and 78%, respectively, at the end of the cycle. The trend observed for hydrogen very similar to that of CO_x and H_2O, suggesting that the prevailing reactions, which result in the oxide reduction, are the total and partial ethanol oxidation. Other by-

products as acetaldehyde, acetone, ethyl acetate, ethylene and ethane were detected mainly at the beginning of the reduction. This means that the formation of these species is strongly connected to the presence of the spinel phases, whereas as soon as the mixed wüstite is formed their amount is strongly suppressed. This has been confirmed by *in operando* investigation by XAS (see below).

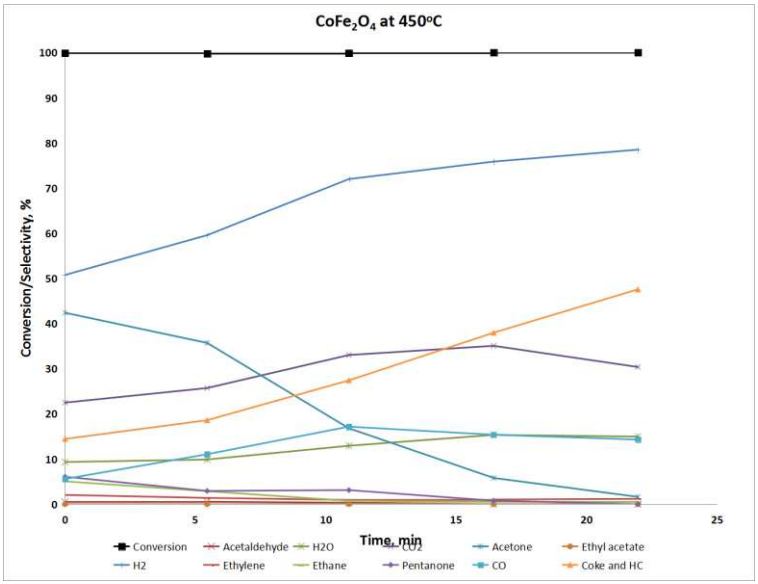

Figure 21: Conversion and Selectivities to the main products obtained for $CoFe_2O_4$ during 20 min reduction at T-450°C. Reproduced from Ref. 1 with permission from the Royal Society of Chemistry.

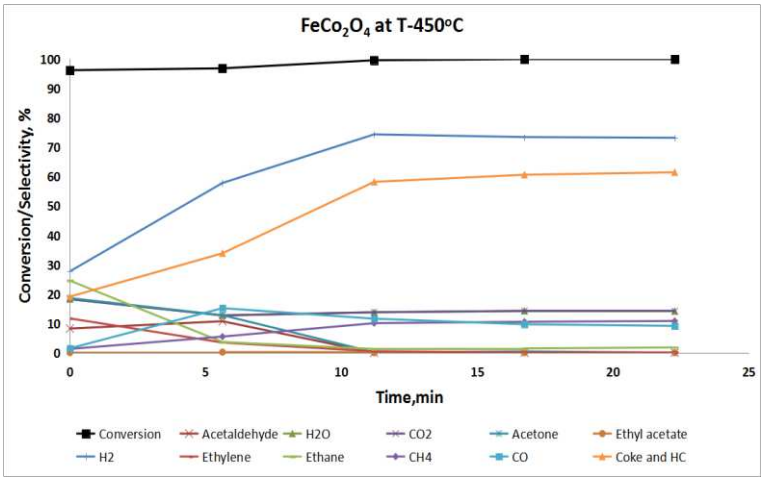

Figure 22: Conversion and Selectivities to the main products obtained for $FeCo_2O_4$ during the 20 min reduction at T-450°C. Reproduced from Ref. 1 with permission from the Royal Society of Chemistry.

After the 1st step with ethanol, the reduced material was then re-oxidized by water steam at 450°C during the same time on stream of 20 min, which corresponds to the 2nd step of the conventional two-step CLR process (Figure 23 and 24). Mass spectroscopy data indicate a significant difference in the amount of produced H_2 and CO_x gases over two spinels, which is proportional to the reduction extent of the solid together with its ability of being re-oxidized by means of H_2O. The higher hydrogen yield (~20 %) is obtained on $CoFe_2O_4$, whereas on $FeCo_2O_4$ its amount is 3-4 times lower (~5%). Beside the hydrogen production, the common feature for all the samples is the formation of CO_x (CO_2 and CO) during the re-oxidation step (Figures 23 and 24), because of the

gasification of carbonaceous residues, previously formed during the reduction step (see CHNS elemental analysis in Table 6 performed after the 1st step with ethanol).

Table 6: C,H,N,S analysis of reduced samples (20 min in ethanol atmosphere: 15 mol % of ethanol in N_2). Reproduced from Ref. 1 with permission from the Royal Society of Chemistry.

Temperature of reduction	Sample name	C %	H %
T-350°C	$FeCo_2O_4$	0.31	0.11
	$CoFe_2O_4$	1.53	0.42
T-450°C	$FeCo_2O_4$	5.64	0.15
	$CoFe_2O_4$	10.65	0.18

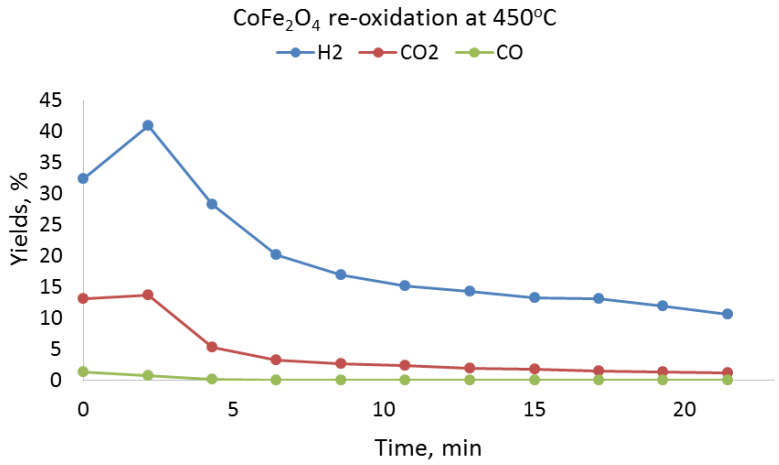

Figure 23: Yields to H_2 and CO_x obtained over $FeCo_2O_4$ during 20 min of re-oxidation with water at 450°C. Reproduced from Ref. 1 with permission from the Royal Society of Chemistry.

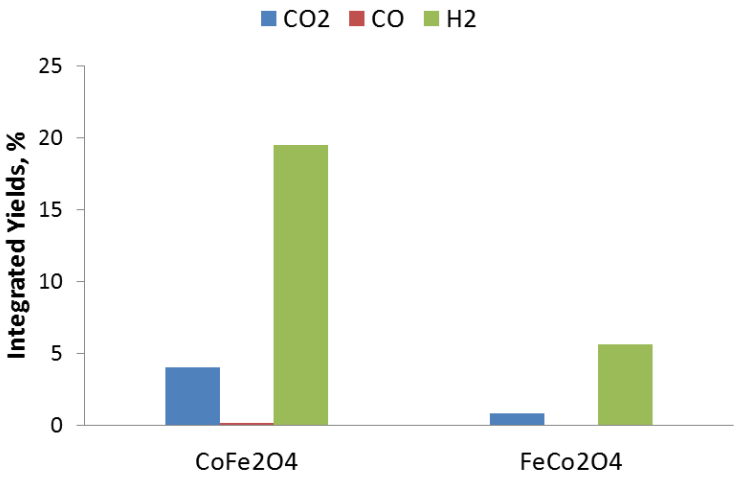

Figure 24: Integrated yields to H_2, CO_x obtained over $CoFe_2O_4$ and $FeCo_2O_4$ during 20 min re-xidation with water at 450°C. Reproduced from Ref. 1 with permission from the Royal Society of Chemistry.

CLR of ethanol: in operando XAS

In order to have an atomic scale insight into the origin of the different chemical activity of the two spinels, *in operando* XAS measurements have been carried out under Chemical-Loop conditions. In particular, we have monitored the Fe K and Co K-edges during ethanol (20 minutes, 5.29% in nitrogen) or water (20 minutes, 8.31% in nitrogen) exposure at 450°C. The working temperature (450°C) was reached in inert atmosphere at 5°C/min, and XAS measurements were also acquired during the heating treatment. Figure 25 shows the XANES and EXAFS spectra after each process step for both samples at the Fe K and Co K edges. After the thermal treatment, the oxidation states of Fe and Co in $FeCo_2O_4$ are almost unchanged, whereas a slight reduction of $CoFe_2O_4$ is evidenced by the decrease of the white line intensity at both edges, as well as by the shift of Fe K-edge energy toward lower values. This behavior could have two explanations: (i) cobaltite was synthesized at higher temperature than ferrite and, therefore, it is expected to be more stable; (ii) the particle size of cobaltite is larger than that of ferrite, therefore, cobaltite is less reactive. Moreover, the EXAFS peaks of both materials after annealing in inert atmosphere are less intense due to an increase of the disorder of the structures (high cation mobility) and to the noise induced by temperature and gas flow. EXAFS data suggest that the metal cations in tetrahedral environment are the most reactive species under these conditions, since the M_{octa}-M_{tetra} interactions suffer the largest drop in intensity. From the LCF analysis (Figure 26, time=0 min), we can conclude that only a small fraction of $CoFe_2O_4$ (about 20%) and of $FeCo_2O_4$ (about 5%) are converted to a wüstite phase after the annealing in inert atmosphere.

In operando quick XAS spectra acquired during the following reduction and re-oxidation cycles (Figure 25), confirm that the two spinels exhibit a rather different reactivity. After the first reduction cycle in ethanol atmosphere, $FeCo_2O_4$ is almost completely reduced: both the Fe K and Co K-edges XANES (Figures 25a and 25b, and the corresponding LCF in Figure 26) and EXAFS (Figures 25e and 25f) data confirm the formation of metal phases. The peak corresponding to M-O bonds disappears, whereas that corresponding to M-M in the metal phase appears. About 50 % of the iron cobaltite is rapidly converted (2 min) to a wüstite phase. This phase, however, has only a transient existence due to the fast reduction to the metal phase. The formation of metal Fe and Co starts as soon as some mixed wüstite phase is formed, and after 10 minutes reaches a plateau that corresponds to the conversion of about 85% of Co and 75% of Fe to metal alloy phases. [61] Both cations are easily reduced; however, this tendency is higher for Co than for Fe, which in general requires a higher temperature and is more efficiently stabilized in the wüstite phase. Overall, the time evolution of the XANES spectra indicates that $FeCo_2O_4$ is rather unstable under reducing conditions and high temperature. Nonetheless, during the successive oxidation cycle with water vapor, the EXFAS spectra remain unchanged, indicating that the reduced phases are quite difficult to re-oxidize (figures 25a and 25b). This limited oxidation explains the low hydrogen yield detected during catalytic measurements for this material. Previous *in situ* X-ray Photoemission Spectroscopy (XPS) study on Co-Mn mixed spinel ferrites[17] on the other hand, indicate that the surface of these materials can be efficiently oxidized by water steam. This apparent contradiction can be solved considering the low surface area of $FeCo_2O_4$, and that XAS is a bulk technique. Moreover, it has been previously reported for other mixed spinels that the rate determining step of water oxidation is the diffusion of oxygen through the newly formed oxide layer.[62] Therefore, we can assume that a thin oxide passivation layer that can be hardly detected by XAS is formed on the metal surface and prevents further oxidation. On the other hand, $CoFe_2O_4$ is reduced to a mixed wüstite in first place and, subsequently, to a Co-Fe alloy. After 2 minutes in ethanol atmosphere, about 80% of Fe and 45% of Co are converted to a wüstite phase (Figure 26). Interestingly, Co prefers to form a metal phase rather than a reduced Co(II) oxide, as demonstrated by the almost concurrent formation of CoO and Co metal. Fe, instead, is quickly and almost quantitatively transformed into wüstite, which is only partially reduced to metal. This quantitative conversion of Fe is in contrast with the behavior of Fe in $FeCo_2O_4$, where was gradually converted both to metallic

and wüstite phases. At the end of the cycle on $CoFe_2O_4$, the reduction of Fe to metal is only 60% to be compared with 90% for cobalt. It has been previously reported that the addition of Co to γ-Fe_2O_3, forming non-stoichiometric spinel, has a strong influence on its reduction properties. Pure iron oxide and spinels are reduced only to FeO, whereas the cobalt doped ferrite can be reduced up to Fe-Co alloys[30] During the subsequent oxidation process, Co is marginally oxidized by water (Figures 25c and 25g); whereas Fe is clearly oxidized to a final oxidation state slightly higher than 2+ (Figure 25d.) The easier oxidation of iron is responsible for the higher yield of hydrogen on $CoFe_2O_4$ with respect to $FeCo_2O_4$. It should be highlighted that we have not found evidence (neither from EXAFS spectra nor from LCF of XANES data) of the formation of single metal spinels (Co_3O_4 or Fe_3O_4).

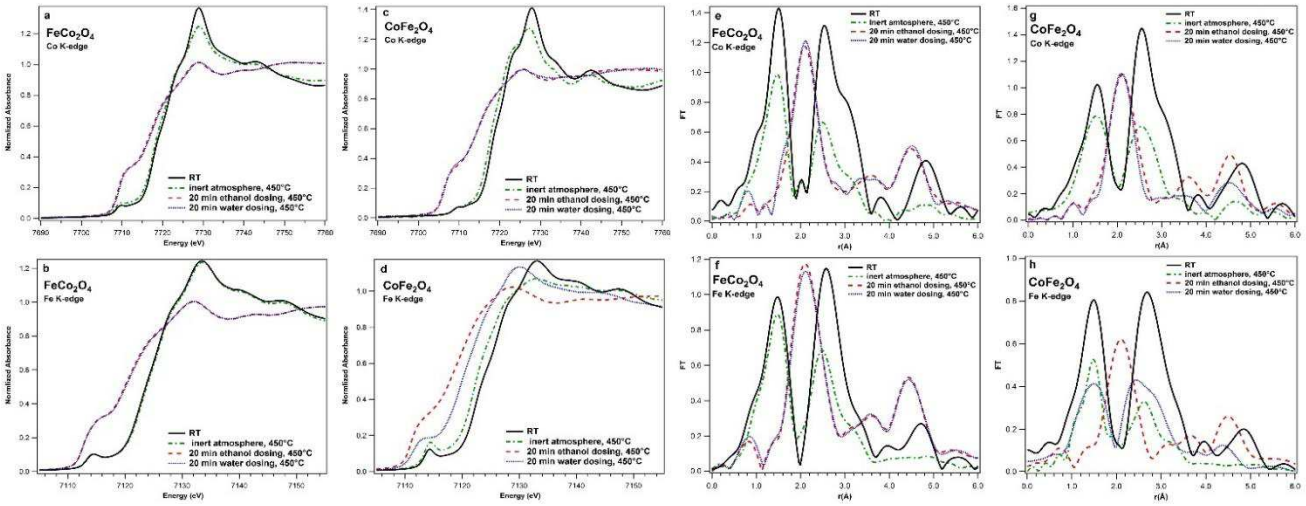

Figure 25: XANES spectra at Co K-edge (a,c) and Fe K-edge (b,d) and Fourier transforms of $k^3\chi(k)$ at Co K-edge (e,g) and Fe K-edge (f,h) of $FeCo_2O_4$ (a,b,e,f) and $CoFe_2O_4$ (c,d,g,h) after three successive steps: annealing in inert atmosphere at 450°C, 20 minutes of ethanol dosing (0.08 ml/h) and 20 minutes of water dosing (0.04 ml/h). Reproduced from Ref. 1 with permission from the Royal Society of Chemistry.

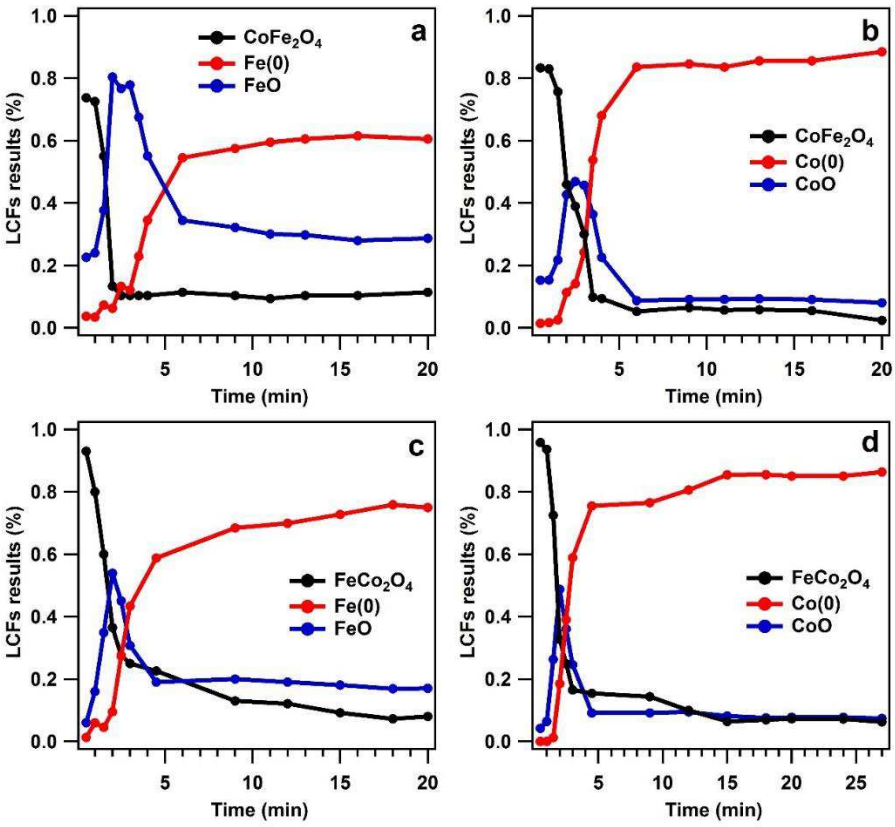

Figure 26: LCFs (% of composition vs temperature) of Fe(b,c) and Co (a,c) K-edge for $FeCo_2O_4$ (a,b) and $CoFe_2O_4$ (c,d) during the treatment in reducing atmosphere (5.3 % ethanol in N_2) at 450°C. Reproduced from Ref. 1 with permission from the Royal Society of Chemistry.

Combining XAS and catalytic tests: main results

Overall, the body of our experimental data indicates that at high temperature (450°C) both spinels are highly active for the total decomposition of ethanol at 450ºC, producing H_2 and CO_x as main products, whereas at 350°C the overall conversion decreases and other reaction paths, especially oxidative dehydrogenation, becomes relevant. The different Co/Fe ratio in the oxides is a key parameter for controlling their chemical activity. The cobalt rich spinel can be easily reduced, but it is very difficult to be re-oxidized by a mild oxidant as water. In contrast, a higher iron fraction makes the system more reversible since an intermediate iron wüstite phase, which is a better oxygen buffer, is stabilized.[63] Concerning the different selectivity in the anaerobic ethanol oxidation $FeCo_2O_4$ strongly favors the oxidative dehydrogenation to acetaldehyde with respect to $CoFe_2O_4$. The very high acetaldehyde yield observed at the beginning of the reaction can be traced back to very active tetrahedral species that are almost immediately converted to less reactive octahedral divalent species. $CoFe_2O_4$ on the other hand shows a less pronounced selectivity toward acetaldehyde. In fact, it was suggested that a decrease of the amount of Fe(III) in tetrahedral sites in Co/Fe mixed spinel promotes dehydration rather than dehydrogenation.[64] Our data indeed, indicate that the ratio of Fe(III) in tetrahedral sites in the two spinels is inversely proportional to acetaldehyde selectivity. Another important parameter that controls the selectivity of the reaction is the type of majority carriers in the material:[65] n-type semiconductors can provide easily electron and favor dehydration, whereas the presence of mobile holes favors oxidative dehydrogenation. $CoFe_2O_4$ is an n-type semiconductor,[63] however upon reduction, it is converted to a wüstite-type oxide that is a p-type semiconductor. This change may explain why as a function of time the acetaldehyde selectivity increases for the cobalt ferrite.

2.5 Conclusion

In this chapter, we focused our attention on the design at the atomic level of spinel-based catalysts. By combining different characterization techniques (XRD, Raman and Mössbauer Spectroscopies), *in operando* Quick-EXAFS and catalysis measurements, we have investigated the structural and chemical properties of two archetypal cobalt/iron mixed spinel ($FeCo_2O_4$ and $CoFe_2O_4$) during each step of the chemical loop reforming of ethanol. CLR of ethanol is a promising technology for the production of high purity hydrogen, which is gaining more and more interest due to its intrinsic sustainability. Nowadays the interest for spinels is gaining more and more momentum in the materials science community, but as demonstrated by a very recent review on this topic[66], this field is still based on a high level of empiricism and there is an urgent need for in operando studies that are capable to unravel the subtle links between structure and activity. These materials have both a spinel structure, but they have different Fe/Co ratio and different degree of inversion. Mainly thanks to X-ray Absorption Spectroscopy, we carefully analyzed the correlation between the site occupancy of the spinel structure of Co/Fe mixed oxides and the reducibility of these materials.

Firstly, we synthesized two different Fe/Co mixed spinels and we have studied the freshly prepared materials. Both materials have spinel structure, as demonstrated by XRD and Raman Spectroscopy. Thanks to X-ray Absorption Spectroscopy, we have determined the oxidation state of Fe and Co and the inversion parameter γ in the two structures (0.8 and 0.6 for $CoFe_2O_4$ and $FeCo_2O_4$, respectively). Then, by means of *in operando* Quick-EXAFS measurements, we captured snapshots of spinel redox chemistry both during ethanol induced reduction and oxidation by water steam. These two reactions constitute the elementary steps of the CLR of ethanol. We have followed in real time the solid state redox processes of these mixed spinels as a response to temperature and reactive atmosphere. In particular, we monitored the reduction of the catalysts during the first step of CLR of ethanol and the oxidation during H_2O steam exposure. These structural data were combined with the analysis of the reaction products in order to identify what are the most chemically active cations inside the spinel structure and what parameters control the chemical activity toward ethanol decomposition. These experiments have highlighted the influence of both coordination and chemical nature of the cations on the catalytic properties. The cations in tetrahedral sites of the spinel structure show a higher reducibility with respect to octahedral ones, independently from their chemical nature. The reduction of the spinel structure leads to the formation of a wüstite phase and of FeCo metal alloys. Conversely, considering the ratio between reduced phases (wüstite and metal alloy), the chemical nature of the cation plays an important role. In fact, the total reduction of Co to Co(0) is faster with respect to that of Fe. This is reflected in the oxidation step of CLR, where the re-oxidization of cobaltite by a mild oxidant such as water is practically ineffective. This different behavior influences the ethanol decomposition selectivity and yield. At mild temperature (350°C) $FeCo_2O_4$ strongly favors the oxidative dehydrogenation to acetaldehyde with respect to $CoFe_2O_4$. Moreover, the very high acetaldehyde yield observed at the beginning of the reaction can be traced back to very active tetrahedral species that are almost immediately converted to less reactive octahedral divalent species. At higher temperature (450°C), both spinels are almost totally reduced to metal phases and are highly active for the total decomposition of ethanol, producing H_2 and CO_x as main products.

In conclusion, our study indicate that $CoFe_2O_4$ is a more promising material than $FeCo_2O_4$ for CLR due to a more reversible chemistry connected to the higher stability of the wüstite phase. Nonetheless, the fundamental knowledge acquired in this study may be a stepping stone for the design of new improved materials to be used as solid oxygen carriers and novel catalysts for the selective oxidation of alcohols and for the production of hydrogen through CLR. In particular, for the first time, we were able to assess the role of chemical nature (Co vs Fe), geometrical site (tetrahedral vs octahedral site) and crystal phase (spinel vs wüstite) on spinel redox

chemistry, laying the basis for a rational design of materials with specific chemical and functional properties. We think that this fundamental knowledge will have a far-reaching impact on materials science and sustainable chemistry because of the ever-increasing importance of oxides in some critical fields such as catalysis and energy conversion. In this chapter, we demonstrate how to capitalize such a knowledge for the design of oxygen carriers for the chemical loop reforming of ethanol, but its exploitation in other chemical looping and carbon capture technologies appears to be equally likely.

In fact, the precise understanding of how some specific structural features at the atomic scale control the chemical reactivity represent an exceptional stepping stone to develop advanced catalysts for the selective conversion of alcohols, alternative solid state oxygen storage systems, and several applied materials that exploit the redox properties of oxides.

References

[1] F. Carraro, O. Vozniuk, L. Calvillo, L. Nodari, C. La Fontaine, F. Cavani and S. Agnoli, *J. Mater. Chem. A*, **2017**, 5, 20808-20817.
[2] M.T. Weller, Inorganic Materials Chemistry, Oxford University Press, **1994**.
[3] G. Voitic, V. Hacker. *RSC Adv.* **2016,** *6* (100), 98267-98296.
[4] G.N. Chaudhari, M.J.Pawar, J. Optoelectron. Adv. Mater., **2008**, 10, 2574-2577.
[5] Y. Sharma, N. Sharma, G.V.S. Rao, B.V.R. Chowdari, Solid State Ionics, **2008**, 179, 587-597.
[6] F. Cheng, J. Shen, B. Peng, Y. Pan, Z. Tao, J. Chen, *Nat. Chem.* **2011,** 3, 79–84.
[7] M. B. Gawande, R. K. Pandey, R. V. Jayaram, *Catal. Sci. Technol.* **2012**, 2, 1113-1125.
[8] C. Yuan, H. B. Wu, Y. Xie, X. W. D. Lou, *Angew. Chem. Int. Ed.* **2014**, 53, 1488-1504.
[9] J. H. Clark, *Green Chem.* **1999**, 1, 1-8.
[10] Y. Liu, G. Zhao, D. Wang, Y. Li, *Natl Sci Rev* **2015**, 2, 150-166.
[11] A. Chieregato; J. M. López Nieto; F. Cavani, *Coord. Chem. Rev*. **2015**, 301–302, 3–23.
[12] V, Polshettiwar, B. Baruwati,; R. S. Varma, *ACS Nano* **2009**, 3, 728-736.
[13] V. E. Henrich, P. A. Cox, *Cambridge Univ. Press* **1994**.
[14] M. R. N. S. Hamdani, R. N. Singh, P. Chartier, *Int. J. Electrochem. Sci* **2010,** 5, 556-577.
[15] S. K. Ngoh and D. Njomo, Renewable Sustainable Energy Rev., **2012**, 16, 6782–6792.
[16] J. Adanez, A. Abad, F. Garcia-Labiano, P. Gayan and L. F. De Diego, Prog. Energy Combust. Sci., **2012**, 38, 215–282.
[17] C. Trevisanut, O. Vozniuk, M. Mari, S. Yurena, A. Urrea, C. Lorentz, J. M. Millet, F. Cavani, *Top. Catal.*, **2016**, 59, 1600–1613.
[18] V. Crocellà, F. Cavani, G. Cerrato, S. Cocchi, M. Comito, G. Magnacca, C. Morterra, *J. Phys. Chem. C*, 2012, **116**, 14998–15009.
[19] A. Khan, P. Chen, P. Boolchand and P. Smirniotis, *J. Catal.*, **2008**, **253**, 91–104.
[20] J. C. Ryu, D. H. Lee, K. S. Kang, C. S. Park, J. W. Kim and Y. H. Kim, *J. Ind. Eng. Chem.*, **2008**, 14, 252–260.
[21] K. Otsuka, C. Yamada, T. Kaburagi and S. Takenaka, *Int. J. Hydrogen Energy*, **2003**, 28, 335–342.
[22] S. Permien, S. Indris, U. Schürmann, L. Kienle, S. Zander, S. Doyle, W. Bensch, *Chem. Mater.* **2016**, 28, 434– 444.
[23] C. Wei, Z. Feng, G. G. Scherer, J. Barber, Y. Shao-Horn, Z. J. C Xu, Adv. Mater. **2017**, 29, 1606800.
[24] X. Wang, Y. Liu, T. Zhang, Y. Luo, Z. Lan, K. Zhang, J. Zuo, L. J. R. Wang, *ACS Catal.* **2017**, 7, 1626–1636.
[25] H. Zhu, S. Zhang, Y. X. Huang, L. Wu, S. Sun, *Nano letters* **2013**, 13, 2947-2951.
[26] T. Maiyalagan, K. A. Jarvis, S. Therese, P. J Ferreira, A. Manthiram, *Nat. commun.* **2014**, 5, 3949.
[27] X. Xie, Y. Li, Z. Q. Liu, M. Haruta, W. Shen, *Nature* **2009**, 458, 746-749.
[28] F. F. Tao, J. J Shan, L. Nguyen, Z. Wang, S. Zhang, L. Zhang, L. Zhang, Z. Wu, W. Huang, S. Zeng P.Hu, *Nat. commun.* **2015**, 6*,* 7798.
[29] P. Cho, T. Mattisson, A. Lyngfelt, *Fuel*, **2004**, 83, 1215-1225.
[30] R. J. Scheffe, M. D. Allendorf, E. N. Coker, B. W Jacobs, A. H.McDaniel, A. W Weimer. *Chem Mater.* **2011,** *23,* 2030-2038
[31] C. Trevisanut, M. Mari, J. M. M. Millet, F. Cavani, *Int. J. Hydrogen Energy* **2015**, 40, 5264-5271.
[32] V. J. Aston, B. W. Evanko, A. W. Weimer, Int. J. Hydrogen Energy **2013**, 38, 9085-9096.
[33] Z. Ma, L. Ren, S. Xing, Y. Wu, Y. Gao. *J. Phys. Chem. C*, **2015**, 119 (40), 23068–23074.
[34] X. Zhou, J. Huang, F.M. Zhang, Y. Zhao, Y. Zhang, Y. Ding. *Dalton Trans.* **2017,** 10.1039/C7DT00302A.
[35] M. Nasrollahzadeh, M. Bagherzadeh, H. Karimi, *J. Colloid Interface Sci.* **2016**, 465, 271–278.
[36] H. Jin, T. Okamoto, M. Ishida, Enery Fuels **1998**, 12, 1272– 1277.
[37] E. Hormilleja, P. Durán, J. Plou, J. Herguido, Peña J.A. *Int. J. of Hydrogen Energy* **2014**, 39, 5267-5273.
[38] B. Ravel; M. Newville, *Synchrotron Radiat.* **2005,** 12, 537–541.

[39] D. Carta, M. F. Casula, A. Falqui, D. Loche, G. Mountjoy, C. Sangregorio, A. Corrias, *J. Phys. Chem. C*, **2009**, 113 (20), 8606–8615.
[40] C.N. Chinnasamy, A. Narayanasamy, N. Ponpandian, K. Chattopadhyay, K. Shinoda, B. Jeyadevan, K.Tohji, K.Nakatsuka, T. Furubayashi, I. Nakatani, *Phys. Rev. B,* **2001**, 63*,* 184108.
[41] C.Trevisanut, O.Vozniuk, M.Mari, S.Yurena, A.Urrea, C.Lorentz, J.-M.Millet, F. Cavani, *Top. Catal*., **2016**, 59, 1600–1613
[42] O. Vozniuk, S. Agnoli, L. Artiglia, A. Vassoi, N. Tanchoux, F. Di Renzo, G. Granozzi, F. Cavani, *Green Chem.* **2016**, 18, 1038-1050.
[43] T. A. S. Ferreira J. C. Waerenborgh M. H. R. M. Mendonça, M. R. Nunes, F. M. Costa, *Solid State Sciences* **2003**, 5, 383–392.
[44] E. Manova, T. Tsoncheva, D. Paneva, I. Mitov, K. Tenchev, L. Petrov, *Applied Catalysis A: General* **2004**, 277, 119–127.
[45] P. Chandramohan, M. P. Srinivasan, S. Velmurugan, S. V. Narasimhan, *J. Solid State Chem.* **2011**, 184, 89–96.
[46] O. Vozniuk, C. Bazzo, S. Albonetti, N. Tanchoux, J.-M. M Millet, F. Bosselet, F. Di Renzo, F. Cavani *ChemCatChem* **2017**, DOI: 10.1002/cctc.201601605R1
[47] D. Carta, M. F. Casula, A. Falqui, D. Loche, G. Mountjoy, C. Sangregorio, A. Corrias, *J. Phys. Chem. C,* **2009**, 113 (20), 8606–8615.
[48] V. Krishnan, R. K. Selvan, C. O. Augustin, A. Gedanken, H. Bertagnolli, *J. Phys. Chem. C* **2007**, 111 (45), 16724–16733.
[49] M. H. Nilsen, C. Nordhei, A. L. Ramstad, D.G. Nicholson, *J. Phys. Chem. C* **2007**, 111 (17), 6252–6262.
[50] G. A. Sawatxky, F. Van Der Woude, A. H. Morrish, *P Phys. Rev*. **1969**, 187, 747.
[51] D. Carta, A. Corrias, G. Navarra, *Journal of Non-Crystalline Solids* **2011**, 357, 2611–2614.
[52] Z. G. Lu, J. H. Zhu, Z. H. Bi, X. C. A Lu, *J. Power Sources* **2008**, 180, 172– 175.
[53] Y. I. Ustinovshikov, P, B. E. Ushkarev, I. V. Sapegina, *Inorg. Mater.* **2006**, 42, 354– 359.
[54] Y. Tamaura, M. Kojima, T. Sano, Y. Ueda, N. Hasegawa, M. Tsuji, *International Journal of Hydrogen Energy*, **1998**, 23(12), 1185-1191.
[55] M. Tabata, K. Akanuma, T. Togawa, M. Tsuji, Y. Tamaura, *J Chem Soc Faraday Trans* **1994**, 90, 1171.
[56] W. C. Cho, C. G. Kim, S. U. Jeong, K. S. Kang, S. D. Kim, *Industrial & Engineering Chemistry Research* **2015,** 54 (12), 3091-3100.
[57] I. Barin, O. Knacke, Springer-Verlag: Berlin, **1973**, 66-74.
[58] C. D. Bohn, C. R Muller, J. P Cleeton, A. N. Hayhurst, J. F. Davidson, S. A Scott, J. S. Dennis, *Ind. Eng. Chem. Res.* **2008**, 47**,** 7623– 7630.
[59] S. Liu, F. He, Z. Huang, A. Zheng, Y. Feng, Y. Shen, H. Li, H. Wu, P. Glarborg, *Energy Fuels* **2016**, 30**,** 4251−4262.
[60] M. D.Allendorf. *Energy & Fuels* **2008**, 22, 4115–4124.
[61] T. Block, N. Knoblauch, M. Schmücker, *Thermochim. Acta* **2014**, 577, 25– 32.
[62] K. S. Go, S. R Son, S. D. Kim, *Int. J. Hydrogen Energy* **2008**, 33, 5986-5995.
[63] N. Bahlawane, PH. Ngamou, V. Vannier, T. Kottke, J. Heberle, K. Kohse-Höinghaus, *Phys. Chem. Chem. Phys.* **2009**, 11, 9224–9232.
[64] G. R. Dube, V. S. A Darshane, *Bull. Chem. Soc. Jpn,* **1991**, 64, 2449-2543.
[65] O. V. Krylov, E. M. Loebl, *Physical Chemistry: A Series of Monographs* **1970,** 17.
[66] Q. Zhao, Z. Yan, C. Chen, J. Chen, *Chem. Rev.* **2017**, 117, 10121−10211.

Chapter 3

Multiscale design of nanostructured Pd/CeO_2 heterogeneous catalysts

3. Multiscale design of nanostructured Pd/CeO_2 heterogeneous catalysts

Palladium is an active catalyst for the decomposition of methanol to syngas, whose chemical activity is largely affected by the interaction with the supporting substrate. Nanostructured Cerium oxide can establish strong electronic interactions with finely dispersed palladium nanoparticles (NPs) leading to a substantial enhancement of their catalytic performance. This synergistic effect is dependent on structural factors such as the nanoparticle size and the crystallographic orientation of the facets because they control the coordination and chemical environment of oxygen anions and cerium cations. To study these structure/activity relationships, we deposited Pd NPs on nanostructured cerium oxides particles exposing mainly the same (100) face, but with different morphology and average dimension (from few nanometers to hundreds of nanometers), and we have investigated their activity toward selective methanol decomposition. The differences in the catalytic properties of the investigated materials are correlated to the morphology of the oxide substrates (nanorods of different aspect ratio, nanocubes or nanopowders), to their surface reducibility in working conditions and to the synergy established with Pd NPs. Moreover, in the next chapter, we will take advantage of this study is in order to design a complex multivariate catalytic system.

3.1 CeO_2

Cerium dioxide (CeO_2), a pale yellow/white powder, is a very well-known cerium compound that it is nowadays employed in many different fields of application such as optics[1], biomedicine[2], polishing materials[3], solid oxide fuel cells[4]. However, heterogeneous catalysis is probably the most studied application of cerium-based materials. For example, more than 40 years ago for the first time, ceria was employed by Ford Motor Company as component in car catalytic converters and nowadays is an irreplaceable element of three-way catalysts (TWCs).[5] This huge exploitation is favored by the abundance of Cerium (is the most abundant of the so-called rare earth elements, about 0.0046 wt % of the Earth's crust) and by its low price.[5] Moreover considering the requirements for the modern society of the development of a more "green" chemistry, and consequently economy, that take in consideration the value versus risk of the elements, cerium is considered an highly exploitable element.[6] Therefore, at least in the short-medium term, the limits to further development of ceria-based technologies are mainly restricted to geopolitical factors (China extracts the 90% of rare earths global production).[6] A part from the most widespread and consolidated use as TWCs and pollution abatement, ceria-based material are studied in several different catalytic applications such as water-gas shift (WGS), steam and dry reforming of hydrocarbons and oxygenates, CO oxidation, alcohols synthesis from syngas, selective hydrogenations and C-C coupling.[7,8] The number of ceria related publications from 1950 to 2015 exceeds 26000, with a constant increase of publications per year. The same trend is showed by papers on ceria associated with the research field of catalysis (Figure 1).[5]

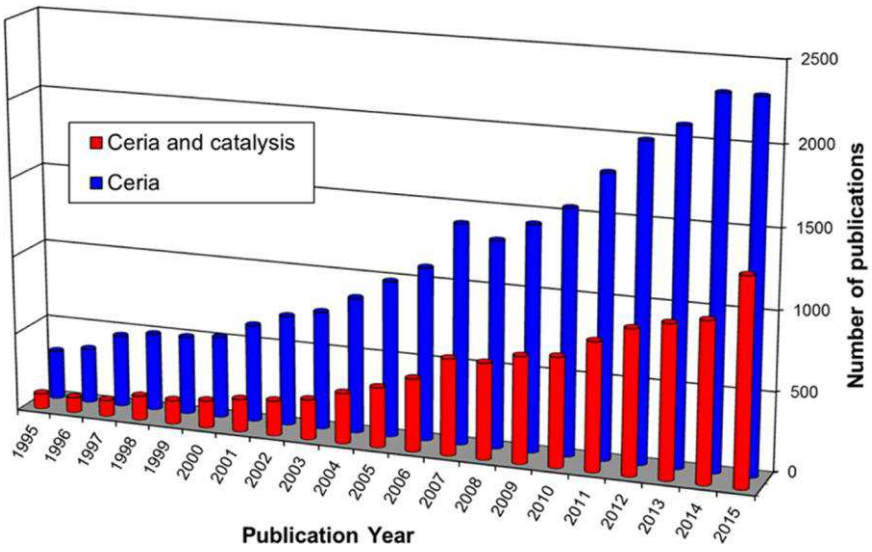

Figure 1: Histogram of number of publications on ceria (blue bars) and publications on ceria associated with catalysis (red bars) from 1994 to 2015. (Source: Web of Science, Jan 9, 2016). Reprinted with permission from T. Montini, M. Melchionna, M. Monai, P. Fornasiero, Chem. Rev. 2016, 116, 5987−6041 . Copyright © 2016, American Chemical Society.

This highlights that despite the huge amount of studies, the fascinating catalytic properties of ceria-based materials have kindled a tremendous interest in the scientific community and are continuously offering new potential applications. In recent years, this was also favored by the development of new and powerful characterization techniques[9] (i.e. operando studies) and theoretical methods[10] that permitted to achieve a deeper insight into the fundamental properties of ceria based materials.

3.2 Structure and surface dependent behavior of ceria

The great interest of ceria-based materials as catalysts is mainly related to their oxygen storage capacity (OSC), so to their ability to shuttle between Ce(IV) and Ce(III) oxidation states maintaining structural integrity. CeO_2 exhibits the fluorite crystal structure, with a face-centered cubic (FCC) unit cell (Fm3m, a=0.541134 nm, JCPDS 34-394).[5] In this structure, eight equivalent nearest-neighbor oxygen anions are coordinated around Ce cations at the corners of a cube. Consequently, each anion has tetrahedral coordination. The reduction of Ce(IV) to Ce(III) leads to non-stoichiometric CeO_{2-y} by oxygen release and with the concomitant formation of oxygen vacancies within the crystal structure. Following the Kröger-Vink notation, this reaction can be expressed as:

$$2Ce_{Ce} + O_O \rightarrow V_O^{\cdot\cdot} + 2Ce'_{Ce} + \frac{1}{2}O_2 \qquad (1)$$

Ce_2O_3 is the stable form of the fully reduced cerium oxide and has hexagonal crystal structure ($P\bar{3}ml$). However, intermediate composition of CeO_{2-y} ($0.5<y<0$) almost retains the FCC structure: Ce cations maintain near FCC-like positions and O-vacancies could be ordered or randomly distributed, depending on temperature, oxygen partial pressure and composition.[11]

Computational studies demonstrated that the oxygen vacancy formation energy is approximately 30% lower on the ceria surface compared to the bulk and strongly depends on the exposed facets.[10] Thus the catalytic behavior of ceria, that are based on its acid-base properties, is strongly controlled by its surface structure.[12] In fact, low-index structural facets present different cerium cations and oxygen anions coordination environments and therefore present different reducibility and vacancies concentration. The three thermodynamically most stable surfaces of ceria are $\{111\}$, $\{100\}$ and $\{110\}$ (Figure 2)).[13,14]

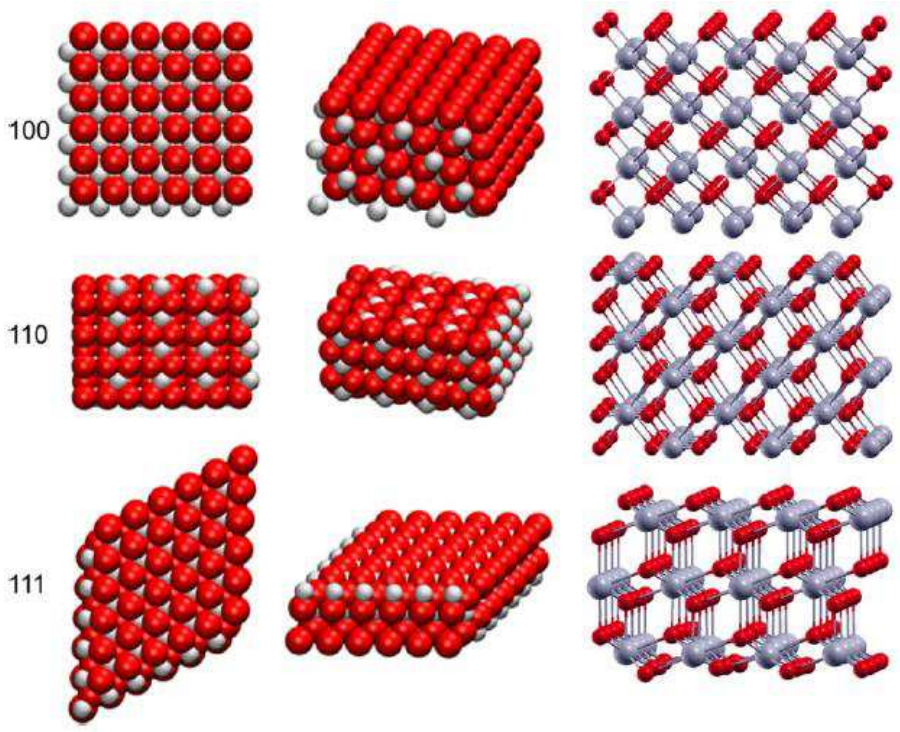

Figure 2: Top, side, and perspective view of CeO_2 (100), (110), and (111) surfaces. Gray and red spheres represent cerium and oxygen ions, respectively. Reprinted with permission from A. Trovarelli, J. Llorca, ACS Catal. 2017, 7, 4716-4735. Copyright © 2017, American Chemical Society.

Other less stable surfaces, like $\{210\}$ and $\{310\}$, are unlikely in real systems because they suffer of faceting and reconstruction processes.[14] For this reason, most of the studies present in the literature are focused on the three more stable low index surfaces. The thermodynamic stability of these surfaces is: $\{111\}>\{110\}>\{100\}$. In all these cases, the coordination number of Ce and O is lower with respect to bulk ceria (O=4; Ce=8). The (111) oriented surface is oxygen-terminated and has not dipole moment because of the repetition of three layer of O-Ce-O maintains charge neutrality (Type 2 surface). The CeO_2 (110) surface exposes both Ce cations and O anions and the charge neutrality is maintained for each layer (Type 1 surface). Conversely, CeO_2 (100) surface exposed Ce-O-Ce-O repeating units that causes a net dipole moment perpendicular to the surface. The main characteristics of these surfaces are summarized in Table 1 (adapted from Ref.12).

Table 1: Characteristics of Low Index Surfaces of CeO_2. Adapted from A. Trovarelli, J. Llorca, ACS Catal. 2017, 7, 4716-4735.

	(111)	(110)	(100)
Coordination Number	O(3), Ce(7)	O(3), Ce(6)	O(2), Ce(6)
Coordinative unsaturated sites	O(1), Ce(1)	O(1), Ce(2)	O(2), Ce(2)
Surface Energy (eV)[a]	0.69(0.68)	1.26(1.01)	2.05(1.41)
Oxygen Vacancy Formation Energy (eV)[15]	2.60	1.99	2.27
[a] Unrelaxed and (relaxed) values calculated from ab initio DFT.[16]			

The trend of oxygen vacancy formation energy is: {110}>{100}>{111}. This is a crucial parameter for characterizing the reducibility of a certain ceria surface. As shown before with the Kröger-Vink notation (1), the reduction of CeO_2 implies that electrons are transferred from an O atom to two adjacent Ce atoms. Consequently, these two Ce atoms are reduced to Ce(III) and an oxygen vacancy is formed. So, the more easily the O vacancy is accommodated by the exposed surface, the most reducible is that surface. The formation of an oxygen vacancy creates a mobile reactive site on the surface and can act as center for the activation of oxygen in oxidation reactions. This is the keystone of the oxygen storage process and therefore of the most interesting catalytic properties of ceria.

In order to characterize the degree of reduction of ceria surface, one of the most useful characterization technique is X-ray Photoemission Spectroscopy (XPS). The photoemission spectrum of Ce3*d* can be fitted with five spin-orbit-split doublets corresponding to the possibly different 4*f* configurations in the photoemission final state (Figure 3). The components labeled v^0 and v^i correspond to Ce^{3+}, whereas the components labeled v, v^{ii}, v^{iii} are ascribed to Ce^{4+}.[17] The spin-orbit-splitting satellite labeled u^{iii} at about 917 eV is indicative of the poorly screened $Ce3d^94f^0O2p^6$ final state, connected only with the presence of Ce^{4+} ions. For this reason, in order to follow easily the degree of reduction of CeO_2 surface is possible to measure the ratio of the area of the u^{iii} doublet versus the total area of the fit Ce3*d* photoemission line. The doublets at lower binding energy v and u, v^{ii} and u^{ii}, result from shake-down processes where electrons are transferred from the O2*p* to Ce4*f* levels in the exited state and correspond to the $Ce3d^94f^2O2p^4$ and the $Ce3d^94f^1O2p^5$ final states, respectively. The two multiplets v^0 and u^0, v^i and u^i, associated with Ce(III), correspond to the $Ce3d^94f^1O2p^6$ and $Ce3d^94f^2O2p^5$ final states, respectively.[17,18]

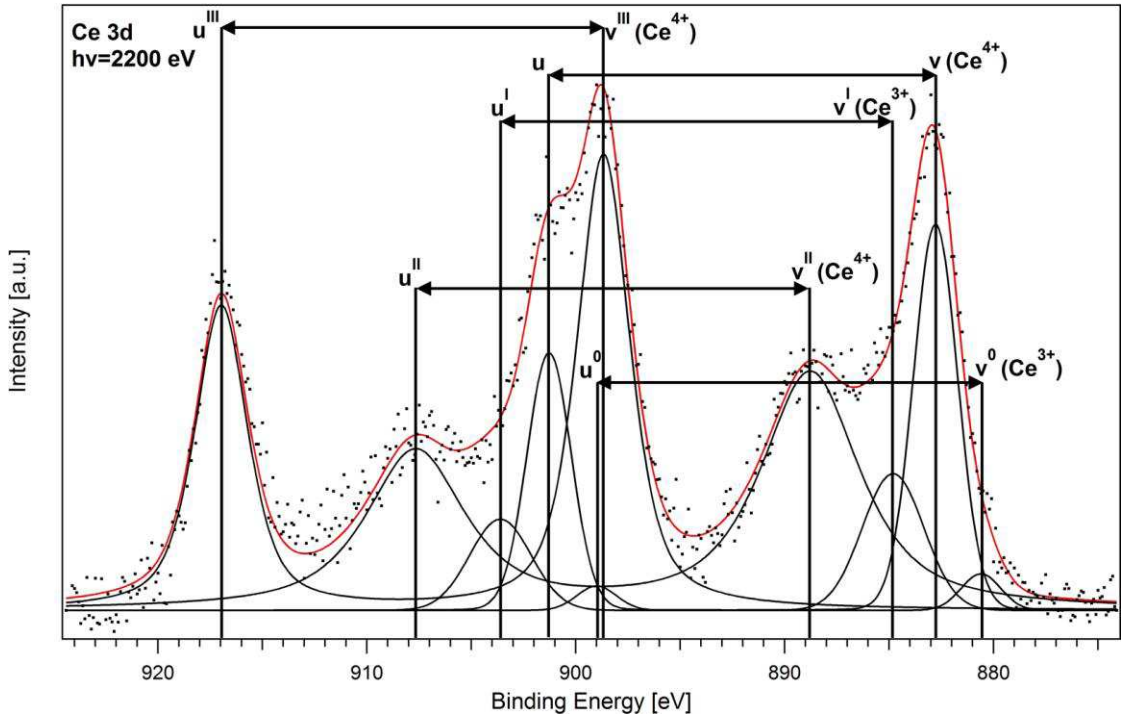

Figure 3: Photoemission spectrum and deconvolution of Ce 3d after activation of the catalyst in hydrogen at 150 °C. Reprinted with permission from L. Artiglia, F. Orlando, K. Roy, R. Kopelent, O. Safonova, M. Nachtegaal, T. Huthwelker, J.A. van Bokhoven, J. Phys. Chem. Lett. 2017, 8, 102−108. Copyright © 2017, American Chemical Society.

3.3 Engineering CeO_2 morphology at the nanoscale

In order to characterize the structural and catalytic (i.e. adsorption and reactions of molecules) properties of ceria with controlled exposed surfaces, it is possible to grow cerium oxide thin films on different substrates. These kinds of model systems are suited for surface science characterization tools (XPS, STM, LEED, TPD) and permit to have a deeper insight into the fundamental properties of the different surfaces exposed by cerium oxide. Cerium oxide thin films can be grown employing several different techniques such as metalorganic chemical vapor deposition[19], magnetron sputtering[20], pulsed laser deposition[21], evaporation of metallic Ce by resistive heating[22] or by e-beam heating[23]. Typically, the depositions were performed in oxidizing atmosphere[22] or a post-deposition O_2 treatment[24] was necessary to achieve a good stoichiometry. Ceria thin films exposing CeO_2 (111) are the most studied in the literature. This kind of thin films can be grown by evaporating metallic Ce in O_2 atmosphere onto the close-packed surfaces of hcp(0001) or fcc(111) single metal surfaces. [11] CeO_2 (100) thin films were also extensively studied in the literature (i.e. grown on SrTiO3(100)[21] and fcc(100) metals substrates[25]). Conversely, only few works focused on the CeO_2(110) surface are reported in the literature.[11]

In the last twenty years, great effort was put on the development of synthesis methodologies of ceria nanoparticles with uniform and controlled morphology. Standard preparation techniques of oxides such as precipitation or coprecipitation methods are usually very fast and simple, but the drawback is the lack of morphological control. In fact, the morphology of a crystal depends on both kinetics and thermodynamic processes that characterize the particle growth process.[26,27] If the growth is controlled by thermodynamics, the crystals will expose the most stable surface and the nanoparticles will have a specific shape. Conversely, kinetic processes may allow the synthesis of nanoparticles exposing facets with higher surface energy. The kinetic control of nucleation and growth rate of the nanoparticles depends on several parameters such as temperature, pH, pressure, concentration, solvent, presence of surfactants and nature of the precursors. There are mainly two approaches to the synthesis of ceria nanoparticles with controlled shape and size: surface capping agents assisted growth and hydrothermal synthesis. The capping agents (inorganic or organic) influence the finale shapes of the nanoparticles by the inhibition of the growth along a specific direction.[28] In fact, capping agents interact differently with different ceria surfaces. For example, dodecanoic acid binds preferentially on the (100) surface and this leads to the increase in the growth rate along the [111] direction (Figure 4)).[29] This strategy permits to synthesize materials with homogeneous particle size and morphology or hollow structures.[30] The main drawback of this approach, especially from the catalysis point of view, is the presence of capping agents on the particles surfaces of the synthesized materials. In fact, the removal of the surfactant is a big problem because of the strong force between the reagent and favorable crystal surfaces.

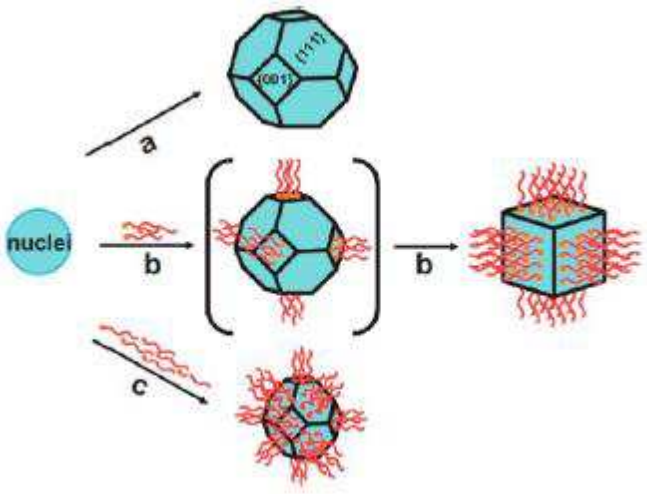

Figure 4: Control of nanocrystal shape through the use of surface capping agents. Interaction of dodecanoic acid with {100} surfaces slows the growth in this direction leading to the formation of nanocubes (path b). In excess of dodecanoic acid, growth in both directions is reduced with the formation of small truncated octahedral particles (path c) compared to path a with no capping agent. Reprinted with permission from A. Trovarelli, J. Llorca, ACS Catal. 2017, 7, 4716-4735. Copyright © 2017, American Chemical Society.

If we want a clean CeO_2 surface, and so the highest number of reactive sites available for catalysis, it is necessary to perform an additional step that removes the capping agents. For this reason, surfactant-free processes to synthesized CeO_2 nanostructures were extensively studied in the literature and are typically related to hydrothermal and solvothermal methods. These methods are based on the preparation of a basic solution containing a Ce precursor that is maintained at high temperature in a closed vessel. As cerium source $Ce(NO_3)_3{\cdot}nH_2O$[31] or $CeCl_3{\cdot}nH_2O$[32] are usually employed. As base, most convenient choice is NaOH, KOH or NH_3. In the hydrothermal method, the water basic solution containing the Ce precursor is transferred into a Telfon-lined autoclave. The autoclave is maintained at a desired temperature (usually 373-473 K) for different times (usually 12-48 h). Finely tuning the synthesis parameters (temperature, time, base and Ce precursor nature and concentrations), it is possible to obtain nanoparticles with different morphology and size. Without capping agents, the nucleation and growth of the nanoparticles is driven by the chemical potential and the viscosity of the solution in hydrothermal conditions and the structural anisotropy of the inorganic compound. Ceria crystal structure is isotropic and CeO_2 nanoparticles commonly crystallize with polyhedral shape. These polyhedral exposes mainly (111) facets, followed by (110) and (100) facets. (Figure 5)

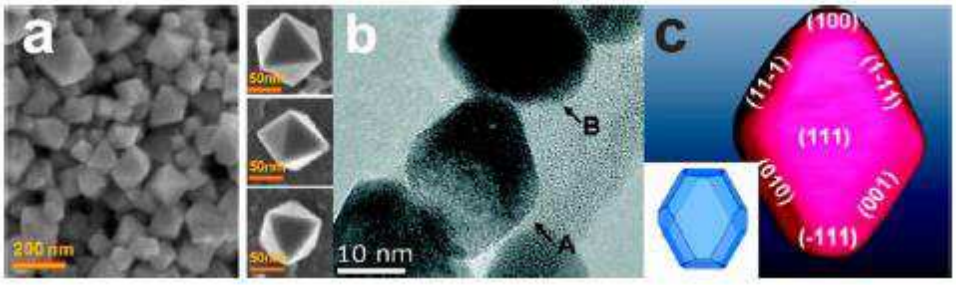

Figure 5: CeO_2 crystals prepared by hydrothermal methods: (a) FE-SEM image of CeO_2 nano-octahedrons and individual nano-octahedron seen from three different views. (b) Bright-field image of large CeO_2 particles and (c) surface 3D rendering view of the structure of particle. Reprinted with permission from A. Trovarelli, J. Llorca, ACS Catal. 2017, 7, 4716-4735. Copyright © 2017, American Chemical Society.

This limitation can be overcome by the presence of anisotropic intermediates, formed during hydrothermal synthesis, and by the influence of the counterions of Ce precursor, that can act as capping agents.[33] Therefore, it is possible to control the growth of ceria nanoparticles along selected directions and to obtain CeO_2 nanostuctures. For example, Mai et al.[31] synthesized single-crystalline and uniform nanopolyhedra, nanorods and nanocubes of fcc CeO_2 (Figure 6). Starting from water solution of cerium nitrate, they optimized different hydrothermal recipes modifying the temperature of the synthesis (100-180°C) and the concentration of NaOH (0.01-9 M) in order to selectively prepare different ceria powders with different morphologies. According to high-resolution transmission electron microscopy, these nanostructures exposed different crystal planes: {111} and {100} for polyhedra, {110} and {100} for rods, and {100} for cubes. The hydrothermal syntheses were confirmed to take place under the dissolution/recrystallization mechanism, whose kinetic can be speeded up raising the pH of the solution. Therefore, they correlated the shape selection to the formation of hexagonal $Ce(OH)_3$ intermediate species and their transformation into CeO_2 at elevated temperature and to the base concentration.

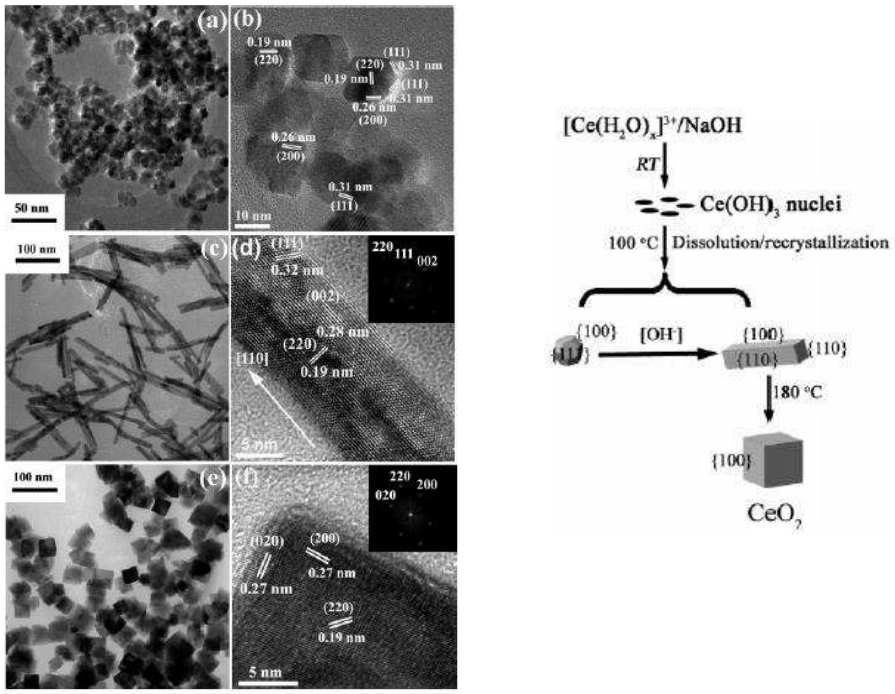

Figure 6: TEM (a) and HRTEM (b) images of CeO2 nanopolyhedra. TEM (c) and HRTEM (d) images of CeO_2 nanorods, inset is a fast Fourier transform (FFT) analysis. TEM (e) and HRTEM (f) images of CeO_2 nanocubes, inset is a fast Fourier transform (FFT) analysis. Schematic diagram (right) for the shape-selective synthesis of CeO_2 nanopolyhedra, nanorods and nanocubes. Adapted with permission from Mai, H. X.; Sun, L. D.; Zhang, Y. W.; Si, R.; Feng, W.; Zhang, H. P.; Liu, H. C.; Yan, C. H. J. Phys. Chem. B 2005, 109, 24380–24385. Copyright © 2005, American Chemical Society.

Starting from the same precursors, Pan et al.[34] developed a large-scale synthesis (RT, atmospheric pressure) of single-crystalline and uniform CeO_2 nanorods that grown along [110] direction. Accordingly to their results, firstly $Ce(OH)_3$ particles are formed. The hydroxy groups limit the lateral growth, so nanorods are formed. The sides of the nanorods may be easily oxidized by oxygen in solution due to the large exposed area, which also limits the lateral growth (Figure 7i). Moreover, they converted the as-prepared nanorods into nanotubes, nanowires, and nanocubes through hydrothermal reactions (Figure 7ii). They resume the hydrothermal process in two fundamental steps: the oxidation of the dissolved Ce(III) to Ce(IV) (rate constant k1) and the growth of the nanorods (rate constant k2). If $k1 > k2$, the process is controlled by the dissolved Ce(III) that is oxidized in solution and then is preferentially deposited on the surface of the nanorods leading to the growth of nanotubes. If $k1 < k2$, the Ce(III) ions prefer to deposit on the tips of the nanorods, which results in the growth of nanowires. At

higher temperatures (120-180°C), the oxidation occurs not only at the surface, but also in the bulk of the nanorod seeds, leading to the formation of nanoparticles and successively nanocubes.

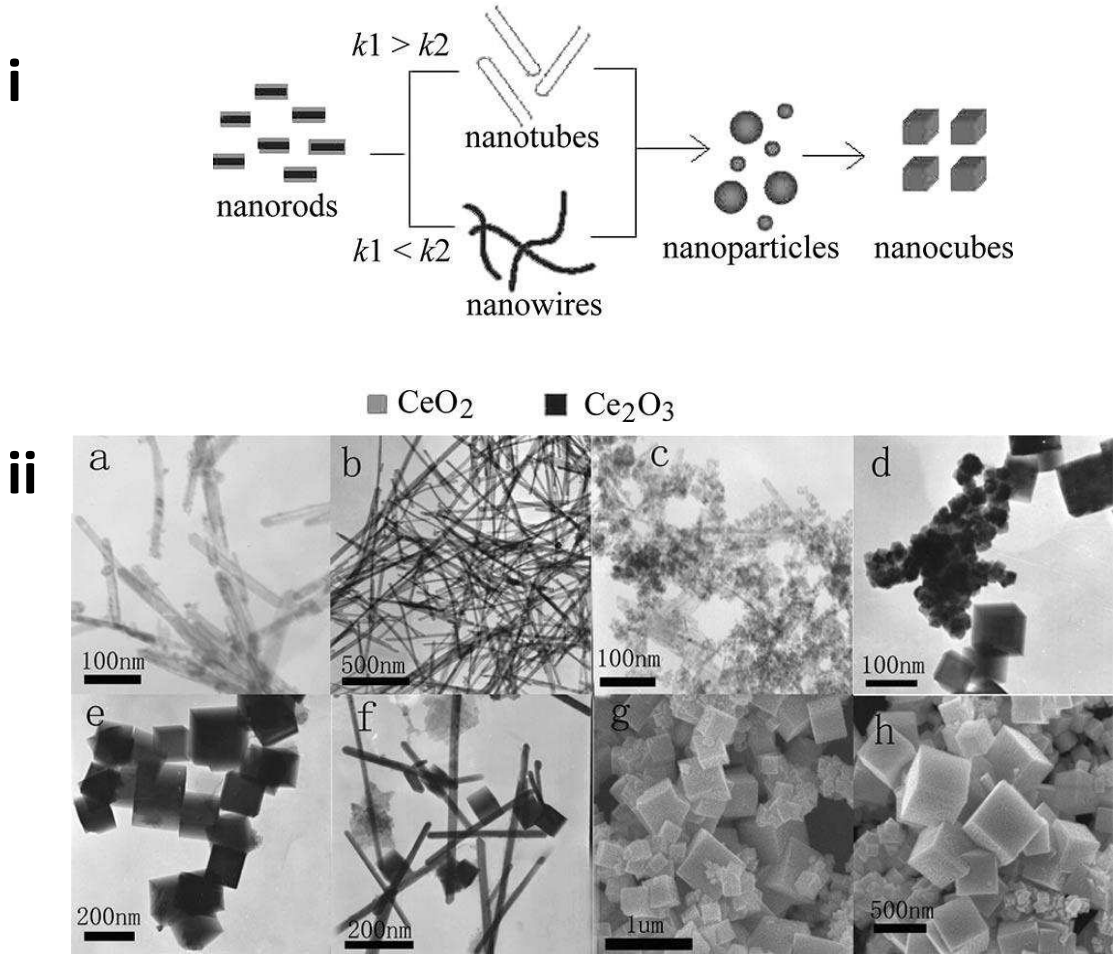

Figure 7: i) Possible conversion mechanism for CeO2 nanorods. k1is represented as the rate constant of the oxidation of the dissolvedCe3+ to Ce4+ and k2 is represented as the rate constant of thegrowth of CeO2 nanorods. ii) TEM images of the conversion of CeO2 nanorods under various hydrothermal conditions: (a) nanotubes (100 °C, 72 h), (b) nanowires (110 °C, 24 h), (c) nanoparticles (120 °C, 24 h), (d) nanoparticles and nanocubes (140 °C, 24 h), (e) nanocubes (160 °C,24 h), (f) nanocubes, nanoparticles, and nanorods (180 °C, 2 h), and (g, h) nanocubes (180 °C, 24 h). Adapted with permission from C. Pan, D. Zhang, L. Shi, J. Fang Eur. J. Inorg. Chem. 2008, 2429–2436. Copyright © 2008 WILEY-VCH Verlag GmbH & Co. KGaA, Weinheim.

As already mentioned, in addition to base concentration, temperature and pressure, also the precursor/counterion nature can influence the final shape of the ceria crystals. Wu et al. [33] determined that chloride and nitrate ions interact differently with (111) or (100) facets of growing ceria particles. This changed the surface free energies and determined the growth rate along different directions. For example, Cl^- favored the growth of elongated 1D structures (nanords, nanowires). Conversely, NO_3^- favored the formation of nanoparticles and nanocubes (Figure 8).

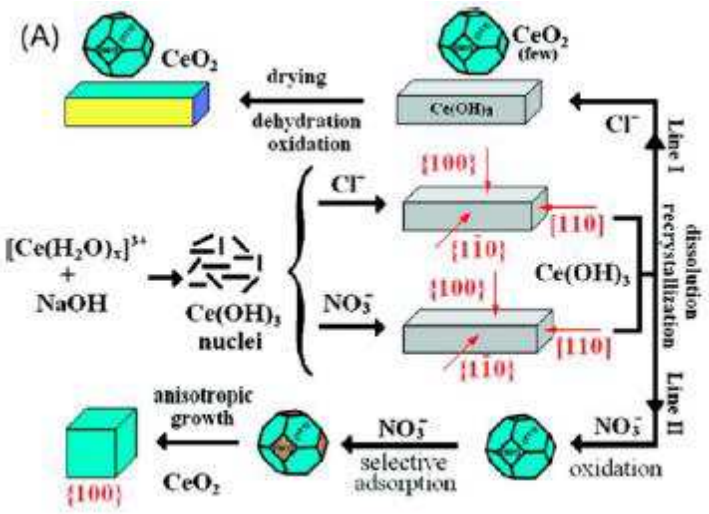

Figure 8: Schematic illustration for the conversion from nanorods to nanocubes. Reprinted with permission from A. Trovarelli, J. Llorca, ACS Catal. 2017, 7, 4716-4735. Copyright © 2017, American Chemical Society.

These examples show the high potentiality of hydrothermal method in the synthesis of ceria nanostructures with uniform morphology and size. However, among all the possible crystal shapes that can be obtained, for catalytic application the most investigated in the literature were nanocubes and nanorods/tubes.

CeO_2 nanocubes are characterized by six {100} facets and their size can vary from few nanometers to hundreds of nanometers. Often corners and edges can expose {111} and {110} facets and their amount can be increased employing capping agents in the synthesis.[35]

CeO_2 with rod-like morphology are more difficult to describe as a "standard" structure as in the case of nanocubes that almost totally exposed {100} facets. In fact, the lower temperature synthesis (100-120°C usually) increases the influence of other parameter such base and precursor nature and concentration on the final material and can lead to different crystal growth directions. The typical growth direction of nanorods is the [110]. Consequently, nanorods typically expose (100) and (110) facets.[8] However, in the literature are reported also ceria nanords that were grown along [111], [211] and [100] directions.[8] This highlights the strong influence of little changes in the synthesis parameters on the final morphology of the rods. Another impartant factor is the dying/calcination step. For example, it was found that the calcination of nanorods at 400-700°C leads to the surface reconstruction of {100} and {110} surfaces into a {111}.[36]

This literature survey highlights that the synthesis of CeO_2 nanocrystals and of model systems with defined exposed surfaces is nowadays well established. The main spur for these experimental works derive from the desire to experimentally verify the huge amount of calculations that predicted the strong surface sensitivity of ceria reactivity and of all its most interesting properties.[5,14] One of the most important kind of study performed on ceria samples exposing different facets is the measurement of OSC. As already mentioned, OSC of ceria is related to its ability of acting as buffer to supply O in slightly reducing atmosphere by reduction to under-stoichiometric CeO_{2-y} (i.e. fuel rich/O_2 deficient operation period of an engine) and to its ability of being easily reoxidized in a later stage (i.e. removing O from O_2 rich exhaust stream). Moreover, the key-point of this redox activity is the absence of structural changes of the fcc structure of ceria.

Mai et al.[31] measured the OSC (400°C) of nanocubes, nanorods and nanopolyhedra exposing respectively (100), (110)+(100) and (111) facets. They divided the OSC results by the surface area of the different samples, in order

to precisely define the shape dependence on the OSC. They found this trend for OSC: nanocubes > nanords >> nanopolyhedra. Therefore, the higher OSC was associated with the higher reducibility of (100) and (110) facets. Moreover, comparing the calculated values with the experimental data, they found that in the case of nanopolyhedra the contribution to oxygen storage is restricted to the surface of the particles. Conversely, for nanorods and nanocubes, experimental OSC was higher than calculated ones, highlighting the contribution of the bulk of the nanostructure to the oxygen storage. It should be noticed that the reducibility of ceria nanostructures is influenced also by the higher density of surface defects with respect to bigger particles.[37] Interestingly, the OSC of nanorods and nanocubes is high also at low temperature (100-200°C).[38,39] This low temperature behavior is not only related to the formation of oxygen vacancies. EPR[40] and Raman[41,42] spectroscopy studies identified the formation of superoxo (O_2^-) and peroxo (O_2^{2-}) species on the surface of reduced ceria nanocrystals. In fact, the reoxidation of the surface by oxygen in this case is due to the dissociation of superoxo/peroxo species into lattice oxygens:

$$O_2(g) \rightarrow O_2^-(a) \rightarrow O_2^{2-}(a) \rightarrow 2O^{2-}(l)$$

In addition to this mechanism, about 20% of adsorbed oxygen desorbed as molecular oxygen through disproportion reactions:

$$O_2^-(a) + O_2^-(a) \quad \rightarrow O_2^{2-}(a) + O_2\ (g)$$

$$O_2^{2-}(a) + O_2^{2-}(a) \quad \rightarrow 2O^{2-}(l) + O_2\ (g)$$

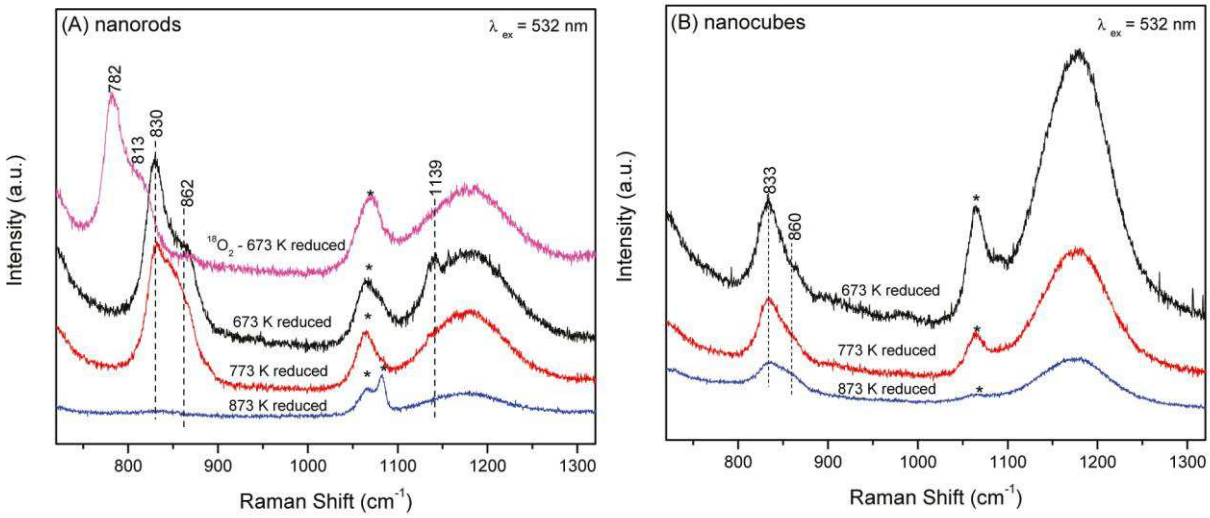

Figure 9: Raman spectra of O_2 adsorption at room temperature on different temperature reduced ceria nanorods (a) and nanocubes (b). Adapted with permission from Y.-J. Wang , H. Dong , G.-M. Lyu , H.-Y. Zhang , J. Ke , L.-Q. Kang , J.-L. Teng , L.-D. Sun , R. Si , J. Zhang , Y.-J. Liu ,Y.-W. Zhang , Y.-H. Huang , C.-H. Yan , Nanoscale 2015 , 7 , 13981. Copyright © 2015, Royal Society of Chemistry.

Comparing nanorods and nanocubes, O_2 desorption was measured at lower temperature in the case of nanorods (70°C vs 200°C). Experimental and theoretical studies showed that superoxo species disappeared at lower temperature with respect to peroxo species. [41,42] This is due to the stronger bond to the surface of peroxo species. For the formation of superoxo species is necessary that Ce(III) ions act as one electron donor centers. In fact, the interaction of oxygen with a surface vacancy site would give a peroxide ion. For these reasons, the formation of superoxo species is associated with the presence of highly defective or faceted surfaces (i.e. nanorods).

Another molecule that was widely investigated to probe the redox properties of ceria is CO. In fact, the CO oxidation is catalyzed by ceria in catalytic converters and in the water-gas shift reaction. CO can reduce ceria through a Mars van Krevelen mechanism: a CO molecule interacts with a surface oxygen atom giving CO_2 or carbonates and consequently creates an oxygen vacancy. The catalytic activity toward CO oxidation generally is nanorods ((110)+(100)) > nanocubes ((100)) > nanoparticles ((111)), as predicted also by computational data.[14,34] Notably, this trend is the reverse of that of oxygen vacancy energy formation.

Together with the OSC properties, the catalytic activity of ceria toward organic reactions is strictly related to its acid/base surface chemistry. The differences in Ce cations and O anions coordination in different surfaces imply a correlation between crystal shape and acid/base properties. The strongest dependence on the surface orientation was found for Lewis basic sites.[43] Conversely, Lewis acid sites seem to be only slightly dependent on crystallographic orientation and in any case they are very weak on ceria surfaces. Using probe molecules like CO_2 and $CHCl_3$, and measuring TPD profiles and IR spectra, the Overbury's group compared the basicity of three ceria nanostructures (rods, cubes, octahedra). Their results highlight that octahedra showed the higher basicity, whereas the lowest was showed by nanorods. This trend is consistent with TPD studies on model systems. For example, desorption spectra of 2-propanol showed that the dehydration pathway is less favored on the (100) surface with respect to the (111) surface.[44] In fact, dehydrogenation reactions are favored on basic sites. Conversely, acid sites favor dehydration reactions. The surface basicity is also influenced by the degree of reduction of ceria. Several studies on models systems[45,46] showed that CeO_2(111) dramatically increases the number of basic sites after reduction, whereas in the case of reduction of CeO_2(100) the effect is less marked.

As highlighted by these examples, the catalytic properties of ceria-based materials can be finely tuned by the careful design of crystal shapes, exposed surfaces, defect density, degree of reduction. In fact, catalytic properties depend on redox, defects and acid/base chemistry of ceria, and nowadays there is a wide choice of synthesis methods that permit us to design ceria nanostructures. Moreover, an accurate knowledge of the correlation between nanocrystals characteristics (shape, degree of reduction, etc) and catalytic activity opens the way to the possibility of the integration of ceria nanostructures in composite materials in order to design multifunctional catalysts that can operate in tandem or cascade scheme reactions.

3.4 Metal nanoparticles on CeO_2

In heterogeneous catalysis, supported metal nanoparticles are one of the most used and studied kind of catalysts. The catalytic properties of these materials depend not only on the nature, shape and size distribution of metal particles, but also the role of the support is crucial: this is known as the "metal-support interaction".[47] For model systems, usually metal particles are deposited over ceria employing the deposition methods typical of surface science (i.e. atomic layer deposition, evaporation of metal by e-beam or resistive heating). Regarding powder systems, metal particles are deposited on pre-formed ceria nanostructures by deposition/precipitation or impregnation method.[48,49] In general, the morphology on of the metal nanoparticles are strongly dependent on many different parameters such as the nature of metal precursors, which in most cases are simple ionic salts, and type of ceria nanostructures, in addition to other standard parameters such as temperature pH and concentration. For example, nanorods exposing (110) facets usually stabilized smaller nanoparticles with respect to nanocubes exposing (100) facets. [50] Together with morphology, the rich surface chemistry of cerium oxide heavily influences the catalytic activity of supported metal particles and metal/ceria catalysts were widely investigated in the literature.[8,11,12] Generally, calculations and experimental data have determined that there is interaction between ceria surface and metal atoms/particles, that is an electron transfer from the supported adsorbed metal to CeO_2. This causes the reduction of ceria surface and could induce a small positive charge on the admetal. XPS studies of metal/CeO_2(111) model systems,[51,52,53] suggest that the r ceria surface is generally reduced, whereas the oxidation of admetal was observed in case of O transfer, mixed metal oxide formation or as a consequence of final state effects associated with small size metal particles.

In metal/ceria systems, the interface between metal particle and ceria surface is crucial for catalysis because many reactions likely occurs at this interface, therefore several fundamental studies have focused on metal/CeO_2(111) model systems in order to shed light on its fascinating interfacial chemistry. [11] For example, TPD studies showed that when methanol is adsorbed on Rh/CeO_2(111) desorption features different from the case of bare ceria or bare metal could be observed. [54] On both catalyst components, methanol adsorbs as H and methoxy species. The results indicated that methoxy species react at the Rh/CeO_2 interface and only CO and H_2 are produced (on bare ceria, on the other hand methanol disproportionates to formaldehyde and methanol). Moreover, at low methanol exposure, single and sharp peaks of CO and H_2 desorption features, together with XPS results, evidence the "capture-zone"[55] effect: methanol adsorbed on ceria rapidly diffuses to Rh nanoparticles. Another important example is the reverse spillover from ceria to metal, which is observed for both water and methanol on Rh/CeO_2(111), or the spillover from metal to ceria, which was observed for formic acid on Pt/CeO_2(111).[11]

Moving to powder systems, many studies focused on the correlation between the catalytic activity and different ceria nanostructures as support for metal nanoparticles. For example, Cui et al.[56] verified that there was a stronger interaction between Cu and ceria nanorods, with respect to nanocubes and nanopolyhedra. Such strong interaction resulted in a higher Cu^+/Cu^0 ratios and in a higher amount of oxygen vacancies concentration. The activity of these Cu/CeO_2 nanostructured catalysts was evaluated for the gas/solid-phase hydrogenation of CO_2-derived diethyl carbonate to methanol. The sample with the stronger metal/ceria interaction (Cu/CeO2 nanorods) was the best performing material. Imamura et al.[57] studied the decomposition of methanol over Pt/CeO_2. Again, they found that a strong metal/support interaction resulted in the acceleration of the kinetic of the rate-determing step (RDS) of the reaction. In this case, the RDS was the abstraction of methoxy hydrogen bound to Pt. They verified that when Pt is oxidized because of the interaction with ceria, one electron is withdrawn from the methoxy group to Pt. Consequently, the C-H bond of the adsorbed methoxy group is weakened and the kinetic of the reaction is faster. Soler et al.[58] supported pre-formed Au nanoparticles on

different ceria nanostructures that exposed different facets (nanocubes, nanopolyhedra, nanorods). They studied these Au/CeO_2 materials as catalysts for the preferential oxidation of CO (COPrOx). Combining catalytic tests and XPS data, they clearly determined a correlation between the performances and the stabilization of oxidized Au species. The as-prepered Au NPs presented only Au(0). In the worst-perfroming material (Au/CeO_2 nanocubes), gold oxidation state is unchanged with respect to unsupported nanoparticles. Conversely, they measured an increase in the catalyst performances (higher conversion and selectivity) for the Au/nanords and Au/nanopolyhedra samples. In these cases, XPS results showed that electron density is transferred from Au to ceria so that the amount of Ce(III) species increases and gold is partially oxidized (Figure 10). The best performing material was Au/nanorods, which was sample with the highest ratio $Au(\delta^+)/Au(0)$. All these examples highlight the importance of the metal/ceria interface on the catalytic properties. When the catalyst is used for oxidation reactions, one of the crucial aspects for the enhancement of the catalytic activity is the stabilization of oxidized metal species on the surface of ceria. Especially the last example clearly demonstrates how different ceria crystal shapes, and therefore different exposed facets, influence the interaction between metal and oxide support and how they determine the catalytic activity of the material.

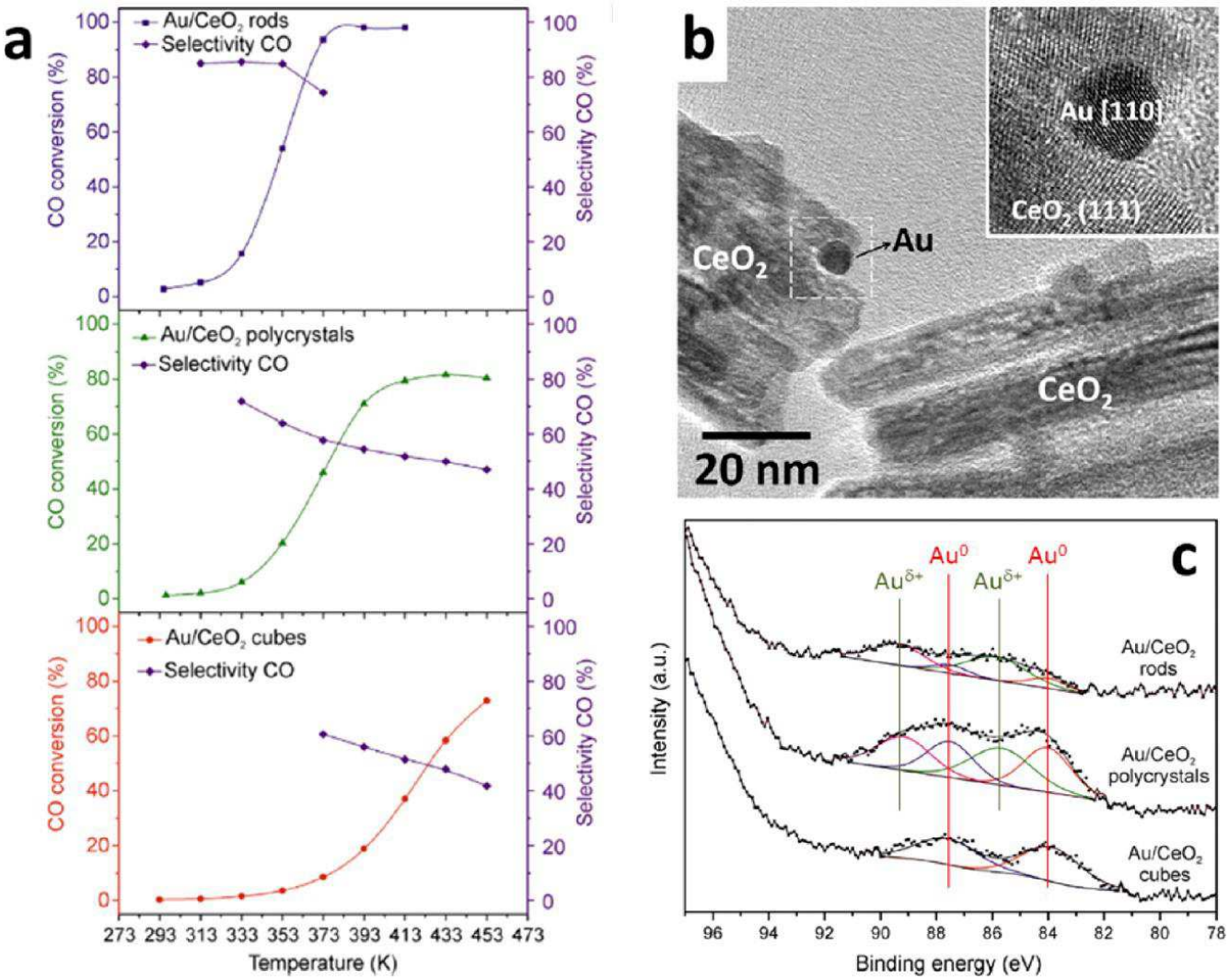

Figure 10: (a) COPrOx catalytic performance of preformed Au nanoparticles dispersed over ceria nanopolyhedra, nanocubes, and nanorods (CO/O2/N2/H2 = 1:1:23:25 molar). (b) HRTEM image of Au/Ceo2 nanorods. (c) Au 4f photoemission spectra. Reprinted with permission from A. Trovarelli, J. Llorca, ACS Catal. 2017, 7, 4716-4735. Copyright © 2017, American Chemical Society.

3.5 Multi-scale design of Pd@CeO_2 heterogeneous catalysts for selective methanol decomposition

The increasing world energy demanding and the intrinsic narrowness of non-renewable energy sources is a theme that is widely discussed in Chapter 1. The studies on renewable and environmentally friendly sources of energy and of raw materials for chemical industries are of crucial importance. In this optics, methanol is considered one of the most important chemical because it can be obtained from bio-sources, can be exploited as fuel and as raw material for the production of CO, H_2 and CO_2. In this section, the attention will be focused on the methanol decomposition to syngas (CO and H_2). The methanol decomposition reaction could be exploited in many different catalytic processes[59], ranging from energy recovery of waste heat[60] (from various industries[61] or from methanol fuel cells[62]) to the synthesis of fine chemicals[63]. Especially the *in situ* production of syngas is nowadays attracting more and more interest in the world of catalysis and is giving a "second youth" to the methanol decomposition reaction. In fact, if the catalyst used for syngas synthesis is rationally integrated in a multifunctional material, the *in situ* produced CO and H_2 (i.e. syngas) could be exploited to carry out a second catalytic reaction in a tandem or cascade reaction scheme.[63] The *in situ* syngas production is very advantageous for the overall safety of the chemical conversion process since minimize the handling of high pressure toxic and flammable gases. The *in situ* production scheme produces a localized high concentration of CO and H_2. In a multifunctional catalyst, if the different catalytic sites are properly arranged, this could heavily influence the catalytic activity of the material. For example, some reactions such as hydroformylation can be carried out at atmospheric pressure instead of the high-pressure reaction currently employed in the industry. This is an obvious economical advantage and it makes the catalytic process more safe (no necessity of the transport and use of high-pressure CO and H_2, simpler and safer reactors needed).

The aim of our study is to correlate the catalytic activity of Pd NPs supported on different nanostructured CeO_2 particles with the morphology, the basicity and the surfaces exposed by the oxide substrates. The catalytic activity is evaluated toward methanol decomposition to syngas. As discussed in this chapter, engineering at the nanoscale the size, morphology, and exposed facets of individual particles, is fundamental to control the surface chemistry of both oxide and metal nanoparticles, and eventually to tune the catalytic activity and synergistically integrate different catalytic sites in a unique composite. Palladium is generally active in the catalytic decomposition of methanol to syngas and its activity is largely affected by the support.[61,64,65] Cerium oxide is one of the most effective catalyst support because it may strongly interact both chemically (e.g. oxygen spillover) and electronically (e.g. electron donation) with finely dispersed metal nanoparticles (NPs).[48,66,5 ,67] Moreover, some crucial properties of ceria such as acid-base and redox properties, which ultimately determine the absorption energy of adsorbates and reaction intermediates and oxygen vacancies formation energy, are closely related to the surface structure. In fact, oxygen anions and cerium cations present different coordination and chemical environment in relation to their location on differently oriented low-index surfaces.[11,68,69,70]

Therefore, controlling the morphology of ceria is a valuable tool to control the physicochemical properties of the supported metal NPs and the efficiency and selectivity of the whole catalytic process. To shed light on the subtle links between structural properties and chemical activity, we synthetized ceria NPs with that mainly expose the same {001} oriented facets, but that differ for overall morphology (rods, cubes, polyhedral NPs) and physical dimension (2 nm to 20 nm). These substrates were then decorated with Pd NPs and their catalytic activity was investigated by using methanol as molecular probe. Methanol adsorption on ceria surfaces was widely investigate in the literature. In fact, methanol is considered a "smart" molecule because it can be used as chemical stimulus to provide fundamental information about density and nature of active surface sites, intermediates species desorption profiles and TOF values for methanol oxidation on metal oxide surfaces.[71] On bare ceria surfaces, the adsorption of methanol follows this reaction:

$$CH_3OH + CeO_2 \rightarrow CH_3OCe + OH(l)$$

Therefore, it implies the formation of methoxy and hydroxyl species. The concentration of methoxy species can be measured by XPS at 200 K, leading to a direct measurement of the density of active sites on the surface of ceria.[46] Moreover, from various methanol TPD studies it was possible to extract different important information: i) methoxy and hydroxyl species are the most stable and that the methanol coverage is higher on CeO_2(100) than on CeO_2(111);[72] ii) CeO_2(111) is primarily a redox-type catalyst and methanol can reduce the ceria surface: by isotopic labeling, lattice oxygen was found in the water produced by the disproportionation of hydroxyl species at 200-300 K; at higher temperature (~573 K) the only reaction products are methanol and formaldehyde (disproportionation of methoxy species); CeO_2(100) showed the production of CO, CO_2, H_2 and H_2O at about 600 K following a basic reaction mechanism (dehydrogenation of methyl groups of methoxy species by O surface anions). Analyzing reduced ceria surfaces, it was determined that: i) the stability of methoxy and hydroxyl species is increased with respect to stoichiometric ceria; ii) CeO_{2-y}(111) showed a transition from redox to basic behavior; iii) O-vacancies are necessary for methanol adsorption, and particularly on CeO_{2-y}(111) their density is dramatically increased as a function of the reduction of ceria.

While the UHV methanol adsorption and reaction studies on model systems are limited to CeO_2(111) and CeO_2(100), Raman and IR Spectroscopes were employed to study the interaction between methanol and different ceria nanocrystals at ambient pressure. Wu et al.[68] studied the adsorption and desorption of methanol in order to investigate the nature of surface sites of ceria nanocrystals with defined surface planes (nanoshapes), including rods (containing {110}), cubes ({100}), and octahedra ({111}) (Figure 11). The adsorption of methanol was performed at room temperature and ambient pressure. After adsorption, their results showed three different methoxy species on the surface of rods and cubes (on-top, bridging and three-coordinate methoxy species). Conversely, on octahedra surfaces, only on-top methoxy species were present. These authors determined that this distribution of methoxy species depends not only on the coordination geometry of surface Ce cations, but also on the number of defect sites on the three nanocrystals. After adsorption, TPD experiments were conducted while the materials were monitored by IR and Raman Spectroscopies and the desorption products analyzed by mass spectrometry. At low temperature (<150°C) a small amount of methanol and formaldehyde (disproportionation reaction) and water desorbed in all cases, whereas at higher temperature, H_2 and CO are desorbed. Syngas is formed after the dehydrogenation of methoxy species via formate species as intermediates. Only in the case of rods, a second intermediate (formyl species) was identified. The lowest CO and H_2 desorption temperature (<250°C) was measured in the case of rods. This is related to a lower stability/higher reactivity of methoxy species on rods surface. Moreover, the adsorption of methanol at RT caused a slight reduction of ceria surfaces in all the cases. The extent of ceria reduction by methanol adsorption follows this trend: rods>cubes>ocathedra. This trend is consistent with the oxygen vacancy formation energies of the respective crystal surfaces. Nonetheless, it should be noticed that Raman Spectroscopy is a bulk technique and the octahedra exhibited the lower surface area. This is probably the reason why the surface reduction was almost undetected in this case. The surface reduction at RT was related to water desorption due to the condensation reaction between surface OH groups (generated by the dissociative adsorption of methanol). Ceria reduction was enhanced at high temperature during methanol desorption. Notably, the water desorption temperature on the three ceria nanocrystals followed the same trend of surfaces reducibility (rods > cubes > octahedra).

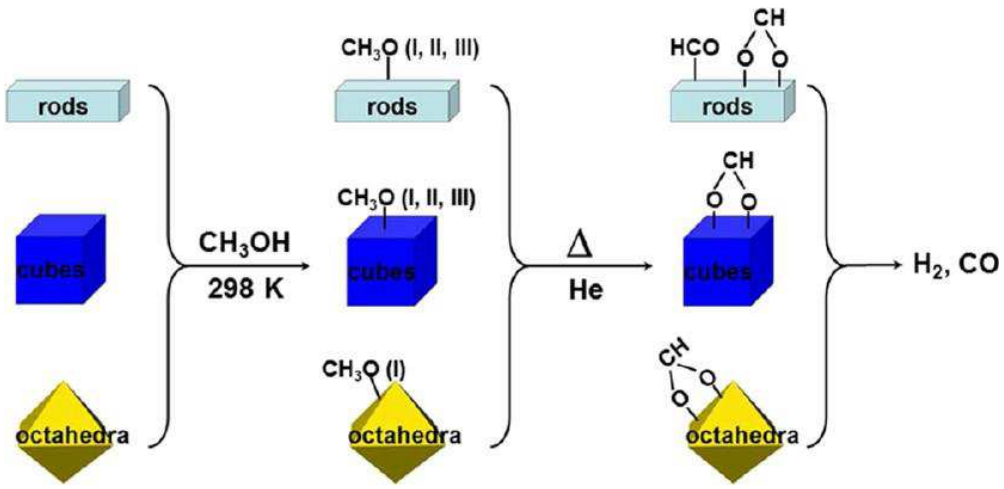

Figure 11: Schematic view of MeOH adsorption on different ceria nanostructures. Reprinted with permission from Wu, Z. L.; Mann, A. K. P.; Li, M. J.; Overbury, S. H. J. Phys. Chem. C 2015, 119, 7340−7350. Copyright © 2015, American Chemical Society.

As indicated by these examples, the adsorption and reaction of methanol on ceria surface are strictly related to the surface reducibility, to the presence of defects on nanocrystals and were widely investigated in the literature. On the other hand, the adsorption and reaction of methanol on metal nanoparticles supported on ceria nanocrystals were are more scarcely investigated in the literature. Many different metals were supported on ceria-based materials and their catalytic activity toward methanol decomposition was studied. As mentioned at the beginning of this section, Pd NPs supported on ceria is one of the best-performing catalyst for methanol decomposition. One aspect that was widely investigated was the correlation between Pd NPs dispersion method and catalytic activity. In fact, the best-performing Pd/CeO_2 catalysts are usually prepared by impregnation, coprecipitation[73] or deposition-precipitation[49] methods. In all the cases, the best-performing materials are those that show the highest interaction between Pd and ceria. As evidenced in the previous section, the key point for the enhancement of the performances of metal/ceria catalyst for oxidation reaction is the stabilization of oxidized metal species. Matsamura's group demonstrated that cationic palladium species (valence close to +1) enhance the transfer of CO from Pd sites to ceria surface at low temperature (even at RT).[48,57,61] In fact, under reaction condition the CO removal from Pd surface readily takes place and frees active sites for the methanol decomposition reaction. However, to the best of our knowledge, there are no works related to the catalysis of methanol decomposition on Pd NPs supported on different ceria nanocrystals. Usually Pd/CeO_2 materials were based on commercial ceria powders (usually considerable as polyhedra exposing (111) surfaces) or mesoporous powders (high surface area in order to maximize the Pd dispersion).

Moreover, most Pd/CeO_2 catalysts preparation methods require a final calcination to convert the Pd precursor to a metal phase. In our study, we investigated an alternative Pd deposition method that does not require a high temperature step. In fact, we deposited very small and finely dispersed Pd NPs by bubbling hydrogen in an aqueous dispersion of CeO_2 and K_2PdCl_4. After this step, our catalysts are ready to use and can be directly activated in the reactor. This also allows to preserve the initial morphology of the ceria support that was obtained by a low temperature synthesis. Our best-performing material is constituted by CeO_2 small nanorods (low aspect ratio) decorated by Pd NPs ($5\%_{wt}$). To the best of our knowledge, its performance is comparable if not superior to the most active Pd/CeO_2 based catalysts for methanol decomposition reported in the literature.[61,57,74] The main advantages of our catalyst preparation method however, are represented by the fact that: i) no calcination steps are needed; ii) both CeO_2 NPs synthesis and Pd deposition are performed at room temperature, without the use of surfactants, efficiently complying with the rigorous guidelines of green chemistry protocols.

By combining a microscopic characterization via High-Resolution Electron Microscopy (HRTEM), Raman and chemical investigation by *in situ* X-Ray Photoelectron spectroscopies (XPS) together with catalytic data obtained by gas chromatography, we were able to document the existence of a synergistic effect between ceria and palladium: very small ceria NPs interact more strongly with Pd leading to formation of very small nanoparticles , which are characterized by a relevant faction of palladium oxides probably because of a more relevant partially oxidized interface. Interestingly, in real catalytic (10 mbar CH_3OH) and reducing conditions (30 mbar H_2), the smaller is the dimension of the supporting oxide the higher is its reducibility and its ability to promote the reduction of palladium NPs.

3.5.1 Experimental section

- Synthesis of CeO_2 small nanorods (SNRs)

Analytical grade $Ce(NO_3)_3\ 6H_2O$ (Sigma Aldrich) and NaOH (WVR) were used as received. We followed the recipe reported by Pan et al. with little modifications.[34] Briefly, an amount of 15 ml of a 16 mM aqueous solution of $Ce(NO_3)_3\ 6H_2O$ was mixed with 105 ml of a 14 M aqueous solution of NaOH in a teflon beaker, vigorously stirred for 30 minutes and then left aging without stirring for 2 days at RT. The product was washed 5 times with deionized water and dried at 60°C for 12 h.

- Synthesis of CeO_2 nanocubes (NCs) and long nanorods (LNRs)

Analytical grade $Ce(NO_3)_3\ 6H_2O$ (Sigma Aldrich) and NaOH (WVR) were used as received. We followed the synthetic protocol reported by Mai et al. with little modifications.[31] Briefly, an amount of 5 ml of a 150 mM aqueous solution of $Ce(NO_3)_3\ 6H_2O$ was mixed with 10 ml of a 9 M aqueous solution of NaOH in a 25 ml Teflon-lined stainless steel autoclave. The autoclave was left in an oven at 180°C (for NCs) or 110°C (LNRs) for 24 h. The product was washed 5 times with deionized water and dried at 60°C for 12 h.

- Deposition of Pd nanoparticles

To prepare a catalyst loaded with a 5% Pd weight percentage in the final material, we mixed 30 mg of K_2PdCl_4 (Sigma Aldrich) and 198 mg of CeO_2 (nanoparticles, nanorods, nanocubes or commercial nanopowder (CNPDs) from Sigma Aldrich) in 100 ml of deionized water. Under stirring at RT, we bubbled a 2:1 N_2:H_2 flow for 30 minutes. Finally, the product was washed 5 times with deionized water and dried at 60°C for 12 h.

- Physicochemical characterization tools.

X-ray photoemission (XPS) spectra were acquired using a conventional x-rays source (1486.6 eV photons). The measurements of the as-prepared materials were taken after a short annealing at 150°C in UHV to remove most adsorbed species (water and contamination debris). The calibration of the binding energy (BE) scale was determined using the C 1s peak as reference. The photoemission lines were separated into individual components (after Shirley background removal) using symmetrical Voigt functions and non-linear least squares routines for the χ^2 minimization. *In situ* XPS measurements were performed employing a custom-made high-pressure cell (base pressure: 10^{-7} mbar) connected to the XPS analysis chamber. After the analysis of the as-prepared catalyst, the sample was transferred in the high pressure cell and exposed static conditions to i) hydrogen, 30 mbar, 1h and to ii) methanol, 10 mbar, 30 min at 300°C. After each step, the sample was transferred back in the analysis chamber in ultra-high vacuum conditions and the photoemission spectra were acquired.

The nano- and micro-scale morphology of materials was investigated by high-resolution transmission electron microscopy (HR-TEM). HRTEM micrographs were performed by Prof. M.C. Paganini (University of Turin) and were acquired using a JEM-2100F Field Emission Electron Microscope operating at 200 kV. Energy Dispersive X-ray Spectroscopy (EDS) data were acquired with the same instrument.

Characterization by Raman spectroscopy was performed using a ThermoFisher DXR Raman microscope. The spectra were recorded using a laser with an excitation wavelength of 532 nm (1 mW), focused on the sample with a 10× objective (Olympus). Raman peak shifts and areas were determined by fitting with Lorentzian lineshapes (R^2> 0.95).

The specific surface area was measured applying the single-point BET method, using a Micromeritics ASAP 2020.

- Evaluation of the catalytic activity

The catalytic activity toward methanol decomposition was evaluated in a fixed-bed continuous-flow quartz reactor (inner diameter: 4mm) under atmospheric pressure. The catalyst powder (20 mg) was placed in the reactor and dispersed in quartz wool. The catalyst was activated in a flow of 20 vol% hydrogen diluted with argon (total flow-rate: 50 sccm) for 1 h at 300°C. Then the sample was cooled to RT and 1 vol% of methanol was fed with an argon carrier (total flow-rate: 50 sccm; weight hourly space velocity: 1500 ml h^{-1} $g\text{-}cat^{-1}$) at different temperatures (from RT to 350°C). The outlet gas was analyzed with an on-stream gas chromatograph (Agilent 490 microGC) equipped with a a thermal conductivity detector and a Molsieve 5A, a CP-WAX 52 and a PORAPLOT-U columns (10 meters) for gas separation. The temperature was stabilized for 15 minutes before each acquisition.

3.5.2 Results and discussion

CeO_2 nanocubes (NCs), small nanorods (SNRs) and long nanorods (LNRs) were synthesized following previously reported recipes with little modifications. These nanostructured materials were compared with commercially available CeO_2 nanopowders (CNPD). These four materials were decorated with Pd NPs (5% weight): the different CeO_2 powders were dispersed in an acqueous solution of K_2PdCl_4, and then molecular hydrogen was bubbled in the solution at RT to reduce the salt and deposit Pd NPs. The amount of Pd was determined by EDS and confirmed the quantitative deposition of Pd (5% weight). XPS and EDS data confirmed that the washing procedure of the samples did not leave any impurities of NaOH or unreacted Pd precursor (no signal ascribable to Na, K or Cl was observed).

The morphology of the ceria samples and their decoration by Pd NPs were studied by TEM and HR-TEM (Figure 12-19). The CeO_2 CNPDs show a wide size distribution (mainly 10-20 nm), variable morphology and expose mainly {100} and {111} oriented facets (Figure 12a, 19). The CeO_2 NCs consistently present highly crystalline cubic nanoparticles terminating with {100} oriented surfaces and exhibit an average size of 16-20 nm (Figure 12b, 18). From TEM micrographs, the CeO_2 SNRs seems to have a quite uniform diameter of about 3-5 nm and a more variable length ranging from 10 to 30 nm (Figure 12d). They tend to aggregate, however, by carefully analyzing HR-TEM micrographs, we verified that the SNRs are composed by rather crystalline nanoparticles. From lattice fringe analysis, it may be deduced that the NPs expose mainly {100} facets (Figure 16). Therefore, we can consider that the SNRs sample is made up by nanorods with a low aspect ratio, or small cubes elongated in one direction. The CeO_2 LNRs have a uniform width of 10±2 nm and a length ranging from 90 to 250 nm (Figure 12c). The long side of the rod exposes the {100} surface, whereas the transversal basal faces are {111} oriented (Figure 12c, 17). Pd NPs are finely dispersed over the different substrates and have a size ranging from 3 to 5 over CNPDs, 2 to 10

nm over NCs and LNRs, and expose mainly (111) facets (Figure 13-15 and 18-19). In the case CeO_2 SNRs, the Pd NPs are exceedingly small (<2 nm) and because of that it was not possible to define clearly their size distribution.

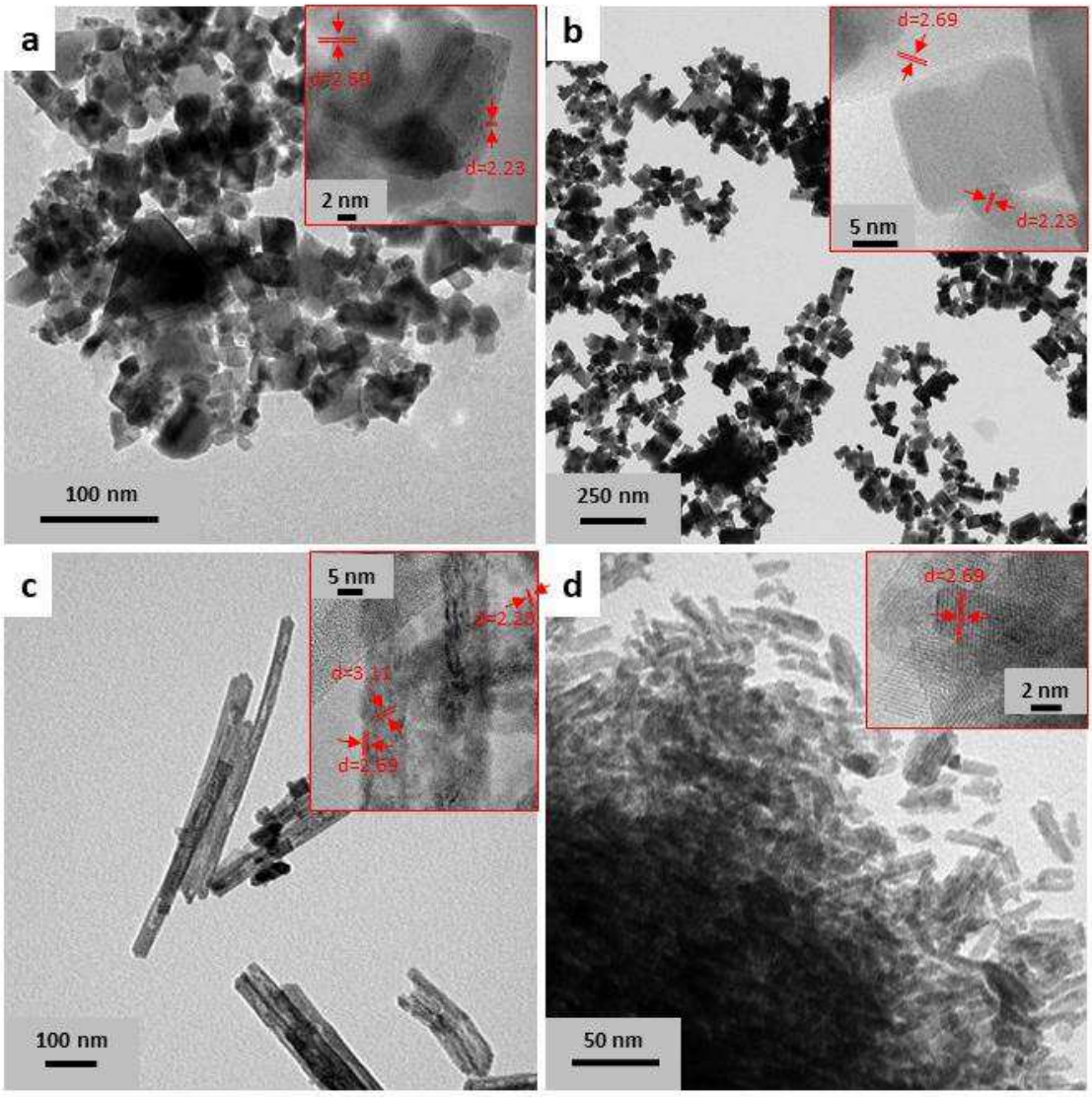

Figure 12: TEM and HRTEM (insets, highlighted interplanar distances (d) are reported in nm) micrographs of as prepared 5%wt Pd/CeO_2 CNPDs (a), 5%wt Pd/CeO_2 NCs (b), 5%wt Pd/CeO_2 LNRs (c) and 5%wt Pd/CeO_2 SNRs (d).

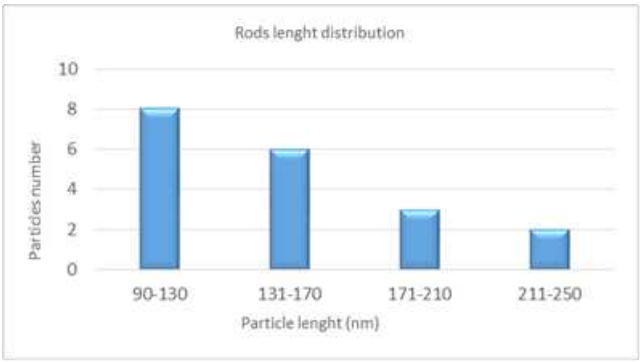

Figure 13: Size distribution histogram of CeO_2 LNRs

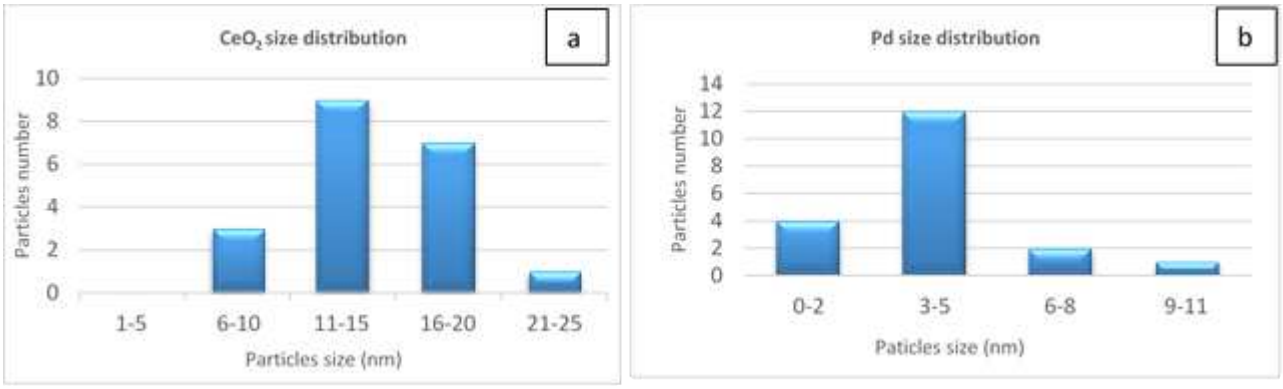

Figure 14: Size distribution histograms of a) CeO_2 CNPDs, b) Pd NPs on CeO_2 CNPDs.

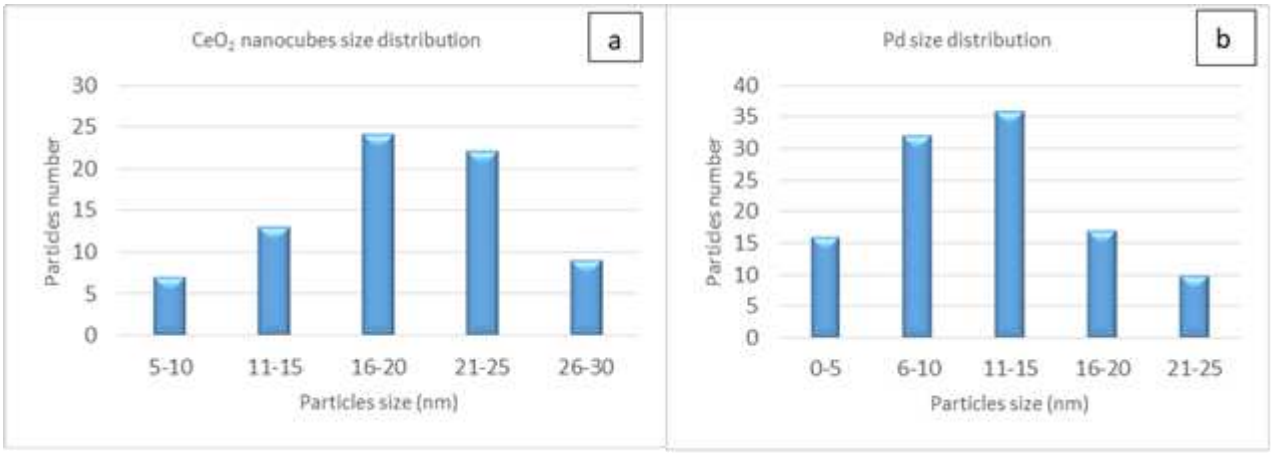

Figure 15: Size distribution histograms of a) CeO_2 NCs, b) Pd NPs on CeO_2 NCs.

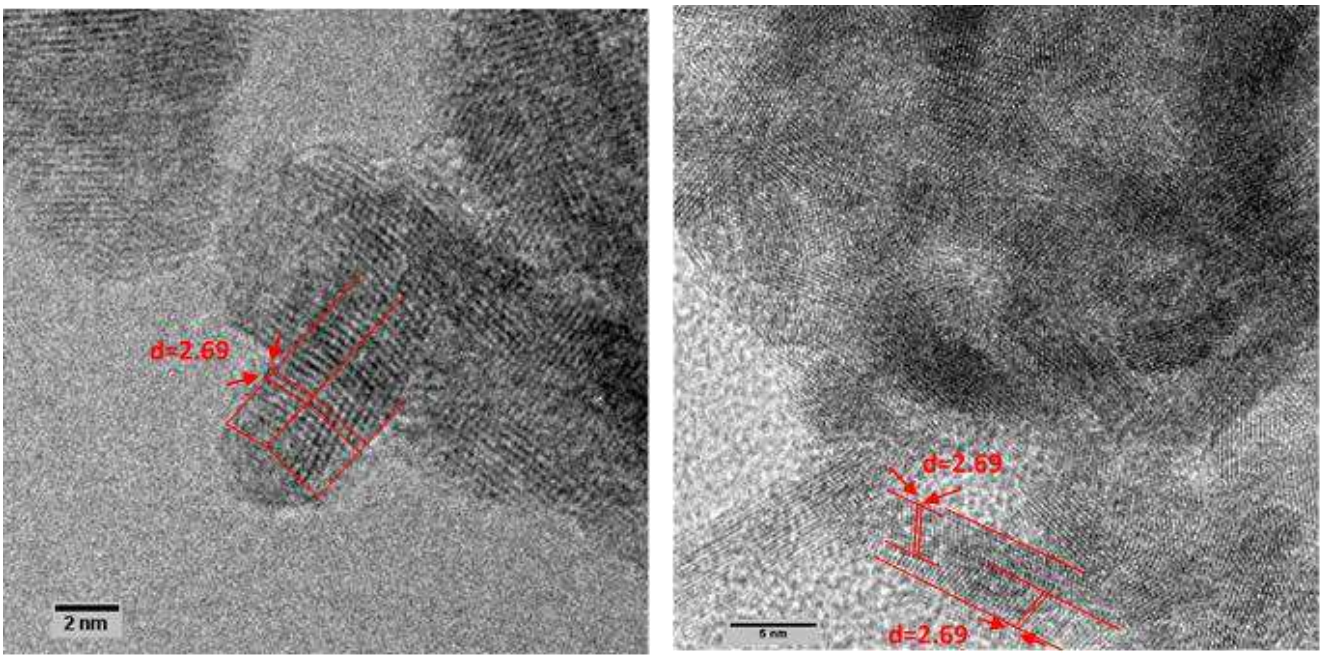

Figure 16: HR-TEM micrographs of 5%Pd/SNRs.

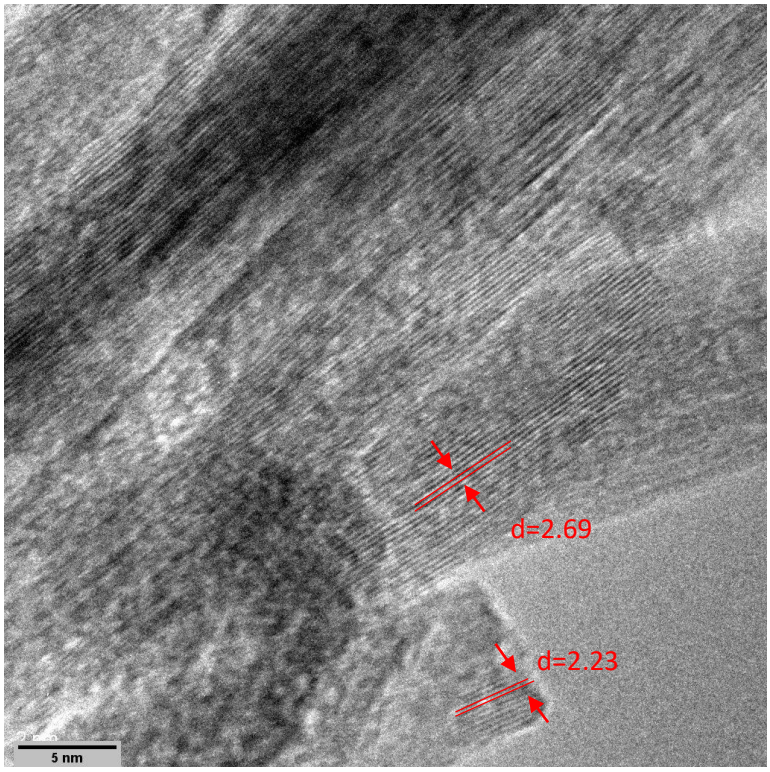

Figure 17: HR-TEM micrographs of 5%Pd/LNRs.

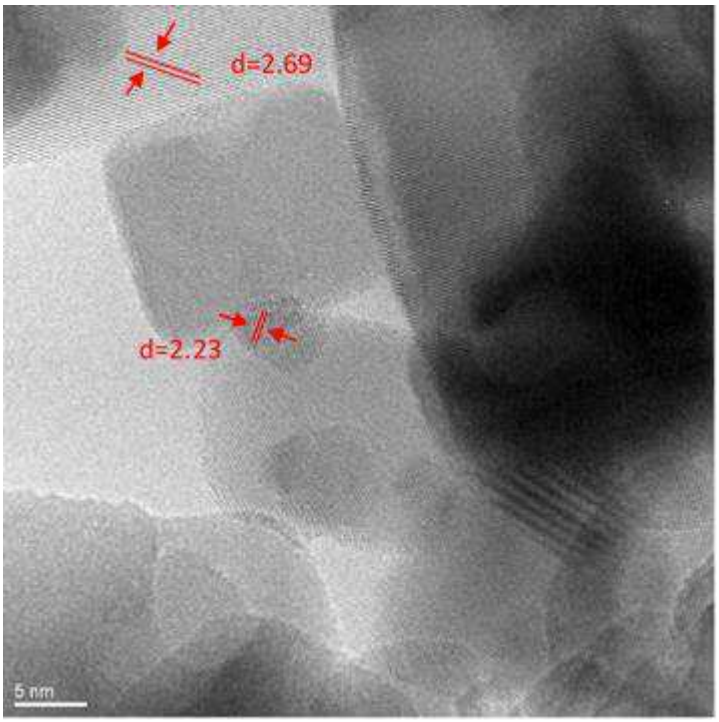

Figure 18:HR-TEM micrographs of 5%Pd/NCs.

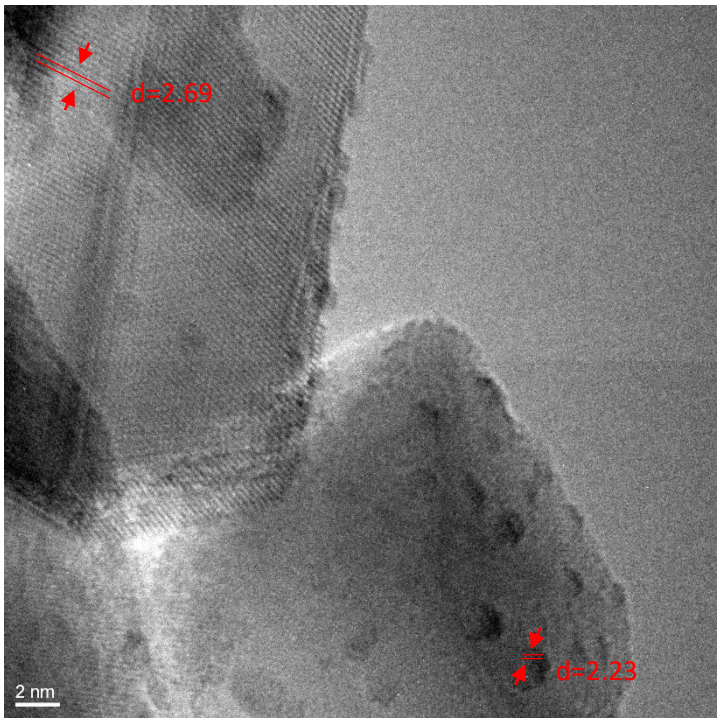

Figure 20: HR-TEM micrographs of 5%Pd/CNPDs

The Raman spectra of CNPDs NCs, SNRs, and LNRs are shown in Figure 20. All samples show the first-order F_{2g} peak typical of CeO_2 at about 465 cm^{-1}, confirming the formation of fluorite CeO_2 nanostructures. The Raman shift and the half-width at half-maximum (FWHM) of the F_{2g} peak depend on the particle size[75,76] and their trend confirms the results of TEM investigations. As expected, the F_{2g} peak of SNRs show the lowest Raman shift (455 cm^{-1}) and the highest FWHM (60 cm^{-1}), whereas commercial CeO_2 F_{2g} peak has the highest Raman shift (464 cm^{-1}) and the smallest FWHM (8 cm^{-1}). Moreover, the intensity of the weak Raman peak near 600 cm^{-1} has been associated with defects (i.e. oxygen vacancies) in CeO_2.[76] Comparing the four samples, the SNRs show the highest oxygen vacancies concentration, whereas CNPDs the lowest. After the Pd NPs deposition, the peak at about 600 cm^{-1} increases its intensity in all the investigated samples, which may be associated with the reduction of the CeO_2 support (Figure 20).[76] In the case of SNRs and LNRs, this effect is stronger than in CNPDs and NCs. These results highlights the higher reducibility of SNRs and LNRs with respect to NCs and CNPDs.

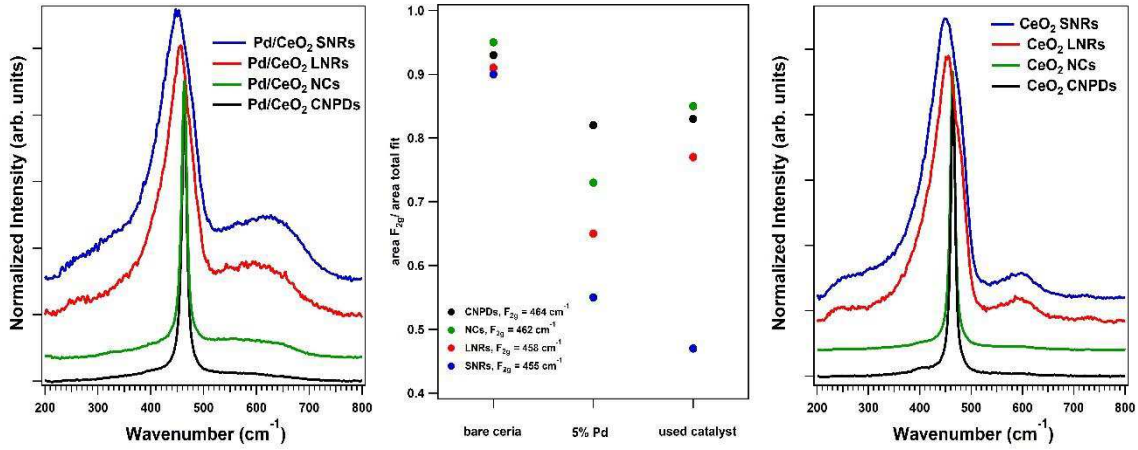

Figure 19: Raman spectra of asprepared bare (right) and 5%wt Pd decorated (left) CeO_2 CNPDs, NCs, LNRs and SNRs and the results of the fitting of Raman spectra in the region 300-800 cm^{-1} for these samples (center).

The catalytic activity toward methanol decomposition was studied in the temperature range between 100 and 350°C in a fixed-bed continuous-flow (1% vol of CH_3OH, 1500 ml h^{-1} g-cat^{-1}) quartz reactor under atmospheric pressure after activating the catalysts with hydrogen (300°C, 1h, 20% of H_2 in Ar). The gas stream out of the reactor was analyzed with an on-stream gas chromatograph. The main results of methanol conversion are summarized in Table 2 and Figure 21. The activity of 5 wt% Pd/CeO_2 SNRs was always higher than that of the other Pd/CeO_2 catalysts in the temperature range between 100-350°C. All Pd/CeO_2 catalysts showed an extremely selective methanol decomposition to CO and H_2, as the best-performing Pd/CeO_2 catalysts reported in the literature.[65] Other products marginally detected were CH_4 and CO_2. CO_2 (Selectivity <0.5 %) was observed mainly at temperature lower than 200°C. Conversely, CH_4 was detected at T>275-350°C in the case of CNPDs and NCs, and between 225 and 350°C in the case of SNRs and LNRs.

Regarding the activity of the catalyst, the temperature of 50% methanol conversion (T_{50}) is usually a standard benchmark. In the case of $5\%_{wt}Pd/CeO_2$ SNRs, we obtained a value of 150°C. Moreover, by the analysis of chemical conversion vs temperature we estimated an activation energy for methanol decomposition of 38 kJ/mol in the temperature range between 125 and 175°C. For the other catalytic systems, the T_{50} of $5\%Pd/CeO_2$ LNRs is 170°C (43 kJ/mol, 150-200°C), that of 5% Pd/CeO_2 NCs is 205°C (51 kJ/mol, 175-225°C) and that of 5% Pd/CeO_2 CNPDs is 220°C (58 kJ/mol, 200-250°C); all data are summarized in table 2.

Table 2: Catalytic results and BET surface area of the investigated materials.

Catalyst	BET surface area (m^2/g)	T_{50} (°C)[a]	T_{100} (°C)[b]	Selectivity (%) at T_{100}	
				CO	H_2
$5\%_{wt}Pd/CeO_2$ CNPDs	60	220	300	99.5	99.7
$5\%_{wt}Pd/CeO_2$ NCs	35	205	275	99.6	98.3
$5\%_{wt}Pd/CeO_2$ LNRS	95	175	225	88.0	99.8
$5\%_{wt}Pd/CeO_2$ SNRs	150	150	200	99.8	99.9
Notes	[a] Temperature of 50% methanol conversion [b] Lower temperature of 100% methanol conversion				

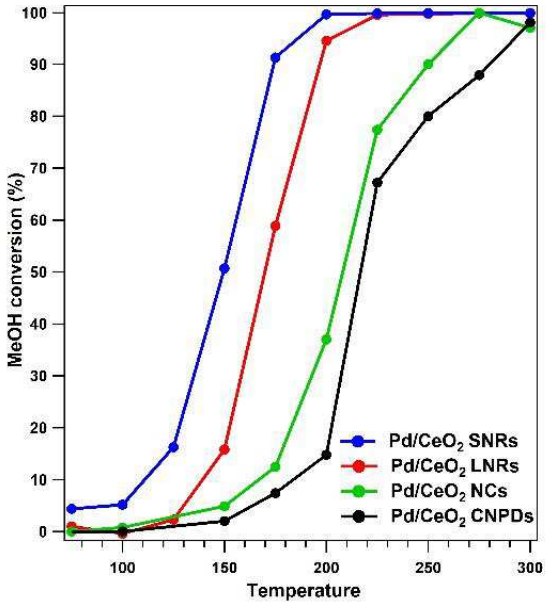

Figure 21: Methanol conversion vs temperature for the catalysts activated at 300°C in H_2.

The catalytic activity of the Pd supported on CeO_2 nanorods and small nanorods is excellent. To the best of our knowledge, it is higher than most of previously reported CeO_2 supported Pd catalysts (i.e. 17% wt Pd/CeO_2: T_{50}=200°C; 5% Pd deposited on mesoporous CeO_2: T_{35}=180°C; 3 wt% Pd/CeO_2: T_{50}=174°C)[61,65] and of other metal/metal oxide catalysts (3 wt% Pt/CeO_2: T_{50}=158°C; 3 wt% Pt/Al_2O_3: T_{50}=182°C).[74]

In order to shed some light of the surface chemistry responsible for this excellent activity and to rationalize the differences observed in our set of catalytic systems we systematically applied X-ray photoemission spectroscopy (XPS) and in particular *in situ* XPS which allows investigating the surface of our catalysts in working condition, without exposing the materials to the atmosphere. This has been done at each different steps of the catalytic process, i.e. for the as-prepared catalyst, after activation and after working conditions. This analysis provided a detailed insight into the Pd oxidation state and the redox properties of the different CeO_2 substrates that could be related to the different catalytic activities. Moreover, these results were compared to the data acquired from the same experiments performed on the bare CeO_2 nanostructures in order to investigate the synergistic effect of Pd on the redox properties of CeO_2 surface.

The results of the separation into chemically shifted components of Ce3*d* and Pd3*d* photoemission lines are summarized in Tables 3 and 4, respectively, and reported in Figures 22, 23 and 24. The photoemission spectrum of Ce3*d* was fitted by using five spin-orbit-split doublets that correspond to the possible different 4*f* configurations in the photoemission final state. The components labeled v^0 and v^i correspond to Ce^{3+}, whereas the components labeled v, v^{ii}, v^{iii} correspond to Ce^{4+} (Figure 22a).[77] The spin-orbit satellite labeled u^{iii} centered at 917 eV is indicative of the poorly screened Ce3$d^9$4f^0O2p^6 final state, and is connected only with the presence of Ce^{4+} ions. For this reason, in order to follow the degree of reduction of CeO_2 surface, we reported in Table 3 the ratio of the area of the u^{iii} component versus the total area of the fit Ce3*d* photoemission line. Therefore, a lower value of this parameter corresponds to a higher reduction of CeO_2 surface. This procedure limits the uncertainty introduced by the fitting procedure. The data reported in Table 3 indicate that the most reduced samples are the SNRs, whereas all the other systems present very similar reduction levels. This is in good agreement with the Raman Spectroscopy data and supports the idea that the major factor affecting the reduction properties of CeO_2 is related to the physical dimension.

Pd 3*d* photoemission lines were fitted employing three spin-orbit doublets corresponding to the Pd oxidation states 0, II and IV. Pd(II) and Pd(IV) were fixed at a binding energy (BE) of 336.7 and 338.2 eV, respectively (Figure 24). Conversely, the energy position of the Pd(0) component was allowed to vary slightly because it could be influenced by the size of the nanoparticles and by the electronic interaction with the ceria substrates. In fact, many studies reported of a strong effect of the oxide substrate on the valence of Pd: the interaction of the metal nanoparticles with the oxide support leads to an electron transfer and/or to the formation of interfacial Pd cationic species.[73,74] Interestingly, the presence of Pd species with valence close to +1, identified by an upward BE shift of about 0.5 eV with respect to the typical position of metal Pd $3d_{5/2}$ (335.0 eV), correlates well with an enhanced catalytic activity toward methanol decomposition.[73,74] As demonstrated by HR-TEM micrographs, the smallest Pd NPs were deposited on CeO_2 SNRs, whereas the largest Pd NPs on CeO_2 NCs and LNRs (about 2-10 nm). Considering that the Pd $3d_{5/2}$ peak maximum in metal Pd is usually reported at 335.0 eV, because of size effect, the Pd(0) component of the Pd NPs on CeO_2 SNRs (335.9 eV, Figure 24a) shows largest shift towards higher BE with respect to the other samples (Figure 24b-d). The different catalysts also show a different amount of oxidized species Pd(II) and Pd(IV), which correlates well with the dimension of the Pd NPs especially in the case of the Pd(IV) components. This suggests that small NPs can be more efficiently oxidized by the ceria substrate forming a more relevant partially oxidized interface, and consequently a more extended reduction of CeO_2 surface.

This hypothesis is also sustained by considering the effects of Pd deposition on the reduction degree of CeO_2. In fact, the decoration of Pd NPs influenced in different ways chemical composition of the various CeO_2 substrates, as demonstrated also by the previously discussed Raman Spectroscopy data. CNPs and NCs Ce3d photoemission lines show only a slight decrease of the Ce^{4+}/Ce^{3+} ratio after Pd deposition (Figure 22c,d and 23c,d). On the contrary, the most evident changes in CeO_2 degree of reduction are shown by LNRs and SNRs (Figure 22a,b and 23a,b). Especially in the case of LNRs, the CeO_2 support was heavily reduced after the Pd deposition, highlighting the strong Pd-CeO_2 interaction.

Table 3: Summary of the separation into chemically shifted components of Ce3d photoemission lines of Pd/CeO_2 catalysts asprepared, activated (H_2) and after exposure to methanol in working conditions (MeOH).

	Ce3*d* fit results: (area u[iii])/(area of total fit)							
	SNRs		LNRs		NCs		CNPs	
	bare	5% Pd	bare	5% Pd	bare	5% Pd	bare	5% Pd
asprepared	0,080	0,072	0,095	0,08	0,092	0,089	0,100	0,092
H_2	0,078	0,042	0,07	0,052	0,094	0,078	0,089	0,087
MeOH	0,051	0,05	0,066	0,055	0,089	0,082	0,087	0,088

Table 4: Summary of the separation into chemically shifted components of Pd3d photoemission lines of bare CeO_2 and Pd/CeO_2 catalysts asprepared, activated (H_2) and after exposure to methanol in working conditions (MeOH).

	Pd3*d* fits results: area %											
	SNRs			LNRs			NCs			CNPs		
	Pd(0) 335,9 eV	Pd (II)	Pd (IV)	Pd(0) 335,55 eV	Pd (II)	Pd (IV)	Pd(0) 335,4 eV	Pd (II)	Pd (IV)	Pd(0) 335,6 eV	Pd (II)	Pd (IV)
asprepared	0,30	0,17	0,51	0,28	0,20	0,52	0,24	0,27	0,49	0,38	0,42	0,2
H_2	0,91	0,09	0	0,59	0,36	0,05	0,75	0,25	0	0,84	0,16	0
MeOH	0,87	0,13	0	0,69	0,25	0,06	0,76	0,24	0	0,85	0,15	0

After activation in hydrogen atmosphere (300°C, 30 mbar, 1h), all the catalysts were reduced. Pd NPs are almost totally reduced to metal Pd in all cases (Figure 24). However, the largest fraction of reduced Pd is found on Pd NPs deposited on CeO_2 SNRs. Quite surprisingly, the most relevant amount of oxidized Pd is observed on LNRs. This may seem an unusual effect considering their close structural relationship with SNRs that have an opposite behavior. However, the reason can be explained by the different size dimension of Pd NPs, the extremely small NPs on SNR are extremely reactive and kinetically fast to respond to variations in the gaseous environment, whereas the bigger NPS supported on the LNRs are kinetically hindered and pinned by the already mentioned strong interaction with the substrate. Moreover, after activation in hydrogen, the most reduced CeO_2 supports (either with or without Pd) are SNRs, followed by LNRs and then by NCs and CNPDs. This seems to suggest that both types of nanorods are easier to reduce with respect to other ceria nanoshapes. While this enhanced reducibility could be associated with the small dimension in SNRs, such explanation would fail in the case of LNRs. On the other hand, both samples were prepared in the lowest temperature conditions, therefore we can deduced that some structural defects intrinsic to their synthesis may be responsible for the facilitated reduction.

The analysis of the Pd 3*d* and Ce 3*d* spectra after the exposure to methanol (300°C, 10 mbar, 30 min), indicates that the CNPs and NCs and LNRs were almost unchanged (Figures 22, 23 and 24) with respect to the H_2 treatment only, evidencing a small reduction or oxidation of Ceria in presence of absence of Pd, respectively.

In the case of SNRs, the exposure to methanol of the metal free NPs leads to a significant increase of the Ce 3*d* (III) components whereas on the metal decorated substrates the trend is reversed. This slight oxidation of CeO_2 may be associated with the higher local concentration of CO (Figure 22a,b) that can eventually leave a surface carbon layer, which can be hydrogenated to CH_4 at the investigated temperature.[78,79] This effect is more significant in Pd/SNRs it is the most active materials with show the lowest $T_{50.}$

Summarizing the XPS data, it results that Ceria in form of SNRs is extremely responsive to the change of the gaseous environment due to the small dimensions and consequent strong interaction between the oxide substrate and supported metal. A similar behavior is observed also for LNRs, but in this case the reduction level of Pd remains lower because of the larger NP dimension. Anyway, both for types of nanorods it is observed the highest synergy between Pd and CeO_2 as demonstrated by the strong reduction of ceria after the H_2 treatment in the systems decorated by Pd compared to those without. Interestingly, even if they exposed the facets with the lowest oxygen formation energy (i.e {100} with respect to LNRs that expose also a small part {111}), NCs do not reach the same amount of reduction in reducing conditions (either in CH_3OH or H_2) as the two different types of nanorods, probably because of their larger size and higher crystallinity due to the higher synthesis temperature.

In general, the different catalytic performances of ceria based systems can be associated with the type of exposed surfaces, the different defectivity (concentration of oxygen vacancies) and reducibility of ceria nanostructures. In fact, the adsorption of methanol on ceria depends on the formation of methoxy and hydroxyl species.[69] These species are more stable on CeO_2 surfaces with a stronger basicity of O anions. Clear surface structure dependence was found for the strength and amount of base sites: (110) > (100) > (111).[69] Moreover, this tendency will be strengthened under reductive reaction conditions and corresponds as well to the trend of reactivity for vacancy defect formation.[69] In the investigated nanostructures, the main exposed facets are the {100}. Interestingly, the worst performing material (Pd/CNPDs) is the one bearing the highest amount of {111} facets (about 1/10 with respect to {100} facets), but the nanorods which also exhibit some limited amount of {111} faces are on the contrary extremely active. In this case, a second and even more important factor is the ceria dimension, which affects both reducibility of the substrate as well as the interaction with supported metal nanoparticles. In fact, the two catalysts with the worst performances are Pd/CNPDs and Pd/NCs. In these cases, the mean ceria particle size is almost the same (about 20 nm) and concentration of oxygen vacancies and ceria reducibility are quite similar (both low), therefore difference in activity can be traced back to the different amount of {100} vs {111} facets. Notably the means size of Pd NPS is higher on NCs than on CNPs, and so this is the catalytic activity. This therefore suggests that the dimension of Pd nanoparticles must be associated with specific properties of the supporting substrate. This is even more obvious from the analysis of the catalytic activity of the two different type of nanorods that are structurally very similar (same shape and crystal orientation), but with rather different dimensions. This “size effect” strongly affects the interaction with Pd nanoparticles leading to a different morphology and chemical synergies. Both Pd/SNRs and Pd/LNRs exhibit a higher specific surface area (Table 2) due to the smaller size of ceria particles and to the high aspect ratio of LNRs. These two ceria nanostructures showed the highest concentration of oxygen vacancies and the highest degree of reduction among the as-prepared catalysts. Moreover, they showed the highest reducibility associated with the activation process in hydrogen atmosphere, pointing out to a synergistic effect between the metal and the metal oxide. Nonetheless, Pd nanoparticles must be retain a significant level of oxidation, as documented by

previous investigation that highlight how the presence of cationic Pd is connected to enhanced catalytic activity, and by the results of CNPs and NCs that undergo a large reduction of the Pd NPs, but without providing a good catalytic performance . In the case of extremely small metal NPs the presence of "activated cationic species" is achieved by an electronic interaction with the substrate and intrinsic size effect as exemplified in the Pd/SNRs system, which exhibits a relevant shift in the BE position of the Pd $3d_{5/2}$ BE form 355.0 eV to 355.9 eV. On the other hand, on larger NPs the same effect can be obtained by a strong chemical interaction with the support that leads to the preservation of a relatively high fraction of oxidized species at the interface. This latter is the case of Pd/LNRs that in reaction conditions maintain the highest amount of Pd(II) and Pd(IV) species.

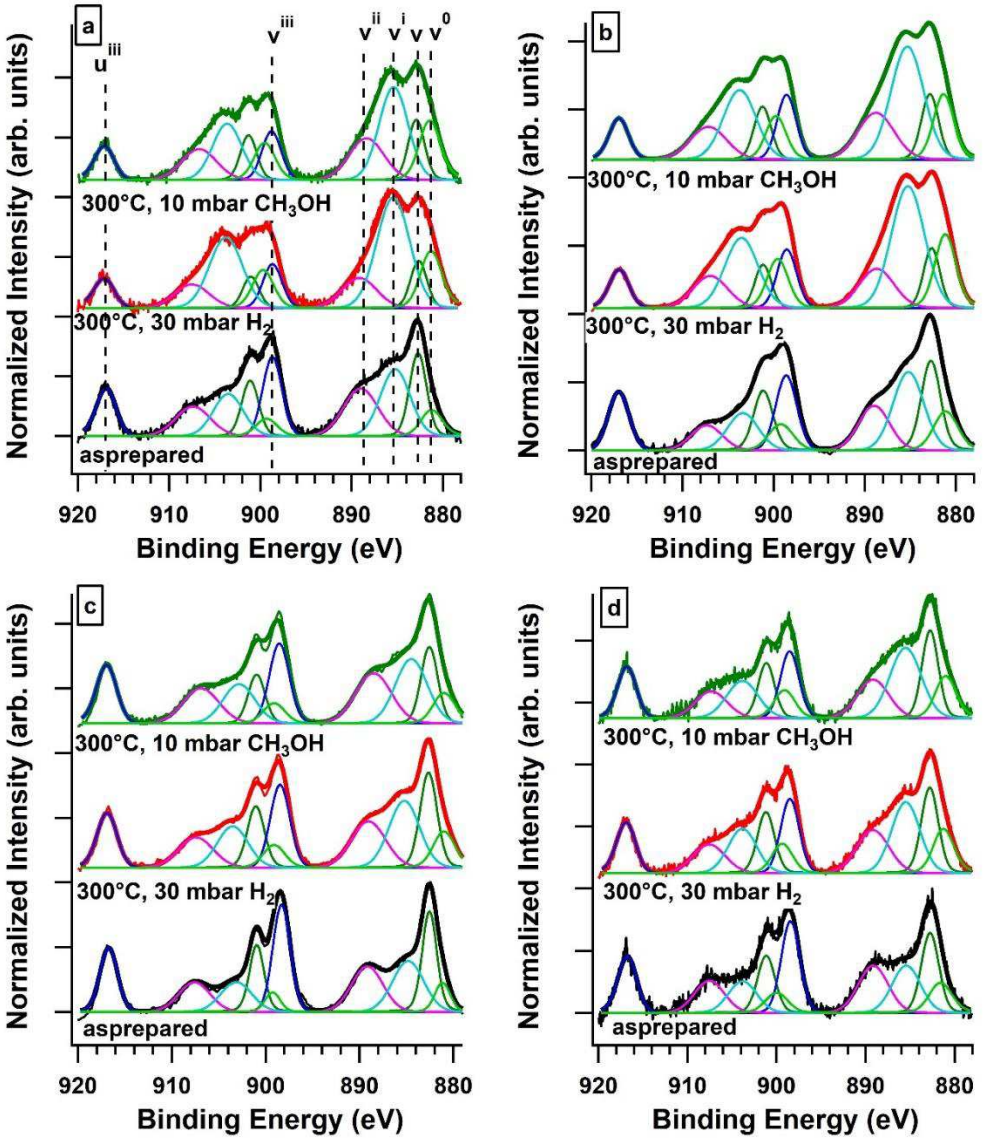

Figure 22: Ce3d photoemission lines, as well as the separations into single chemical components, of a) 5%wtPd/CeO_2 SNRs, b) 5%wtPd/CeO_2 LNRs, c) 5%wtPd/CeO_2 NCs and d) 5%wtPd/CeO_2 CNPDs of asprepared, activated and after exposure to methanol in working conditions.

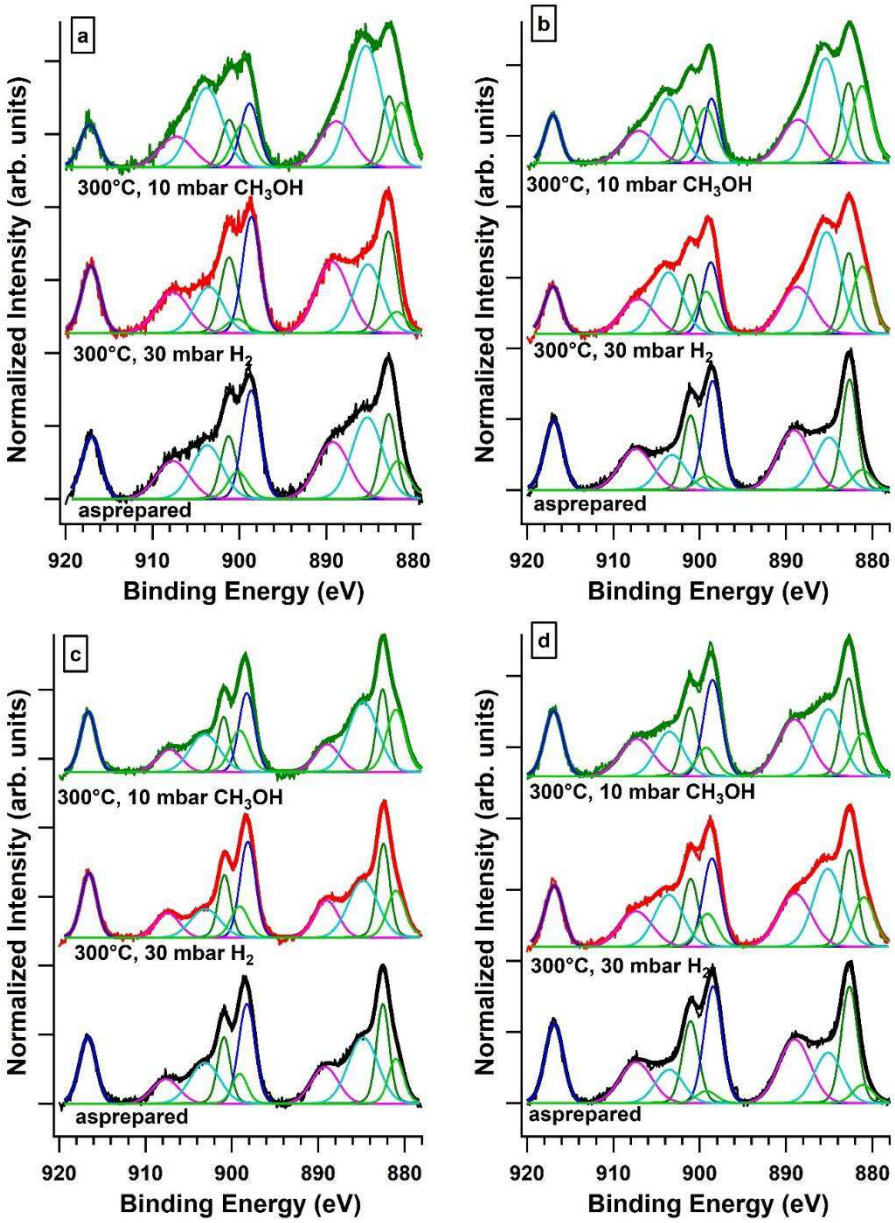

Figure 23: Ce3d photoemission lines, as well as the separations into single chemical components, of a) CeO_2 SNRs, b) LNRs, c) NCs and d) CNPDs of asprepared, activated and after exposure to methanol in working conditions.

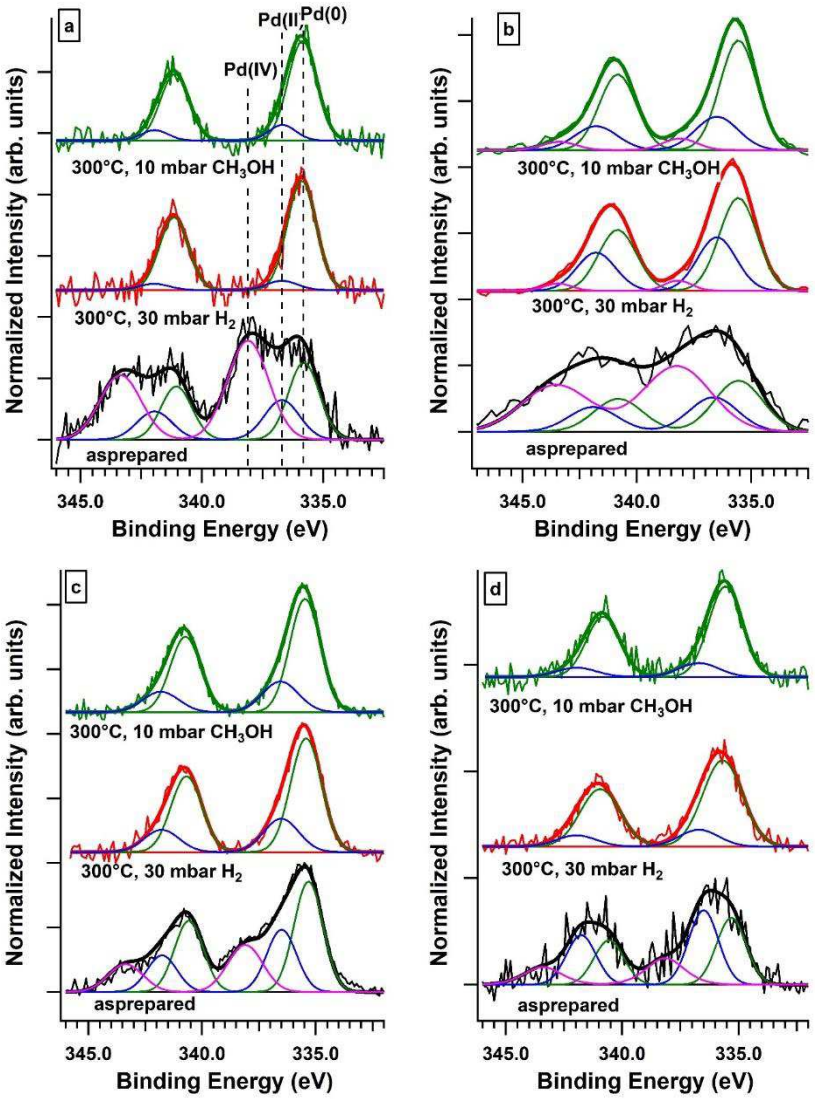

Figure 24: Pd 3d photoemission lines, as well as the separations into single chemical components, of a) 5%wtPd/CeO_2 SNRs, b) 5%wtPd/CeO_2 LNRs, c) 5%wtPd/CeO_2 NCs and d) 5%wtPd/CeO_2 CNPDs of as prepared, activated and after exposure to methanol in working conditions.

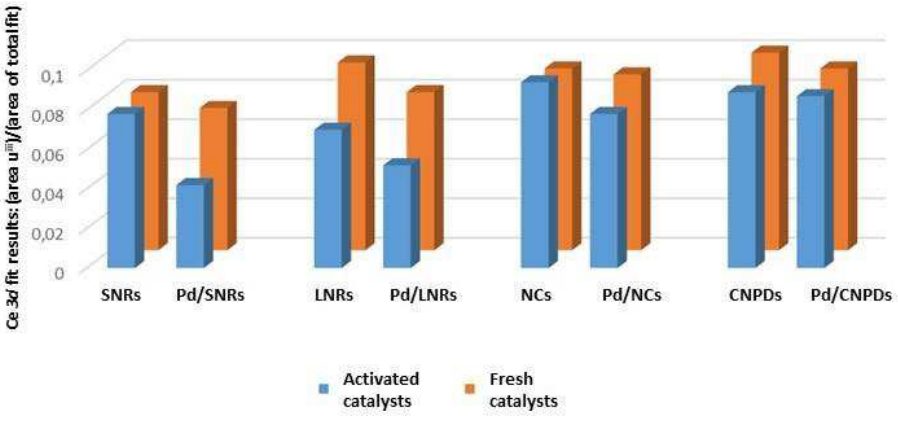

Figure 25: Histogram of the ratio between area of u^{iii} components versus the total area of the fitted Ce3d photoemission line of the different asprepared and activated catalysts (with and without Pd).

3.5 Conclusion

Pd nanoparticles were deposited over different CeO_2 nanostructures that exposed mainly {100} surfaces: small nanords (SNRs), nanorods (LNRs), nanocubes (NCs) and commercial nanopowders (CNPDs). Pd NPs (5% weight) were deposited by a novel deposition method based on hydrogen bubbling in a dispersion of Pd precursor and CeO_2 nanostructures at room temperature, without the need of a calcination step. These materials were investigated as catalysts for the selective decomposition of methanol to syngas, in order to study the effect of the oxide support size, defectivity and redox properties on the catalytic activity of the metal phase. All the catalysts showed high methanol conversion and high selectivity toward the production of CO and H_2. Pd supported on CeO_2 SNRs was the best performing system among the different investigated materials, exhibiting the lowest methanol conversion T_{50} (150°C). *In situ* XPS highlights that the catalysts performances improve (lower T_{50}) with the increase of the Pd-CeO_2 interaction, which favors a higher reducibility of CeO_2 surface as well as the preservation of relatively oxidized palladium species that are the most active in the catalytic process. This higher reducibility of the oxide support seems related to the reduction of the ceria particles size and to the increase of their defectivity (oxygen vacancies concentration), as demonstrated by Raman and XPS spectroscopies. On the other hand, the presence of highly reactive Pd NPs is also another factor promoting the reduction of the substarte itself. This points to the importance of synergistic effects in nanocatalysts.

Notably, the synthesis of the best performing materials was performed at RT and without the use of organic solvents or surfactants, satisfying green chemistry protocols. These results highlight the fundamental role of the exposed surface of the oxide substrate and the importance of the investigation of the correlation between nanostructures morphology and catalytic activity in order to finely design a heterogeneous catalyst at the nano (shape) and atomic scale (oxygen vacancy defects). The production of syngas at low temperature is interesting for different kinds of applications, from energy recovery of waste heat to the emerging field of tandem catalysis. From the tandem catalysis point of view, the *in situ* production of syngas is very important because it represents one of the most basic raw chemicals and is involved in a very large number of chemical processes. Therefore, the *in situ* production of syngas form methanol could permit to carry out different reactions (i.e. hydroformylation or hydrogenation reactions) as one-pot operations. In fact, as future perspective, this kind of nanostructured catalysts could be integrated in a multifunctional material in order to produce *in situ* the syngas and exploit it in a tandem reaction scheme (i.e. hydroformylation reactions). In the next chapter, we will further discuss this new rising field in catalysis we will discuss about the design of a tandem catalyst based on the Pd/CeO_2 nanostructures, which have been thoroughly investigated in this chapter.

References

[1] R. Si, Zhang, W. Y. L. P. You, C. H. Yan, *Angew. Chem., Int. Ed.* **2005**, *44*, 3256.
[2] C. Mandoli, F. Pagliari, S. Pagliari, G. Forte, P. Di Nardo, S. Licoccia, E. Traversa, *Adv. Funct. Mater*. **2010**, 20, 1617−1624
[3] C. Sun, H. Li, L. Chen, *Energy Environ. Sci.*, **2012**, 5, 8475-8505
[4] H. Y. Yahiro, K. Baba, H. Eguchi, J. Arai, *Electrochem. Soc.* **1988**, *135*, 2077–2080
[5] T. Montini, M. Melchionna, M. Monai, P. Fornasiero, *Chem. Rev.* **2016**, 116, 5987−6041
[6] Critical Materials Strategy; DOE/PI-0009; U.S. Department of Energy: Washington, D.C., **2011**; 1−196.
[7] L.Vivier, D. Duprez, *Chemsuschem*, **2010** 3,654-678.
[8] A.Trovarelli, Catalysis by Ceria and Related Materials, 2nd Ed., Imperial College Press, London, **2013**.
[9] K. Mudiyanselage et al *Angew. Chem. Int. Ed.* **2013**, 52, 5101-5105
[10] J. Paier, C. Penschke, J. Saurer, *Chem. Rev* **2013**
[11] D.R.Mullins, *Surface Science Reports*, **2015,** 70, 42-85.
[12] A. Trovarelli, J. Llorca, *ACS Catal.* **2017,** 7, 4716-4735.
[13] P.W. Tasker, *J.Phys.C-Solid State Phys.* **1979**, 12, 4977-4984.
[14] J.C. Conesa, *Surf. Sci.* **1995**, 339, 337-352.
[15] M. Nolan, S.C. Parker, G.W. Watson, *Surf. Sci.* **2005**, 595, 223-232.
[16] M. Nolan, S. Grigoleit, D.C. Sayle, S.C. Parker, G.W. Watson, *Surf. Sci.* **2005**, 576, 217-229.
[17] P. Burroughs, A. Hamnett, A. F. Orchard, G. Thornton, , *J. Chem. Soc., Dalton Trans.* **1976**, 17, 1686−1698.
[18] M. Engelhard, S. Azad, C. H. F. Peden, S. Thevuthasan, *Surf. Sci. Spectra* **2004**, 11, 73−81.
[19] R. Lo Nigro, R.G. Toro, G. Malandrino, I.L. Fragala, *J. Mater. Chem.* **2005,** 15, 2328–2337.
[20] S.N. Jacobsen, U. Helmersson, R. Erlandsson, B. Skarman, L. R. Wallenberg, *Surf. Sci.* **1999**, 429, 22–33.
[21] S.H. Overbury, D.R. Huntley, D.R. Mullins, K.S. Ailey, P.V. Radulovic, *J. Vac. Sci.Technol. a-Vac. Surf. Film*. **1997**, 15, 1647–1652.
[22] D.R. Mullins, P.V. Radulovic, S.H. Overbury, *Surf. Sci.* **1999**, 429, 186–198.
[23] P. Luches, F. Pagliuca, S. Valeri, *J. Phys. Chem. C*, **2011**, 115, 10718–10726.
[24] S.G. Ma, J. Rodriguez, J. Hrbek, *Surf. Sci.* **2008**, 602, 3272–3278.
[25] C.Y. Tian, Y. Du, S.W. Chan, *J. Vac. Sci. Technol. a-Vac. Surf. Film.* **1997,** 15, 85–92.
[26] C. Burda, X. B. Chen, R. Narayanan, M. A. El-Sayed, *Chem. Rev.* **2005**, 105, 1025−1102.
[27] K. J. M. Bishop, C. E. Wilmer, S. Soh, B. A. Grzybowski, *Small* **2009**, 5 (14), 1600-1630.
[28] S. W. Yang, L. Gao, *J. Am. Chem. Soc.* **2006**, 128, 9330−9331.
[29] J. Zhang, S. Ohara, M. Umetsu, T. Naka, Y. Hatakeyama, T. Adschiri, *Adv. Mater.* **2007**, 19, 203−206.
[30] R. O. Fuentes, L. M. Acuna, M. G. Zimic, D. G. Lamas, J. G. Sacanell, A. G. Leyva, R. T. Baker, *Chem. Mater.* **2008**, 20, 7356−7363.
[31] Mai, H. X.; Sun, L. D.; Zhang, Y. W.; Si, R.; Feng, W.; Zhang, H. P.; Liu, H. C.; Yan, C. H. *J. Phys. Chem. B* **2005**, 109, 24380−24385.
[32] P. X. Huang, F. Wu, B. L. Zhu, X. P. Gao, H. Y. Zhu, T. Y. Yan, W. P. Huang, S. H. Wu, D. Y. Song, *J. Phys. Chem. B* **2005**, 109, 19169−19174.
[33] Q. Wu, F. Zhang, P. Xiao, H. S. Tao, X. Z. Wang, Z. Hu, Y. N. Lu, *J. Phys. Chem. C* **2008**, 112, 17076−17080.
[34] C. Pan, D. Zhang, L. Shi, J. Fang *Eur. J. Inorg. Chem.* **2008**, 2429–2436
[35] I. Florea, C. Feral-Martin, J. Majimel, D. Ihiawakrim, C. Hirlimann, O. Ersen, *Cryst. Growth Des.* **2013**, 13, 1110−1121.
[36] N. Ta, J. J. Liu, S. Chenna, P. A. Crozier, Y. Li, A. Chen, W. Shen, *J. Am. Chem. Soc.* **2012**, 134, 20585−20588.
[37] E. Aneggi, D. Wiater, C. de Leitenburg, J. Llorca, A. Trovarelli, *ACS Catal.* **2014**, 4, 172−181
[38] Y. Ishikawa, M. Takeda, S. Tsukimoto, K. S. Nakayama, N. Asao, *Adv. Mater.* **2016**, 28, 1467−1471.
[39] J. Zhang, H. Kumagai, K. Yamamura, S. Ohara, S. Takami, A. Morikawa, H. Shinjoh, K. Kaneko, T. Adschiri, A. Suda, *Nano Lett.* **2011**, 11, 361−364.

[40] A. Bruix, J.A. Rodriguez, P.J. Ramirez, S.D. Senanayake, J. Evans, J.B. Park, D. Stacchiola, P. Liu, J. Hrbek, F. Illas, *J. Am. Chem. Soc.* **2012**, 134, 8968–8974.
[41] Z.L. Wu, M.J. Li, J. Howe, H.M. Meyer, S.H. Overbury, *Langmuir*, **2010**, 26, 16595–16606.
[42] Y.M. Choi, H. Abernathy, H.T. Chen, M.C. Lin, M.L. Liu, *Chemphyschem* **2006,** 7, 1957–1963.
[43] Wu, Z. L.; Mann, A. K. P.; Li, M. J.; Overbury, S. H. *J. Phys. Chem. C* **2015**, 119, 7340−7350.
[44] D.R. Mullins, P.M. Albrecht, F. Calaza, *Top. Catal.* **2013,** 56, 1345–1362.
[45] R.M. Ferrizz, G.S. Wong, T. Egami, J.M. Vohs, *Langmuir,* **2001**, 17, 2464–2470.
[46] D.R. Mullins, M.D. Robbins, J. Zhou, *Surf. Sci.* **2006**, 600, 1547–1558.
[47] M. Ahmadi, H. Mistry, B. R. Cuenya, *J. Phys. Chem. Lett.* **2016**, 7, 3519−3533.
[48] W-J- Shen, Y. Matsumura, *Phys. Chem. Chem. Phys.,* **2000**, 2, 1519-1522.
[49] W-J. Shen, M. Okumura, Y. Matsamura, M. Haruta, *Appl. Catal. A* **2001**, 213, 225.
[50] N. Yi, R. Si, H. Saltsburg, M. Flytzani-Stephanopoulos, *Appl. Catal. B* **2010**, 95, 87−92.
[51] M. Skoda, M. Cabala, I. Matolinova, K.C. Prince, T. Skala, F. Sutara, K. Veltruska, V. Matolin, *J. Chem. Phys.* **2009**,130
[52] G.N. Vayssilov, G. N. Vayssilov, Y. Lykhach, A. Migani, T. Staudt, G. P. Petrova, N. Tsud,T. Skála,A. Bruix,F. Illas, K. C. Prince, V. Matolı´n, K. M. Neyman, J. Libuda, *Nat. Mater.* **2011,** 10, 310–315.
[53] C.T. Campbell, *Surf. Sci. Rep.* **1997**, 27, 1–111.
[54] J. Zhou, D.R. Mullins, *J. Phys. Chem. B* **2006,** 110, 15994–16002
[55] J. Libuda, H.J. Freund, *Surf. Sci. Rep.* **2005**, 57, 157–298.
[56] Y. Y.Cui, W.L. Dai, *Catal. Sci. Technol*. **2016**, 6, 7752−7762.
[57] S. Imamura, T. Higashihara, Y. Saito, H. Aritani, H. Kanai, Y. Matsamura, N. Tsuda, *Catal. Today***, 1999**, 50, 369-380.
[58] L. Soler, A. Casanovas, A. Urrich, I. Angurell, J. Llorca, *Appl. Catal. B* **2016**, 197, 47−55.
[59] J. Spivey, *J. Catalysis. s.l. : Cambridge : Royal Society of Chemistry, **2002**. 67-84.*
[60] Q. Zhang, G. Liu, L. Wang, X. Zhang, G. Li, *Energy Fuels* **2014**, 28, 4431−4439
[61] M.P. Kapoor, Y. Ichihashi, K. Kuraoka, W-J. Shen, Y. Matsamura, *Catalysis letters*, **2003**, 88, 83-87.
[62] W.H. Cheng, *Acc. Chem. Res*. **1999**, 32, 685.
[63] Y. Yamada, C.K. Tsung, W. Huang, Z. Huo, T. Soejima, C.E. Aliaga, G.A. Somorjai, P. Yang, *Nat. Chem.,* **2011**, 3(5), 372-6.
[64] L. Fan, K. Fujimoto, *J. Catal.* **1997**, 172, 238
[65] Y. Liu, T. Hayakawa, T. Ishii, M. Kumagai, H. Yasuda, K. Suzuki, S. Hamakawa, K. Murata, *Applied Catalysis A: General*, **2001**, 210, 301-314.
[66] L. Artiglia, F. Orlando, K. Roy, R. Kopelent, O. Safonova, M. Nachtegaal, T. Huthwelker, J.A. van Bokhoven, *J. Phys. Chem. Lett.* **2017**, 8, 102−108
[67] H. Tan, J. Wang, S. Yu, K. Zhou, *Environ. Sci. Technol*. **2015**, 49, 8675−8682
[68] Z. Wu, M. Li, D.R. Mullins, S. H. Overbury, *ACS Catal*. **2012**, 2, 2224-2234.
[69] A. Trovarelli, J. Llorca, *ACS Catal*. **2017**, 7, 4716−4735.
[70] M. Zabilskiy, P. Djinovic´, E. Tchernychova, O. P. Tkachenko, L. M. Kustov, A. Pintar, *ACS Catal.* **2015**, 5, 5357−5365.
[71] M. Badlani, I.E. Wachs, *Catal. Lett.* **2001**, 75, 137–149.
[72] P.M. Albrecht, D.R. Mullins, *Langmuir*, **2013,** 29, 4559–4567.
[73] Y. Usami, K. Kagawa, M. Kawazoe, Y. Matsumura, H. Sakurai, M. Haruta, *Stud. Surf. Sci. Catal.* **1998,** 118, 83.
[74] Y. Matsumura, W.J. Shen, *Topics in Catalysis*, **2003**, 22, 3-4.
[75] G. W. Graham W. H. Weber C. R. Peters R. Usmen, *J. Catal.*, **1991,** 130, 310-313.
[76] Y. Lee, G. He, A. J. Akey, R. Si, M. Flytzani-Stephanopoulos, I. P. Herman, *J. Am. Chem. Soc.*, **2011**, **133**, 12952.
[77] P. Burroughs, A. Hamnett, A. F. Orchard, G. Thornton, J. Chem. Soc., *Dalton Trans*. **1976**, 17, 1686−1698.
[78] M.A. Vannice, C. Sudhakar, M. Freeman, *J. Catal.*, **1987,** 108, 97.
[79] C. Diagne, H. Idriss, I. Pepin, J.P. Hindermann, A. Kiennemann, *Applied Catalysis,* **1989,** *50,* 43-53

Chapter 4

Multiscale design of nanoreactors for heterogenous catalysis

4. Multiscale design of nanoreactors for heterogenous catalysis

In this chapter, we tackled the design of nanoreactors for heterogeneous catalysis and their integration in multifunctional nanostructured materials. As nanoreactors, we investigated a relatively new class of inorganic-organic hybrid microporous materials that are kindling a tremendous interest in the scientific community due to their exceptional properties: Metal Organic Frameworks (MOFs).[1] MOFs are composed of inorganic nodes (meatal clusters or ions) joined together by organic linkers. The inorganic components that compose MOFs are termed secondary building units (SBUs) or metal nodes, whereas the organic linkers are polytopic ligands named struts or links. The self-assembly of SBUs and struts, under proper conditions, lead to the formation of a 3D crystalline microporous structure with excellent thermal and chemical stability. Due to the microporous structure of MOFs, the surface area of these materials are tremendously high. To date, highest Brunauer–Emmett–Teller (BET) surface area reported for a MOF is ca. 7000 m^2/g.[2] To date this is the highest measured porosity of any material. However, the surface area is only one of the fascinating properties of MOFs, as we will discuss later in this chapter. One of the main interesting aspect of MOFs is their modularity: changing the nature of ligand and of SBUs or synthesizing composite materials it is possible to tune the catalytic activity of these materials.

In particular, we studied MOFs with organic linkers bearing sites that were poised for post-synthetic metalation (PSM) chemistry (i.e. MnMOF[3], UiO-67 bipy[4]). As anticipated, in catalysis MOFs micropores can be seen as nanoreactors. This paves the way to the possibility of finely tuning the chemical environment of these nanoreactors by changing the nature of organic ligand/metal node or by the coordination of metal cations (through PSM) in order to have new active sites. We focused our attention on a Mn(II)-based MOF (hereafter MnMOF).[3] This work was carried out in collaboration with Prof. Doonan group at the University of Adelaide, the same group that reported for the first time the synthesis of this MnMOF. [3] MnMOF linker provides a flexible di-pyrazole chelating unit poised for post-synthetic metal binding. We quantitatively metalated MnMOF by a variety of transition metal ions (i.e. Co(II), Co(III), Rh(I), Fe(II), Fe (III) and mixture of them). We tested the catalytic activity of Rh metalated MnMOF. Rh-metalated MnMOF was studied as catalyst for hydroformylation reaction (in collaboration with Prof. Paganelli at University of Venice).

Finally, we combined the knowledge acquired with these studies and the studies on Pd/CeO_2 presented in the previous chapter. We designed the synthesis of multifunctional catalysts based on core@shell structure of Pd/CeO_2 (core) and post-synthethic metalated MOFs (shell). The materials were synthesized using different methods like solvothermal synthesis and layer-by-layer growth[5]. The goal is to combine MOFs with the metal/oxide system that were the object of our previous investigations for design nanostructured tandem catalysts.[6] In this kind of multifunctional catalytic material composed by two entities (i.e. the metal/oxide active interface and the porous MOF shell bearing a specific catalytic center), one of the reactants (A->B) is produced in situ (reaction "1"). This facilitates a second reaction (reaction "2" B+C->D), which is catalyzed by the other moiety of the same material. This project aims to tackle as a whole the preparation of MOFs in form of *thin* films and use them as model systems for the study of synergistic chemistry in confined spaces. The end game will be the development of new tandem catalysts for a series very fundamental reactions. In particular, we want to develop new catalytic schemes for the activation of small molecules such as CO, H_2, CH_3OH, HCOOH, C_2H_4 in order to obtain more complex fine chemicals.

One of our target reaction is the tandem catalysis of ethylene hydroformylation. In the tandem reaction scheme, CO and H_2 will be produced *in situ* through methanol decomposition catalyzed by Pd/CeO_2 catalysts presented in the previous chapter. In the same material, but on different catalytic sites (Rh-sites in MnMOF shell), the hydroformylation reaction will be carry on thanks to the in situ produced CO and H_2. From a general point of view, the tandem catalysis approach will permit to simplify (i.e. one-pot reactor), to make less dangerous (i.e. in

situ production of hazardous chemicals) and more environmentally friendly (i.e. less purification steps and less wastes) several different reactions.[7] It has to be highlighted that the activity of a tandem catalyst stems from a synergic effect of the different material active sites and it is not simply the sum of properties of the single components. Therefore, the MOF growth must rationally design: it should permit the feeding of methanol at the Pd/ceria interface and its active catalytic sites should be in a position favorable to work synergistically with the metal/oxide interface. The growth of thin layers of MnMOF is not yet reported in literature and the synthesis work was very challenging. We investigated different approaches, but the most promising results that we will discuss in this thesis were obtained with the layer-by-layer growth of MnMOF on CeO_2 nanocubes.

4.1 Metal Organic Frameworks

In literature, the first evidences of the synthesis of a MOF with permanent microporosity was reported by Prof. Yaghi group in 1998.[8,9] In particular, the synthesized a material, named MOF-2, with formula Zn(BDC)(H_2O) (BDC=1,4-benzenedicarboxylate). MOF-2 crystal structure is composed of square, $Zn_2(–COO)_4$ $(H_2O)_2$ paddlewheel-like secondary building units (SBUs) connected by BDC struts. The resulting two-dimensional grid network is held together by strong hydrogen-bonding interactions among the axial water molecules as well as the carboxylate moieties on the paddlewheel units. They demonstrated that MOF pores were filled with DMF and H_2O molecules (from the solvents used for the synthesis), that could be removed under vacuum with heating to yield the desolvated structure Zn(BDC) with permanent microporosity. Continuing these studies, the same group reported the synthesis of MOF-5, probably the most famous and cited material in the MOF field.[10] In fact, MOF-5 is a perfect example to highlight the main fascinating properties of MOFs. It is based on an octahedral zinc carboxylate cluster, $Zn_4O(–COO)_6$, connected via ditopic, linear, BDC linkers. This gives rise to a porous primitive cubic network topology. Apart from the facile preparation route and the high porosity, another feature of MOF-5 is that it was synthesized via a modular approach. Thus, by simply modifying the structure metrics of the organic struts it was possible to obtain several isoreticular (same topology as MOF-5, called IRMOFs, Figure 1) MOFs. From that point, researches exploit the modularity of MOFs structures by rationally assembly different SBUs and struts. Nowadays, more than 20,000 MOFs are known and the number is constantly increasing.[11]

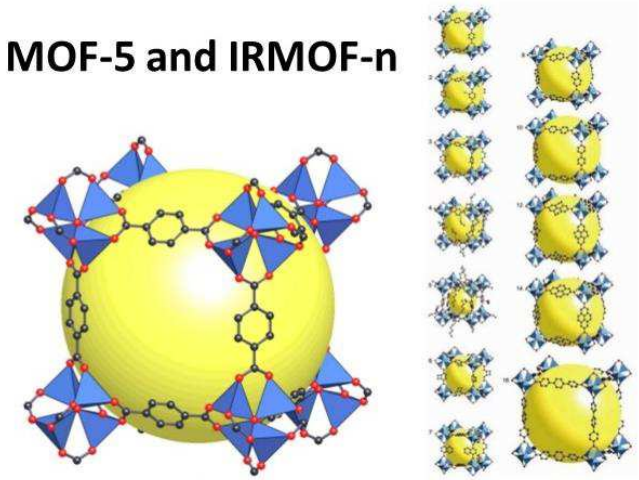

*Figure 1: Single crystal x-ray structures of MOF-5 (left) and IRMOF-n (n = 1 through 7, 8, 10, 12, 14, and 16), labeled respectively. Color scheme is as follows: Zn (blue polyhedra), O (red spheres), C (black spheres), Br (green spheres in **2**), amino-groups (blue spheres in **3**). The large yellow spheres represent the largest van der Waals spheres that would fit in the cavities without touching the frameworks. All hydrogen atoms have been omitted, and only one orientation of disordered atoms is shown for clarity. Adapted with permission from "Mohamed Eddaoudi, Jaheon Kim, Nathaniel Rosi, David Vodak, Joseph Wachter, Michael O'Keeffe, Omar M. Yaghi, Science 295, (5554), 2002 pp. 469-472.". Copyright © 2002, The American Association for the Advancement of Science.*

MOFs are commonly synthesized via solvothermal processes to facilitate the growth of single crystals for diffraction studies. The SBU precursor (i.e. metal salts) and ligand are dissolved in a solution (organic solvent, mixture of solvents or water/organic solutions) and MOFs are formed exploiting the self-assembly of these components. For each MOF the synthesis parameter must be optimized: some MOFs could be synthesized at RT, for some others solvothermal conditions are needed. Obviously, modifying the temperature of the synthesis it is possible to influence the kinetics and thermodynamics of MOF crystal growth and modify their final size and morphology. Another strategy to influence nucleation and growth of MOFs crystals is to add organic molecules (usually monocarboxylic acids like acetic acid or benzoic acid) that can act as "modulator". In this case, the modulator competes with the ligand to the coordination of SBUs. Consequently, the presence of modulator slow down the growth kinetic of the crystals and usually lead to the growth of less defective crystal structures.

4.2 MOFs and catalysis

In the field of catalysis, MOFs are widely studied since they exhibit ultra-high surface areas (up to 7,000 m^2/g), and interconnected pore cavities that can be precisely tuned from a couple of Å to some nm. This can allow for controlling the diffusion of gaseous and liquid species and to facilitate stereochemically selective chemical reactions. [12,13] Because MOFs combine organic and inorganic moieties they exhibit intermediate properties between standard heterogeneous (e.g. zeolites) and homogeneous (e.g. metalorganic compounds) catalysts, possibly presenting the advantages of both types of systems. As we have seen in MOF-5 example, MOFs can be functionalised either at the level of metal nodes (i.e. by providing coordinatively unsaturated metal ion sites, CUS), or in the organic linkers (i.e. by introducing special functional groups) with catalytic centers that can play an active role in specific catalytic processes. [14] In fact, if the organic linkers have moieties like ammonia, di-pyridine or di-pyrazole that are not coordinating the metal nodes, it is possible to post-synthetic metallated (PSM) the MOFs.[15]

Related to these properties of MOFs, recently in catalysis has been developed the concept of *chemistry in confined spaces.* This concept is kindling more and more the interest of chemists due to radical new phenomena that have been documented.[16] Special nanoreactors such as molecular flasks[17] or homogeneous supramolecular catalysts bearing sterically hindered ligands,[18] have been exploited to build a confined reaction ambient. The results of these investigations are substantiating the idea that, exactly as for natural enzymes, whose secondary and tertiary structures are pivotal to drive the catalytic substrate through a unique low energy reaction path,[19] so in artificial catalysis the second and third coordination sphere of the active site are largely responsible for the selectivity and efficiency of the reaction. Since MOFs synthesized via a modular approach their ordered microporous structures can be easily modified. Thus there is incredible potential to study, in detail, the chemistry within the confined spaces of the MOF pores. In contrast to homogeneous systems MOFs are solid and crystalline, accordingly, the structure of the active site is perfectly reproduced throughout the material, providing a much simpler more controlled and denser system that may be investigated in a rigorous manner by using a wider number of experimental techniques.

In the second instance, the *confined space* can impact in a very direct way on the selectivity by excluding certain molecules from reaching a precise site, because of specific size requirement, (molecular sieving) or it may prevent the formation of specific by-products because they are associated with a sterically hindered transition state.

Therefore, looking with the eyes of the molecules, each MOF crystal could be considered as an ordered array of interconnected nanoreactors where, thanks to the modularity of MOFs, the chemical and steric environment that the regent molecules will encounter could be suited for specific applications.

An interesting strategy for imparting new catalytic properties to a MOF is the post-synthetic metalation (PSM) process.[15] In fact, with this strategy is possible to coordinate transition metal cations or complexes to unsaturated metal nodes or to free chelating unit of ligand (if available). One of the most studied case in literature is the UiO-67 bpydc MOF.[4] In this Zr-based MOF, it is possible to coordinate to the open 2,2'-bipyridine (bpy) chelating sites contained in the organic linker different metal cations (i.e. Pd(II), Pt(II) and Cu(II)) by soaking MOF powder in metal salt solutions.[20] For example, UiO-67-bpydc readily forms complexes with $PdCl_2$. The resulting MOF has therefore a new active site in its structure. Moreover, the crystallinity of the MOF ensure that the active site is perfectly reproduced throughout the material. This material exhibited efficient and recyclable catalytic activity for the Suzuki-Miyaura cross-coupling reaction, proving the accessibility to the active site introduced by PSM method.

This concept of the *confined space* is also employed to describe the catalysis based on composite materials. In fact, by the combination of MOFs with metal or metal oxide nanoparticles (NPs), it is possible to synthesize composite materials with new catalytic properties.[21] The catalytic and structural properties of MOFs can be efficiently coupled with the reactivity of the NPs. However, the *confined space* can act also in a subtler way, by allowing the access to the active center, but limiting the molecular motion. In this way for example, only certain functional groups of the targeted catalytic substrate will be able to get in contact with the active site and therefore to be converted. This elusive effect can be very effective in *tandem catalysis* because it may control the selectivity of a complex chemical transformation. As a matter of effect, this approach is supposed to be at the origin of the high selectivity observed in a *tandem* Knoevenagel reaction catalyzed by Pd nanoparticles encapsulated by an IRMOF-3 shell (Figure 2),[22] and recently it has been more rigorously demonstrated by IR investigations in the case of Pd nanoparticles supported inside zeolites Beta for the selective reduction of nitroarene.[23]

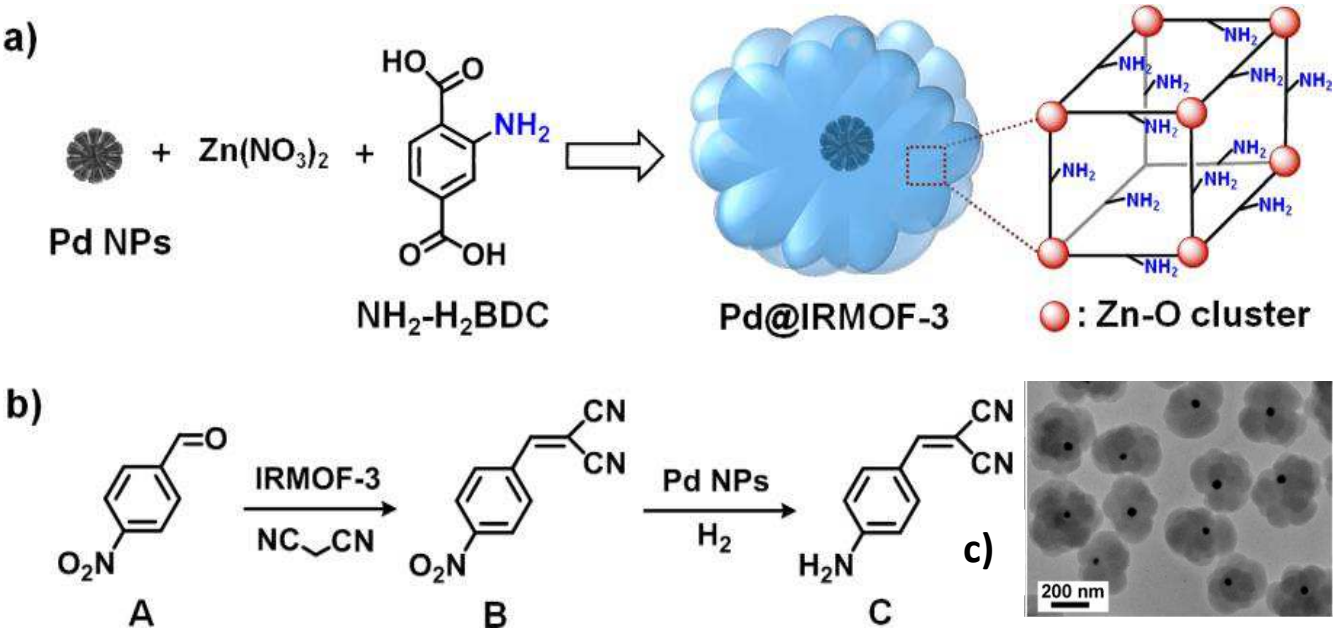

Figure 2: Synthetic Route for the Core–Shell Pd@ IRMOF-3 Hybrids via the Mixed Solvothermal Method (Pd NPs stabilized by a coating of PVP) and (b) Model Cascade Reactions Involving Knoevenagel Condensation of A and Malononitrile via the IRMOF-3 Shell And Subsequent Selective Hydrogenation of Intermediate Product B to C via the Pd NP Cores. TEM micrograph of the nanocomposites (c). Adapted with permission from: Zhao et al J. Am. Chem. Soc. 2014, 136, 1738–1741. Copyright © 2014, American Chemical Society.

Tandem or *synergistic* catalysis is a new approach in catalysis and refers to the possibility to couple different chemical reactions in a single reaction environment (*one-pot*) by exploiting multiple catalytic centers.[24,25,26] In this way the consumption of energy, production of wastes and especially the chemical work-up are strongly reduced due to the elimination of intermediate purification and separation steps. The ability to produce *in situ* the reactants for a multi-step reaction also allows great logistics advantages, especially if some of the chemicals necessary at some point of the synthesis, are unsafe to handle (e.g. highly pressurized gases such H_2) or potentially toxic (e.g. CO, HCl etc). The possibility to start from very simple and basic raw materials and their progressive conversion through *one-pot* processes toward more and more complex compounds is a structural solution to significantly improve the sustainability of chemical industry. Within the current state of the art of chemistry, this seems to be quite a challenge, however the example of enzymes demonstrates that even highly complex chemical compounds can be synthesized in very mild conditions within a unique environment through the combination of intertwined anabolic paths. In fact, enzymes allow the practical realization of this type of chemical synthesis by exploiting their sophisticated chemical composition and articulated spatial structure. Because of these features, complex chemical transformations can be efficiently performed even at low temperature, in high dilution conditions with perfect molecular selectivity. On the contrary, the artificial catalysts so far developed are intrinsically simple and most of the tandem process envisaged in man-made catalysis are limited to very simple reactions and generally comprise a unique catalyst that maybe perform several similar reactions,[25] therefore the disruptive potential of tandem catalysis is still far from being realized. Nowadays, the huge hurdle to overcome is the design of sufficiently flexible and versatile materials that meet the requirements of high selectivity and activity necessary for *tandem* catalysis.

Only very recently, the potential of MOFs as *tandem catalysts* has been eventually recognized leading to some interesting results that corroborate the idea that these materials represent a unique platform for revolutionizing the current catalysis paradigm. [27] The ground breaking effect that MOFs can have in the catalysis field can be further amplified because, as we previously discussed, MOFs can host additional functional units (i.e. metal nanoparticles, polyoxometallates, guest molecules and ions) becoming therefore an integrated platform for advanced chemical conversions and in particular tandem catalysis.[28] Their unique properties as support materials are obviously connected to their huge surface area and microporosity that can have a profound effect on the hosted entity, being able to impart enhanced activity and better selectivity. The literature on MOFs is very rich of these type of composites, but the field of *tandem* catalysis on MOFs is still in its infancy. Very simple reactions made up only by two or three steps, in general quite similar, have been studied, providing evidence of their technical feasibility and large potentiality, but without addressing fundamental questions or going into the details of the microscopic mechanism of such reactions. A high level of empiricism is still driving this research; a lot of fascinating hypothesis have been emerged in some works, however clear views and strong experimental demonstrations of the operating principles of *tandem* schemes in MOFs are still missing. This is indeed a feature that is common to many studies on MOFs, where the materials complexity precludes a detailed understanding of their chemistry.

The study of *rationally designed model systems,* (i.e. ordered and perfectly reproduced single type of structural units designed with atomic scale precision), could permit to investigate by a reductionist approach even highly complicated chemical reactions.[29] In other catalysis fields (i.e. catalysis at metal/metal oxide interface), the results of such an approach were able to transform catalysis from an empiric practice based on *trial and error* to a sophisticated discipline based on rational understanding and capable of *ab initio* tailor-made design.

Therefore, the achievement of the fine control over the spatial localization of the self-assembly sites of MOFs on a substrate (i.e. metal or metal oxide NPs) is fundamental in order to obtain a rational understanding of the

catalytic properties of MOF/NPs composite materials. Should be noticed that the use of *thin* MOFs films as *model tandem* catalysts is still completely unexplored. In fact, with their intrinsic high complexity, synthesis and characterization of ultrathin MOFs *model tandem* catalysts are highly challenging, but the possible exploitation of MOFs for tandem reactions could represent a groundbreaking technological platform for the advancement of green chemistry and sustainable processes.

Typically, there are two approaches for the synthesis of NPs/MOF composite materials. They are called "ship in a bottle" or "bottle around ship" synthesis. In the first case, the NPs precursors can be loaded inside MOF pores through CVD or impregnation methods.[30] Successively the NPs can be formed through thermal decomposition of the precursors, chemical reduction or solvothermal processes. Another technique that has been recently employed in the literature to deposit metal NPs in MOF cavities is the Atomic Layer Deposition (ALD).[31] In fact, one of the advantage of post-synthesis metalation from the vapor-phase is the elimination of purification and activation steps and of problems associated with site blocking by solvent molecules. Conversely, in the second case, MOF crystals are grown by solvothermal methods around pre-formed NPs (usually coated with stabilizing agents like PVP).

Recently, was proposed an alternative strategy to nucleate metal NPs inside the pores of post-synthetic metalated MOFs. It was demonstrated that, finely tuning the activation temperature of the PSM UiO-67 bpydc, it was possible to selectively break the nitrogen-metal bonds, while maintaining the MOF porosity and crystallinity.[32] This could be an alternative route for the deposition of very small and highly dispersed metal NPs inside MOF cavities. In fact, the uniform dispersion of NPs inside the micropores is ensured by the crystallinity of the PSM MOF, where the position of the NPs precursors (i.e. cation coordinated to a chelating unit of the ligand) is perfectly reproduced throughout the material at the beginning of the process.

However, from a general point of view, these preparation routes of NPs/MOF composites present some intrinsic experimental difficulties: some clusters may nucleate on the external surface or grow uncontrollably until they completely fill the pores. All these problems would make the understanding and control of a tandem scheme quite difficult. On the contrary the use of thickness controlled MOFs films would allow to observe the same chemistry but with the benefit of keeping the system simple enough for a rational understanding. Some previous investigations have been demonstrated that core@shell metal@MOFs systems can be extremely efficient tandem catalysts.[22] In these studies however, there was no clear control of the thickness (typically > 50 nm, see Figure 2) and morphology of the MOF shell. Metal cores in general are covered by relatively thick PolyVinylPyrrolidone layers or by other coupling agents in order to favor the heterogeneous nucleation of the MOFs phase. The resulting system therefore is highly defective, very difficult to model and presents an indirect and quite imperfect metal/MOF interface, which prevent to exploit all the potential of synergistic interfacial chemistry. This is the main reason why no detailed understanding of the tandem process has been so far obtained.

Nowadays, an area of significant interest in MOFs synthesis is to achieve fine control over the spatial localization of the self-assembly sites. This challenge is not only related to the tandem catalysis field, but is a fundamental research field for the integration of MOFs in technological relevant devices (i.e. sensors, gases separation)[33]. Several strategies were reported in literature, ranging from bottom-up to top-down techniques.[34] For example, it is possible to coat different surfaces by electrochemical (both anodic and cathodic) depositions.[35] In the case of anodic deposition, the anode is composed by the same metal that formed the SBUs of the desired MOF. The anode is immersed in a ligand containing solution and the electrochemical treatment converts the anode surface into MOF thin film. If the anode is patterned (i.e. lithographed metallic substrate), then is possible to grow patterned MOF coatings. Similarly, by proper functionalization of a surface, is possible to grow patterned or

continuous MOF thin films with different approaches, ranging from seeding in solvothermal synthesis to Langmuir-Blodgett deposition.[34]

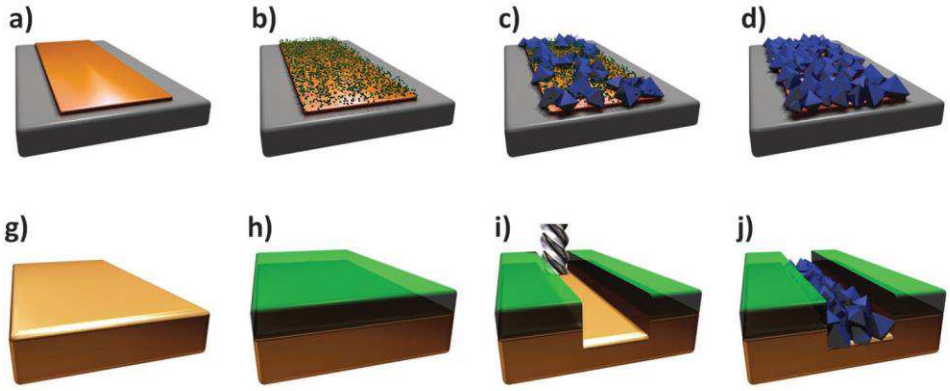

Figure 3: (a–d) Schematic of the electrochemical method proposed by Ameloot et al. for depositing HKUST-1 on copper substrates. (a) A copper pattern (orange) is produced using standard lithographic techniques, and connected as the anode in an electrochemical cell. (b) Voltage is then applied, releasing Cu cations into solution. (c) The ligand (H3BTC) in solution reacts with the metal cations concentrated near the anode surface, growing the MOF crystals (blue). (d) The concentration of the metal precursor remains higher over the uncoated regions of the anode, promoting MOF growth on these areas, resulting in a dense coating. Schematic of MOF patterns produced using precision milling combined with electrochemical deposition: (g) A copper substrate is coated with (h) a PEEK layer, and (i) a meandering channel is cut via a precision milling process. (j) Electrochemical synthesis is then used to deposit HKUST-1 crystals in the channels. Adapted with permission from Paolo Falcaro, Raffaele Ricco, Cara M. Doherty, Kang Liang, Anita J. Hill and Mark J. Styles, MOF positioning technology and device fabrication Chem. Soc. Rev., 2014,43, 5513-5560. Published by The Royal Society of Chemistry.

One of the most interesting approaches for the synthesis of MOF thin films is the so-called layer-by-layer approach. It was firstly proposed for the growth of MOF thin films on flat surfaces in order to study the formation of MOFs in a more rational way.[36] With this approach, the educts (SBUs and ligand) are combined in a sequential fashion (Figure 4). In fact, this method is based on repeated cycles of immersion of the substrate in solutions of the SBUs precursor and solutions of organic ligand. Between each step, the material is rinsed with fresh solvents in order to eliminate unreacted precursors/ligand. In literature, layer by layer approach was exploited to study the kinetic of the individual steps of MOF growth and to grow highly oriented MOF films (also called surface-mounted MOF, SURMOF) with well defined thickness.[36,37,38] Moreover, this approach paved the way to the growth of novel MOF-like ordered structures composed by different layers, even with nonperiodic combinations of different metal ions and/or different linkers. [39] Usually, the substrate employed for layer by layer growth are COOH-terminated Self-Assembly Monolayers (SAMs) functionalized substrates. However, if the ligand of the target MOF interact strongly with the substrate surface it is possible to avoid the presence of SAMs (Figure 5).[40] This is particularly desirable if we wanted to exploit the substrate not only as a nucleation center for the SURMOF growth, but also as an active component of the final material (i.e. tandem catalysis).

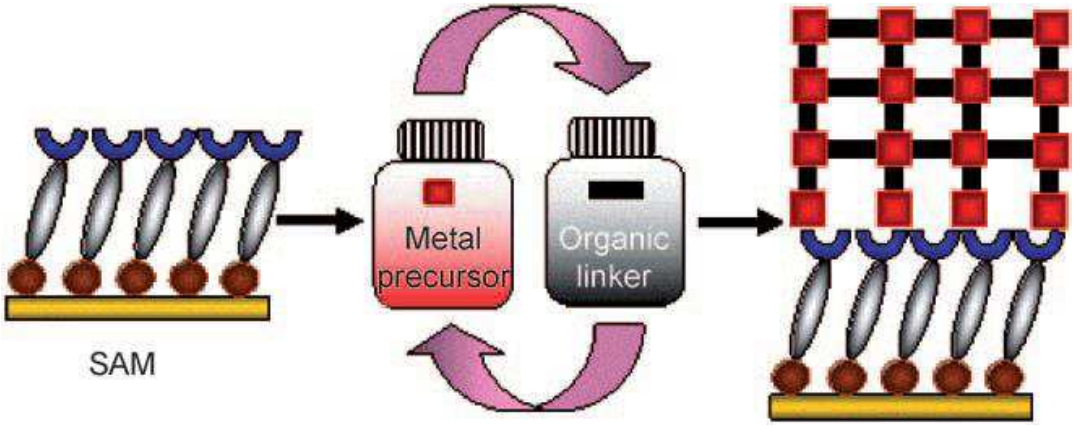

Figure 4: The step-by-step approach for the growth of the SURMOFs on a SAM-functionalized substrate. The approach involves repeated cycles of immersion in solutions of the metal precursor and solutions of organic ligand. Between steps the material is rinsed with solvent. Reprinted with permission from "Osama Shekhah, Hui Wang, Denise Zacher, Roland A. Fischer, and Christof W_ll Growth Mechanism of Metal–Organic Frameworks: Insights into the Nucleation by Employing a Step-by-Step Route Angew. Chem. Int. Ed. 2009, 48, 5038 –5041". Copyright © 2009 WILEY-VCH Verlag GmbH & Co. KGaA, Weinheim.

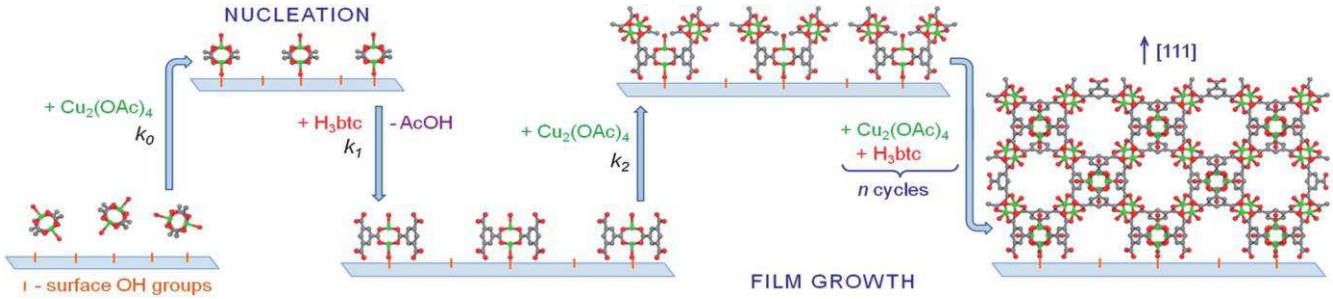

Figure 5: Schematic representation of the proposed model for Cu3(btc)2 nucleation and growth on oxide surfaces. The atoms are shown as follows: Cu –green, O – red, C – gray. Reprinted with permission from "Vitalie Stavila, Joanne Volponi, Aaron M. Katzenmeyer, Matthew C. Dixon and Mark D. Allendorf, Kinetics and mechanism of metal–organic framework thin film growth: systematic investigation of HKUST-1 deposition on QCM electrodes† Chem. Sci., 2012, 3, 1531". Copyright © 2012, Royal Society of Chemistry

4.3 Post-synthetic metalation of a Mn-based MOF

In this section, we will focus our attention on a Mn(II)-based MOF: $[Mn_3(L)_2(L')](1)$ (hereafter MnMOF).[3] L and L' are crystallographically unique forms of the deprotonated ligand bis(4-(4-carboxyphenyl)-1H-3,5-dimethylpyrazolyl)methane, LH_2. Structurally, MnMOF is composed by two-dimensional layers of trinuclear $Mn_3(II)(L)_2$ nodes pillared by the L' form of the ligand. In the L form, the carboxylate and pyrazole donors coordinate the Mn_3 nodes. Conversely, in the L' form only the carboxylate donors are involved into the Mn coordination. Therefore, for each metal node, L' provides a flexible di-pyrazole chelating unit poised for post-synthetic metal binding (Figure 6). In fact, by simply soaking MnMOF powders in different metal salt solutions is possible to saturate these free di-pyrazole units with metal cation (i.e. Co(II), Rh(I)). In order to explore the possibilities offered by PSM process on MnMOF, we have screened the insertion of different metal cations that are potentially interesting in the field of heterogeneous catalysis: Co(II), Co(III), Fe(II), Fe(III), Rh(I) and mixture of them. The obtained materials were investigated combining P-XRD and SEM, in order to verify how the PSM process influenced the crystallinity of the materials. We quantified the degree of metalation using inductively coupled energy-dispersive X-ray analysis (EDX) (Table 1).

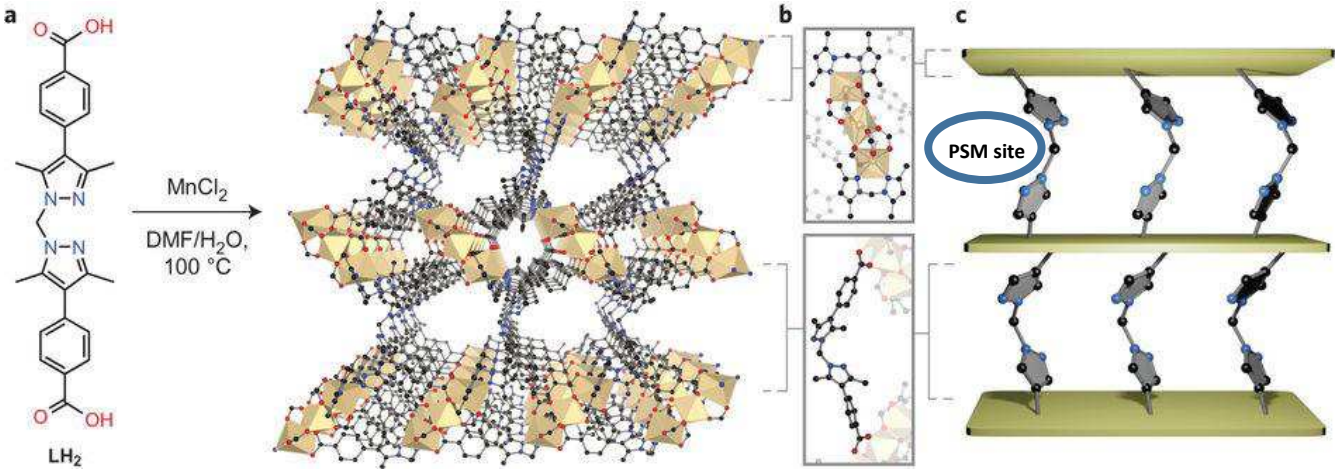

Figure 6: Synthesis of MnMOF from LH_2 and $MnCl_2$, and a perspective view of the single-crystal X-ray structure of this material along the c axis. Coloured spheres represent O (red), N (blue) and C (black), and the Mn centres are shown as beige polygons. b, Enlargements of the trinuclear Mn(II) nodes of MnMOF showing the coordination environment of the three Mn centres and one complete molecule of L' flanked by two trinuclear Mn(II) nodes, highlighting the pillaring ligand moiety. c, Schematic representation of MnMOF with the layers represented as mustard coloured planes and chemical detail highlighting the di-pyrazole coordinating site (Post sytnthetic metalation available site) in L'. Adapted with permission from : Witold M. Bloch, Alexandre Burgun, Campbell J. Coghlan, Richmond Lee, Michelle L. Coote, Christian J. Doonan and Christopher J. Sumby NATURE CHEMISTRY, 6, 2014. Copyright © 2014, Springer Nature.

4.3.1 Experimental section

Materials synthesis

Unless otherwise stated, all chemicals were obtained from commercial sources (Sigma Aldrich, Alfa Aesar) and used as received.

Synthesis of MOF ($[Mn_3(L)_2(L')]$) (hereafter MnMOF): The ligand LH_2 was synthesized following a previously reported procedure.[3] MnMOF was synthesized as previously reported by Bloch et al.[3] Briefly, 24.7 mg of $MnCl_2 \cdot 4H_2O$ and 31.6 mg of LH_2 (1.7:1 molar ratio) were dissolved in 6 mL of dimethylformamide (DMF)/H_2O (2:1 vol. ratio) and heated in oven at 100 °C for 48 h in a screw-cap vial. The obtained colourless crystals (yield: 70%) were washed in DMF (x3), methanol (x5) and dried under vacuum for 12 hours.

Post-synthetic metalation of MnMOF:

- Rh(I): the as-syntesized material, MnMOF (25 mg), was solvent exchanged with dry acetonitrile. The solvent was replenished 5 times and the crystals were allowed to soak in dry acetonitrile for 10 minutes in between each wash. Then 18 mg of $[Rh(CO)_2Cl]_2$ were added to the acetonitrile dispersion of MnMOF and the resulting mixture was left at RT for 60 h. Then, the solvent was exchanged for fresh dry acetonitrile (×7). The solvent was decanted, and the pale yellow crystals of Rh/MnMOF were dried under vacuum for 12 hours.[3]
- Co(II): the as-syntesized material, MnMOF (25 mg), was solvent exchanged with methanol. The solvent was replenished 5 times and the crystals were allowed to soak in methanol for 10 minutes in between each wash. Then 30 mg of $CoCl_2 \bullet 6(H_2O)$ were added to the methanol dispersion of MnMOF and the resulting mixture was left at 60°C for 48 h. Then, the solvent was exchanged for fresh methanol (×7). The solvent was decanted, and the pink crystals of Co/MnMOF were dried under vacuum for 12 hours. [3]
- Co(II):Fe(III)=2:1 : the as-syntesized material, MnMOF (25 mg), was solvent exchanged with methanol. The solvent was replenished 5 times and the crystals were allowed to soak in methanol for 10 minutes in between each wash. Then $CoCl_2 \bullet 6(H_2O)$ and $FeCl_3 \bullet 6(H_2O)$ (molar ratio 2:1, total weight=30 mg) were added to the methanol dispersion of MnMOF and the resulting mixture was left at 60°C for 48 h. Then, the solvent was exchanged for fresh methanol (×7). The solvent was decanted, and the pale blue crystals of Co/MnMOF were dried under vacuum for 12 hours.
- Co(II):Fe(III)=1:2 : the as-syntesized material, MnMOF (25 mg), was solvent exchanged with acetonitrile. The solvent was replenished 5 times and the crystals were allowed to soak in acetonitrile for 10 minutes in between each wash. Then $CoCl_2 \bullet 6(H_2O)$ and $FeCl_3 \bullet 6(H_2O)$ (molar ratio 1:2, total weight=30 mg) were added to the acetonitrile dispersion of MnMOF and the resulting mixture was left at 60°C for 48 h. Then, the solvent was exchanged for fresh acetonitrile (×7). The solvent was decanted, and the pale blue crystals of CoFe/MnMOF were dried under vacuum for 12 hours.
- Co(II):Fe(II)=2:1 : the as-syntesized material, MnMOF (25 mg), was solvent exchanged with acetonitrile. The solvent was replenished 5 times and the crystals were allowed to soak in acetonitrile for 10 minutes in between each wash. Then $CoCl_2 \bullet 6(H_2O)$ and $FeCl_2 \bullet 4(H_2O)$ (molar ratio 2:1, total weight=30 mg) were added to the acetonitrile dispersion of MnMOF and the resulting mixture was left at 60°C for 48 h. Then, the solvent was exchanged for fresh acetonitrile (×7). The solvent was decanted, and the pale blue crystals of CoFe/MnMOF were dried under vacuum for 12 hours.

- Fe(III): the as-syntesized material, MnMOF (25 mg), was solvent exchanged with acetonitrile. The solvent was replenished 5 times and the crystals were allowed to soak in acetonitrile for 10 minutes in between each wash. Then 30 mg of $FeCl_3 \bullet 6(H_2O)$ were added to the acetonitrile dispersion of MnMOF and the resulting mixture was left at 60°C for 48 h. Then, the solvent was exchanged for fresh acetonitrile (×7). The solvent was decanted, and the pale blue crystals of Fe/MnMOF were dried under vacuum for 12 hours.
- Co(III):Fe(II)=1:2 : the as-syntesized material, MnMOF (25 mg), was solvent exchanged with acetonitrile. The solvent was replenished 5 times and the crystals were allowed to soak in acetonitrile for 10 minutes in between each wash. Then $Co(acac)_3$ and $FeCl_2 \bullet 4(H_2O)$ (molar ratio 1:2, total weight=30 mg) were added to the acetonitrile dispersion of MnMOF and the resulting mixture was left at 60°C for 48 h. Then, the solvent was exchanged for fresh acetonitrile (×7). The solvent was decanted, and the pale blue crystals of CoFe/MnMOF were dried under vacuum for 12 hours.

Characterization techniques

Powder X-ray diffraction (P-XRD) data were collected on a Bruker Advanced D8 diffractometer (capillary stage) using Cu Kα radiation (λ = 1.5418 Å, 50 kW/40mA). Wide Angle (WAXRD) XRD patterns were recorded in the diffraction angular range 5−40° 2θ by a Philips X'Pert PRO diffractometer, working in the reflection angle geometry and equipped with a graphite monochromator on the diffracted beam (Cu Kα radiation),

Scanning Electron Microscopy and Energy Dispersive X-ray Spectroscopy were acquired using a field emission electron source equipped with a GEMINI column (Zeiss Supra VP35).

Characterization by Raman spectroscopy was performed using a ThermoFisher DXR Raman microscope. The spectra were recorded using a laser with an excitation wavelength of 532 nm (1 mW), focused on the sample with a 10× objective (Olympus).

Gas adsorption isotherm measurements were performed on an ASAP 2020 Surface Area and Pore Size Analyser. Activation of samples was carried out by heating the sample at 120°C for 12 hours in vacuum. UHP grade (99.999%) N_2 were used for all measurements. The temperatures were maintained at 77 K (liquid nitrogen bath).

4.3.2 Results and discussion

EDX results of the PSM materials highlights how the metalation occurred in essentially quantitative yield (saturation of all vacant dypyrazole chelating units) in almost all the cases. The best results were obtained in the case of PSM with Co(II) in methanol and with Rh(I) in dry acetonitrile. In these cases, the degree of metalation was essentially quantitative and the crystallinity (Figure 7) and crystals morphology (Figure 8) of the final material was maintained. When we tried the simultaneous insertion two different cations in the MOF structure (Co and Fe) we verified that the molar ratio of the starting precurors was not maintained. In fact, it seems that Co posses an higher affinity towards dypyrazole sites in the MOF, leading to a Co/Fe molar ratio higher than expected. Moreover, we verified that Fe(III) was able to substitute Mn(II) in the MOF structure, leading to a heavy loss of crystallinity of the material (Table 1, Figure 7 and 8d).

Table 1: Resume of EDX analyses of some post-synthetic metalated MnMOF samples. The XRD pattern of these samples are reported in Figure X. For the sake of clarity, is reported only the EDX quantification of transition metals (C, O, N and Cl are not reported).

Solvent	Metal salts	Salts molar ratio	EDX (atomic %)			
			Mn	Co	Fe	Rh
Methanol	Co(II)	\	76%	24%	\	\
Methanol	Co(II), Fe(II)	2:1	78%	14%	8%	\
Acetonitrile	Co(II), Fe(II)	2:1	76%	19%	5%	\
Acetonitrile	Co(II), Fe(III)	1:2	83%	13%	4%	\
Acetonitrile	Co(II), Fe(III)	2:1	79%	15%	6%	\
Acetonitrile	Co(III), Fe(II)	2:1	84%	13%	3%	\
Acetonitrile	Fe(III)	\	8%	\	92%	\
Acetonitrile	Rh(I)	\	55%	\	\	45%

Notes: 100% of metalated dipyrazole sites corresponds to an atomic ratio between Mn and chelated M metal of 3. In the case of Rh(I) metalation, each dipyrazole site host 2 Rh atoms, therefore for 100% of metalation the atomic ratio between Mn and Rh is 1.5.

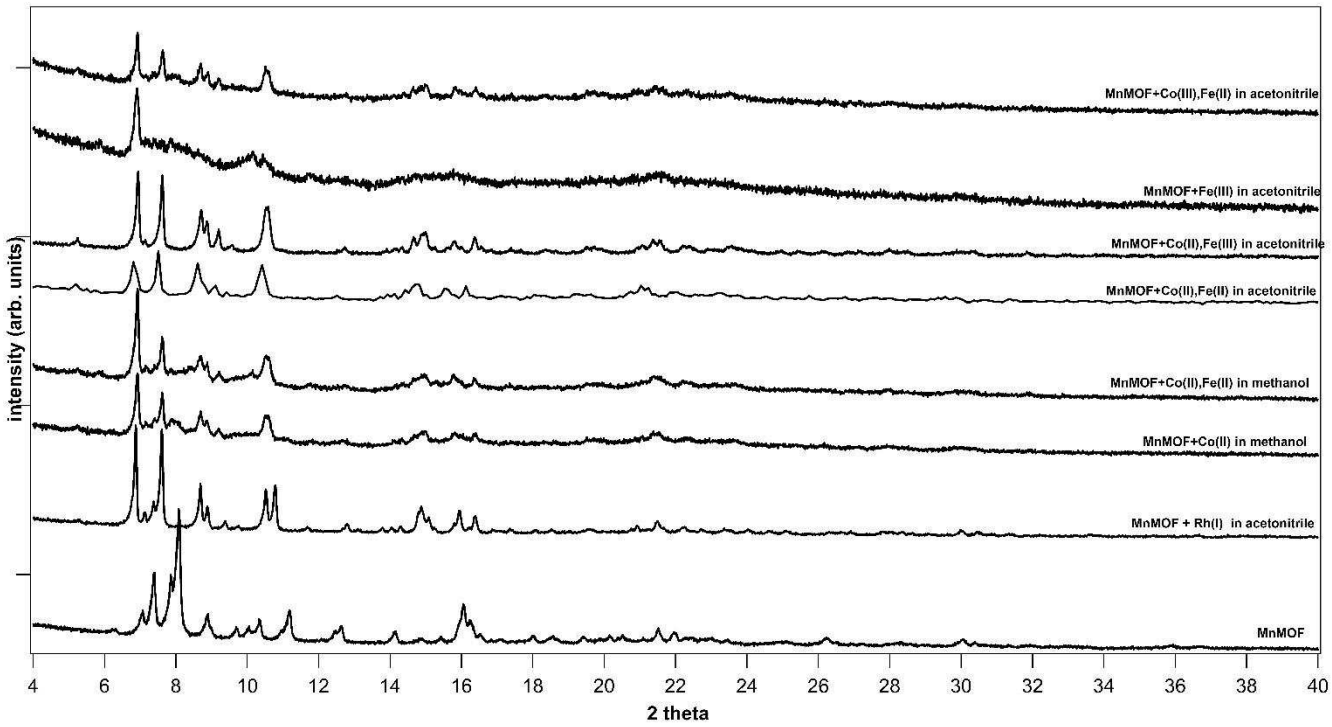

Figure 7: P-XRD patterns of various PSM MnMOF samples.

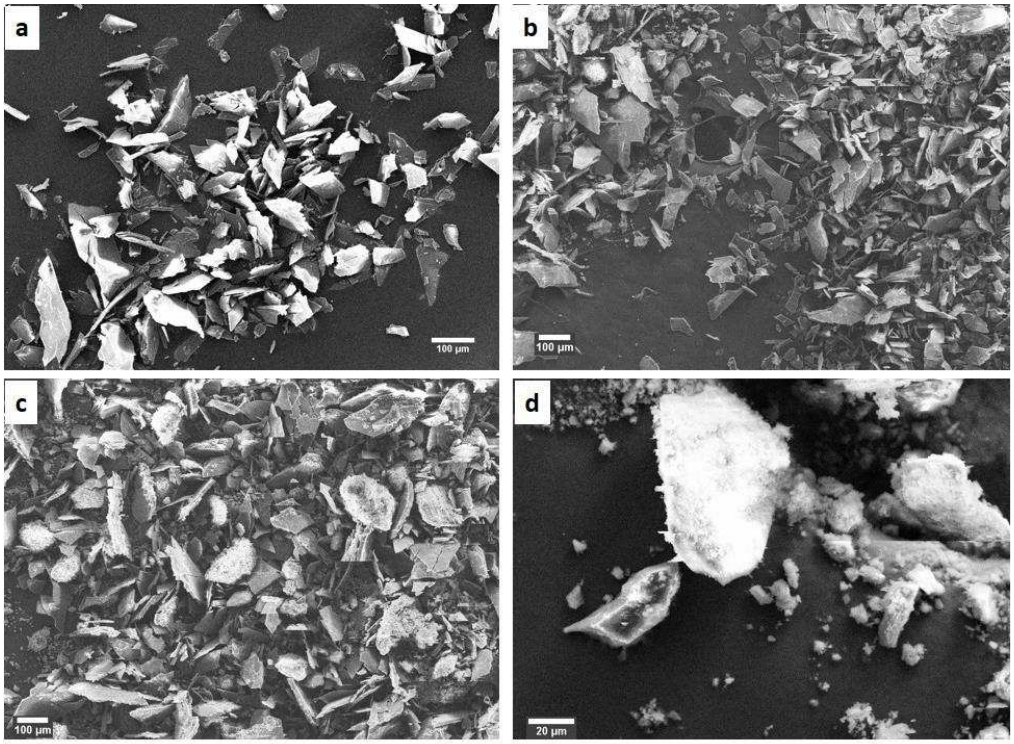

Figure 8: SEM micrographs of a) MnMOF (a), Co(II)/MnMOF (b, solvent:methanol), CoFe/MnMOF (c, molar ratio Co(II):Fe(II)=2:1, solvent:acetonitrile) and Fe(III)/MnMOF (d, solvent:acetonitrile).

After this screening of possible PSM processes, we decided to focus our attention on the PSM of MnMOF with Rh(I). In fact, Rh is one of the most investigated catalyst for hydroformylation reaction. Keeping in mind that this reaction could be exploited in a tandem reaction scheme (with the in situ production of syngas), we wanted to verify if the Rh(I) sites in the MOF structure are catalytically active for this reaction. Prior to test the catalytic activity of the Rh/MnMOF, we have performed a deeper characterization of this material by means of BET analysis, XRD, EDX and Raman Spectroscopy.

The 77 K N_2 adsorption-desorption isotherms of MnMOF and of Rh/MnMOF are reported in Figure 9. MnMOF isotherm profile shows a step between P/P_o of 0.005–0.06 (P and Po are the measured and saturation pressure of nitrogen, respectively). As expected, this low-pressure step is consistent with a degree of structural flexibility of MnMOF. The flexibility was associated with the rotation of the pyrazole moieties and concomitant pore enlargement. [3] A total N_2 uptake of 180 $cm^3\ g^{-1}$ (STP) was observed and the BET analysis of the data yielded a surface area of 480 m^2g^{-1}. The post-synthetic metalated Rh/MnMOF adsorption-desorption isotherm (Figure 10) afforded a Type 1 profile and a BET surface area of 640 m^2g^{-1}. Therefore, the overall porosity of the structure is maintained. Further, we note that the low-pressure step of the isotherm observed for MnMOF disappears, since when the Rh(I) species are coordinated by di-pyrazole chelating units the structural flexibility of the framework is lost.

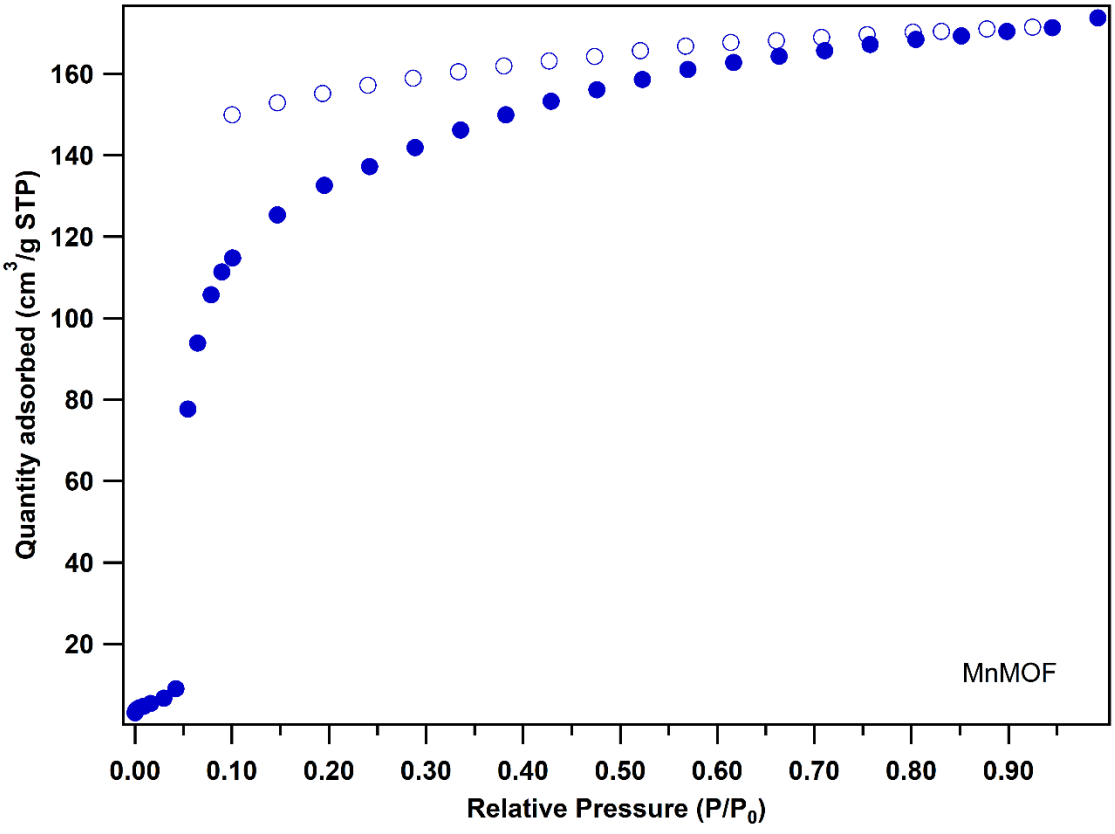

Figure 9: N_2 77K isotherms of MnMOF.

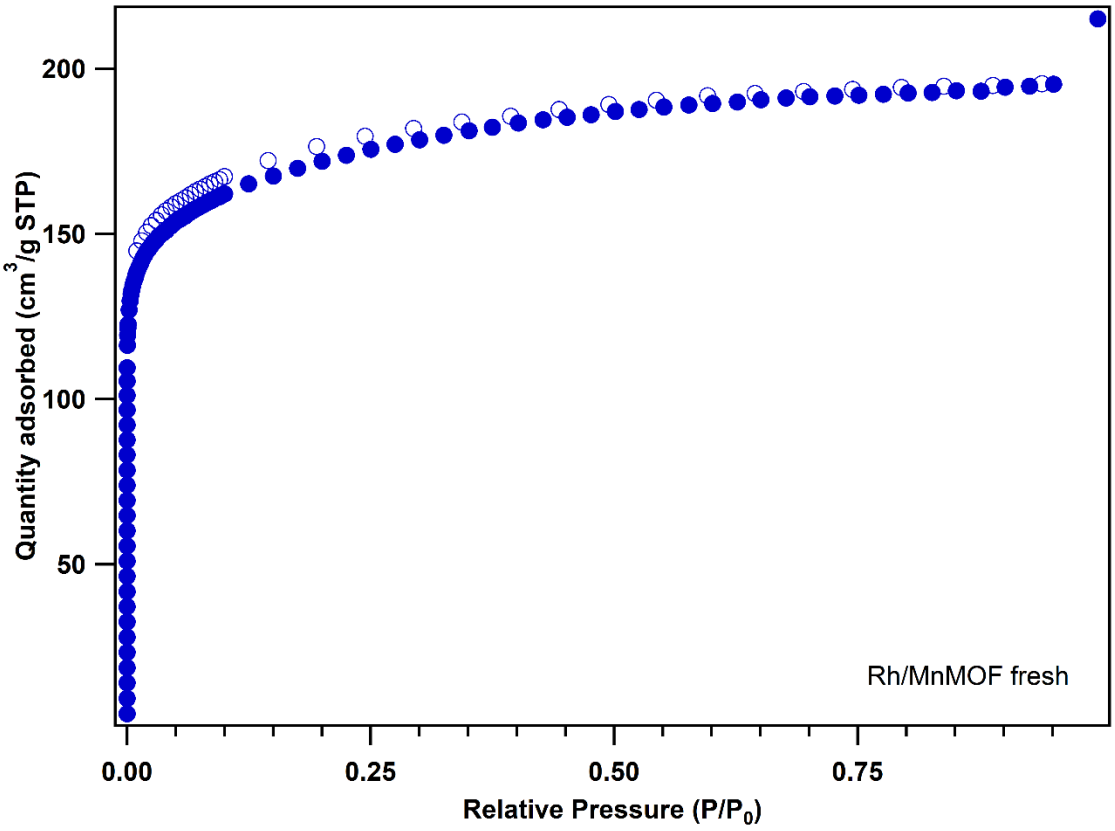

Figure 10: N_2 77K isotherms of Rh/MnMOF (fresh catalyst)

The structural integrity of MnMOF after metalation was also investigated by Raman Spectroscopy results. Figure 14 shows the Raman spectra of MnMOF and of Rh/MnMOF. These data are in line with the XRD and adsorption-desorption isotherms results and confirmed that there was no formation of Mn or Rh oxide clusters in the material. Compared to bare MnMOF, Rh/MOF Raman spectra showed only small differences in band relative intensities. However, the major differences can be used as fingerprint to confirm the successful metalation of the MnMOF. In fact, in the region 1100-1200 cm^{-1} are measurable the ring vibrations associated to pyrazoles moieties. As consequence of Rh(I) coordination by di-pyrazole moieties, we can observe that the two well separated peaks at 1140 and 1155 cm^{-1} of bare MnMOF are merged in a unique peak centered at 1145 cm^{-1} in Rh/MnMOF. Our hypothesis is that the two separate peaks of bare MnMOF arise from the presence of both Mn-coordinated and free di-pyrazole moieties in bare MnMOF. Conversely, in the case of metalated MnMOF, all the di-pyrazole are coordinating a metal and this caused the disapperaing of the clear separation between the two peaks. We encountered this particular feature also in the analysis of other metalated MnMOF (i.e. Co(II)), therefore we can conclude that this is a fingerprint of the metalation in this kind of material. Moreover, in the case of Rh/MnMOF, Raman spectroscopy is very useful in order to identify the chemical environment of the Rh. In fact, in the ranges 1950-2150 and 2230-2350 cm^{-1} we measured the typycal features of carbonyl gropus. This confirmed that we have coordinated Rh(I) species in the nanoreactor, because the oxidation of Rh to Rh(III) must lead to the loss of the carbonyl groups coordinated to the metal (as previoosly demonstrated by Bloch. et al)[3].

These results, combined with P-XRD data and EDX data, confirmed the design of the nanoreactor was successful. In fact, we quantitatively inserted in the MnMOF micropores the Rh sites that we plan to exploit for the catalysis of hydroformylation reaction. We then turned our efforts to assessing the potential of Rh/MnMOF to catalyse

the hydroformylation of styrene; an aromatic olefin that is a widely studied model substrate for functionalized olefins.

Catalytic tests

Hydroformylation experiments were carried out by the group of Prof. Paganelli at the University of Venice. The reactor was a 150 ml stainless steel autoclave and in order to avoid the catalyst deterioration due to the friction effect of stirring, we used a modified glass vial as shown in Fig. 11.

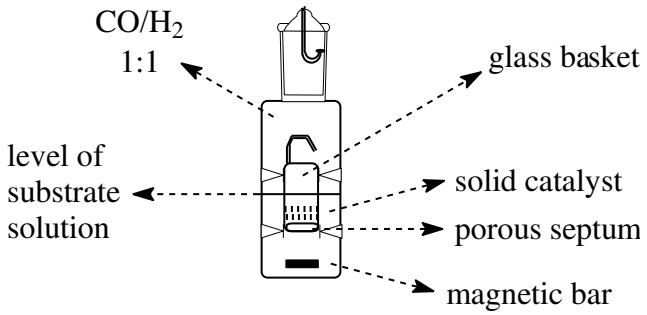

Figure 11: schematic view of the reactor employed for hydroformylation experiments.

The glass device consists of a vial modified to be able to hold a glass basket having a porous septum as the bottom (porous size = 40-90 μm); the catalyst is positioned in the basket, which is partially immersed in the substrate solution, whereas the magnetic stirring bar is on the bottom of the vial. This method allows to have an efficient stirring without any mechanical stress of the catalyst. The recycle of the catalyst, at the end of the reaction, can be easily performed by transferring the glass basket in a vial containing a fresh substrate solution.

Hydroformylation of styrene

The reactions were carried out using a stainless steel autoclave equipped with the glass device depicted above. In a typical run, the basket containing the catalytic complex was introduced, under a nitrogen purge, in the glass vessel containing styrene in anhydrous toluene. The vessel was transferred into a 150 ml stainless steel reactor which was pressurized with syngas at 4-8 MPa and heated at 50-80°C for 18h (see Table 2). After cooling at room temperature, the residual gases were released and the reaction products were analysed by GC and GC-MS. The basket containing the catalyst was removed from the glass vial and the catalyst washed several times with anhydrous toluene, dried under vacuum and reused in recycle experiments.

Catalytic tests results

The catalytic activity of Rh/MOF was tested in the hydroformylation of styrene (**I**) as this aromatic olefin is a widespread studied model substrate for functionalized olefins [A]. A first oxo-experiment was carried out at 8 MPa of syngas (CO/H_2 = 1) and 50°C for 18h with a substrate to rhodium catalyst molar ratio = 1000: the substrate conversion was practically negligible (6%), with the almost exclusive formation of the branched aldehyde **II** (Exp.1, Table 2). By increasing the reaction temperature at 80°C, the catalytic system was very active showing complete substrate conversion and total chemoselectivity. The regioselectivity towards the branched aldehyde **II**, even if lower than that exerted by homogeneous modified rhodium carbonyl complexes, was quite good (80%) (Exp. 2, Table 2). The recovered solid catalyst was furtherly reused in three consecutive experiments: the catalytic activity remained high in the first and second recycle reaction (95% and 81% conversion, respectively) but it

strongly decreased when reused in a third experiment (62%) (Exp. 3-5, Table 2). Given that the MOF largely maintains its structural integrity subsequent to catalysis (see next paragraph) the observed decrease in activity is likely due to the small rhodium content in the catalytic system which can be partially deactivated by impurities such as trasce amounts of oxygen present in the reaction medium and/or by a small degree of leaching. Despite the organic phase, after every experiment, appeared practically colourless, we evaluated a possible leaching phenomenon; so, the organic phase recovered after the first reaction, was used as catalyst for the homogeneous hydrogenation of undec-1-ene in toluene: after 18 h at 80°C and 8 MPa of hydrogen, undecane was formed in negligible amount (4%) so excluding a relevant rhodium leaching. In all the experiments, neither ethylbenzene nor alcohols were detected in the reaction mixtures and both chemo- and regioselectivity remained practically unchanged. An attempt to reduce the syngas pressure to 4 MPa gave a rather disappointing result: after 18h at 80°C the substrate conversion was only 60% and in two consecutive recycle experiments the catalytic activity dramatically decreased affording 18% and 11% conversion, respectively (Exp. 6-8, Table 2); moreover, the regioselectivity towards the branched aldehyde **II**, the main reaction product, was lower than that observed at 8 MPa. A plausible explanation of this result, on the basis of the generally accepted mechanism of the rhodium-catalyzed hydroformylation, could be that at 4 MPa of syngas the migratory insertion on a CO bound to the rhodium atom to form the branched acylrhodium specie is slower than that at 8 MPa and, as a consequence, it undergoes a β-hydride elimination giving the linear Rh-alkyl specie that subsequently affords the corresponding linear aldehyde. Very recently, deuteroformylation studies on styrene at 40 and 80 psia CO, in the presence of the homogeneous catalyst Rhodium bis(diazaphospholane) (BDP), demonstrated that deuterium scrambling, hence Rh-alkyl isomerization, is inhibited by increased CO pressure and decreased temperatures. In particular, the reactions at higher temperature (313 K) and low CO pressure (20 psia) allowed for greater isomerization of the catalyst to the thermodynamically favored linear acyl intermediate while at higher CO pressures (115 or 200 psia), the isomerization was slowed so favoring the branched pathway. Moreover, isomerization by reversion of the acyl complex to the alkyl one is slower at high pressure because such reversion requires CO dissociation.[41]

Table 2: Hydroformylation of styrene (I) catalyzed by MOF

Exp.	T (°C)	P (MPa) (CO/H_2 =1)	Conv. (%)[a]	b-Aldehyde (**II**) (%)	n-Aldehyde (**III**) (%)
1	50	8	6	5.5	0.5
2	80	8	100	80	20
3[b]	80	8	95	76	19
4[b]	80	8	81	65	16
5[b]	80	8	62	50	12
6	80	4	60	43	17
7[b]	80	4	18	13	5.0
8[b]	80	4	11	8	3

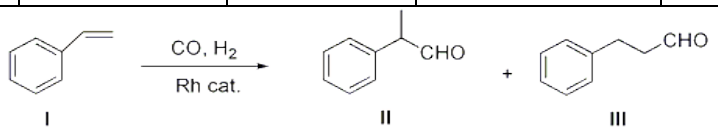

Reaction conditions: styrene (500 mg = 4.81 mmol); cat. = 4.46 mg; styrene/Rh (molar ratio) = 1000/1; solvent (toluene) = 1 ml; t = 18h.

[a] Determined by GC. [b] Reaction carried out by using the catalyst recovered from the previous experiment

Noteworthy, when the catalyst recovered from the second recycle experiment at 4 MPa of syngas was reused in the styrene hydroformylation at the same reaction conditions but under a pressure of 8 MPa (experiment not reported in Table 2), not only the substrate conversion was increased up to 75% but the regioselectivity was the same observed in the previous experiments carried out at 8 MPa of syngas.

Characterization of used catalyst

After the catalytic tests, Rh/MOF was recovered and characterized. From SEM/EDX analysis, we verified that the morphology of MOF crystals and the ratio Mn/Rh were unchanged.

XRD patterns confirmed that the catalyst maintained it crystallinity. Moreover, after catalytic tests, the adsorption-desorption isotherms of Rh/MOF still showed a Type 1 profile and a BET surface area of 444 m^2g^{-1}. Therefore, the microporosity of the catalyst is maintained after the catalytic test, but BET surface area seems to be lower than the one of the fresh catalyst (640 m^2g^{-1}). This loss of surface area could be associated with the loss of activity of the catalyst after repeated catalytic tests. However, considering that the XRD pattern of used catalyst was almost identical to the one of the fresh catalyst, this loss cannot be associated to a loss of crystallinity of the structure. One possibility is that the loss of surface area is related to the obstruction of some micropores with some reaction products.

The structural integrity of Rh/MOF after catalytic tests is also supported by Raman Spectroscopy results. Compared to the fresh Rh/MOF, Raman spectra of used catalyst is almost identical (Figure 14). These data are in line with the XRD and adsorption-desorption isotherms results and confirmed that there was no formation of Mn or Rh oxide clusters in the material after the catalytic tests. However, in the ranges 1950-2150 and 2230-2350 cm^{-1} was not detected the typycal features of carbonyl gropus, suggesting that the chemical environment of Rh in the used catalyst is changed with the respect to of the starting material.

At the time of writing, we are investigating the catalytic properties of another PSM MnMOF: Co(II)/MnMOF. Moreover, we are synthesizing the ester of the LH_2 molecule. Once obtain the ester, we will coordinate it with Rh(I) and Co(II) in order to obtain the same catalytic sites present in the MnMOF, but not constrained in the micropores. In this way, we will compare the catalytic activity of the various materials and we will study the effects of metal nature (Rh or Co) and we will investigate if there is a “confined space” effect on selectivity due to the micropores (i.e. branched vs linear reaction products).

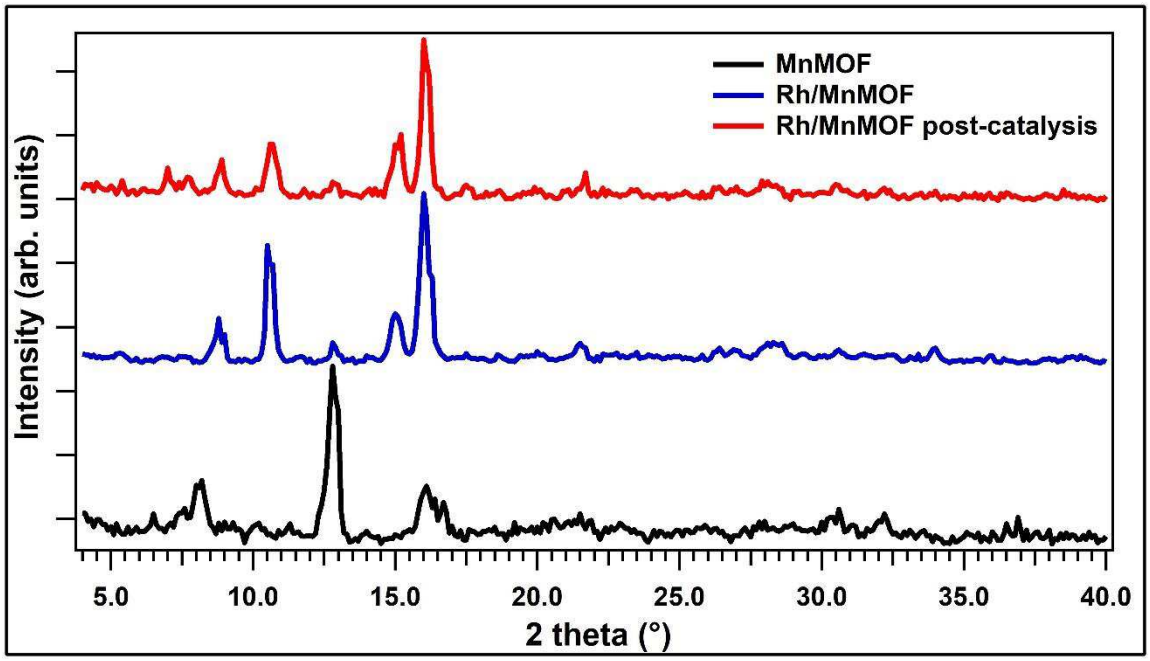

Figure 12: WAXRD of MnMOF and of Rh/MnMOF (pre/post catalysis)

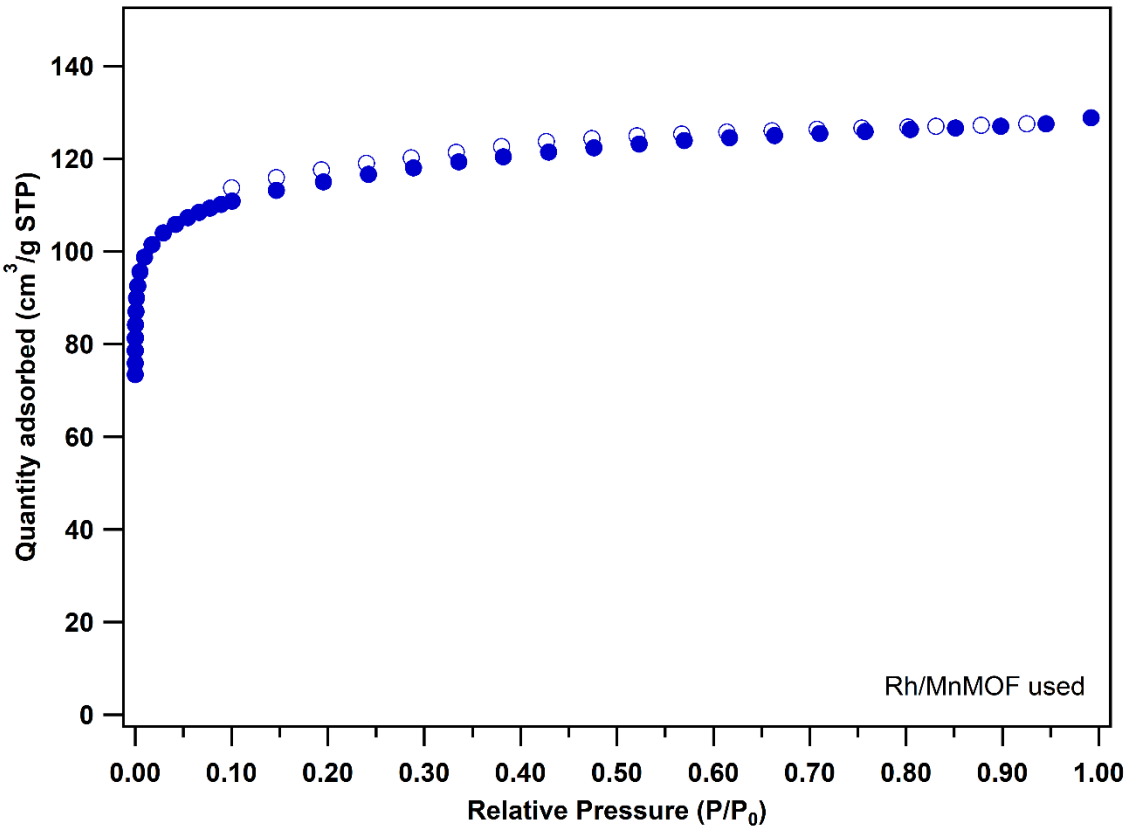

Figure 13: N_2 77K isotherms of Rh/MnMOF-used

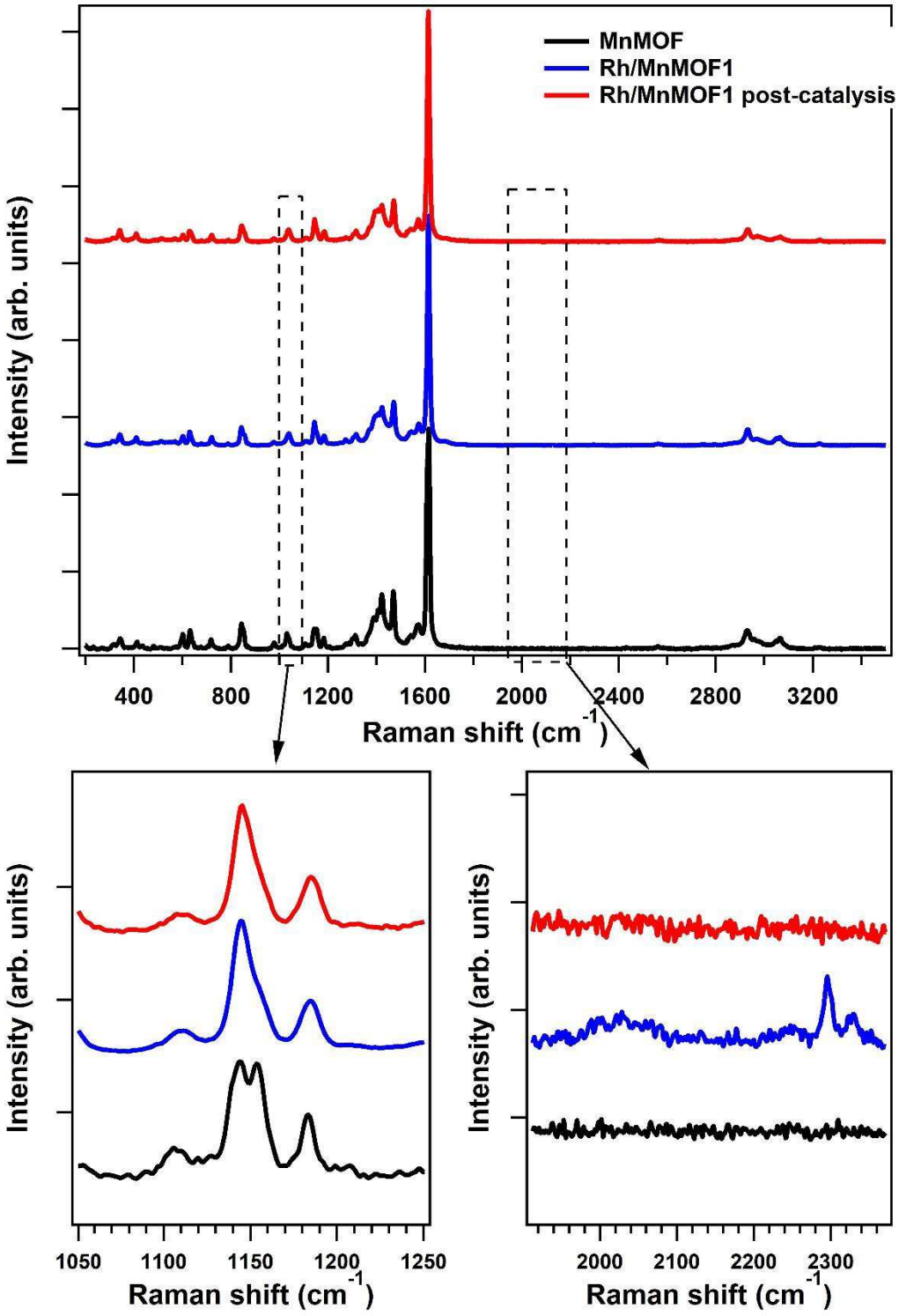

Figure 14: Raman spectra of MnMOF and of Rh/MnMOF (pre/post catalysis)

4.4 Layer by layer growth of MnMOF for the design of nanostructured core@shell materials

The goal of this study is to combine MOFs with metal/oxide systems for the design of nanostructured tandem catalysts with core@shell morphology. At the heart of this project there is the knowledge acquired by the studies on Pd/CeO_2 catalyst (previous chapter) and on MnMOF (see previous paragraphs). The core@shell morphology will be obtained growing thin films of MOFs around metal or metal oxide nanoparticles. In this kind of multifunctional catalytic material composed by two entities (i.e. the metal/oxide active interface and a MOF shell bearing a specific catalytic center) one of the reactants (A->B) is produced *in situ* (reaction "1") and exploited to carry out a second reaction (reaction "2" B+C->D), which is catalyzed by the other moiety of the same material. The layer-by-layer approach permits a fine control on the MOF thickness. We will exploit this fine control in order to investigate the effect of the MOF shell thickness on the synergic catalytic activity. The materials were characterized by means of TEM, Raman Spectroscopy, XPS, EDS, XRD and BET.

Precisely, in this study the target material is a tandem catalyst for ethylene hydroformylation. In this tandem approach, hydroformylation should carried out exploiting the *in situ* produced syngas, which is obtained by methanol decomposition. Tandem catalysis of ethylene hydroformylation was firstly experimentally demonstrated by Yamada et alii.[6] These authors studied a tandem catalyst based on multiple metal–metal oxide interfaces. The catalyst was synthesized by assembling platinum and cerium oxide nanocube monolayers of less than 10 nm on a silica substrate. The two distinct metal–metal oxide interfaces, CeO_2–Pt and Pt–SiO_2, were used to catalyze two distinct sequential reactions. The CeO_2–Pt interface catalyzed methanol decomposition to produce CO and H_2, which were subsequently used for ethylene hydroformylation catalysed by the nearby Pt–SiO_2 interface. Consequently, propanal was produced selectively from methanol and ethylene on the nanocrystal bilayer tandem catalyst (Figure 15). In our study, the core of the catalyst will be designed in order to be active for selective methanol decomposition to CO and H_2, while the shell will be designed to be active for hydroformylation reactions. The porosity of the MOF shell is one of the key-point of the design of the target material. In fact, through the pores should be possible to feed the reactants to the core of the particle. Moreover, *in situ* produced molecules will be forced to go through the MOF shell and should be able to react with the active present therein.

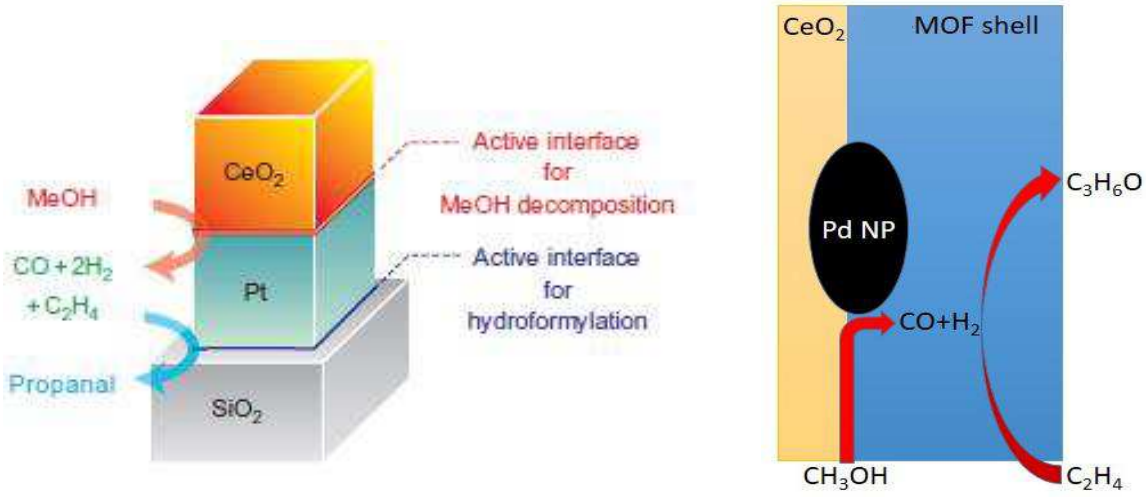

Figure 15: Illustration of the CeO_2–Pt–SiO_2 tandem catalyst (left, adapted with permission from Yamada Y. et al , Nature Chemistry, 3, 372–376 (2011) Copyright © 2011, Springer Nature) and schematic view that highlight the active sites of our core(Pd/CeO_2)@shell(MOF) tandem catalyst.

The study of such a complex material is divided in three steps. Firstly, we have separately investigated the catalytic properties of the materials that will composed the core and the shell of our target tandem catalyst. Later, we have investigated the synthesis of the whole core@shell catalyst. The last step will be the study of the tandem catalytic activity of the core@shell material. At the time of writing, we have only started the characterization of the catalytic activity of the core@shell material, therefore in this thesis we will not present these data.

The core of the target material will be composed by Pd NPs supported over CeO_2 nanocubes. The synthesis and characterization of this material was discussed in the previous chapter. As already discussed, this system has a good catalytic activity toward selective methanol decomposition to CO and H_2. Obviously, this is mandatory if we wanted to produce in situ CO and H_2 at the core of the tandem catalyst. Moreover, the regular morphology of CeO_2 nanocubes (exposing (100) facets) should be an advantage for homogeneous growth of MOFs thin films. Another key-point is the working temperature of the core for the methanol decomposition. In the case of Pd/CeO_2 NCs, the temperature for the quantitative conversion of methanol was relatively (below 250°C). In fact, in a composite material including MnMOF, the maximum operation temperature is mainly limited by the thermal stability of the MOF. Considering that in the literature the decomposition temperature of metalated MnMOF was about 360°C (TGA in inert atmosphere)[3], we must design a core that could operate well below this temperature.

The shell of the target material will be composed by a thin film of MnMOF grown following a layer-by-layer approach. The structure and catalytic properties of this MOF were discussed in the previous paragraphs. The MnMOF is endowed with vacant di-pyrazole units that can be metalated. Therefore, through post-synthetic metalation processes, we can introduce different active sites in the pores of the MOF shell. In this particular case, we plan to introduce Rh sites in the MOF pores because Rh-based catalysts are known to be active for hydroformylation reactions. However, the growth of thin films of MnMOF are not yet reported in the literature, so in the first part of this study we optimized the synthesis parameters of MnMOF around CeO_2 nanocubes (i.e. SBUs precursors, synthesis temperature, solvents). We investigated also an alternative route to synthesize thin films of MnMOF, employing solvothermal synthesis and CeO_2 nanocubes as nucleation centers.[42] However, with these syntheses we could not obtain a fine control of the morphology of the final material (i.e. aggregation of NCs, uncontrolled MOF nucleation).

4.4.1 Experimental section

Materials synthesis

Synthesis of Pd/CeO_2 NCs: the synthesis of CeO_2 nanocubes and the deposition of Pd NPs were described in detail in the previous chapter. Briefly, CeO_2 NCs were synthesized by hydrothermal synthesis, starting from cerium nitrate and NaOH. Pd NPs were deposited over CeO_2 NCs bubbling hydrogen through a solution containing H_2PdCl_4 and ceria powder.

Layer-by-layer synthesis of MnMOF on CeO_2 NCs: Firstly, we dispersed 1 g of CeO_2 NCs in 100 ml a solution of LH_2 in DMF (0.1 mg/ml). The suspension was left under stirring overnight at 50°C. Then, CeO_2 LH_2-functionalized NCs were recovered by repeated cycles of washing and centrifugation (5x DMF, 3x EtOH). In order to start with the layer by layer cycles, we prepared two starting solutions of LH_2 in DMF (1 mg/ml) and of $Mn(OAc)_2{\cdot}4(H_2O)$ in ethanol (1 mg/ml). These solutions were kept at 60°C during the synthesis. The MOF thin film was grown on the surface of CeO_2 by dispersing 250 mg of CeO_2 LH_2-functionalized NCs alternatively in 15 ml of EtOH and 250 µl of $Mn(OAc)_2{\cdot}4(H_2O)$ starting solution or in 15 ml of DMF and 250 µl of LH_2 starting solution. During each cycle, the dispersions were kept at 60°C under vigorous stirring for 15 minutes. After each step, 3 cycles of washing (2 with the solvent in use, one with the solvent that will be used in the next step) were performed in order to remove the unreacted precursors and avoid the uncontrolled nucleation of MOF crystals. The schematic view of this process is reported in Figure 16.

Solvothermal syntheses of MnMOF over CeO_2 NCs: 10 mg of CeO_2 LH_2-functionalized NCs were dispersed in 6 ml of DMF/H_20 (2:1, v/v) solution containing different amount of LH_2 and MnC_{l2} $4H_2O$ and left in pre-heated oven at 100°C for different times (1-24 hours). Alternatively, the dispersion was left under stirring at 100°C for different times.

Characterization techniques

The nano- and microscale morphology of materials was studied by scanning electron microscopy (SEM) and by conventional and high-resolution transmission electron microscopy (TEM and HR-TEM). SEM images were acquired using a field emission source equipped with a GEMINI column (Zeiss Supra VP35), micrographs were obtained with an acceleration voltage of 5 or 10 kV using in-lens high-resolution detection. STEM micrographs were acquired with the same instrument (30 kV). TEM images were acquired using a FEI Tecnai 12 microscope with an acceleration voltage of 100 kV. HRTEM micrographs were acquired using a JEM- 2100F Field Emission Electron Microscope operating at 200 kV. Energy dispersive X-ray spectroscopy (EDS) elemental maps were acquired with the same instrument. Grazing incidence X-ray diffraction (GIXRD) patterns were collected using a Philips PW 1710 diffractometer equipped with a Cu Kα radiation tube operating at 40 kV and 40 mA and with an incidence angle of 1°. Characterization by Raman spectroscopy was performed using a ThermoFisher DXR Raman microscope. The spectra were recorded using a laser with an excitation wavelength of 532 nm (1 mW), focused on the sample with a 10× objective (Olympus). Gas adsorption isotherm measurements were performed on an ASAP 2020 Surface Area and Pore Size Analyzer. Activation of samples was carried out by heating the sample at 120°C for 12 hours in vacuum. UHP grade (99.999%) N_2 were used for all measurements. The temperatures were maintained at 77 K (liquid nitrogen bath).

4.4.2 Results and discussion

As previously mentioned, to tackle the challenging synthesis of the designed core@shell material we started from the study of the LbL synthesis of MnMOF on CeO_2 nanocubes. We obtained the most encouraging results following the recipe described in the experimental section described above. Briefly, we firstly functionalized NCs with the ligand of the MnMOF. Then, we exposed alternatively to an ethanol solution of $Mn(OAc)_2{\cdot}4(H_2O)$ and to a DMF solution of LH_2, the LH_2-functionalized NC powder. One LbL cycles is considered as the exposure of NC powders first to SBUs precursor and then to LH_2, carefully washing the product between each step in order to remove the unreacted precursors of MnMOF. Hereafter, we will name the obtained material as Nx(MnMOF/NCs), where N is the number of LbL cycles.

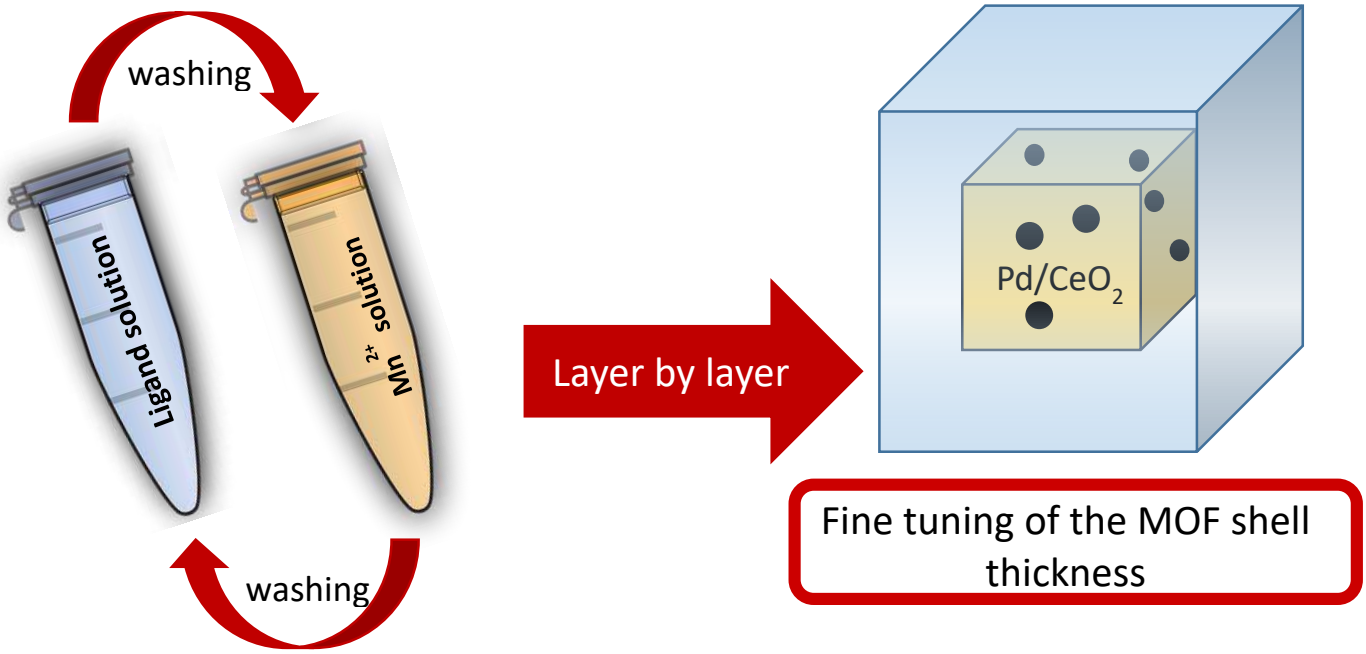

Figure 16: schematic view of the LbL synthesis of core@shell material

The morphology, structure and chemical composition of LBL grown nanocomposites were investigated by different characterization techniques and several important features can be distinguished. STEM micrographs of 15x(MnMOF/NCs) showed the typical morphology of a core@shell material (Figure 17). The NCs of ceria are easily identifiable. Around ceria particles, we can observe a lighter shell (about 15 nm) that uniformly surrounds the cubes. EDX analysis on this sample confirmed the presence of Mn, C, N, O and Ce, as expected.

The formation of the MnMOF shell is supported by Raman Spectroscopy results. Figure 18 shows the Raman spectra of 5x, 10x and 15x MnMOF@NCs samples. These data confirmed that there was no formation of bare Mn oxide clusters in the materials. In order to have a qualitative analysis of the amount of MnMOF compared to ceria, we have normalized the Raman spectra with respect to the intensity of the F_{2g} peak (460 cm^{-1}) of CeO_2. Notably, we can observe the increase of the main MOF peak (1615 cm^{-1}) with increasing LbL cycles. Compared to bare MnMOF, the MnMOF@NCs Raman spectra show only small differences in band intensity (Figure 19).

However, the main characterization techniques employed for the analysis of MOFs are XRD and BET analysis, since they allow determining the presence of a crystal order and regular microporosity. In the case of a thin shell of MOF, both analyses are very challenging because of the low amount (maximum thickness in our samples: 15 nm) of investigable material.

In fact, we were not able to measure any XRD pattern attributable to MnMOF in the case of 5x, 10x and 15x MnMOF/NCs samples. The unique measured peaks were those of ceria XRD pattern. We tried to measure GI-XRD in order to improve the surface sensitivity of the analysis, but even this attempt was unsuccessful. Despite the good results obtained from STEM, Raman Spectroscopy and EDX, XRD data seem to indicate that the obtained shells are amorphous.

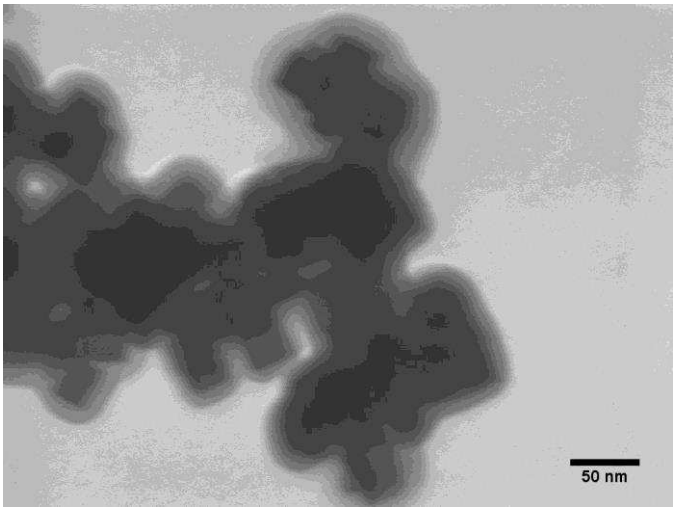

Figure 17: STEM (30 kV) micrograph of 15xMnMOF/NCs sample.

Therefore, in order to increase the crystallinity of the shell, we tried to perform a post-synthetic crystallization (PSC) step on the various materials. The powders were dispersed in DMF and left in oven at 100°C overnight. After washing with fresh DMF, we characterized the PSC 5x, 10x and 15x MnMOF/NCs samples.

Raman spectra still show the characteristic features of MnMOF, but comparing to the normalized spectra of the samples pre and post crystallization step we can observe a reduction of the intensity of the MOF peaks (Figure 19). This is not unexpected, since a crystallization of the shell could lead to a loss of part of the amorphous material. The morphology of PSC samples was investigated by HR-TEM. HR-TEM micrographs of PSC 5x and 15x MnMOF/NCs samples are reported in figure X. HR-TEM micrographs showed the typical core@shell structure, for which CeO_2 NC cores of ~30 nm in diameter are coated by a uniform shell of about 2 nm in the case of the 5 cycles sample and of about 10 nm in the case of the 15 cycles (Figure 20). These results are in line with Raman data. Comparing the micrographs of PSC 15x sample with the STEM micrographs of the amorphous 15x sample, we can observe that the shell thickness seems to be slightly reduced. This loss of material is therefore compatible with the loss of the intensity of MOF peaks in Raman spectrum. EDX elemental mapping were performed on the PSC 15xMnMOF/NCs sample. EDX confirmed the presence of C, N, O, Mn and Ce. Moreover, from the elemental map (Figure 21) we can observe how the MnMOF components are uniformly distributed over the ceria NCs, forming a uniform shell around them.

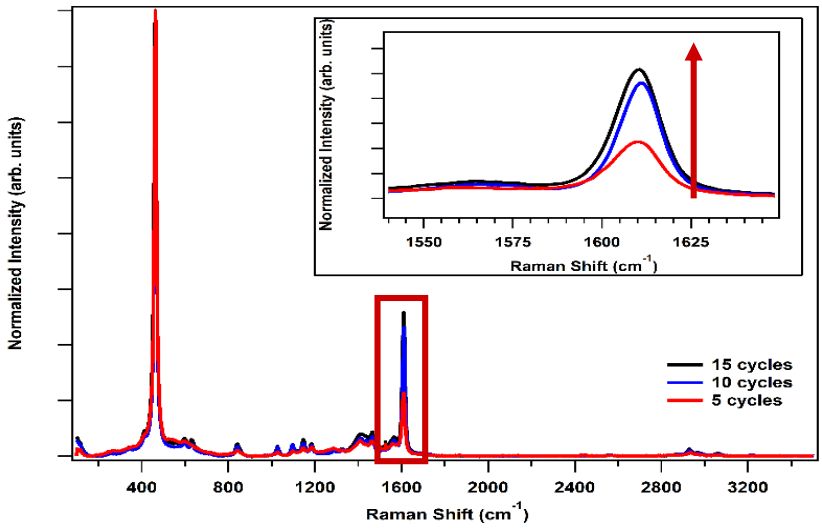

Figure 18: Raman spectra of LbL synthesized core@shell material. In this graph are reported the spectra for the samples synthesized with 5, 10 and 15 cycles of LbL growth.

Finally, we performed crystal structure analysis from GIXRD pattern of PSC 15xMnMOF/NCs sample (Figure 22). This analysis reveals two sets of peaks, which are ascribed to face-centered cubic phase of CeO_2 and to a second crystalline phase characterized by a large unit cell. The peaks of this second crystal phase could be assigned to some peaks of the XRD pattern of the bulk MnMOF (i.e. (120), (220) (014)). Notably, the main peak (2θ=8.1°) corresponds to the main peak of the P-XRD pattern of MnMOF and corresponds to the (110) peak.

From the analysis of this pattern, and considering the results just discussed, we can deduce two hypotheses: either we have grown a highly oriented shell of MnMOF or we have synthesized a different kind of crystalline structure based on the same ligand and SBUs precursor of MnMOF. However, the correspondence between the most intense peak of the diffraction pattern of bare MnMOF and of the composite material (excluding the ceria pattern) reinforces the first hypothesis. Considering the lattice parameters of ceria (a=b=c= 5.42 Å; α=β=γ=90°) and of MnMOF (a=12.289 Å, b=32.302 Å, c=25.974 Å; α=γ=90°, β=93.57°) we calculated the lattice mismatch in order to evaluate the possibility of the epitaxial growth of MnMOF over (100) surface of ceria. Among the simplest possible epitaxial relationships, the smallest lattice mismatch resulted of the type MnMOF(100)[010]//CeO_2(100)[001], which implies along the b direction a -0.7% strain considering 6 ceria units cells and along the c axis a -4.1% strain considering 5 ceria unit cells. In this case the angle between b and c is 90°, like in the substrate lattice. From these calculations, if the MnMOF grew epitaxially, the growth along the [100] direction should be favored. Many other epitaxial relationships can be envisaged as well, but in general they would require a higher strain, for example the MnMOF(001)[100// CeO_2(100)[011] would require a strain up to 6% in one direction. An exact determination of the crystallographic orientation is extremely challenging and would necessitate the use of advanced tools such as cryo-TEM. Moreover, it cannot be excluded that during the hydrothermal crystallization step of the synthesis the ceria surface act merely like a grapho-epitaxial support offering only a support directing the texture but not interfacial crystallographic order.

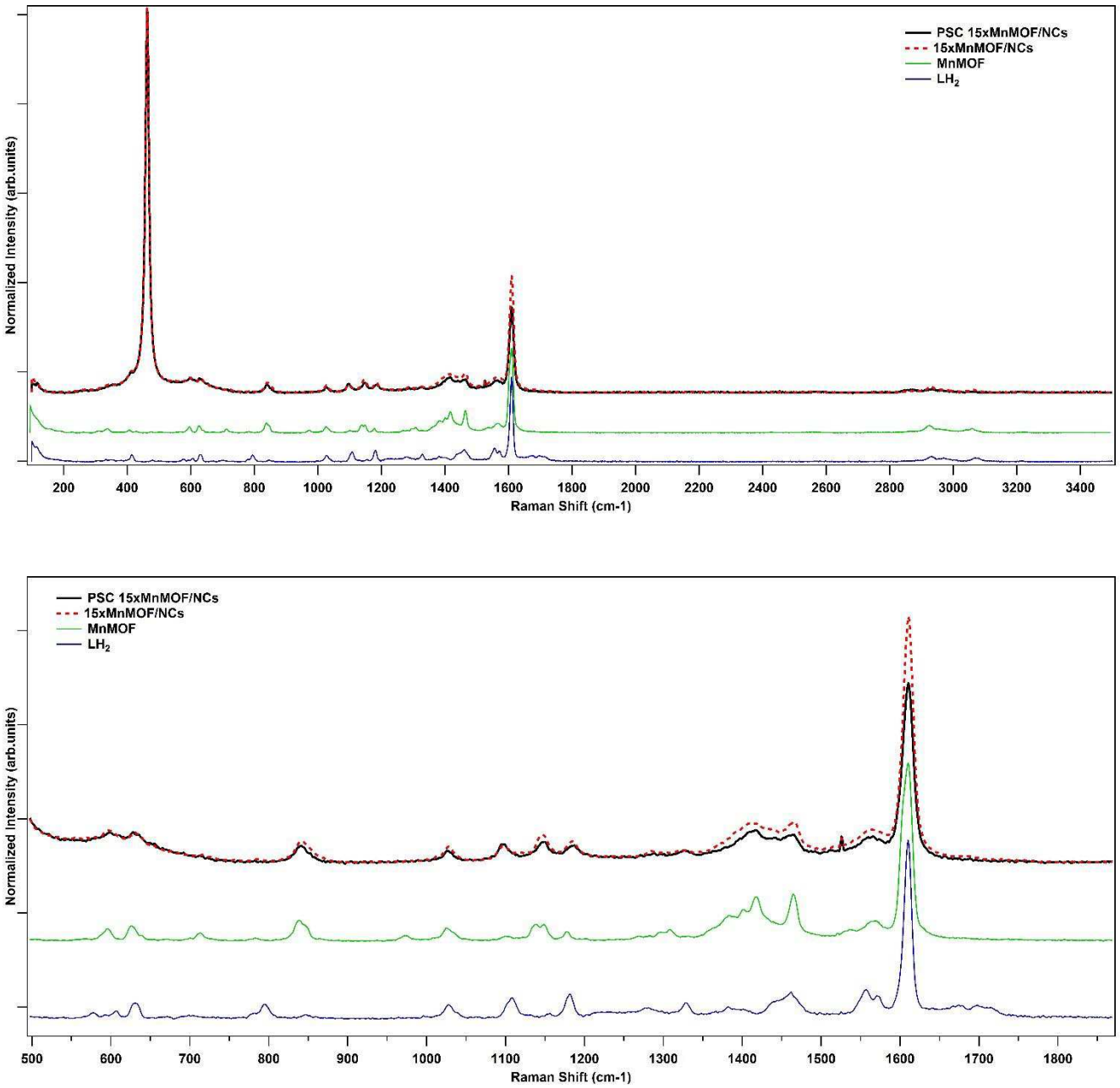

Figure 19: Raman spectra (up: full range; down: enlargement of 500-1900 cm^{-1} range) of LbL synthesized core@shell materials (PSC 15xMnMOF/NCs sample and 15xMnMOF/NCs sample), of bulk MnMOF and of LH_2.

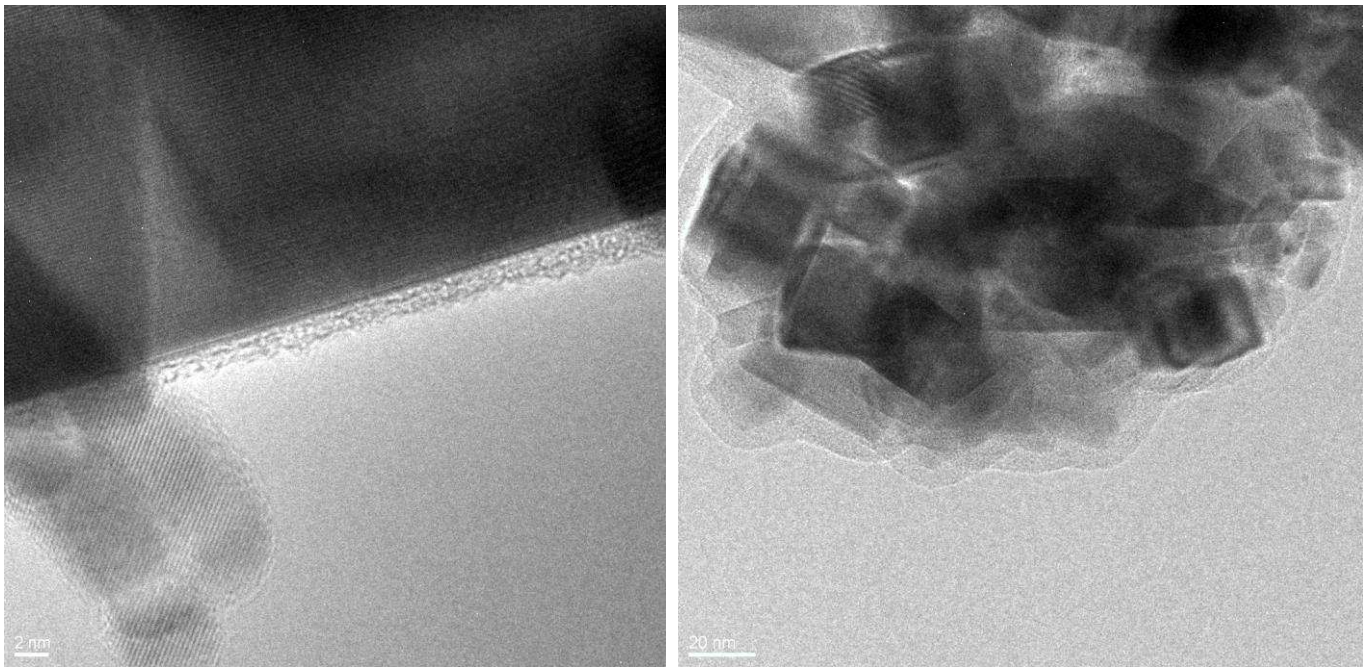

Figure 20: HR-TEM micrographs of post-synthetic crystallized core@shell materials synthesized through 5 (left) and 15 (right) cycles of LbL growth.

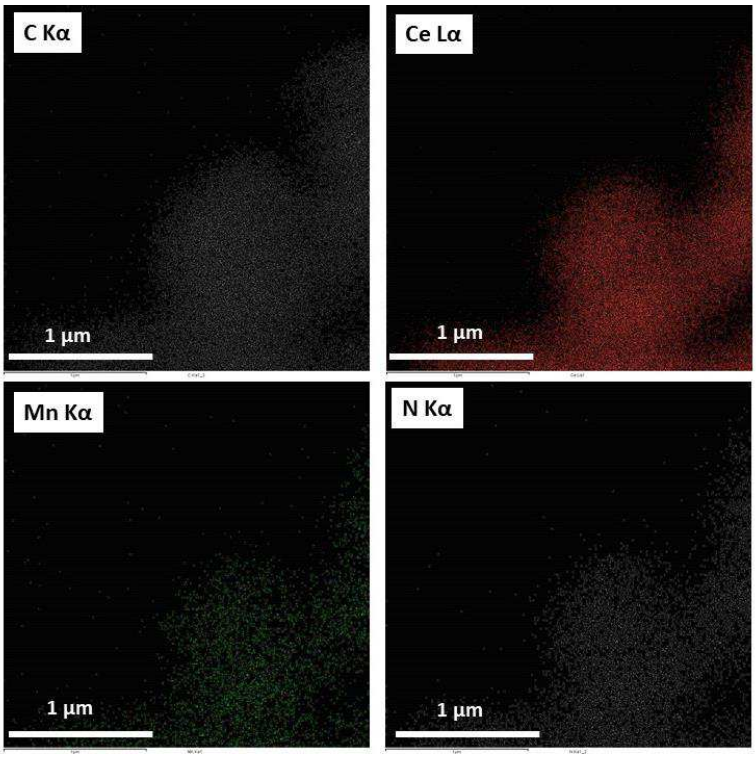

Figure 21: EDX chemical maps of PSC 15xMnMOF/NCs sample.

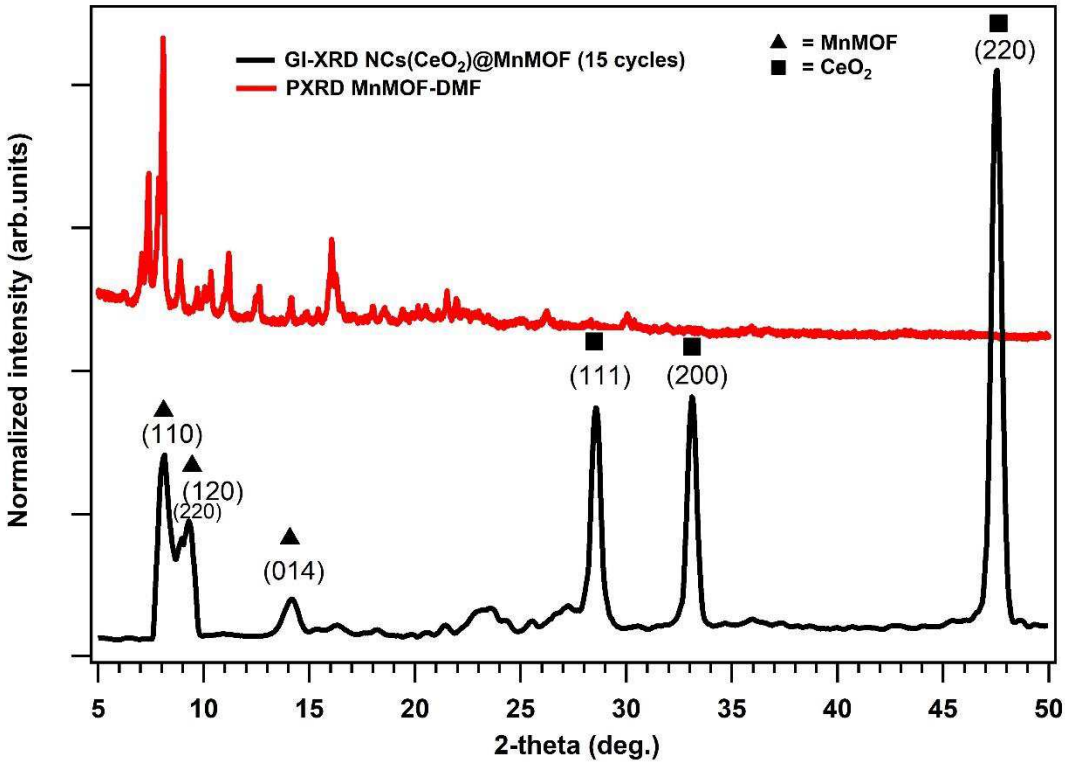

Figure 22: P-XRD pattern of MnMOF and GI-XRD pattern of PSC 15xMnMOF/NCs sample.

In order to verify the presence of micropores, we compared the results of 77 K N_2 adsorption-desorption isotherms of bare CeO_2 NCs and of the PSC 15x MnMOF/NCs sample (Figure 23a). For bare NCs, isotherm exhibited a Type II profile, and a total N_2 uptake of 103 $cm^3\ g^{-1}$ (STP) was observed. BET analysis of the data yielded a surface area of 34 m^2g^{-1}. In the case of the core@shell material, isotherm afforded a Type II profile and a total N_2 uptake of 208 $cm^3\ g^{-1}$ (STP) was observed. BET analysis of the data yielded a surface area of 93.6 m^2g^{-1}. However, at low partial pressure (P/P_o of 0.001–0.01) we can observe that there is a little stepped increased of N_2 uptake, which is a behavior usually correlated to the presence of microporosity. Moreover, we performed the *t-plot* analysis on both samples. This kind of analysis is used to estimate the microporous and mesoporous volumes.[43] Considering the adsorption isotherm $N_{ads}^0(P)$ (in mol/g) of a given gas on a flat surface with a specific surface area S (in m^2/g), this model assumes that the adsorbed phase has an average density equal to the bulk liquid density ρ_0 (in mol/m^3). Therefore, N_{ads}^0 (P) can be converted into the average thickness of the film adsorbed on the surface $t(P) = N_{ads}^0(P)/\rho_0 S$. The function t(P) is known as the t-curve. The t-plot is obtained by plotting for each pressure the adsorbed amount $N_{ads}(P)$ as a function of t(P). If the t-plot of a solid is a straight line, this solid has the adsorption behavior of a flat surface and the proportionality constant is simply the surface area of this solid. Briefly, all linear regimes in a t-plot provide evidence that adsorption, for that specific pressure range and adsorbate, is taking place similarly as on a flat surface and the slope of the straight line gives the value of the surface area. In contrast, any departure from the linear regime indicates the presence of a porosity getting filled and corresponding to pore sizes given by the pressure at which this departure is observed. In the case of materials containing only micropores, none of the linear regimes are getting through the origin of the t-plot, and the intercept of the linear fit in the low pressure range is classically taken as the microporous volume of the solid. Figure 23b shows the t-plots (and the relative fits obtained from Broekhoff-De Boer model) of bare CeO_2 NCs and of the PSC 15x MnMOF/NCs sample. As expected, in the case of bare NCs the intercept of the fit is negative in

the whole range of partial pressures analyzed, indicating the absence of microporosity. Conversely, in the case of core@shell material t-plot analysis confirmed the presence of microporosity (micropore volume=0.045cm^3/g; micropore area=12.44m^2/g).

Concluding, the high BET surface area of PSC 15x MnMOF/NCs (almost three times higher than NCs) and the t-plot analysis point to the presence of microporosity in the composite material. Combining these results with XRD, Raman, TEM and EDX results, we can conclude that we have successfully synthesize a thin shell of a microporous material around CeO_2 nanocubes. At the time of writing, we are trying to synthesize a thicker shell in order to obtain more detailed information about the nature of the microporous shell from our analyses (mainly from XRD and BET). In this way, we will undoubtedly confirm if the shell has the structure of MnMOF or if it is composed by a MOF with a slightly different structure.

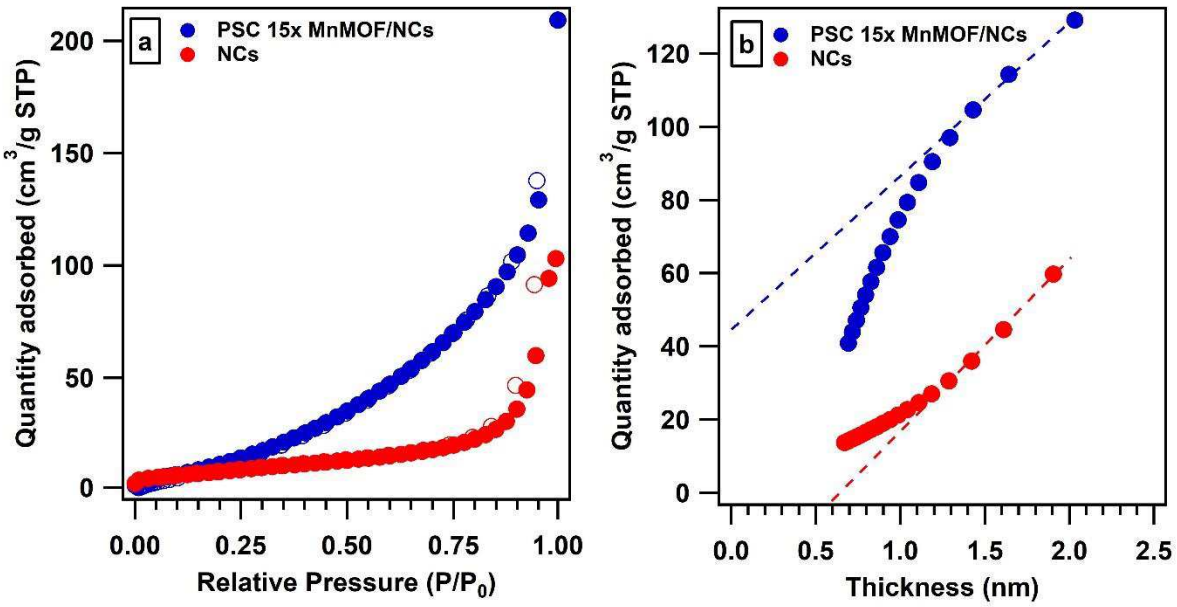

Figure 23: N_2 77K isotherms (a) and relative t-plots (b) of NCs and of PSC 15xMnMOF/NCs.

In order to verify the accessibility of vacant di-pyrazole moieties in the shell of the composite material, we tried to perform a post-synthetic metalation reaction with Rh(I) on the PSC 15xMnMOF/NCs sample. Similarly to the case of bulk MnMOF, we soaked precursor the powder of the core@shell material at RT in concentrate dry acetonitrile solution of Rh(I). After 24h, we washed the powders with fresh acetonitrile and we characterized the sample by XPS. From XPS spectra (Figure 24), we could detect the presence of Rh, Mn, N, C, O and Cl in the sample. The BE of Rh $3d_{3/2}$ was 308.2 eV, which is typical of Rh(I) species. Moreover, the surface atomic ratio between Mn and Rh resulted 3.1, a value compatible with the PSM of about half of the vacant di-pyrazole moieties of MnMOF. Overall, these data indicate that we were able to PSM the shell of the composite material. Therefore, this is another clue pointing towards the MnMOF nature of the microporous shell.

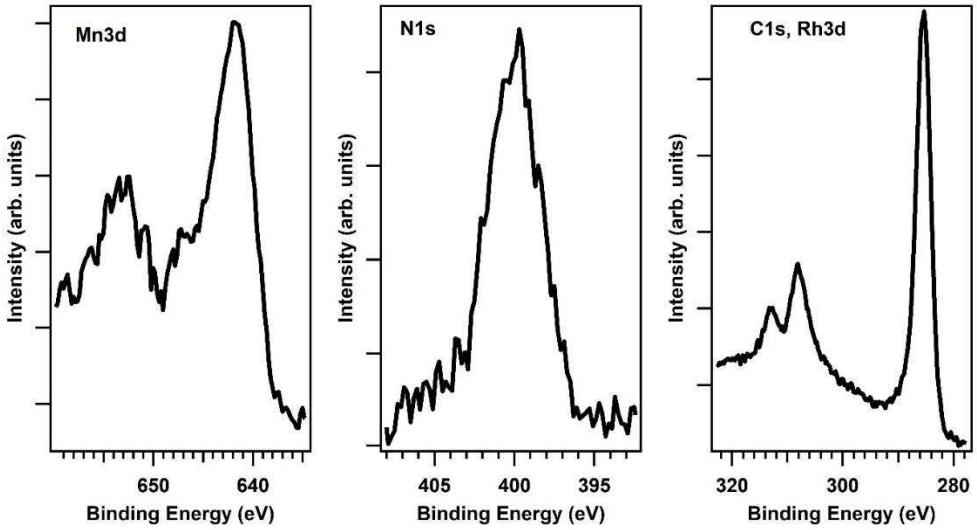

Figure 24:Mn 3d, N1s, Rh3d and C1s photoemission line of PSC 15xMnMOF/NCs after post-synthetic metalation with Rh(I).

The LbL results discussed above are the outcome of a long synthetic work, where we optimized several synthesis parameters such as temperature, precursor concentration, solvents, etc. For example, no shell growth was found when we operated the LbL cycles at RT. However, one of the most interesting parameters of this LbL growth is the nature of SBUs precursor. In the reference paper, bulk MnMOF was synthetized starting from $MnCl_2 \cdot 4H_2O$ and its ligand in DMF/H_2O (2:1 vol. ratio) solution. Therefore, we started our study on LbL growth of MnMOF employing separated solutions of manganese chloride and of the ligand in DMF/H_2O solutions or in aqueous (Mn(II)) or DMF (LH_2) solutions. In both cases, we observed that we obtained the precipitation of MnO clusters, as demonstrated by Raman Spectroscopy (one example is reported in Figure 25). In the LbL growth, the nature of SBUs precursor plays a fundamental role. A striking example was reported in the literature for the LbL growth of HKUST-1 (a Cu(II) paddle wheel based MOF).[38] Under typical solvothermal conditions, the nature of Cu(II) ion source (i.e. nitrate, acetate, chloride) did not affect the HKUST-1 synthesis. Conversely, comparing the LbL growth using copper acetate or copper nitrate as Cu(II) source, it was demonstrated that the LbL growth proceedes only using copper acetate and is suppressed using copper nitrate as SBUs precursor. This finding was rationalized by considering that in solutions of copper acetate the dominant unit present is the acetate-bridged paddle wheel, which has the same coordination geometry of the SBUs of the target MOF. Taking inspiration from this study, we decided to use manganese(II) acetate ethanolic solution as SBUs precursor in the LbL synthesis of MnMOF in order to avoid the precipitation of manganese oxide clusters. In fact, in MnMOF nodes the Mn(II) cations are coordinated by bidentate ligands: this coordination geometry is similar to that of manganese acetate and seems to facilitate the formation of SBUs. Conversely to the LbL growth with manganese chloride, using manganese acetate as SBUs precursor we had no evidence of the formation of bare manganese oxide clusters.

We have also investigated different approaches for the synthesis of CeO_2/MnMOF composite materials, but the results highlighted that was not possible to tackle the main goal of our study that is the fine control of the morphology of the final materials. For example, we tried to synthesize MnMOF crystals around ceria particles by dispersing LH_2 functionalized CeO_2 NCs in the DMF/H_2O solution containing MOF precursors used for the synthesis of bulk MnMOF. In this case, the NCs should act as nucleation centers for MOF crystals. Once prepared the dispersion, we transferred it in a screw cap vial that was introduced in an oven at 100°C. We modified the molar ratio between MOF precursors and ceria and we investigated the effect of different reaction times (1h-24h). In this kind of synthesis, the main problem was the stability of ceria powders dispersion. In fact, without

the aid of any stabilizer (i.e. PVP, surfactants), the ceria powder rapidly tends to settle on the bottom of the vial and MOF crystals start to nucleate randomly in the solution (see Figure 26).

In order to avoid the problem of ceria powders settling, and the consequent loss of their effect as nucleation centers, we tried to perform the same solvothermal synthesis under continuous stirring. In these cases, ceria powders were more uniformly dispersed in the composite materials compared to the syntheses performed in oven. Nevertheless, we did not obtain a precise control of the morphology, ceria particles seem to partially agglomerates and the crystals of MOF were too big for our purposes (>10 µm, see Figure 27).

These results highlight that if we want to obtain a fine control on the core@shell morphology of the composite material (i.e. tuning the thickness of the shell) the LbL approach is the best way to go. Only with the control at the nano scale of the shell thickness we can think of obtaining a *rationally designed model systems.* Given the complexity of tandem catalysis, this is fundamental for the rational understanding of the catalytic properties of

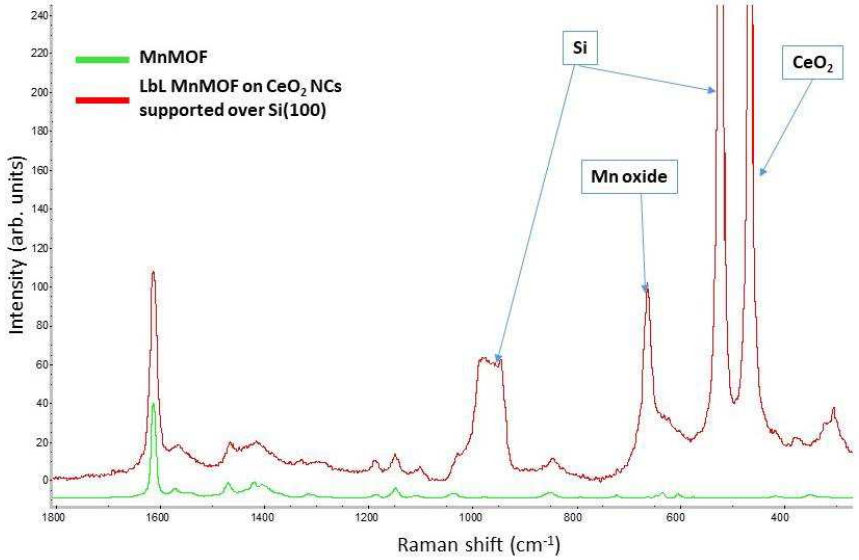

Figure 25:Raman spectra of MnMOF and of MnMOF synthesized through LbL syntehsis (15 cycles) on CeO_2 NCs supported over Si(100) wafer. In this case, the SBUs precursor was $MnCl_2$ (dispersed in DMF/H_2O 2:1 solution)

MOF/NPs composite materials and for the possible exploitation of these materials for tandem reactions that could represent a groundbreaking technological platform for the advancement of green chemistry and sustainable processes.

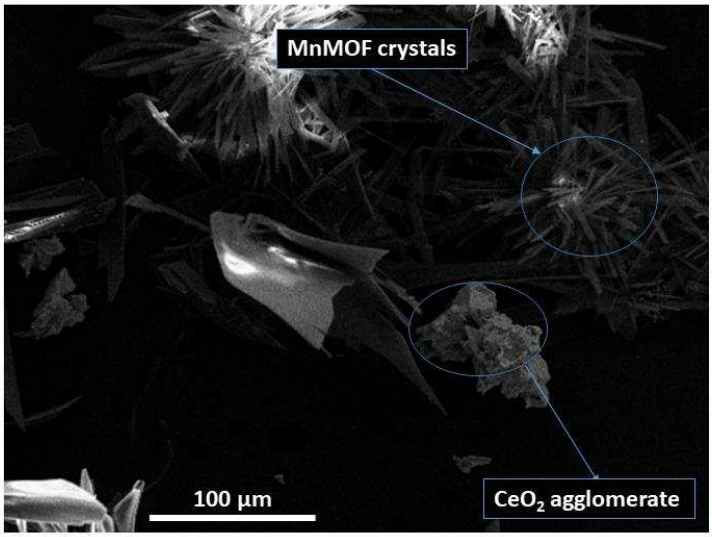

Figure 26: SEM micrograph of solvothermal synthesized MnMOF in CeO_2 NCs containing suspension.

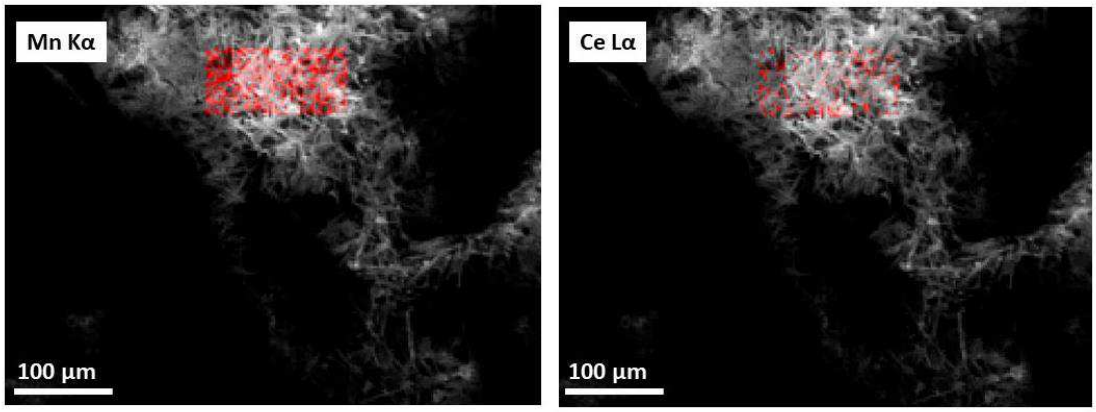

Figure 27: EDX chemical maps (Mn Kα and Ce Lα) overlapping SEM micrographs of solvothermal synthesized MnMOF in CeO_2 NCs containing suspension under vigorous stirring.

4.5 Conclusion

In this chapter, we studied the design of nanoreactors for heterogeneous catalysis and their integration in multifunctional nanostructured materials. As nanoreactors, we investigated a new class of inorganic-organic hybrid microporous materials: Metal Organic Frameworks. In particular, we studied a MOF (MnMOF, developed by Prof. Doonan's group) which is composed by an organic linker that possesses sites poised for post-synthetic metalation (PSM) in its crystal structure. The resulting PSM MOF has therefore a new active site in its structure. Moreover, the crystallinity of the MOF ensures that the active site is perfectly reproduced throughout the material. In this way, we can design at the atomic scale the confined space of MOF micropores, in order to introduce new active site for catalysis realizing an authentic tailored nanoreactor. The internal surfaces of MOFs in fact, constitute a quite special confined environment subjected to a multitude of interactions that strongly depend on the actual structure of the MOFs (geometrical dimension of pores, chemical nature of nodes and linkers, addition of metal active sites through PSM). We investigated the quantitative metalation of MnMOF with a variety of transition metal ions, in order to perform a screening of the possibilities given by PSM (i.e. Co(II), Rh(I), Fe(II), Fe(III), Co(III) and mixture of them). After this screening, we focused our attention mainly on the PSM with Rh(I). Rh-based materials are widely employed in hydroformylation catalysis, and in the literature there are only a few examples of Rh NPs supported in MOF pores for hydroformylation reaction. However, to the best of our knowledge, there are no examples of hydroformylation reaction catalysis operated by Rh PSM MOFs (catalysis exploited by Rh cation/complex coordinated to MOF structure). This is a quite notable results since it demonstrate that MOF linkers can be use as sites for the heterogeneization of molecular catalysts preserving they high activity but endowing the sytem of higher selectivity connected to the size effect of mof porosity and an easier recyclability given the solid state nature of MOFs . We tested the catalytic activity of Rh metalated Mn MOF for styrene hydroformylation reaction (in collaboration with Prof. Paganelli at University of Venice), obtaining good results in terms of conversion, selectivity and stability of the catalyst. Moreover, at the time of writing, we are investigating the effects of metal nature (replacement of Rh with Co) and, by the analysis of the catalytic activity of the metalated ester of the ligand molecule, we are investigating the influence of the micropores "confined space" on the product selectivity (i.e. branched vs linear reaction products).

In the literature, was demonstrated that a multifunctional material (nanocrystal bilayer of metal and metal oxides) could catalyze ethylene hydroformylation reactions in a tandem reaction scheme, employing the in situ produced CO and H_2. As highlighted in this chapter, tandem catalysis approach is a new concept that could have a great impact on the catalysis field, permitting to simplify and to make less dangerous and more environmentally friendly several different reactions.

In the previous chapter, we have investigated Pd/CeO_2 catalysts for methanol decomposition to syngas. Combining the knowledge acquired on PSM of MnMOF with the studies on Pd/CeO_2, our project is to design a multifunctional catalysts based on core@shell structure of Pd/CeO_2 (core) and post-synthetic metalated MOFs (shell). We have demonstrated that through PSM is possible to introduce Rh(I) sites in the MnMOF micropores, in order to introduce active sites for hydroformylation reaction. If we apply this concept to the thin shell of MnMOF, one possible target reaction for our core@shell multifunctional material could be ethylene hydroformylation, with the *in situ* production of CO and H_2 (through methanol decomposition catalyzed by Pd/CeO_2 core) necessary to carry out hydroformylation reaction (catalyzed by Rh-sites in MnMOF shell). However, the activity of a tandem catalyst is not simply the sum of properties of the different components, but depends on the synergistic work of the different material components. Therefore, the core@shell catalyst morphology must be highly controlled at several length scales and rationally conceived. The synthesis of thin shell of MnMOF was very challenging, since the growth of thin layers of MnMOF are very limitedly reported in

the literature. The design of this kind of core@shell composite material must be done both at the nanoscale (i.e. shape selection of CeO_2 core, deposition of Pd NPs, growth of thin shell of MnMOF) and at the atomic scale (i.e. introduction of Rh(I) active sites in MnMOF micropores through PSM). At the time of writing, this project is not yet concluded. We have presented in this chapter the most promising results obtained through the layer-by-layer growth of MnMOF on CeO_2 nanocubes, whereas the characterization of the catalytic activity of these core@shell materials is only started and the data are not presented in this thesis.

From a general point of view, this kind of core@shell multifunctional material is fascinating because of its versatility. We have demonstrated the possibility of introduce in the MnMOF structure, through post synthetic metalation, different types of transition metal cations. If we apply this kind of approach to the MnMOF shell, we could tune its catalytic activity introducing different active sites in the porous shell (Figure 28) and therefore tune the overall catalytic activity of the multifunctional material by designing at the atomic scale the confined environment of MOF micropores.

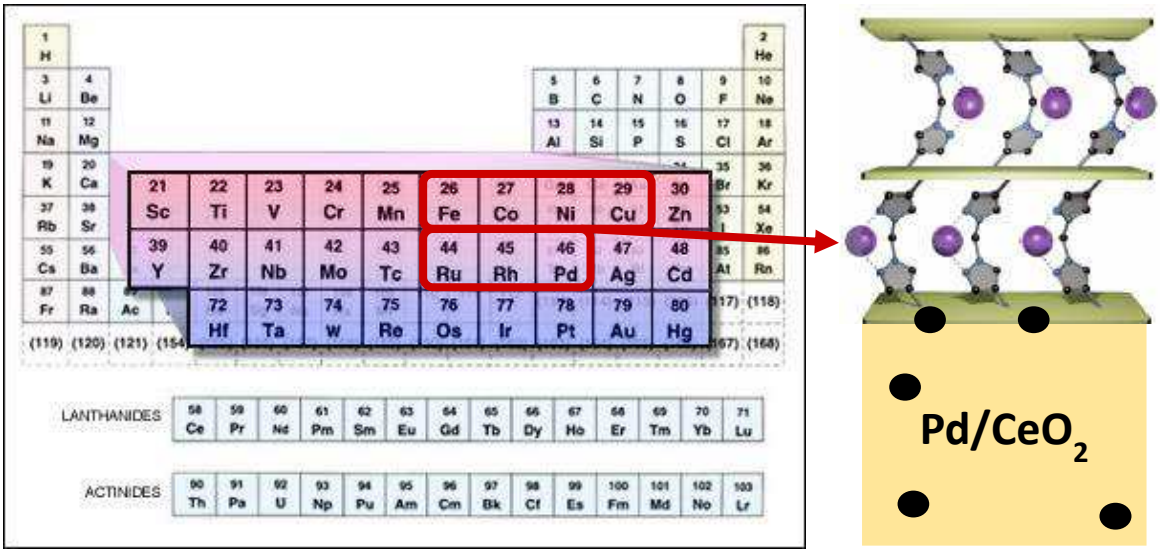

Figure 28: Schematic view of a section of the designed core@shell material. In this scheme, we highlight the vacant di-pyrazole sites of MnMOF shell and we summarize the transition metals that could be coordinated in the shell.

References

[1] H. Furukawa, K. E. Cordova, M. O'Keeffe, O. M. Yaghi *Science* **2013,** 341, 1230444

[2] O. K. Farha, I. Eryazici, N. C. Jeong, B. G. Hauser, C. E. Wilmer, A. A. Sarjeant, R. Q. Snurr, S. T. Nguyen, A. Ö. Yazaydın, J. T. Hupp, *J. Am. Chem. Soc.*, **2012**, *134* (36), 15016–15021.

[3] W. M. Bloch, A. Burgun, C. J. Coghlan, R. Lee, M. L. Coote, C. J. Doonan, C. J. Sumby, *Nat. Chem*., **2014**, 6

[4] M. J. Katz, Z. J. Brown, Y. J. Colo´n, P. W. Siu, K. A. Scheidt, R. Q. Snurr, J. T. Hupp, O. K. Farha, *Chem. Commun.,* **2013**, 49, 9449-9451.

[5] M. C. So, S. Jin, H. Son, G. P. Wiederrecht, O. K. Farha, J. T. Hupp, *J. Am. Chem. Soc.*, **2013**, 135 (42), 15698–15701.

[6] Y. Yamada, C.K. Tsung, W. Huang, Z. Huo, T. Soejima, C.E. Aliaga, G.A. Somorjai, P. Yang, *Nat. Chem.,* **2011**, 3(5), 372-6.

[7] M. J. Climent, A. Corma, S. Iborra, M. J. Sabater, *ACS Catal.,* **2014**, 4 (3), 870–891.

[8] H. Li, M. Eddaoudi, T.L. Groy, O.M. Yaghi, *J. Am. Chem. Soc.*, **1998**, 120, 8571–8572.

[9] O.M. Yaghi, C.E. Davis, G. Li, H. Li, *J. Am. Chem. Soc.*, **1997,** 119, 2861–2868.

[10] H. Li, M. Eddaoudi, M. O'Keeffe, O.M. Yaghi, Nature, **1999**, 402, 276–279.

[11] M. Eddaoudi D. B. Moler, H. Li, B. Chen, T. M. Reineke, M. O'Keeffe, O. M. Yagi *Acc. Chem. Res.* **2001**, 34, 319-330.

[12] A. Corma, H. García, F. X. Llabrés i Xamena *Chem. Rev*., **2010**, 110 (8), 4606–4655.

[13]J. Y. Lee, O. K. Farha, J. Roberts, K. A. Scheidt, S.B. T. Nguyen, J. T. Hupp, *Chem. Soc. Rev.*, **2009**, 38, 1450–1459.

[14] J. Gascon, A. Corma, F. Kapteijn, F. X. Llabrés i Xamena, *ACS Catal.,* **2014**, 4, 361−378.

[15] J. D. Evans, C. J. Sumby, C. J. Doonan, *Chem. Soc. Rev*., 2014,43, 5933-5951.

[16] R. Poli, *Effects of Nanoconfinement on Catalysis*. **2017** Springer Science and Business Media.

[17] M. Otte, *ACS Catal.*, **2016**, *6*, 6491–6510.

[18] S. H. A. M. Leenders, R. Gramage-Doria, Bas de Bruin, J. N. H. Reek *Chem. Soc. Rev*., **2015**, 44, 433-448.

[19] A. White, Principles of biochemistry (Eds.: A.White, P. Handler, E. L. Smith), Blakiston Division, McGraw-Hill, New York, **1968**.

[20] H. Fei, SM.Cohen, *Chem Commun.* **2014**, 50(37), 4810-2.

[21] Q. Yang, Q. Xu, H.L. Jiang, *Chem. Soc. Rev*., **2017**,46, 4774-4808.

[22] M. Zhao, K. Deng, L. He, Y. Liu, G. Li, H. Zhao, Z. Tang, *J. Am. Chem. Soc.*, **2014**, *136*, 1738-1741.

[23] J. Zhang, L. Wang, Y., Shao, Y. Wang, B. C. Gates, F.-S. Xiao, *Angew. Chem. Int. Ed.* **2017**, doi:10.1002/anie.201705761

[24] J. A. Mata, F. E. Hahnd, E. Peris, *Chem. Sci.*, **2014**, 5, 1723-1732.

[25] J. C. Wasilke, S. J. Obrey, R. T. Baker, G. C. Bazan, *Chemical reviews*, **2005**, *105*, 1001-1020.

[26] F.-X.Felpin, E. Fouquet, *ChemSusChem* **2008**, 1, 718 – 724.

[27] Y.-B. Huanf, J. Liang, Xu-S. Wang, R. Cao, *Chem. Soc. Rev.*, **2017**, 46, 126-157.

[28] Q.-L. Zhu, Q. Xu, Chem. Soc. Rev., **2014**, 43, 5468.

[29] G. Ertl, "Reactions at surfaces: from atoms to complexity", *Nobel Lecture*, December 8, **2007**.

[30] H. R. Moon, D.-W. Lim, M. Paik Suh, *Chem. Soc. Rev*., **2013**, 42, 1807-1824.

[31] J. E. Mondloch, W. Bury, D. Fairen-Jimenez, S. Kwon, E. J. DeMarco, M. H. Weston, A. A. Sarjeant, S. T. Nguyen, P. C. Stair, R. Q. Snurr, O. K. Farha, J. T. Hupp, *J. Am. Chem. Soc*., **2013**, 135 (28), 10294–10297.

[32] L. Braglia, E. Borfecchia, K. A. Lomachenko, A. L. Bugaev, A. A. Guda, A. V. Soldatov, B. T. L. Bleken, S. Øien-Ødegaard, U. Olsbye, K. P. Lillerud, S. Bordiga, G. Agostini, M. Manzoli, C. Lamberti *Faraday Discuss*., **2017**, 201, 265-286.

[33] M. S. Denny, Jr., J. C. Moreton, L. Benz, S. M. Cohen, *Nature Reviews Materials* , 1, Article number: 16078 (**2016**)

[34] P. Falcaro, R. Ricco, C. M. Doherty, K. Liang, A. J. Hill, M. J. Styles, *Chem. Soc. Rev.*, **2014**, 43, 5513-5560.

[35] I. Stassen, M. Styles, T. Van Assche, N. Campagnol, J. Fransaer, J. Denayer, J.-C. Tan, P. Falcaro, D. De Vos, R. Ameloot, *Chem. Mater.*, **2015**, 27 (5), 1801–1807.

[36] O. Shekhah, H. Wang, S. Kowarik, F. Schreiber, M. Paulus, M. Tolan, C. Sternemann, F. Evers, D. Zacher, R. A. Fischer, C. Woll, *J. Am. Chem. Soc.* **2007,** 129, 15118-15119.

[37] V. Stavila, J. Volponi, A. M. Katzenmeyer, M. C. Dixon, M. D. Allendorf, *Chem. Sci.*, **2012**, 3, 1531.

[38] O. Shekhah, H. Wang, D. Zacher, R. A. Fischer, C. Woll, *Angew. Chem. Int. Ed.* **2009**, 48, 5038 –5041.

[39] D. Zacher, K. Yusenko, A. Botard, S. Henke, M. Molon, T. Ladnorg, O. Shekhah, B. Schopbach, T. de los Arcos, M. Krasnopolski, M. Meilikhov, J. Winter, A. Terfort, C. Woll, R. A. Fischer, *Chem. Eur. J.* **2011**, 17, 1448 – 1455.

[40] O. Shekhah, L. Fu, R. Sougrat, Y. Belmabkhout, A. J. Cairns, E. P. Giannelis, M. Eddaoudi, *Chem. Commun.,* **2012**, **48**, 11434–11436.

[41] A.C. Brezny, C.R. Landis, *J. Am. Chem. Soc.*, **2017,** 139, 2778−2785.

[42] D. Buso, K. M. Nairn, M. Gimona, A. J. Hill, P. Falcaro, *Chem. Mater.*, **2011**, 23 (4), pp 929–934.

[43] A. Galarneau, F. Villemot, J. Rodriguez, F. Fajula, B. Coasne, *Langmuir* **2014**, 30, 13266−13274.

Chapter 5

Multiscale design of nanostructured hybrid materials

5. Multiscale design of nanostructured hybrid materials

In this chapter, we will discuss the multiscale design of hybrid materials based on 2D materials: graphene and MoS_2. The preparation of these nanostructured composite materials was carried out through a one-pot synthesis in microreactors using the aerosol process. In fact, each aerosol microdroplet contains the material precursors and can be considered as a microreactor for the synthesis of nanostructured materials. Aerosol process is an extremely versatile method to synthesize nanostructured materials because by changing the composition of the starting solution it is possible to obtain materials with an increasing level of complexity. However, the structure and composition of the final material depends very significantly on process parameters (such as pressure, gas flow, furnace temperature, etc).

This strong coupling between chemistry and process, called "integrative chemistry", is a powerful route to design both the morphology and composition of the condensed matter from the macroscopic to the nanoscopic scale.[1] This kind of approach is quite efficient end extremely versatile. At its core it envisages a combination of soft chemistry, soft matter, complex fluid dynamics and different processes (i.e. thermal decomposition in reactive atmosphere, confinement forces due to capillary compression, micro-scale chemical reactors) that permits to have a wide gamut of tools to control the structures and the functionalities of the final product. By virtue of this strategy, it is possible to obtain hybrid materials with hierarchical architectures and with properties that can emerge either from the organic or the inorganic moiety or even from the synergy between the two.

There are virtually infinite ways to combine simple systems to obtain innovative materials with present and future applications in various fields such as catalysis, energy, sensing, biomaterials or drug carriers. In this context aerosol processing is a versatile technique because it permits to synthetize inorganic or hybrid materials characterized by a complex structure.[2] For example, aerosol processing allows the synthesis of hierarchically structured porous materials, mesoporous microspheres or hybrid composites.[2,3] Furthermore, the aerosol technique is easily scalable, economic and has very fast processing times, allowing the production on a large scale.

One of the fields of greatest interest where is necessary to produce large quantities of product with low cost, is that of energy, which therefore represents a perfect arena where aerosol processing could be determinant for the development of new materials. Researchers are particularly focused on valid substitutes for platinum-based catalysts for the oxygen reduction reaction (ORR) in the fuel cells and for the hydrogen evolution reaction (HER). In the context of photocatalytic water splitting, the optimization of a low-cost catalyst could open a promising route to capture, convert and store solar energy as H_2 that subsequently could be used as fuel.[4] Nowadays MoS_2 NPs supported on reduced graphene oxide (rGO), synthetized by solvothermal synthesis, have proven to be active HER electro- and photo-catalysts.[5,6] Nevertheless, Graphene-based materials are useful not only as support (active or not) for other compounds[4] but also quite active per se. A large number of works has demonstrated that doped-carbon materials with a graphitic structure show pronounced catalytic activity for various chemical processes, including the ORR[7] quoted above. Dually doped graphene materials, the relationship between chemical state and activity and the synergistic interactions among defects, are particular fascinating topics at the forefront of research, whose comprehension is expected to lead to the development of a new generation of applied materials..[8,9]

These considerations on aerosol process, together with the hopes for a fast development of carbon-based materials[7], outline a credible scenario for the development of devices with a multitude of applications (Figure 1), including low cost nonprecious metal or metal-free catalysts based on graphene, or high surface area electrodes for sensors and energy storage.[10]

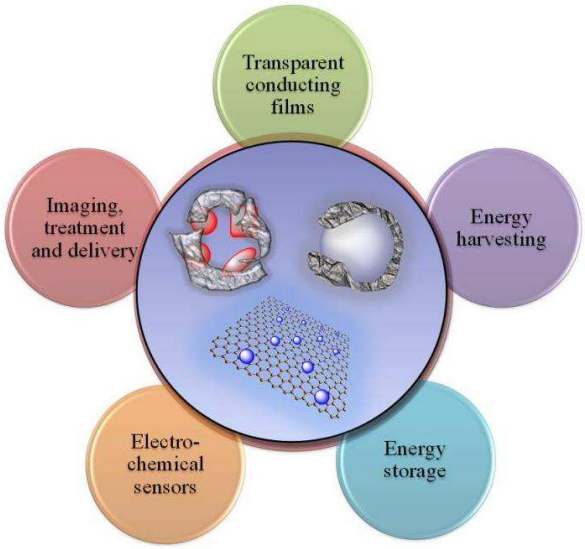

Figure 1: Future research prospects and challenges in the field of graphene-nanoparticles hybrid materials. K. T. Nguyen and Y. Zhao, Nanoscale, 2014, 6, 6245. Published by The Royal Society of Chemistry.

In the present study, aerosol processing was used as a fast and simple method to modify graphene sheets by introducing heteroatoms and forming chemically modified graphenes (CMGs).[11,12,13] Moreover, by adding a soluble salt in the precursor solution, which undergoes aerosolization, we were able to prepare nanohybrids made up by N-doped crumpled graphene (N-cGO) filled with a second component, in this case MoS_2 (hereafter N-cGO/ MoS_2). Differently from other techniques that are generally adopted for the preparation of similar nanocomposites, e.g. solvothermal synthesis[14] or solid-solid or solid/gas reactions[15], the aerosol processing allows a surgical design of morphology and chemical composition, but at the same time, it maintains high yield and exceptionally short synthesis time.

MoS_2 is one of the most studied candidates for the substitution of Pt as electroactive catalyst in the hydrogen evolution reaction (HER). It is a nontoxic, environmentally friendly and abundant semiconductor that exhibits all the preconditions to build a sustainable technology. However, bulk MoS_2 at the present time is not yet a valid competitor of commercial catalysts based on Pt due to poor performances.[16,17] In fact, one of the main limitations of MoS_2 as electroactive catalyst toward HER stems from its poor electron conductivity. Therefore the combination of MoS_2 and graphene, which exhibits exceptional electron transport properties, can be quite advantageous in order to overcome these problems. [18,6,19] Moreover, the stabilization of small MoS_2 nanoparticles (NPs) on graphene surface offers a simple way to maximize the number of edge sites, which are known to be the active phase for the HER.[20,21] On the other hand, the use of CMGs opens the way towards new concepts for the fabrication of advanced materials. Actually, by aerosol process, p-type MoS_2 NPs can be easily prepared and efficiently dispersed on nitrogen doped graphene forming localized p-n nanojunctions[6] which are quite efficient for the separation of photogenerated charge carriers. Actually, N-cGO/MoS_2 nanohybrids result to be extremely active in the photoelectrochemical hydrogen generation.

This hybrid system can be considered a bifunctional material since it is based on the strong interaction between two moieties (creation of a p-n nanojunction between N-cGO and MoS_2) within a unique catalytic reaction (photoinduced hydrogen evolution reaction). The *in situ* hydrogen production is an important reaction in the field of tandem catalysis, because H_2 could be immediately employed in a successive reaction after the *in situ* production, therefore a more complex synthesis can become safer and more sustainable. The sustainability of this process is highlighted by the role of the solar light (reduction of the overpotential necessary to start the hydrogen production) and by the absence of noble metals. Moreover, the structure of this hybrid could be considered a model for the synthesis of various catalysts and the experience acquired with this synthesis will be very important for the synthesis of other nanostructured materials. In fact, the particular process and the crumpled graphenic structure ensure a good dispersion of MoS_2 NPs (with a size of about 4 nm). This control over the NPs dispersion is fundamental for the synthesis of a tandem catalyst, in which the formation of spatially controlled heterointerfaces is exploited to control and orchestrate the catalytic activity.

As the reader will appreciate from the discussion of the characteristic of aerosol process and of the experimental results in this chapter, the aerosol synthesis of N-cGO-MoS_2 nanohybrids is a striking example of multiscale design of a catalyst. At the atomic scale, we will introduce a dopant (N) in the graphenic structure; at the nano scale, we will obtain a fine dispersion of MoS_2 NPs maximizing the number of active sites; and at the micro scale, we will avoid the restacking of graphene sheets due to their crumpled morphology.

5.1 Aerosol process

An aerosol is defined as a colloidal dispersion of liquid droplets or solid particles in a carrier gas. Liquid droplets or solid particles have diameter smaller than one µm; larger particles or droplets in a gas make a suspension, however this classification is not clear-cut. Aerosol or spray drying methods are extensively both in research and industrial processes because they are low-cost, involve a limited number of preparation steps and are compatible with on-line continuous production. In the simplest case, the method consists of atomizing a solution into droplets dispersed in a gas that carries them onto a substrate. Droplets can be atomized by different methods, all associated with a mechanical destabilization of the solution/gas interface such as air jets, rotary disks and ultrasonic nebulizers. In order to have an efficient aerosol processing the starting solution has to be a stable (for the process duration) colloidal dispersion or a solution. The solution components can be varied and mixed in different ways, allowing the preparation of a large variety of systems. In fact, it is possible to control the stoichiometry of the reacting mixture before processing, to have a relative control over shape and/or size, and to tailor the reactors to develop patterning of the final products (Figure 2). This flexibility represents a key factor to generate nanostructured materials: it is adaptable, simple and allows combinatorial synthesis. This versatility, combined with the advantages of the sol–gel chemistry related to the Evaporation Induced Self Assembly (EISA) typical of aerosol processes, permits the synthesis of several hierarchically structured hybrid or metal oxide materials.

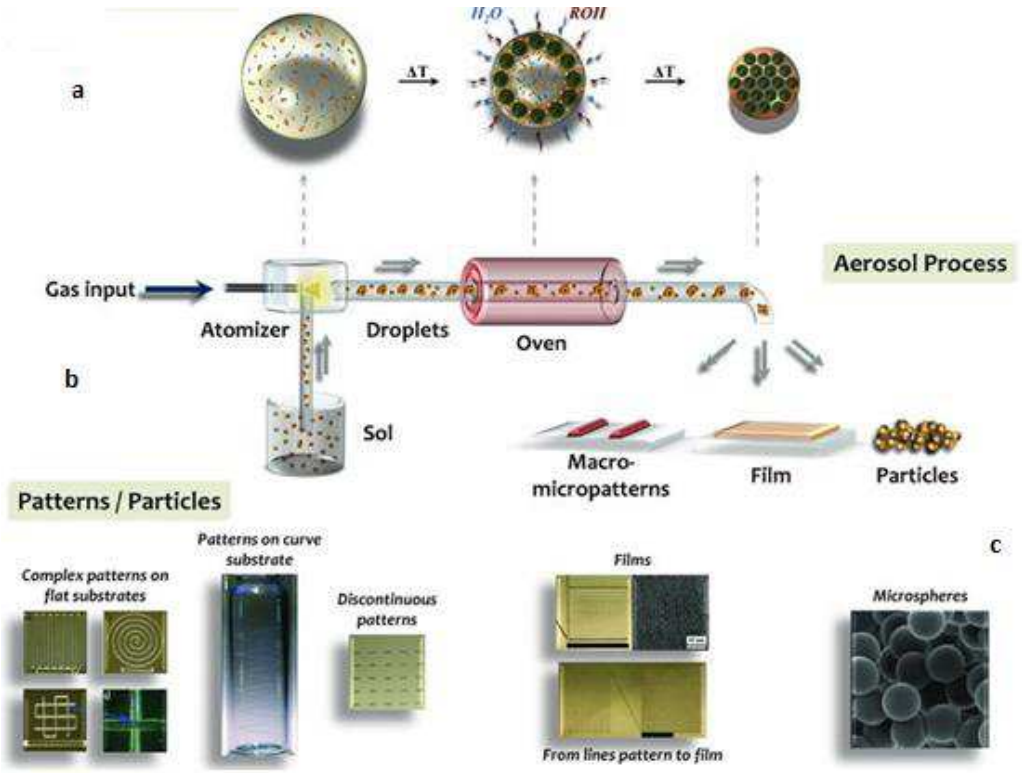

Figure 2: (a) schematic representation of evaporation induced self assembly mechanism via spray-drying processes. (b) General diagram of an aerosol set-up. (c) Examples of the resulting materials obtained via aerosol process: various patterns printed by an aerosol robocaster and mesoporous microspheres. Reprinted with permission from C. Boissiere, et al. Adv. Mater. 2011, 23, 599–623. Copyright © 2011 WILEY-VCH Verlag GmbH & Co. KGaA, Weinheim.

From as careful perusal of literature, it readily comes out the versatility of aerosol processing. In fact, there are so many different materials synthesis that cannot be listed here, considering also that this is a field in constant expansion. In fact, the research linked to aerosol processing varies from the synthesis of innovative mesoporous materials, by combining sol-gel growth of inorganic or hybrid networks with self-assembled surfactant mesophases, to the synthesis of core-shell morphologies with applications in drug delivery.[1]

Considering for example the synthesis of mesostructured materials, the advantage of aerosol process over sol-gel preparation is that the initially stoichiometry of the solution is retained in the final product. Indeed, different inorganic precursors do not necessarily have to interact attractively with each other to be incorporated into the final material (Figure 3, 4). Due to this advantage, different elements (Al, Ca, Fe, Pd, etc.) were incorporated in silica matrices in order to improve catalytic, thermal bioactivity or other properties. Non-silica powders are less studied, but also works dedicated to non-silicate mesostructured ceramics are present in the literature (for example based on TiO_2, ZrO_2 and CeO_2 employing PEO-based polymers as structuring agents)[1].

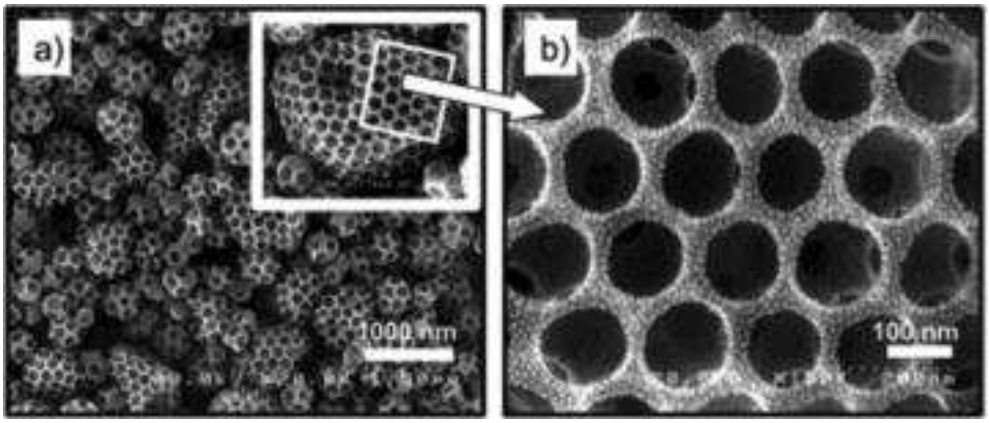

Figure 3: SEM image of a) a power and b) its surface morphology obtained from a mix of 178 nm polystyrene latexes and 5nm SiO_2 colloids. Reprinted with permission from C. Boissiere, et al. Adv. Mater. 2011, 23, 599–623. Copyright © 2011 WILEY-VCH Verlag GmbH & Co. KGaA, Weinheim.

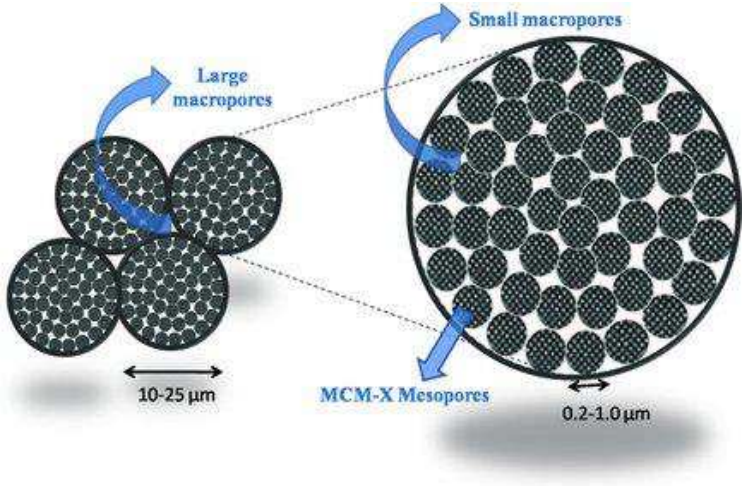

Figure 4: Scheme of composite micron-size hierarchical particles prepared by spray-drying of submicron size mesostructured colloids. Reprinted with permission from C. Boissiere, et al. Adv. Mater. 2011, 23, 599–623. Copyright © 2011 WILEY-VCH Verlag GmbH & Co. KGaA, Weinheim.

Recently, aerosol processes were employed also in the field of microporous materials. The group of C. Boissiere developed a one-pot aerosol synthesis and processing of several benchmarked MOFs (i.e. ZIF-8, HKUST-1). Combining different aerosol flows (i.e. aerosol of the ligand solution and aerosol of SBUs precursor, in order to avoid MOF nucleation in the starting solution) they combine spray drying and EISA methods in order to obtain nanoparticles of MOFs of about 100 nm assembled in hollow microspheres (Figure 5).[22]

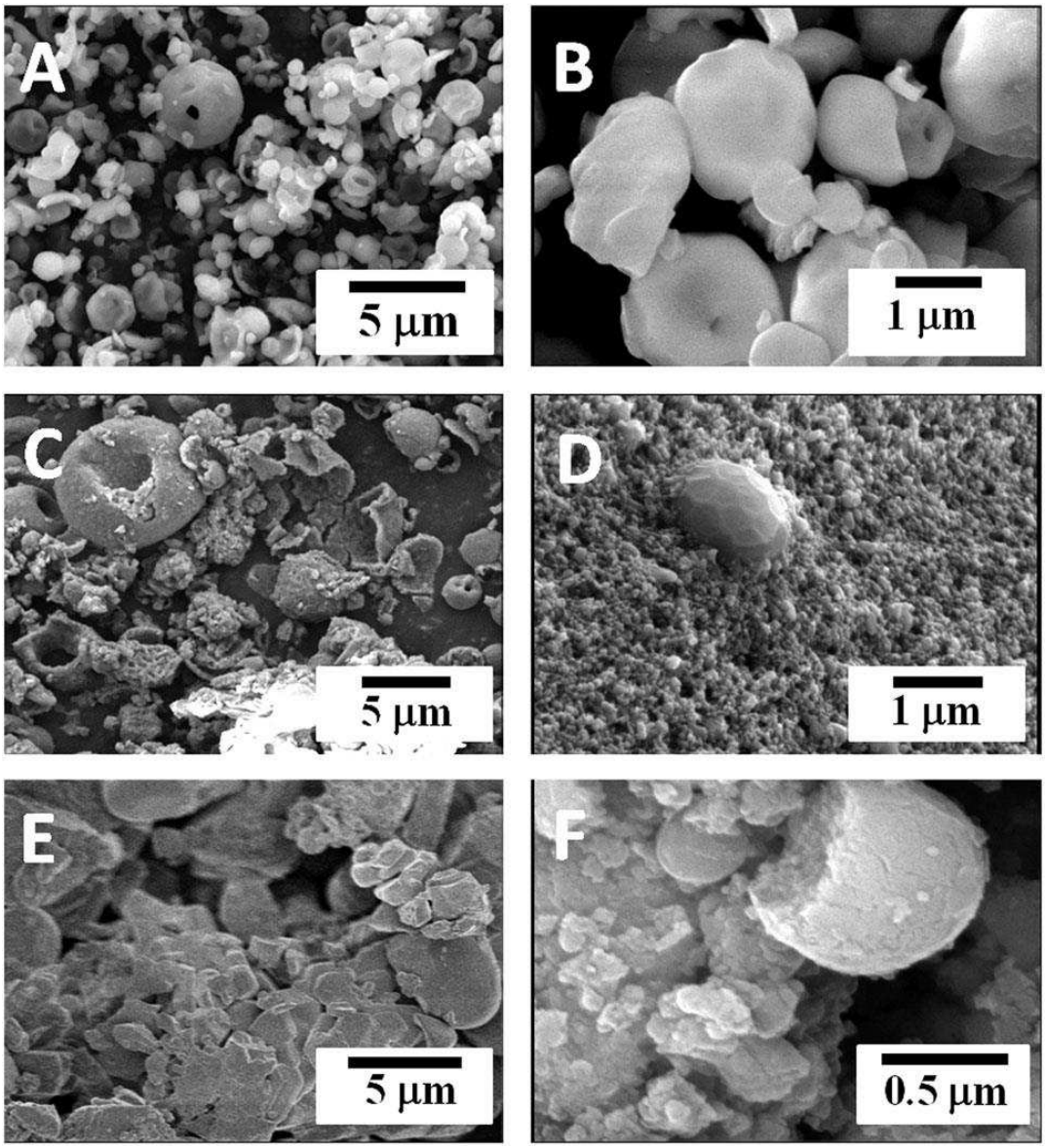

Figure 5: SEM images of Fe3BTC2 (a) as-made; (b) activated (i.e. solvent molecule removed from the micropores), HKUST-1 (c) as-made; (d) activated and ZIF-8 (e) as-made (f) activated. Reprinted with permission from A. G. Marquez et al. Chem. Commun., 2013, 49, 3848—3850. Copyright © 2013, Royal Society of Chemistry.

All these possibilities represent the perfect springboard for the creativity of materials scientists: with such a large variety of preparation routes and their hierarchical combination, the ways to obtain innovative materials are exponentially increased, making possible the realization of structures that without aerosol processing are very difficult to achieve or could only be imagined.

5.2 Graphene

During the last few years, graphene, a perfect monolayer of C sp^2 atoms arranged in a honey-comb network, and chemically modified graphene (CMG) systems have been studied in the context of several applications, due to their excellent electrical, mechanical and thermal properties.[23,24] This new carbon allotrope has soon become the rising star of materials science and recently it has been followed by an entire constellation of related materials, such as quantum dots, nanoribbons, nanobubble, etc. After the initial hype on graphene connected to the first pioneering works pointing out its exceptional properties[23], some consolidated streams of research devoted to more applicative applications are thriving. This growing attention has led to increase more and more the number of publications, so that in 2010 the number of scientific papers on graphene exceeded 3000/yr.[25] It is anticipated that graphene will withstand the normal seven-step sequence for any new technology: hope–hype–boom–bust–disillusionment–shakeout–profitability and meet expectations for profitability even faster than the other carbon allotropes.[26] Right now graphene related materials are reached a more mature age[27], still characterized by an intense base research, but also focused on large-scale industrial applications. [26]

Aerosol processing can be the base for developing a scalable and versatile production of graphene-based materials. The most consolidated strategy to chemically modify graphene for obtaining CMG or to create new nanohybrid materials, which are composite systems made up by graphene and other nano-objects such as nanoparticles, usually starts from graphite oxide.[28] Graphite oxide is a compound of carbon, oxygen and hydrogen that when it is dispersed in a solution yields single sheets and is called graphene oxide (GO) in analogy to graphene. To this day, no certain model of GO exists, however the most credited structure is the so called Lerf Klinowski (LK) model[29], that can be seen like a graphene sheet with various functional groups at the surface and at the edges, for examples epoxy bridges, carboxyl groups and hydroxyl groups (as tertiary alcohols). According to the LK model[29], GO sheets can be divided in two regions: aromatic regions with perfect unsaturated benzene rings and regions with aliphatic six-membered rings. The relative size of the two regions is not constant, but depends on the oxidation degree. However, the typical compositions of GO, obtained by wet chemical methods, corresponds to a C/O atomic ratio ranging from 4:1 to 2:1. The functional groups lie above and below the carbon plane forming a layer of oxygen atoms of variable concentration, constituting an arrangement of negatively charged oxygen layers, whereas the sheet edges terminate with C-OH and -COOH groups. To date, it has been found that the greater the surface polarity is, the better the dispersability (typically about 1–4 mg/ml in water).[30] The carbon plane is nearly flat, and only the carbons attached to OH groups have a slightly distorted tetrahedral configuration, resulting in some wrinkling of the layers. The observed formation of phenol (or aromatic diol) groups during deoxygenation indicates that the epoxide and the C-OH groups are very close to one another. Anyway, the distribution of functional groups in every oxidized aromatic ring does not need to be identical, and both the oxidized rings and aromatic entities are distributed randomly.

In Figure 6 is represented a schematic view of a graphene oxide sheet, according to the LK model, and a scheme of a generic CMG-based nanohybrid.

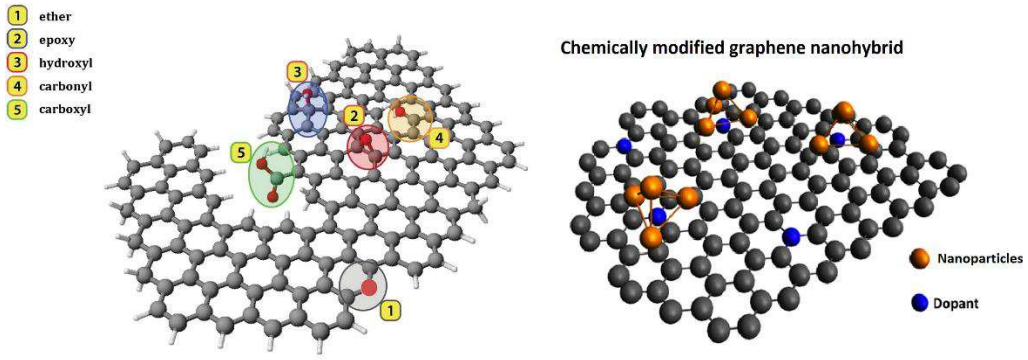

Figure 6: (left) schematic view of a graphene oxide sheet, according to the LK model; (right) schematic view of a generic CMG-based nanohybrid. Adapted from M. Favaro et al. ACS Catal. 2015, 5, 129-144.

Graphene oxide is a quite promising raw material due to its easy handling and manipulation (i.e. it is water soluble, producible in high yield, easy to assemble into different morphology)[30]. GO forms a stable dispersion in water, therefore it is a perfect candidate for aerosol processing, offering different ways to obtain large quantities of CMG-based or hybrid materials.[31,32,33] Particularly attractive is its crumpled form (i.e. micrometric GO sheets collapsed to form paper-like nanospheres[31]), since the wrinkling of GO sheets allows obtaining special active sites (i.e. strain induced chemical activity),[32] high surface area[31], but also maintaining good electrical conductivity[34] and a special nanostructure[31]. In Figure 7, crumpled GO is compared with different graphene-based structures, according to three fundamental properties: number of graphene layers, average lateral dimension and atomic carbon/oxygen ratio.[26]

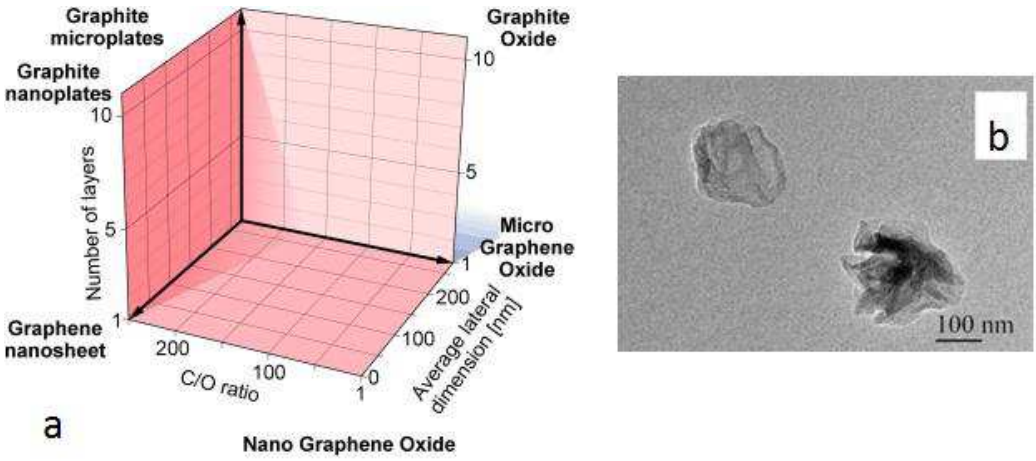

Figure 7: (a) Classification grid for the categorization of different graphene types according to three fundamental GBM properties: number of graphene layers, average lateral dimension, and atomic carbon/oxygen ratio. The different materials drawn at the six corners of the box represent the ideal cases according to the lateral dimensions and the number of layers reported in the literature. The values of the three axes are related to the GBMs at the nanoscale, but it is feasible to expand the values to the microscale, adapted from P. Wick, et al. Angew. Chemie Int. Ed. 2014, 2–7.; (b) TEM image of crumpled GO, adapted from X. Ma et al. Nano Lett. 2011, 12, 486–489.

5.2.1 Crumpling of graphene

The crumpling of two-dimensional materials is a quite general phenomenon that can be analysed by the same model either in the macroscopic or microscopic world. A paper or a biological membrane can be both seen like 2D materials because the thickness is very small relative to the sheet area, and the bending and folding of a planar sheet into a crumpled conformation is similar in the two cases. If a confining force is applied to a 2D sheet, ridges form, which eventually grow and interacts until a compact 3D conformation is reached. Non interacting materials, such papers, obey the scaling law:

$$M \, \alpha \, R_M^D \quad (1)$$

Where M is the sheet mass, R_M is the particle diameter and D is the fractal dimension of the crumpled sheet. D varies as $2 \leq D \leq 3$, where D=2 is a flat sheet and D=3 is a sphere. [31]

GO is water-soluble, and light scattering experiments of GO in aqueous solution have shown that D=2,15, consistently with a nearly planar material.[35] Those 2D nanosheets are attracting more and more attention given their special features and morphology. Theoretically, GO nanosheets have a large specific surface area of over 2500 m^2/g making them ideal 2D supports for various applications, from catalysis to sensors.

Since GO forms a stable dispersion in water, it is the perfect candidate for the mass production of CMG based materials. Furthermore it can be synthesized in large quantities by oxidizing inexpensive graphite powder, following Hummer's method[13] or different variations of this method. The principal issue concerning the use of these 2D nanosheets is their natural tendency to aggregate (restacking) due to strong intersheet adhesion (Van der Waals attraction). As a consequence of restacking, there is a reduction of the accessible surface area that compromises the advantage of the 2D structure. One possible solution is to turn the 2D nanosheets into 3D crumpled balls, and it is in this passage that aerosol processing is fundamental. A GO aqueous suspension can be atomized into fine droplets. In proper conditions, because of the rapid solvent evaporation in the aerosol droplets crumpled GO particles are formed by capillary compression: it is called evaporation-induced crumpling. This method is simple, has short processing time and can be applied in continuous production (Figure 8).

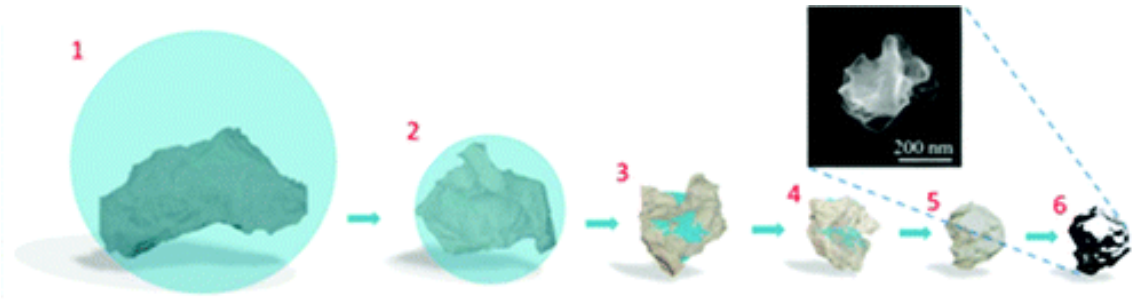

Figure 8: Schematic illustrating rapid H_2O loss and subsequent crumpling of GO nanosheets. Numbers represent the increasing time passed in the hot furnace. Reprinted with permission from W. Wang, et al. J. Phys. Chem. Lett. 2012, 3, 3228–3233. Copyright © 2012, American Chemical Society.

In spite of the simplicity of this idea, several parameters are involved in the crumpling such as precursor concentration and evaporation rate.

Wang et alii[36] have studied the correlations between confinement force and different parameters. The solvent evaporation rate (k) of a single droplet can be calculated starting from the droplet mass (m_d) and the evaporation time (τ_e):

$$k = {m_d}/{\tau_e} \quad (2)$$

The evaporation time, considering a continuum region, can be estimated as:

$$\tau_e = \frac{R\rho_d T_d D_d^2}{8 D_g P_d M} \quad (3)$$

where R is the gas constant, ρ_d is the droplet density, T_d is the droplet surface temperature (the water boiling point is assumed if the furnace temperature overcome 100°C), D_d is the droplet diameter, D_g is the gas-phase diffusion coefficient of the solvent, P_d is the vapour pressure of the solvent at droplet surface and M is the solvent molecular weight.

According to the model developed by Wang et alii, the confinement force *F* is proportional to the mass concentration of the precursor *C* ($F \propto C^{1.57}$) and to the evaporation rate k ($F \propto k^{4.72}$, so dependent on the furnace temperature), but it is inversely proportional to particle diameter D_p ($F \propto {D_p}^{-4}$). So experimentally if the precursor concentration is fixed, considering droplets size constant, the only parameter that influences the confinement force is the evaporation rate. In this situation, if the evaporation rate is slow, only GO nanosheets with ripples (called rippled GO) are formed. On the other hand, crumpled GO balls are obtained when the confinement force is strong. The minimum value of the confinement force for which GO can undergo crumpling, is 30 μN as calculated by Wang et alii.[36] However, research about crumpled GO is at its early stage and there is not yet a complete understanding of all the parameters involved.

Despite crumpling, the materials maintain over 1500 m^2/g of the accessible surface area, a value typically larger than those of conventional laminar or porous materials. In addition, crumpled structures have many edges and wrinkles that are extremely useful because connected to a higher reactivity. One example of the correlation between deformation and reactivity is the study of Wu et al.[32], who deposited monolayer graphene on a Si wafer substrate decorated with SiO_2 nanoparticles and used this substrate to graft aryl radicals using diazonium salts. By means of micro-Raman mapping, they found that the aryl radicals selectively react with the graphene regions above the NPs (Figure 9). This chemical reactivity enhancement was attributed to the strain energy increase induced by the local mechanical deformation of graphene.

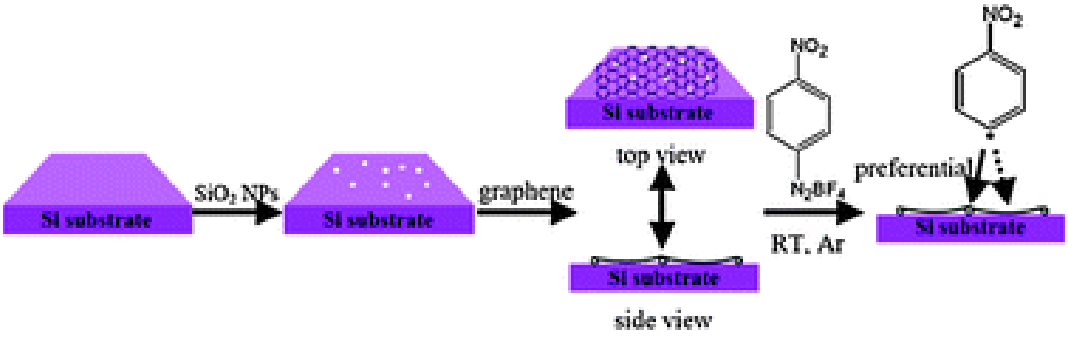

Figure 9: Transferring graphene onto substrates decorated with SiO2 NPs facilitated the selective functionalization with aryl radicals in regions of high local curvature. Reprinted with permission from Q. Wu et al. Chem. Commun., 2013, 49, 677-679. Copyright © 2012, Royal Society of Chemistry.

Other typical features of crumpled GO, studied by Luo et al[37], are that the particles have remarkably aggregation resistance either in solution or solid state, and remain largely intact and redispersible after chemical treatments, wet processing, annealing and even at high pressure compression (Figure 10).

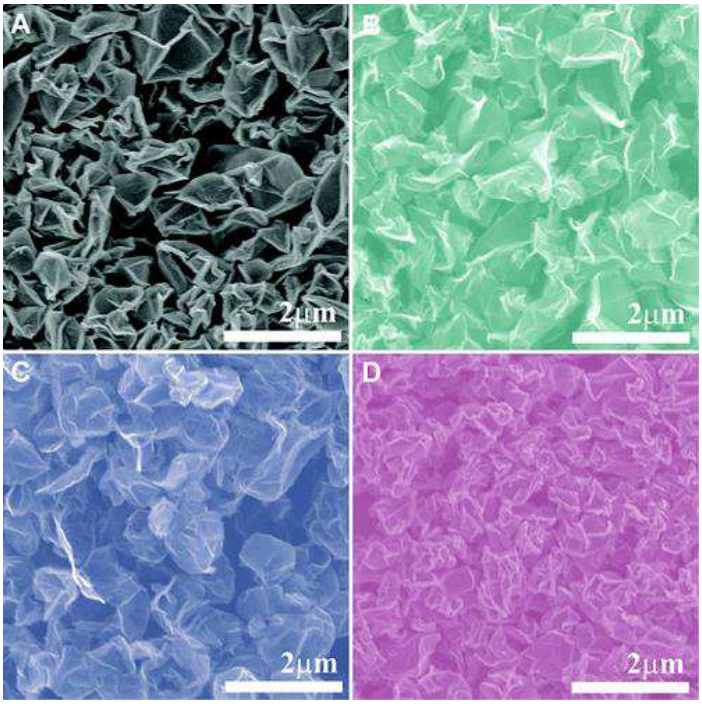

Figure 10: SEM images showing that crumpled morphology of GO is retained after (a) solution processing in methanol, (b) thermal shock at 400 °C, (c) microwave reduction, and (d) hydrazine reduction. Reprinted with permission from J. Suk, et al. ACS Nano 2010, 4, 6557–6564. Copyright © 2010, American Chemical Society.

Concerning the doping of cGO, during last years, chemically modified graphene based systems have been studied in the context of several applications, due to their excellent electrical, mechanical and thermal properties. One of the fields of greatest interest is the energetics and in particularly the research for valid substitutes of platinum for electrocatlysts in fuel cells. [34]. In this context, the graphene oxide (GO) is a promising carbon based starting materials due to its chemical reactivity and water solubility[12], whereas the crumpling of GO sheets allows obtaining many active sites but maintaining a high specific surface area.

The doping of graphene via CVD is a consolidated process.[38] Also the doping via annealing in gas precursor (NH_3, H_2S, Figure 11)[39] or by hydrothermal method[40] are well known in literature, but nowadays a one-step process which combines crumpling and doping of GO has not been studied yet.

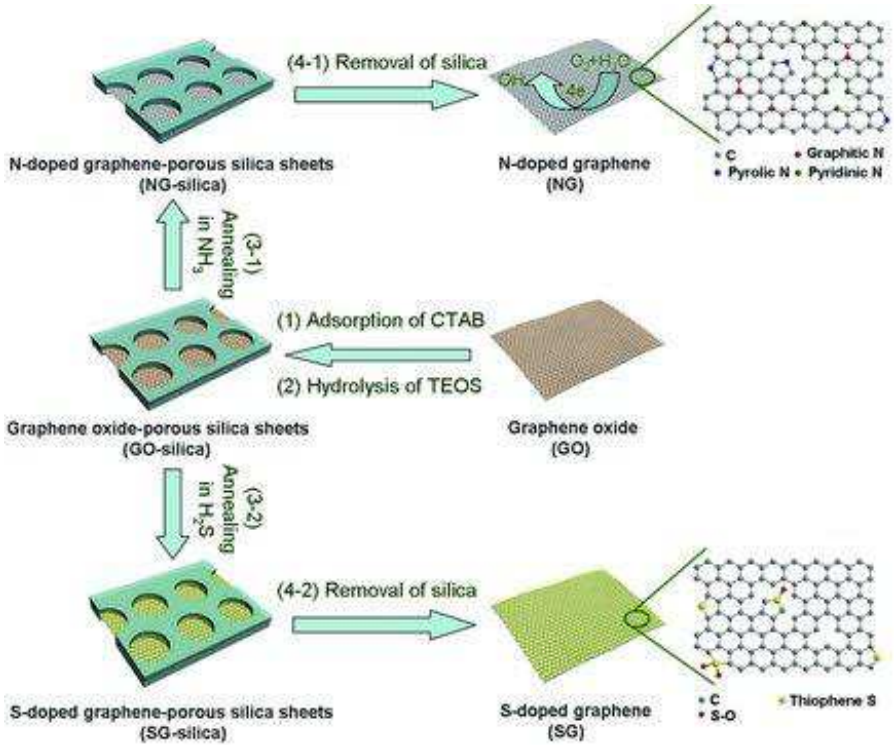

Figure 11: Schematic illustration of the fabrication of N and S-doped graphene: (1) and (2) hydrolysis of TEOS around the surface of graphene oxide with the aid of a cationic surfactant, cetyltrimethyl ammonium bromide (CTAB); (3-1) thermal annealing of GO-Silica sheets in ammonia at 600, 800, 900 and 1000 °C, respectively; (3-2) thermal annealing of GO-Silica sheets in H_2S gas at 500, 700 and 900 °C, respectively; and (4-1 and 4-2) removal of silica by HF or NaOH solution. Reprinted with permission from D. Wei et al. Nano Lett. 2009, 9, 1752–1758. Copyright © 2009, American Chemical Society.

The idea is that if a doping precursor is water-soluble, or at least well dispersible, it can be added to the starting GO containing solution used in the aerosol processing. During the flight of aerosol droplets through a hot furnace, the precursor undergoes thermal decomposition and reaction, while at the same time GO is crumpling. Moreover, the evaporation of the solvent helps the formation of possible direct chemical bonds between the precursors and the GO sheets. The result is the formation of doped CGO. Among the possible heteroatoms that can be introduced into the graphene lattice S, N have been provided the most promising results in the field of metal free electrocatalysts for ORR[41]. The addition of a crumpled structure to these types of catalysts can represent an interesting solution to maintain a high surface area, and to achieve a higher catalytic activity by exploiting the enhanced chemical activity of highly curved graphene sheets.

5.3 Graphene-based nanohybrids and Hydrogen Evolution Reaction

Aerosol processing of solutions containing GO is a powerful method to obtain graphene-based nanohybrids, which are composite materials made up by the integration of graphene with another nano-object, such as nanoparticles, large biomolecules, molecular compounds, etc. The advantage of the combination between aerosol processing and GO is that it is possible to have a starting solution already containing secondary precursors, that can be used for the introduction in the final materials of an additional component (e.g. nanoparticles, chemical modifier ect.). In this context, every aerosol droplet can be seen as a microreactor and, during water evaporation, different types of complex functional nanostructures can be synthetized.

For example, Chen et alii[33] have realized cargo-filled graphene nanosacks starting from a solution of GO and Ag NPs (Figure 12). In this case the droplets have 6 µm diameter and, with a GO concentration of 0,5 mg/ml, 10-15 sheets per droplet, as confirmed by HRTEM analysis. GO accumulates at water-air interface and, when droplet dries, the AgNPs are trapped into a graphene nanosack. This situation could be a model for graphene nanosacks because in the starting solution it is possible to include various types of NPs, or also different NPs in the same solution. Those components have to be water-soluble or highly dispersible and to diffuse faster than GO (so they do not accumulate at the drying front). Several potential applications can be envisaged for this structure: composite materials, electrodes, oxidation protection and drug delivery from sack leakage or biodegradation of GO.

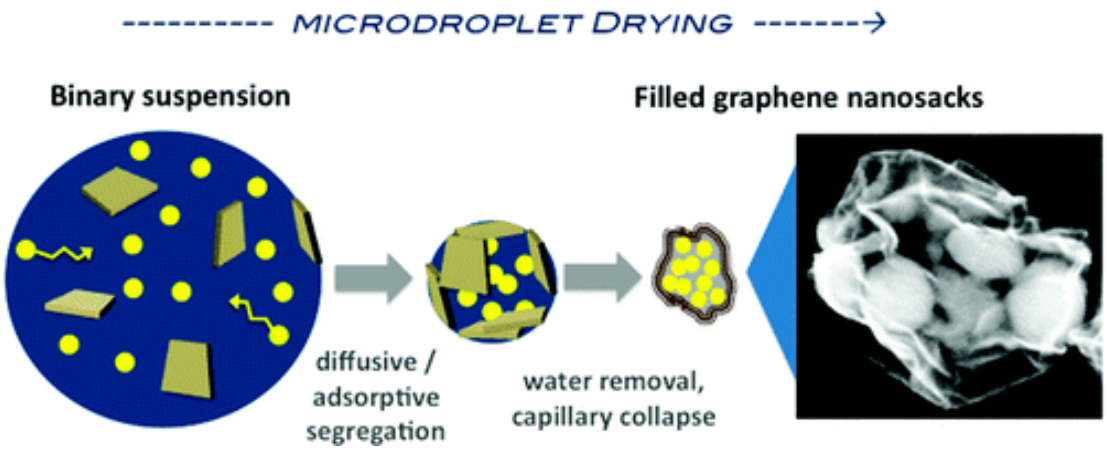

Figure 12: Conceptual model for the colloidal self-assembly of filled graphene nanosacks. Microdroplet drying leads to GO adsorption and scavenging at the receding gas–water interface and partial segregation followed by sack closure and collapse by capillary forces. Reprinted with permission from Y. Chen, et al. Nano Lett. 2012, 12, 1996–2002, Copyright © 2012, American Chemical Society.

A different approach to CGO-based hybrids entails the *in situ* growth of nanocrystals on GO sheets. Mao et al.[34] have included in the starting solution ions that adsorb on the surface of GO sheets, which act as a substrate for the localized crystallization or thermal decomposition (Figure 13). Starting from $Mn(NO_3)_2$, $SnCl_4$, $AgNO_3$ and H_2PtCl_6 these authors have successfully synthetized hybrid CG-nanocrystals of Mn_3O_4, SnO_2, Ag and Pt nanocrystals decorating the surface of GO sheets. In this case, the aerosol particles were carried by a gas flow through a preheated horizontal tube furnace. During the flight in the tube furnace, the droplets quickly dry and consequently the GO sheets start to crumple and at the same time the thermal decomposition or chemical reduction of the precursors lead to nanocrystals formation. CG-Mn_3O_4 and CG-SnO_2 were tested as electrode in

supercapacitors and lithium-ion batteries, obtaining performances better than conventional flat graphene-based hybrid materials. Interestingly, the aerosol processing allows the possibility to deposit directly onto various current-collecting substrates the CG-based hybrids, so capitalizing on their great potential for energy applications

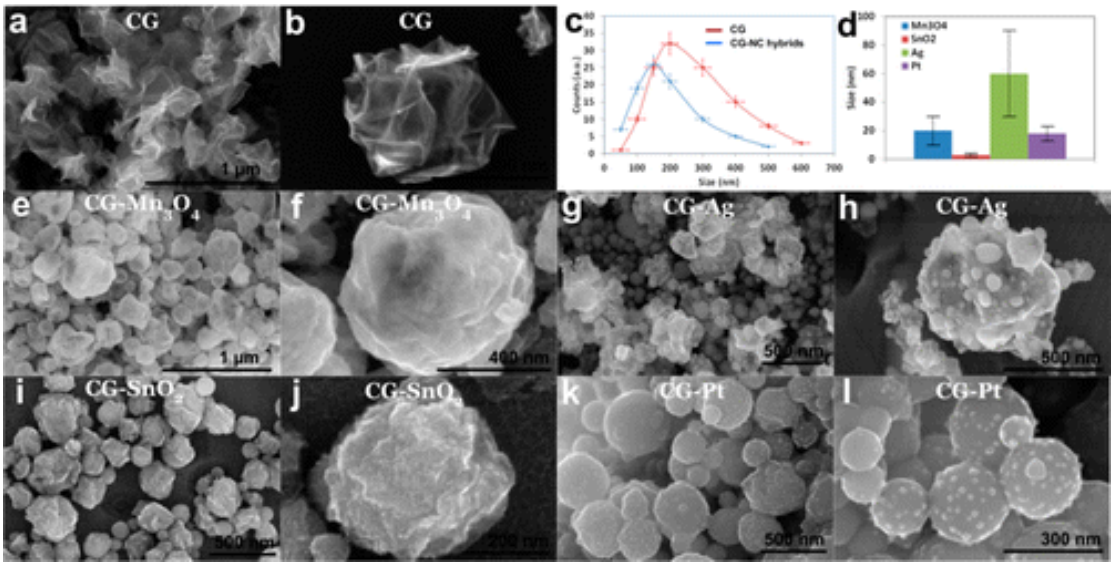

Figure 13: SEM images of bare CG and CG–nanocrystal hybrids: (a,b) bare CG balls; (e,f) CG–Mn3O4 nanocrystal hybrids; (g,h) CG–Ag nanocrystal hybrids; (i,j) CG–SnO2 nanocrystal hybrids; (k,l) CG–Pt nanocrystal hybrids. (c) Size distributions of bare CG and CG–nancrystal (NC) hybrids. (d) Measured size ranges of nanocrystals from SEM and TEM images. Reprinted with permission from S. Mao, et al. ACS Nano 2012, 6, 7505–7513. Copyright © 2012, American Chemical Society.

Another example of *in situ* growth of nanocrystals on CG is the study conducted by Mao et al.[34], who prepared bi-functional electrocatalysts composed of CG-CoO_x nanohybrids. The crumpled structure realized by aerosol processing offers a large surface area with stable anchoring sites for nanocrystals and minimizes the restacking of graphene sheets, enabling the full use of the whole catalyst surface area. Their study demonstrates that these nanohybrids show an ORR performance comparable with that of commercial Pt/C catalysts and an OER activity among the best reported for Co-based catalysts. Structures with these characteristics are very attractive for applications in fuel cells and electrolyzers and offer the possibility of developing a new class of non-precious metal carbon based catalysts.

In this context, we looked for new crumpled-graphene based nanohybrids for energy applications and we studied the synthesis of N-cGO-MoS_2 nanohybrids.

The research for a valid substitute to Pt as HER catalyst is fundamental for the diffusion on large scale of fuel cells. Nowadays the high cost of Pt-based catalysts is one of the major limiting factors to the diffusion of this technology. Moreover, the production of chemical fuels by using sunlight is an attractive and sustainable solution to the global energy and environmental problems. Photocatalytic water splitting is a promising route to capture, convert and store solar energy as H_2.

According to the literature, the hydrogen evolution reaction involves three possible reaction steps[42]:

1. Volmer step $H^+ + e^- \rightarrow H_{ad}$
2. Heyrovsky step $H^+ + H_{ad} \rightarrow H_2$
3. Tafel step $2H_{ad} \rightarrow H_2$

Therefore, HER may follow two mechanisms: Volmer-Heyrowsky or Volmer-Tafel according to the different rate-determing step of the reactions. However, in both cases the first step is the adsorption on hydrogen atoms at the surface of the catalyst. This step could limit the overall reaction rate: if the free energy of hydrogen adsorption (ΔG_H) to the surface is too weak (low concentration of H_{ad}) or too strong (hindering of desorption processes) the reaction rate will slow down. This is described by the so-called "volcano plot" which correlate the catalytic activity (HER exchange current) with ΔG_H (Figure 14).

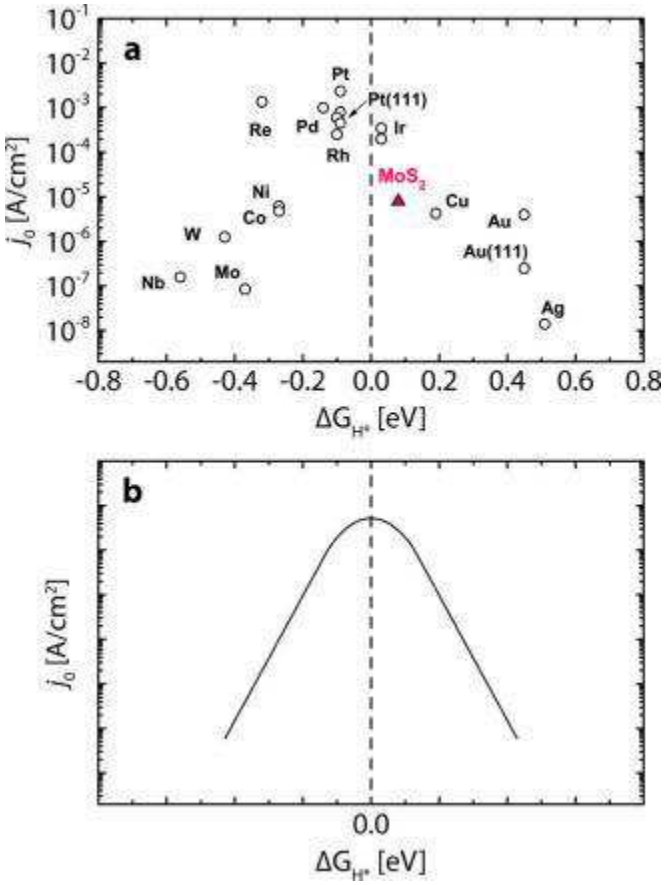

Figure 14: Exchange current density as a function of hydrogen adsorption free energy for various HER catalyst materials. (a) The experimental "volcano plot" for the HER is shown and Pt, with slightly negative hydrogen absorption energy, has the highest HER activity. (b) The theoretical HER volcano, adapted from Parsons, predicts catalysts with hydrogen binding energy equal to zero will have the highest activity. Reprinted with permission from J. D. Benck, et al. ACS Catal. 2014, 4, 3957-3971. Copyright © 2014, American Chemical Society.

It is clear that in order to maximize the HER catalytic activity the design of the catalyst if fundamental: it is not only a matter of choosing the best material, but the design of the surface (i.e. maximizing the number of active sites per unit of area) plays a key-role in the overall reaction rate.

MoS_2 is widely used as an electrocatalyst for HER. MoS_2 is a nontoxic, environmentally friendly and abundant semiconductor, so it has the entire precondition to be a candidate for a sustainable development. It belongs to the family of two-dimensional layered metal chalcogenide materials that have the general formula MX_2 (M=metal, X=chalcogen) and its bulk structure is similar to the graphene layer in graphite, with individually sandwiched S-Mo-S layers held together by Van der Waals interactions in hexagonally packed structures (Figure 15).[21] The thermodynamically stable surface of bulk MoS_2 consist of catalytically inert basal plane sites. [20] Moreover, should be mentioned that the electron/hole mobility along a basal plane is more than 2000 times faster than perpendicularly between the layers. Its activity toward HER is attributed to active sites located along the edges of its two dimensional layered crystal structure.

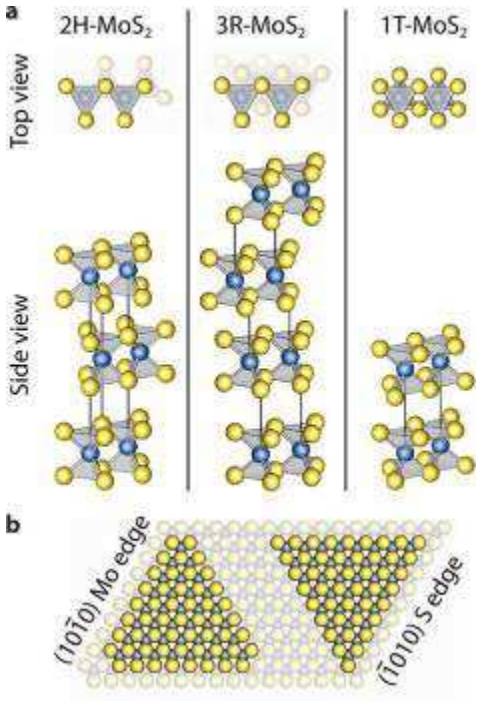

Figure 15. (a) Structure of the 2H, 3R, and 1T polytypes of MoS_2. (b) Top view of the Mo edge and S edge of a bulk MoS_2 crystal. Reprinted with permission from J. D. Benck, et al. ACS Catal. 2014, 4, 3957-3971. Copyright © 2014, American Chemical Society.

To expose as much active sites as possible, it is therefore necessary to grow nanostructured MoS_2. One example is the growth of single sheets of MoS_2 on Au(111) by deposition of Mo in a H_2S atmosphere followed by annealing in H_2S as reported by Helveg et al. (Figure 16). [43] The result is the formation of nanoplatelets with truncated triangular shape, exposing Mo and S edges. Combining catalytic tests and Scanning Tunneling Microscopy (STM) studies, they confirmed that the overall reaction rate scaled with the perimeter length of MoS_2 sheets rather that with their surface area. Moreover, was demonstrated that hydrogen adsorption depends on the coverage of sulfur at the Mo edge. The most favorable hydrogen binding towards HER was found for the Mo-edge covered by sulfur monomers, whereas edges exposing only Mo or only S seems to be catalytically inactive.[44]

Once again this highlight the importance of the design of the catalyst, in this case focused on the attempt of maximizing MoS_2 edge sites. In literature, confirming the great interest in this field, several MoS_2 nanostructure were reported in the last years: nanowires[45], nanoparticles[46], vertically aligned thin films[47], amorphous molecular cluster[48], etc.. All these studies confirmed that the improvement in MoS_2 performance was related to the increase

of the number and reactivity of active sites, to the reduction of the contribution of poor electrical transport in the direction perpendicular to the platelets and to the improvement electrical contact between different active sites.[49]

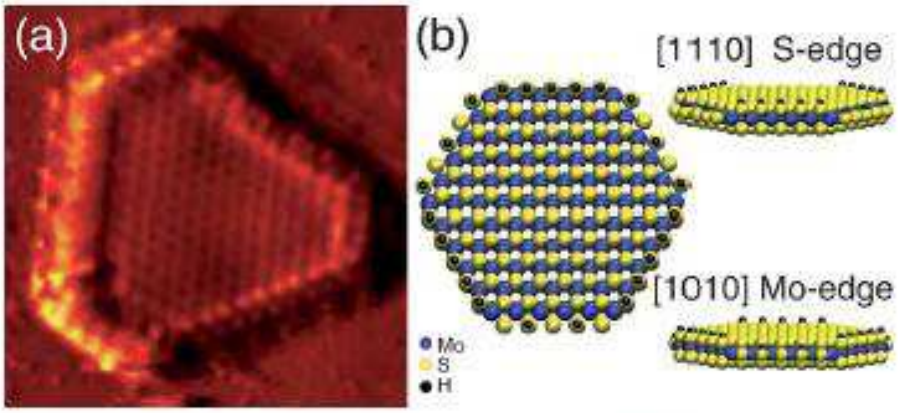

Figure 16: (a) STM on MoS_2 nanoplatelets on Au(111); (b) molecular model of a platelet exposing both Mo and S edges. Reprinted with permission from A.B. Laursen et al, Energy Environ. Sci., 2012,5, 5577-5591, Copyright © 2012, Royal Society of Chemistry.

In order to improve the electrocatalytic properties of MoS_2, another strategy is to synthesize supported MoS_2 nanostructures. MoS_2 NPs supported on rGO, prepared by solvothermal synthesis, have proven to be active HER electocatalysts.[50] Another example of graphene-supported MoS_2 NPs was reported by A. J. Smith et al..[51] They synthesized crumpled reduced graphene through aerosol process, in order to avoid the restacking of graphene sheets. In a successive step, they impregnated the crumpled rGO particles in a solution containing MoS_2 precursor (ammonium tetrathiomolybdate). Finally, through thermal decomposition of MoS_2 precursor in controlled atmosphere, they obtained a MoS_2 coating on crumpled rGO particles, which was active for HER. In these cases, rGO was considered as a support to improve electron conduction and the dispersion of small NPs in order to maximize the number of active edge sites. Interestingly, hybrid materials based on graphene and MoS_2 were investigated also as photoelectrocatalyts for HER. Meng et al.[6], following hydrothermal methods, have synthetized n-doped rGO over which p-type MoS_2 nanoplatelets have been grown. Every nanoplatelet on a rGO nanosheet forms a nanoscale p-n junction: charge recombination is suppressed and therefore the photogeneration of electron-hole pairs is enhanced. In this system, MoS_2 acts not only as catalytic centre, but also as a photocenter for absorbing solar light to generate charge carriers. Simultaneously, n-doped rGO does not act only as conductive support, but its doped structure is fundamental for the creation of p-n nanojunctions. This is a good example of multiscale design of a catalyst. In fact, the material was designed both at the atomic scale (N-doping of graphene) and at the nanoscale (synthesis of MoS_2 NPs). It should be noticed that from the point of view of the photocatalysis, MoS_2 itself has negligible photocatalytic activity. It has shown photocatalytic activity coupled with $Ru(bpy)_3^{2+}$-based photosensitizer molecules,[52] indicating that the limit may be an insufficient charge separation (Figure 17). This suggests that if MoS_2 is employed in a photoelectrocatalytic system, the design of the material must be carefully studied in order to be able to use efficiently the generated electron-hole pairs.

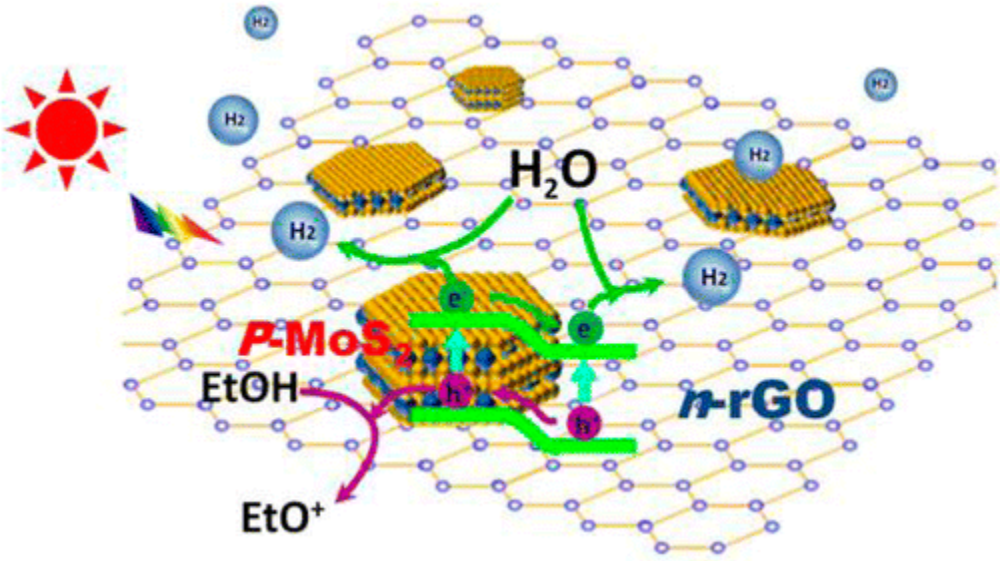

Figure 17: schematic view of p-type MoS_2 nanoplatelets deposited on the n-type nitrogen-doped reduced graphene oxide (n-rGO) nanosheets to form multiple nanoscale p–n junctions in each rGO nanosheet. The p-MoS_2/n-rGO heterostructure shows significant photocatalytic activity toward the hydrogen evolution reaction (HER) in the wavelength range from the ultraviolet light through the near-infrared light. Reprinted with permission from. F.Meng et al. J. Am. Chem. Soc. 2013, 135, 10286–10289. Copyright © 2013, American Chemical Society.

The aerosol processing can be a new method to synthetize MoS_2 based nanohybrids with photocatalytic or electrocatalytic activity for HER. Aerosol synthesis starting from aqueous solution of $(NH_4)_2MoS_4$, with a reactor temperature of 700°C, lead to corrugated spheres of MoS_2 with a diameter of the order of 100 nm.[53] The aim of this study is to realize a new N-cGO-MoS_2 nanohybrid through a one-step aerosol processing. The underlying idea is that the crumpling process, since it can preserve a high surface area of GO, makes available a large number of sites where the MoS_2 NPs can grow or alternatively can induce the formation of MoS_2-filled GO nanosacks depending on the process parameters. With this approach, we could design the final catalyst from the micro to the atomic scale in a fast one-step process.

5.4 Fast One-Pot Synthesis of MoS_2/Crumpled Graphene p-n Nanonjunctions for Enhanced Photoelectrochemical Hydrogen Production

In the following paragraphs, we will demonstrate how aerosol processing allows preparing in high yield and short time hierarchical graphene nanocomposites with special crumpled morphology. [54,31,55,56] By modular insertion of suitable precursors in the starting solution, it was possible to synthesize different types of graphene based materials ranging from heteroatoms doped graphene nanoballs, to hierarchical nanohybrids made up by nitrogen doped crumpled graphene nanosacks that wrap finely dispersed MoS_2 nanoparticles. These materials were carefully investigated by microscopic (SEM, standard and HR TEM), grazing incidence X-ray diffraction (GIXRD) and spectroscopic (high resolution photoemission, Raman and UV-visible spectroscopy) techniques, evidencing that nitrogen dopants provide anchoring sites for MoS_2 nanoparticles, whereas crumpling of graphene sheets drastically limits aggregation. The activity of these materials were tested toward the photo-electrochemical production of hydrogen, obtaining that N-doped graphene/MoS_2 nanohybrids were seven times more efficient with respect to single MoS_2 because of the formation of local p-n MoS_2/N-doped graphene nanojunctions, which allow an efficient charge carrier separation.

5.4.1 Experimental Section

Structural characterization tools.

High-resolution X-ray photoemission (HR-XPS) spectra were acquired at the BACH beamline at ELETTRA synchrotron facility (Trieste, Italy) using 1000 eV photons and a total energy resolution of 0.27 eV. The measurements were taken after a short annealing at 300°C in UHV. The calibration of the binding energy (BE) scale was determined using the Au $4f_{7/2}$ photoemission line as reference (samples deposited over Au coated silica filters). Conventional XPS were acquired using a conventional x-rays source (1486.6 eV photons). The measurements of the as-prepared materials were taken after a short annealing at 150°C in UHV. The calibration of the binding energy (BE) scale was determined using the Si 2p photoemission line as reference (samples deposited over Si(100) wafer). The XPS peaks were separated into individual components (after Shirley background removal) using symmetrical Voigt functions and non-linear least squares routines for the χ^2 minimization.

The nano- and micro-scale morphology of materials was studied by scanning electron microscopy (SEM) and transmission electron microscopy (TEM). SEM images were acquired using a field emission source equipped with a GEMINI column (Zeiss Supra VP35), micrographs were obtained with an acceleration voltage of 5 or 10 kV using in-lens high-resolution detection. TEM images were acquired using a FEI Tecnai 12 microscope with an acceleration voltage of 100 kV. STEM and HRTEM micrographs were acquired using a JEM-2100F Field Emission Electron Microscope operating at 200 kV. Energy Dispersive X-ray Spectroscopy (EDS) elemental maps were acquired with the same instrument. Grazing incidence X-ray diffraction (GIXRD) patterns were collected using a Philips PW 1710 diffractometer equipped with a Cu Kα radiation tube operating at 40 kV and 40 mA and with an incidence angle of 1°. Characterization by Raman spectroscopy was performed using a ThermoFisher DXR Raman microscope. The spectra were recorded using a laser with an excitation wavelength of 532 nm (1 mW), focused on the sample with a 50× objective (Olympus). Raman maps were recorder using the same parameters, but with the 100× objective. UV−visible-NIR absorption spectroscopy was performed using a Cary 5000 spectrometer (Varian), in the 500−1200 nm range. Powder samples were dispersed in ethanol, forming a stable colloidal

dispersion. All spectra were recorded using 1 mm optical path quartz cells. The concentration and the experimental parameters were tuned to minimize scattering effects.

Electrochemical Characterization.

Electrochemical measurements were carried out in a conventional three-electrode cell, using an Ar-saturated 0.5 M H_2SO_4 solution as electrolyte. An Ag/AgCl (KCl_{sat}) electrode (calibrated as 0.217 V vs RHE) and a glassy carbon rod were used as reference and counter electrodes, respectively. Working electrodes were prepared by collecting the MoS_2 NPs and the N-cGO/MoS_2 nanohybrids in Toray paper (TGP-H-60), as described above, and adding 2.5 µL of Nafion solution (8 vol. %, Sigma Aldrich). Commercial MoS_2 (Sigma-Aldrich) was drop-casted on Toray paper and used as reference. Materials activity toward HER was evaluated by recording polarization curves from a certain potential to -0.4 V vs RHE using a scan rate of 2 mVs^{-1}. For each material, the starting potential was set at 50 mV more positive than its open circuit potential (OCP). To investigate the possible activity enhancement due to the p-n nanojunction formed between the smallest MoS_2 NPs and the N-cGO, i-t curves were recorded at different potentials (-0.1, -0.15, -0.25 V vs RHE) in absence and presence of light, using a white LED lamp (OSRAM - 9 LED Star Oslon 150 white 1170 lm/cm^2@350 mA) as light source. The current densities were normalized to the electrode geometric area (in cm^2) and the amount of Mo (in mg) for a better comparison among different materials. Impedance spectroscopy was performed in the frequency range between 100 and 0.1 KHz on different materials drop-casted on glassy carbon electrodes. All the experiments were performed at room temperature.

Synthetic procedures.

In order to reach the final goal of this work, i.e the preparation of N-cGO/MoS_2 nanohybrids, we investigated the synthesis by means of aerosol process of progressively complex nanosystems, namely cGO, nitrogen doped cGO, MoS_2, and doped cGO/MoS_2. All synthesis protocols are based on the formation of an aerosol operated by a Sonaer ultrasonic 2.4 MHz nebulizer (particle size about 1.7±1 µm) starting from an aqueous precursor solution. Facing new materials for the first time, the integrated aerosol reactor needs constant *ad hoc* modifications for optimizing differently tailored syntheses. Therefore, in the present work we developed from scratch a furnace assisted aerosol reactor specifically devoted to the preparation of these nanocomposites based on 2D materials.

The aim was to develop a system that, through the switching of simple connections, allows working in different configurations (i.e. at low vacuum or near ambient pressure, using reactive or inert gases, etc.). The basic structure is constituted by the particle generator, connected by a homemade flange directly to the quartz tube (inner diameter: 2.5 cm) that goes through a hot-wall CVD tube furnace (Carbolite MTF 12/25/250).

Particles generated by the ultrasonic nebulizer are forced to pass through a tubular furnace (RT-1200°C), by using a mixture of N_2 and H_2 as carrier gas (see Figure 22). Crumpling process takes place during the whole time-of-flight of the aerosol droplets, but mainly during the passage through the hot furnace, where water evaporation is very fast. Si(100) wafers, gold coated silica filters (EPM2000), and Toray paper were used as substrates for collecting the particles. Typical collection time was 30 min. In order to find the optimal parameters for the synthesis of the desired materials, we have investigated the effect of different experimental parameters (precursors concentration, furnace temperature, carrier gas flow and composition).

As previously discussed, the confinement force that causes the GO sheet crumpling is proportional to the solvent evaporation rate and to the precursor concentration, while it is inversely proportional to aerosol droplet size. The size of the droplet is defined by the operative frequency of particle generator and to the viscosity of the solvent. Therefore, in our case, the droplet size could be considered a constant since we always employed aqueous solutions and the same particle generator. Conversely, modifying the furnace temperature (400-1000°C) and the gas flow (50-500 sccm) we can influence the solvent evaporation rate and consequently the crumpling and the reduction degree of GO, the thermal decomposition of MoS_2 precursor, and the doping. By changing the precursors concentration, we can modify the crumpling of graphene and the final distribution/agglomeration of MoS_2 NPs. Moreover, modifying the carrier gas composition (i.e. adding for example a reducing gas such as H_2) it is possible to influence the GO reduction degree and doping, and the thermal decomposition of MoS_2 precursor.

Hereafter, we will present some experimental results (Raman spectroscopy, SEM, and conventional laboratory XPS) obtained during the optimization of the synthesis parameters, in order to provide the reader with an overview of the correlation between them and the materials morphologies and compositions.

- *Furnace temperature: influence on GO crumpling and reduction.*

Furnace temperature is one of the most important parameter in crumpling process, because at higher temperature the aerosol droplet evaporation is faster and the confinement force is stronger. The effect on the crumpling was studied analyzing samples obtained varying the furnace temperature from 600°C to 1000°C. In order to carry out these studies, we collected the crumpled particles directly on a Si(100) substrate using 500 sccm of N_2 as carrier gas. SEM images show that the increment in the furnace temperature leads to the aggregation of single crumpled balls. However, in spite of this aggregation, by carefully analyzing the SEM micrographs it results that the single particles size ranges from 400 to 100 nm in all the samples and that all the particles are morphologically similar.

Raman spectra ($\lambda_{exc} = 532$ nm, $P_{Laser} = 4$ mW, 100x objective, Figure 18) were collected on cGO synthesized at different furnace temperatures. The intensity ratio between D (~ 1350 cm^{-1}) and G (~ 1600 cm^{-1}) bands as a function of the temperature, $I_D/I_G\,(T)$, is a useful parameter to check the reduction GO. The creation of small new sp^2 patches due tothe reduction of GO, induces an increase of the D band and consequently a larger I_D/I_G ratio. Consequently, GO samples annealed at higher temperature have a higher I_D/I_G ratio.

Here we report the $I_D/I_G\,(T)$ for cGO synthetized at different temperature:

$$I_D/I_G\,(600°C) = 1.0 \quad I_D/I_G\,(800°C) = 1.0 \quad I_D/I_G\,(1000°C) = 1.1$$

The small increase of the D band can also be explained cGO is explained because the crumpling can introduces also some sp^3 defects into the sp^2 lattice, as underlined below in the XPS data.

These are average value of I_D/I_G because in the same sample there could be little variations (in a range of ±0,05) from spot to spot in the ratio value. In addition, the Raman shift of G and D band Raman shift could change slightly in the same sample, but only in a range of 2 or 3 cm^{-1}. These small changes within a sample were found

in all the samples analysed. The average values are centred at 1599 cm^{-1} and at 1356 cm^{-1}, respectively. Considering the Raman spectra of the as prepared GO, a significant shift to higher frequency can be noticed in the G band frequency as a result of the crumpling process. This can be associated with the reduction of GO due to high furnace temperature.

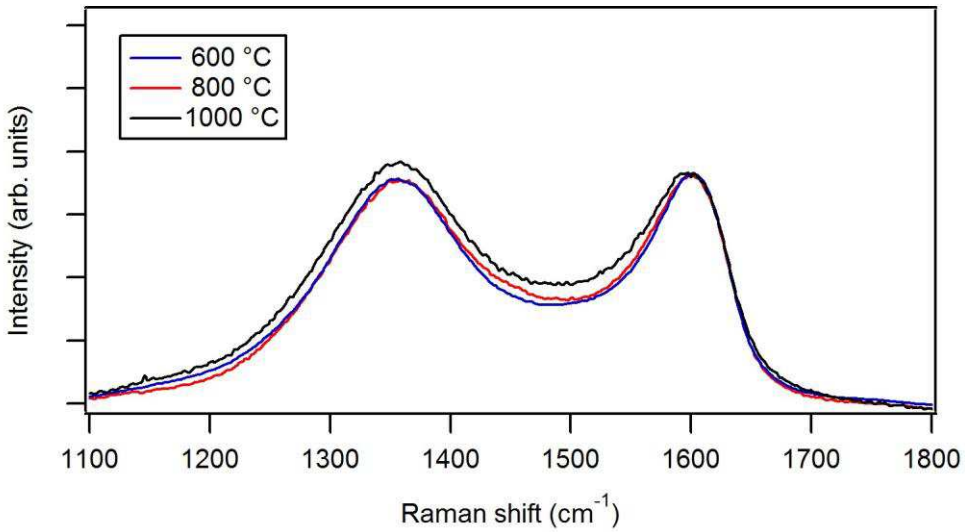

Figure 18: Evolution of the Raman spectra (D and G band) of cGO collected on Si(100) and synthesized with different furnace temperature (600, 800 and 1000°C).

XPS allows us to understand the effect of our synthesis parameters on the chemical composition of the GO papers by the analysis of the carbon chemical state. For the samples synthesized with a furnace temperature of 600, 800 and 1000°C the C 1*s* photoemission lines, deconvoluted into seven single peak components, are shown in Figure 19. The details of the C 1*s* photoemission line fitting will be discussed in the Main results paragraph. Here it is important to notice that the main component of the C 1*s* photoemission lines is related to sp^2 hybridized carbon (black curves in Figure 19) in the samples synthesized at 600°C and 800°C. Instead, in the sample obtained at 1000°C the sp^3 component (blue curves in Figure 19) is the most intense, and this could be related to a higher degree of crumpling of the sheet structure, that can induce many defects in the sp^2 domains.

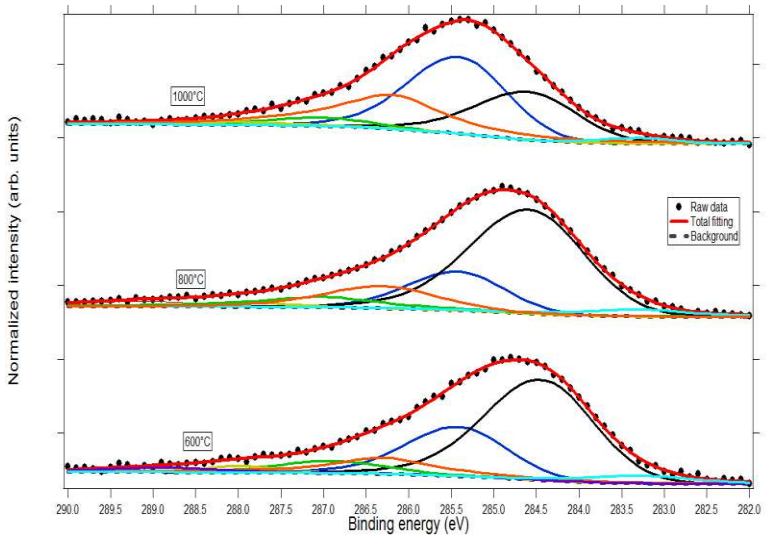

Figure 19: C1s photoemission lines of cGO synthesized with furnace temperature of 600°C (lower), 800°C (medium) and 1000°C (upper).

- *Doping and crumpling of GO*

We have investigated different types of graphene doping: N-doping and N-S doping. We present here the results obtained for the S-N doping with the furnace temperature maintained at 900°C, using 500 sccm of N_2 or N_2/H_2 as carrier gas and collecting the particles on a Si(100) substrate. With lower furnace temperature (i.e. 500-600°C) we verified that the degree of doping was very low and therefore these data will not be discussed here. The data related to N-doped cGO will be discussed in the Main Results paragraph.

In order to obtain S-N doping, we mixed to a 1 mg/ml GO aqueous solution L-cysteine or thiourea in order to have a mass ratio of 5:1 with respect to GO. In Table 1 we summarized the results of XPS analysis on these samples. Notably, the S/N content in the dual doped samples is approximately equal to the S/N content of the precursors (1:2 for thiourea and 1:1 for L-cysteine). From the deconvolution of S 2s and N 1s photoemission lines, we verified that the component of oxidized S and N species was very high in these samples. Therefore, in the case of thiourea (Figure 20), in order to lower the amount of oxidized species, we investigated the effect of the introduction of H_2 in the carrier gas (N_2/H_2=10/1 (v/v)). These data suggest that employing molecular hydrogen in gas streamis useful in order to decrease the amount of oxidized dopants in favor of the reduced defects, especially in the case of N species.

Table 1: Summary of quantitative surface analysis by XPS on doped and crumpled GO samples.

	GO+thiourea (with H_2)	GO+thiourea	GO+L-cysteine
N/C % (at/at)	5.5	5.3	10
S/C % (at/at)	2.5	2.4	11
SO_x/S_{tot} %	80	100	100
NO_x/N_{tot} %	0	20	15

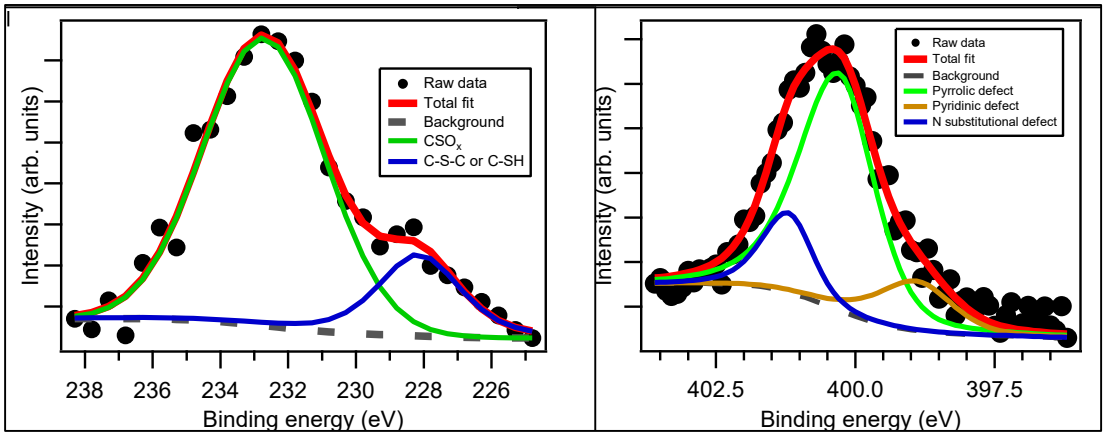

Figure 20: S2s (left) and N1s (right) photoemission lines of a sample of S-N doped cGO, synthesized employing nitrogen and hydrogen as gas carriers (heteroatoms precursor: thiourea.)

As previously mentioned, heteroatoms doped graphene is currently studied as substitute of Pt in fuel cells. Therefore, as future perspective, these kinds of doped and crumpled graphene materials could be tested for the ORR electocatalysis.

- *Effect of MoS_2 precursor ($(NH_4)_2MoS_4$) concentration on hybrid material morphology*

In order to investigate the effects of $(NH_4)_2MoS_4$ concentration on the MoS_2-cGO nanohybrids synthesis, we present here the results extrapolated from the analysis of various synthesis carried out with a nitrogen flow of 500 sccm, a furnace temperature of 900 °C and as substrate a piece of Si (100) wafer. In the starting aqueous solutions, the GO concentration was maintained at 0.5 mg/ml, while the ammonium tetrathiomolybdate concentration was varied from 5 to 0.1 mM. The decision to change the MoS_2 precursor concentration, keeping fixed other parameters, derives from the analysis of the first sample synthetized with an ammonium tetrathiomolybdate concentration of 5 mM. As we can observe in the SEM micrograph in Figure 21, it is clear that the collected product is almost totally formed by MoS_2 NPs. In the Raman spectra of this sample the characteristic D and G band of GO were barely visible, and only the peaks related to MoS_2 were clearly measurable. Decreasing the MoS_2 precursor concentration, we finally obtained a good dispersion of MoS_2 NPs on the crumpled graphene sheets, as we will show in the Main Results paragraph.

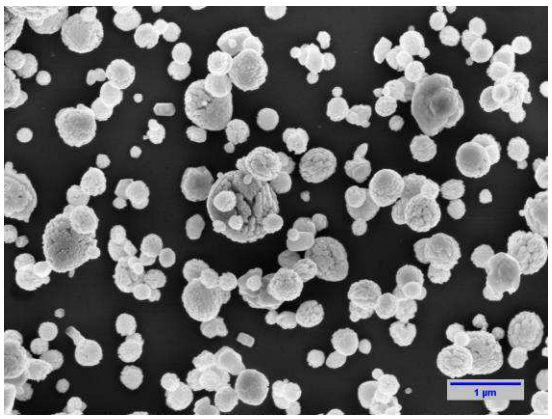

Figure 21: SEM image of the product collected on Si(100) starting from a solution with GO concentration of 1 mg/ml and ammonium tetrathiomolybdate concentration of 5 mg/ml.

- *Optimized synthesis parameters*

The optimized experimental parameters for the synthesis of the materials that will be the focus of our discussion (cGO, N-doped cGO, MoS_2 NPs, N-cGO/MoS_2) were:

Furnace temperature = 900°C

Carrier gas composition = N_2/H_2, 9:1 (v/v)

Carrier gas flow = 100 sccm

The precursor solutions for the different materials were optimized as follows:

c-GO: GO suspension (0.5 mg/ml)

N doped c-GO: GO suspension (0.5 mg/ml) in 5M NH_3 (Sigma-Aldrich) solution.

MoS_2 NPs: 1 mM $(NH_4)_2MoS_4$ aqueous solution (Sigma-Aldrich)

N-cGO/MoS_2: GO suspension (0.5 mg/ml) in 5M NH_3 (Sigma-Aldrich) and 1 mM $(NH_4)_2MoS_4$ (Sigma-Aldrich).

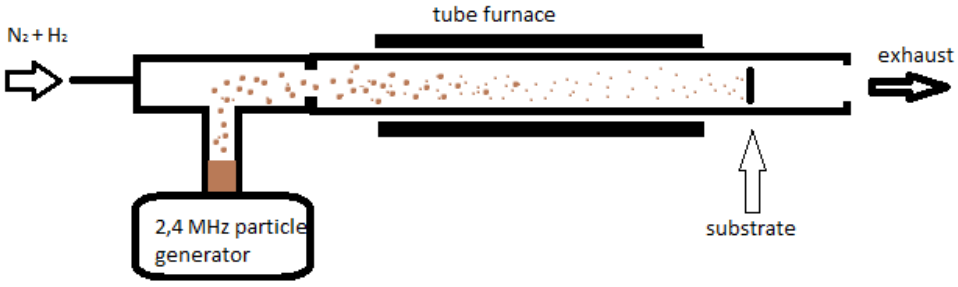

Figure 22: schematic view of the experimental setup.

5.4.2 Results and Discussion

In this work, we investigated the preparation by aerosol technique of progressively more complex nanosystems, namely pure and doped cGO, MoS_2 NPs, MoS_2/cGO composites and eventually N-cGO/MoS_2 nanohybrids. Notably, all materials were prepared using the same synthesis protocol (e.g. forming an aerosol transported by a H_2/N_2 gas carrier through a furnace kept at 900°C), simply by adding a further component (i.e. a NH_4OH to induce nitrogen doping, and $(NH_4)_2MoS_4$ for the formation of MoS_2 NPs) in solution that undergoes aerosolization (see scheme 1). The structural and chemical properties of these systems were thoroughly investigated by spectroscopic and microscopic techniques, and the knowledge acquired on the single component materials, allowed us to rationally design a new nanohybrid based on a p-n junction between MoS_2 and N-doped graphene that exhibits excellent catalytic activity for photoelectrochemical hydrogen generation. From this point, the images and portion of the text are reproduced with permission from "F. Carraro, L. Calvillo, M. Cattelan, M. Favaro, M. Righetto, S. Nappini, I. Pís V. Celorrio, D. J. Fermín, A. Martucci, S. Agnoli and G. Granozzi, Fast One-Pot Synthesis of MoS2/Crumpled Graphene p−n Nanonjunctions for Enhanced Photoelectrochemical Hydrogen Production, ACS Appl. Mater. Interfaces 2015, 7, 25685−25692." Copyright 2015 American Chemical Society.

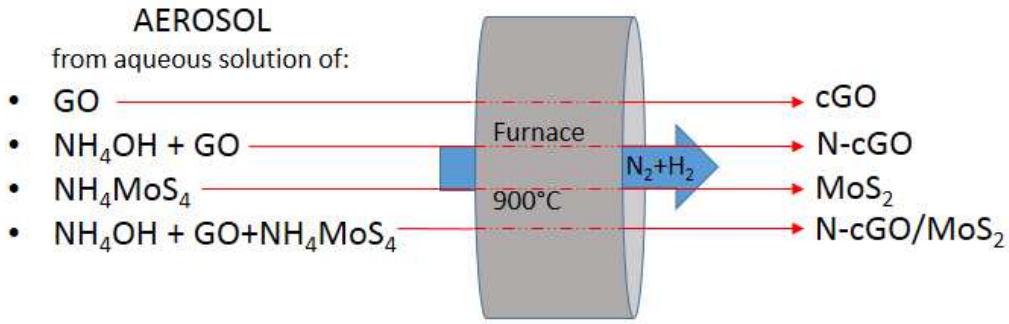

***Scheme 1**: schematic representation of the rationale for materials.*

*Physico-chemical characterization***.**

The chemical composition of the different materials was studied by HR-XPS employing synchrotron radiation. Figures 1a and 1b shows the C 1s and N 1s photoemission spectra of N-cGO. The C 1s photoemission line (Figure 24a,c) was separated into six chemically shifted components according to the standard procedure reported in literature:[57,58,59] the most intense peak, centered at 284.4 eV, is associated with sp^2 hybridized carbon atoms, whereas the peak at 285.4 eV can be related either to sp^3 hybridized carbon component, which is connected to the crumpling of the sheets, or to C-N bonds. The features centered at 286.2, 286.8 and 287.9 eV are associated with tertiary alcohols[60], epoxy[61] and carbonyl groups[60], respectively. These three components are strongly reduced with respect to pristine GO (see the C 1s spectra reported in Figure 23). A minority component associated with defective carbon atoms is found at 283.7 eV.[62,63] The successful nitrogen doping of graphene by aerosol processing, as well as the nature of the N functional groups formed, was determined by separating the N 1s photoemission line into three chemically shifted components (Figure 24b). The peak centered at 398.5 eV is associated with pyridinic defects, whereas the components at 400 eV and 401.3 eV are related to pyrrolic and N substitutional defects, respectively.[59,64] Elemental analysis, carried out by considering the area of the C 1s and N 1s peaks and their corresponding sensitivity factors, indicates a nitrogen content of about 4% (at %). To the

best of our knowledge, this is the first example where the aerosol technique is used for preparing CMGs. A detailed investigation of the doping process was beyond the scope of the present work; however, as we mentioned in the Experimental details section, we want to underline that by using other simple water soluble precursors, it is possible to introduce into GO a full range of dopants (N, S) in different combinations.

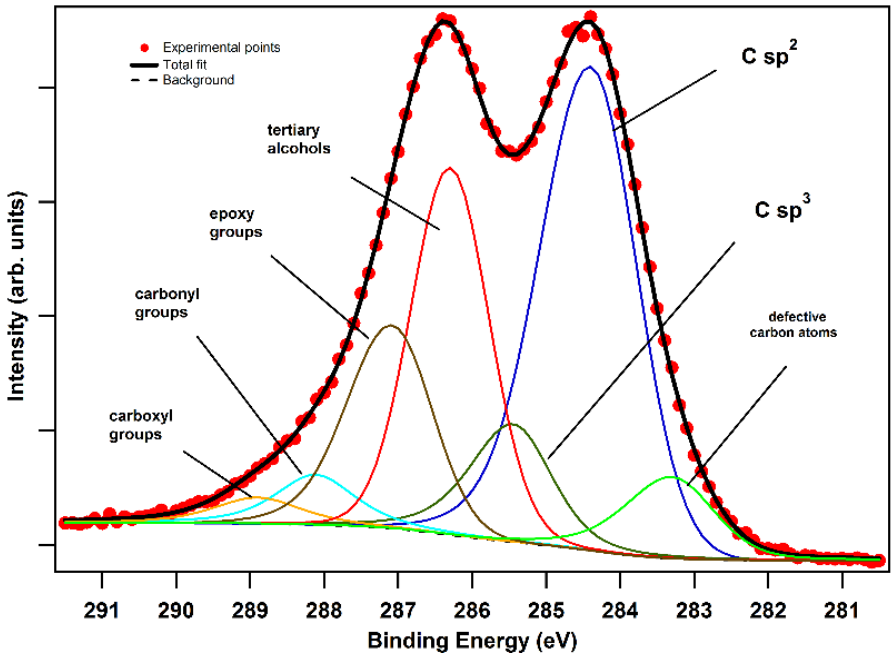

Figure 23: C 1s photoemission line of as-prepared GO.

In the case of the N-cGO/MoS_2 nanohybrids, the C 1s photoemission line was separated into five components (Figure 24a,c). The only significant difference with respect to N-cGO is the absence of the minority component related to defective carbon at 283.7 eV.

In N-cGO/MoS_2, the N 1s and Mo $3p_{3/2}$ photoemission lines overlap, making difficult the analysis of the N-doping. We noticed an anomalous intensity ratio between Mo $3p_{3/2}$ and Mo $3p_{1/2}$ peaks that can be associated with the presence of the N 1s photoemission line. In order to separate both contributions, the Mo 3p spectral region was carefully separated into two single chemically shifted components with a fixed spin orbit split of 17.6 eV, as shown in Figure 24d

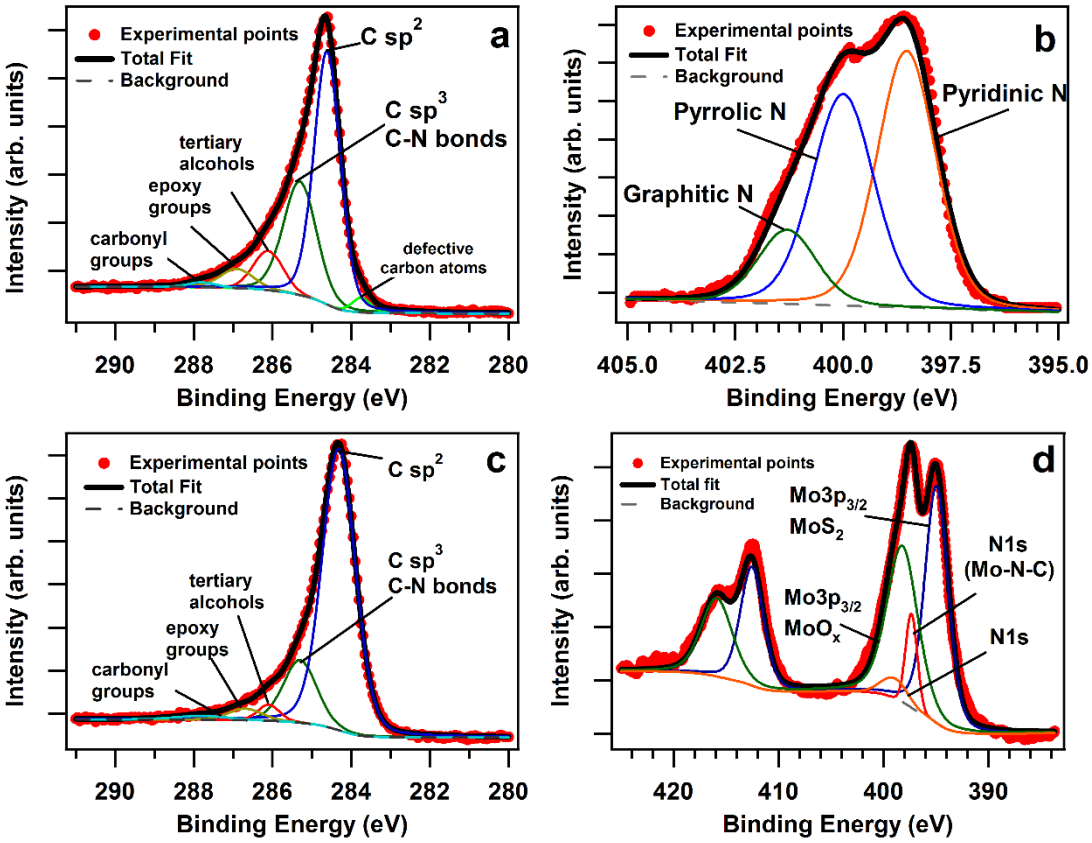

Figure 24: (a) C 1s and (b) N 1s photoemission lines of N-cGO; (c) C 1s and (d) Mo 3p and N 1s photoemission lines of N-cGO/MoS_2 nanohybrids.

The Mo $3p_{3/2}$ component related to MoS_2 is centered at 395 eV, whereas the Mo $3p_{3/2}$ components centered at 398.3 eV is related to MoO_x oxidized species.[65] The presence of MoO_x species is not unexpected since the XPS data were collected on ex-situ prepared samples and MoS_2 edges can partially be oxidized in air.[66] To increase the accuracy of the fitting procedure, the ratio between these Mo species was based on the deconvolution of the Mo 3d photoemission line (see below). Subsequently, two additional components related to the N 1s region were added; one at 397.4 eV attributed to C-N-Mo species,[67] and another one centered at 399.2 eV associated with C-N bonds, which includes the contribution of pyridinic and pyrrolic groups and of N substitutional defects.[64,59] Quite interestingly, the presence of C-N-Mo bonds indicates that N heteroatoms in doped cGO act as nucleation centers for the MoS_2 NPs. This hypothesis is also supported by the fact that the component at 397.5 eV cannot be related to N doping of MoS_2, or to the formation of MoN, because this component is not present in the spectrum of bare MoS_2 NPs synthesized in presence of ammonia (Figure 25).

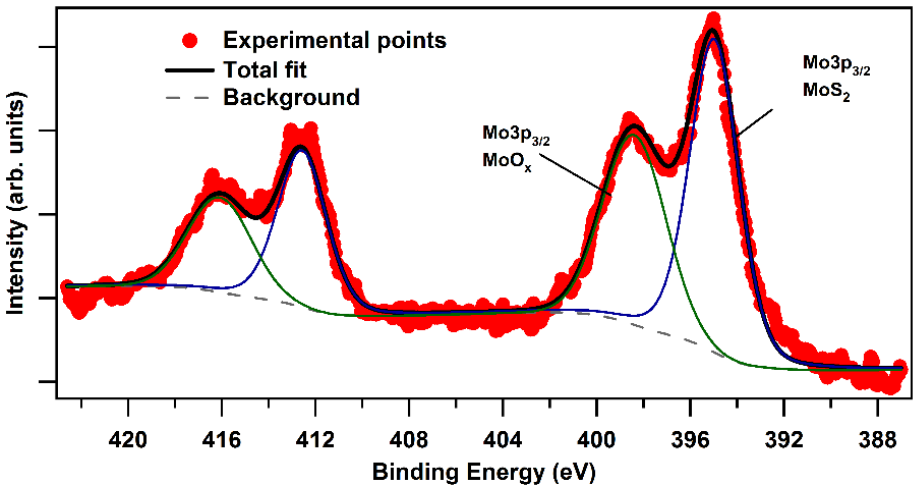

Figure 25: Mo 3p photoemission line of MoS_2 NPs synthesized in presence of ammonia.

The Mo 3*d* photoemission line was taken into consideration and fitted by three components with a fixed spin orbit separation of 3.13 eV, one related to MoS_2 (229.2 eV) and the others related to MoO_3 and MoO_x (233.0 and 231.6 eV respectively) species, whereas the S 2*s* photoemission line was fitted by a single component centered at 226.4 eV (Figure 26).[68,45] To quantify experimentally the MoS_x composition, we considered the intensity ratio between the S 2*s* and Mo 3*d* peaks and compared it with the value measured on commercial MoS_2 powder as reference for a 2:1 stoichiometry. By using this procedure, we verified that MoS_x NPs are slightly under-stoichiometric in sulfur content (x=1.7). Moreover, by considering the area of the C 1*s*, Mo 3*d* and S 2*s* peaks and their corresponding sensitivity factors, we determined a MoS_2/C ratio of about 26% (at %).

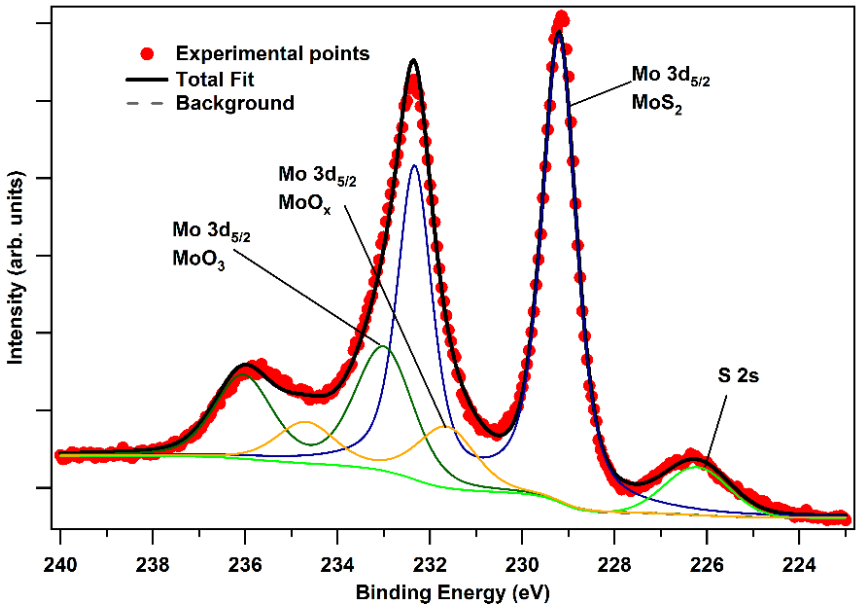

Figure 26: S 2s and Mo 3d photoemission lines of N-cGO/MoS_2.

SEM and TEM investigations were carried out to study the microscopic structure of the prepared materials. SEM micrographs clearly document the crumpling of GO sheets and the formation of deeply wrinkled and globular structures (Figure 27a, b), whose size ranges from 100 to 500 nm. No morphological differences can be observed between N-doped and undoped cGO materials (Figure 27c) indicating that the presence of dopants plays only a minor role in the physical process of crumpling. SEM images of the N-cGO/MoS_2 nanohybrids (Figure 27e, f) show that the surface of graphene is decorated with MoS_2 NPs characterized by bimodal size distribution: large aggregates ranging from 50 to 100 nm, and NPs smaller than 10 nm, which are scattered on the GO surface.

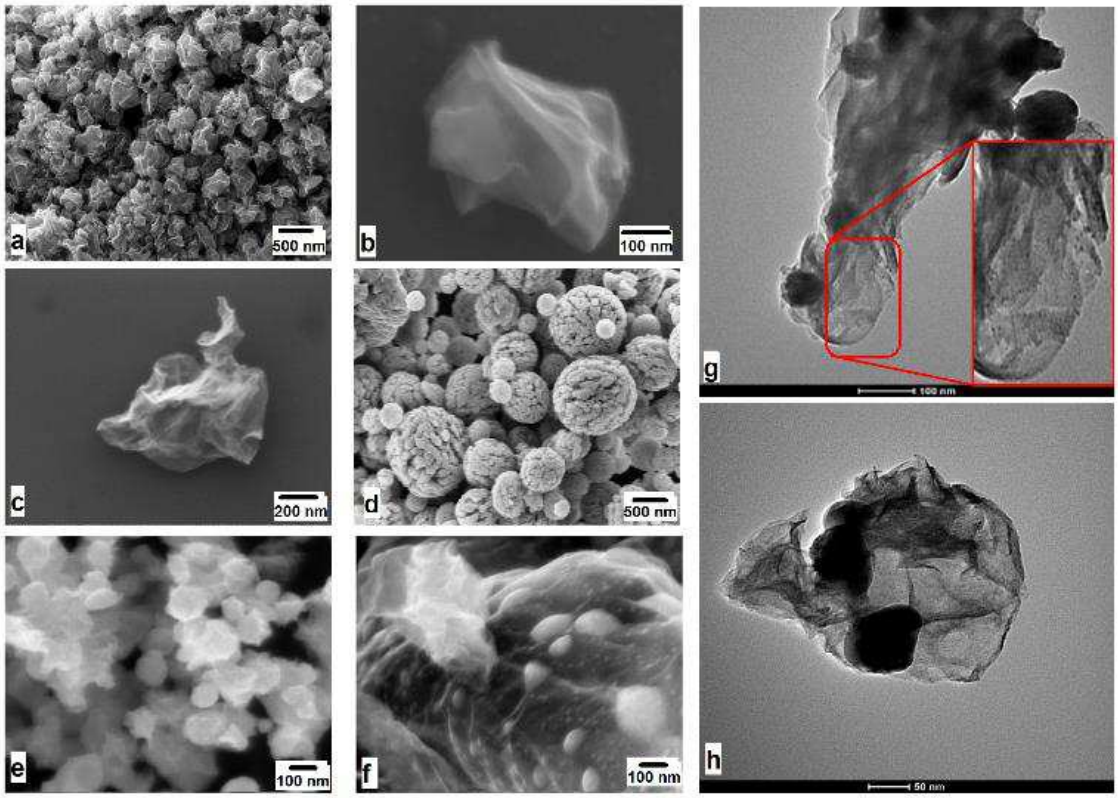

Figure 27: SEM micrographs of (a, b) pristine cGO, (c) N-cGO, (d) MoS_2 NPs obtained in absence of GO sheets, and (e, f) N-cGO/MoS_2 nanohybrids. TEM micrographs (g, h) of N-cGO/MoS_2 nanohybrids.

The larger structures present morphological features very similar to those obtained by direct aerosol synthesis of MoS_2 NPs starting from $(NH_4)_2MoS_4$ in the absence of GO sheets (see Figure 27d). In this case spherical particles with deep crevices and rough surfaces are formed, whose dimensions (diameter ranging from 200 to 1000 nm) correlate well with the dimension of aerosol droplets. Actually, each aggregate consists of smaller units quite homogeneous in size (about 50 nm) that are densely assembled into globular superstructures, and are due to precipitation and aggregation processes driven by water evaporation from every aerosol microdroplet. Therefore, SEM data indicate that the presence of GO sheets in microdroplet reactors drastically modifies the final structure of MoS_2 particles since it prevents NP aggregation.

TEM micrographs of N-cGO/MoS_2 nanohybrids (Figure 27g, h) confirm the bimodal growth of MoS_2 in presence of GO sheets, as evidenced by the presence of large globular aggregates of MoS_2 with a diameter of about 50 nm that can be either attached to the GO surface or more frequently enclosed inside the c-GO, forming nanosacks

as reported in previous works for metal and oxide NPs.[54] Moreover, very small NPs, smaller than 10 nm, can be easily detected on less crumpled sheets (see inset in Fig 27g).

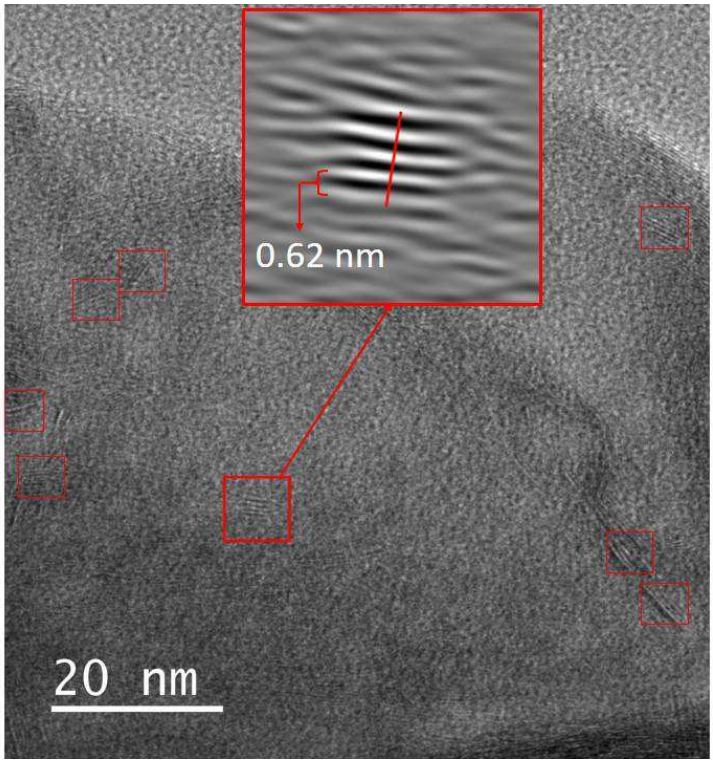

Figure 28: HRTEM micrograph of N-cGO/MoS_2 nanohybrids presenting MoS_2 NPs highlighted by red squares.

HR-TEM analysis (Figure 28) shows that the smallest NPs have a diameter of ~ 3 nm and that nanostructured MoS_2 grown on graphene surface is crystalline as determined by the lattice spacing corresponding to the (002) facet (0.62 Å)[69]. The GIXRD patterns (Figure 29b) confirm that MoS_2 NPs grown on graphene as well as synthesized by aerosol method, are crystalline with a hexagonal structure (2H phase).[70,71] A sharp (002) peak is observed, along with peaks from other reflection groups. The position of the (002) diffraction peak is slightly shifted to lower angle (14.02° for the nanohybrids and 13.75° for MoS_2 NPs) compared to what is reported in [AMCSD 0009788], indicating a lattice expansion as already reported in the literature.[72] An estimation of the mean crystallite size determined by the line broadening of the (002) diffraction peak yields about 4 nm diameter. The peak at 24°, typical of reduced GO, cannot be identified in cGO, N-cGO and N-cGO/MoS_2 nanohybrids (Figure 29a, 29b).[6] This is correlated to the special synthesis method: the crumpling of the graphenic structure avoids the restacking of the graphene sheets and prevents to measure a clear diffraction peak.[12]

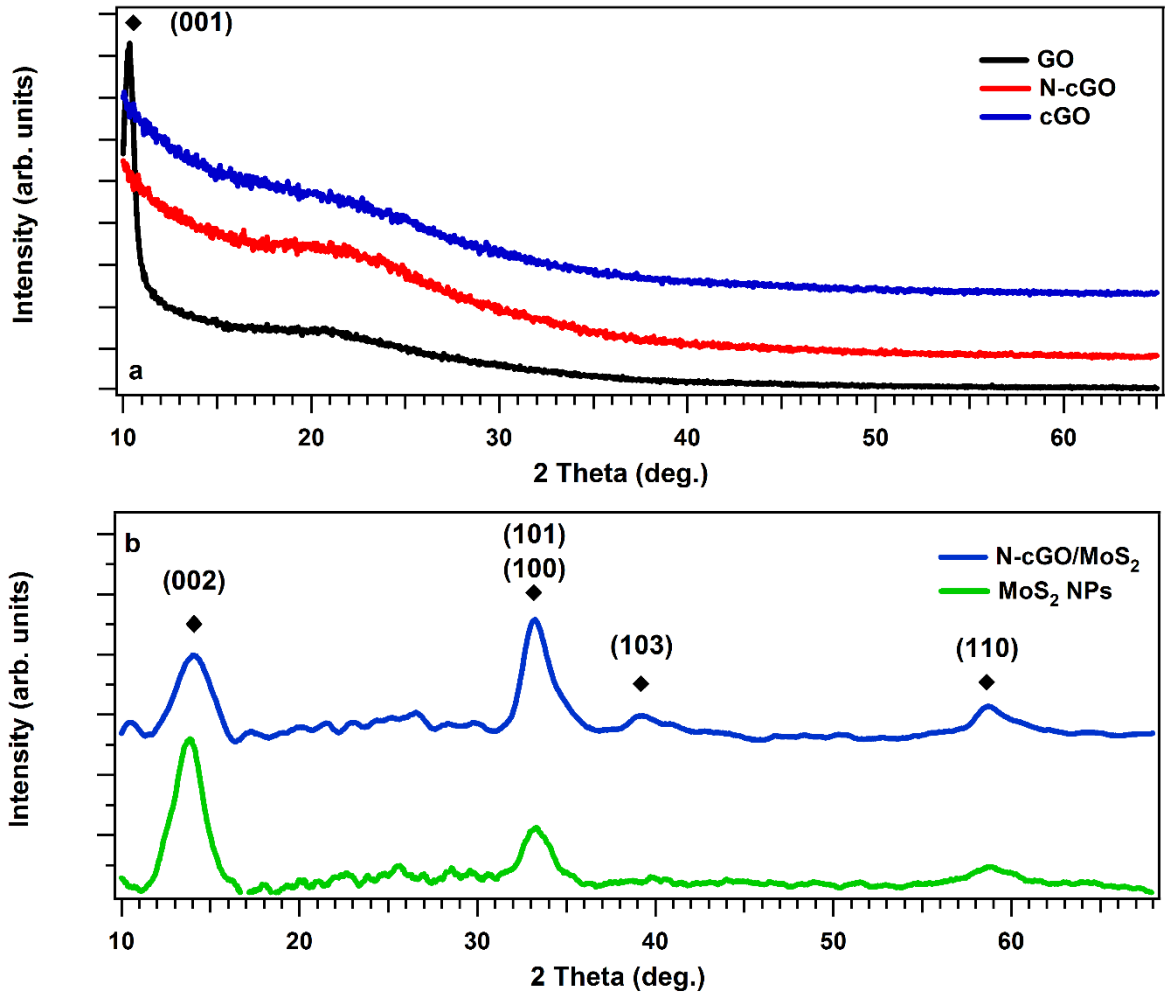

Figure 29: GIXRD patterns of (a) GO, N-cGO and cGO; (b) MoS_2 NPs and N-cGO/MoS_2.

In conclusion, the mean size of MoS_2 aggregates in the composite with graphene is one order of magnitude smaller with respect to materials obtained without GO (60 nm vs 600 nm). The presence of GO sheets in the aerosol droplets therefore has a twofold effects: it favors the nucleation of small MoS_2 NPs on the GO surface, and prevents aggregation of the NPs because GO crumpling can encapsulate and keep separated different aggregates. The uniform dispersion of MoS_2 on the crumpled surface of graphene is confirmed also by C Kα, Mo Kα and S Kα elemental maps obtained by EDS (Figure 30).

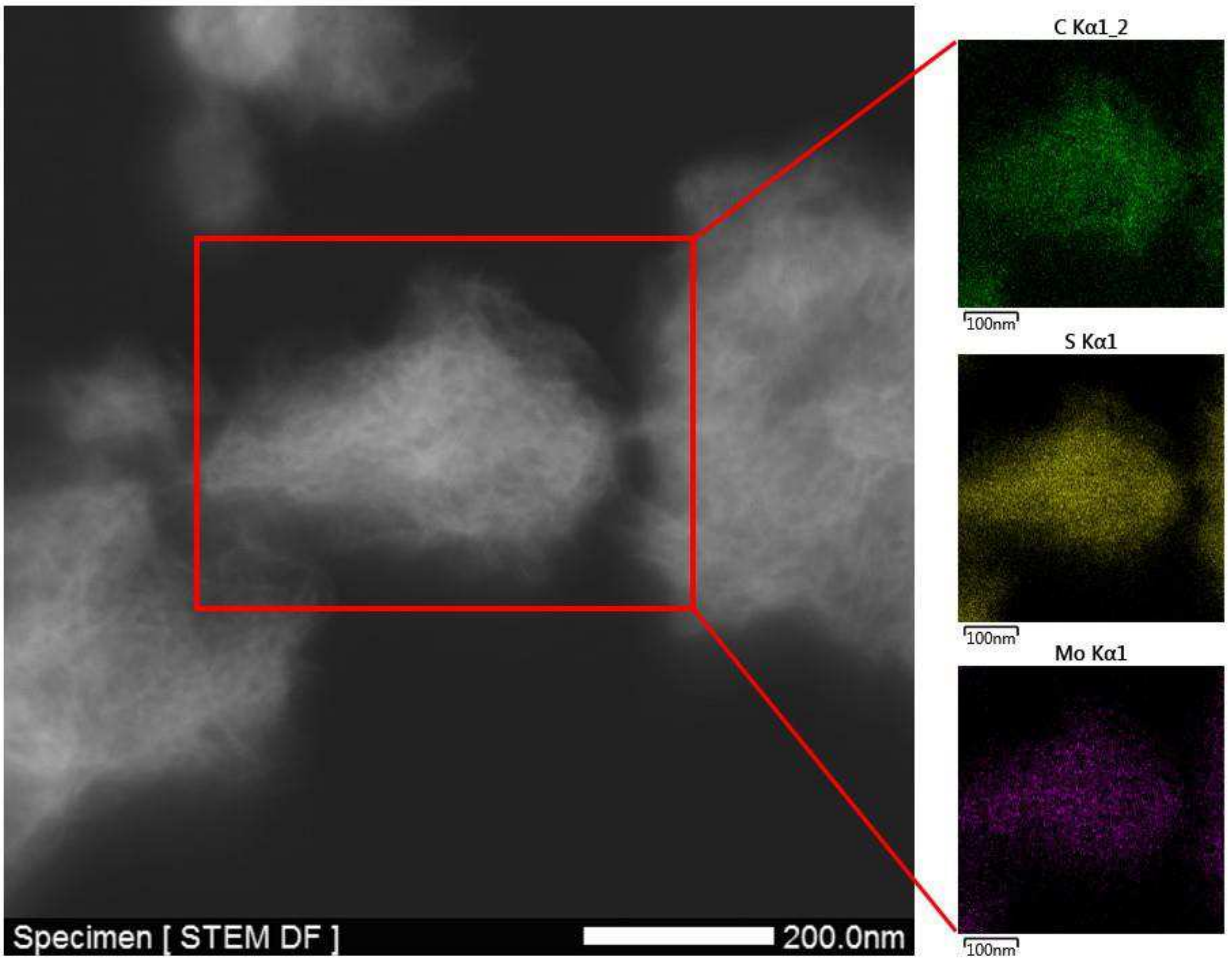

Figure 30: STEM micrographs of N-cGO/MoS_2 (accelerating voltage: 200 kV, on the left) with the EDS elemental maps (on the right) of C, Mo and S from the area highlighted by the red rectangle.

Raman spectroscopy is very useful to characterize the composition of the product, since GO and MoS_2 show characteristic Raman fingerprints. Raman spectra (Figure 31a) of N-cGO/MoS_2 nanohybrid present the characteristic D (~1350 cm^{-1}), G (~1590 cm^{-1}), 2D (~2700 cm^{-1}) and D+D'(~2900 cm^{-1}) bands of graphene[73] and the A_{1g} (~410 cm^{-1}) and E^1_{2g} (~385 cm^{-1}) mode of MoS_2.[74] The D/G band intensity ratio is higher with respect to pure cGO synthesized at the same temperature (not reported here). This could be attributed to the presence of N defects that locally break the carbon sp^2 lattice symmetry.[75] The Raman frequencies of E^1_{2g} and A_{1g} peaks related to MoS_2 increase monotonously with the number of layers in MoS_2 flakes, while the intensity and width of the peaks vary arbitrarily. This behavior has been related to increased electronic transition energies or elongated interlayer atomic bonds in ultrathin MoS_2.[76] In our N-cGO/MoS_2 nanohybrids, the wavenumber separation between A_{1g} and E^1_{2g} mode of MoS_2 in different points of the same sample varies from 25 to 27 cm^{-1}, this means that MoS_2 NPs are mainly composed by multiply stacked layers as in bulk MoS_2.[76]

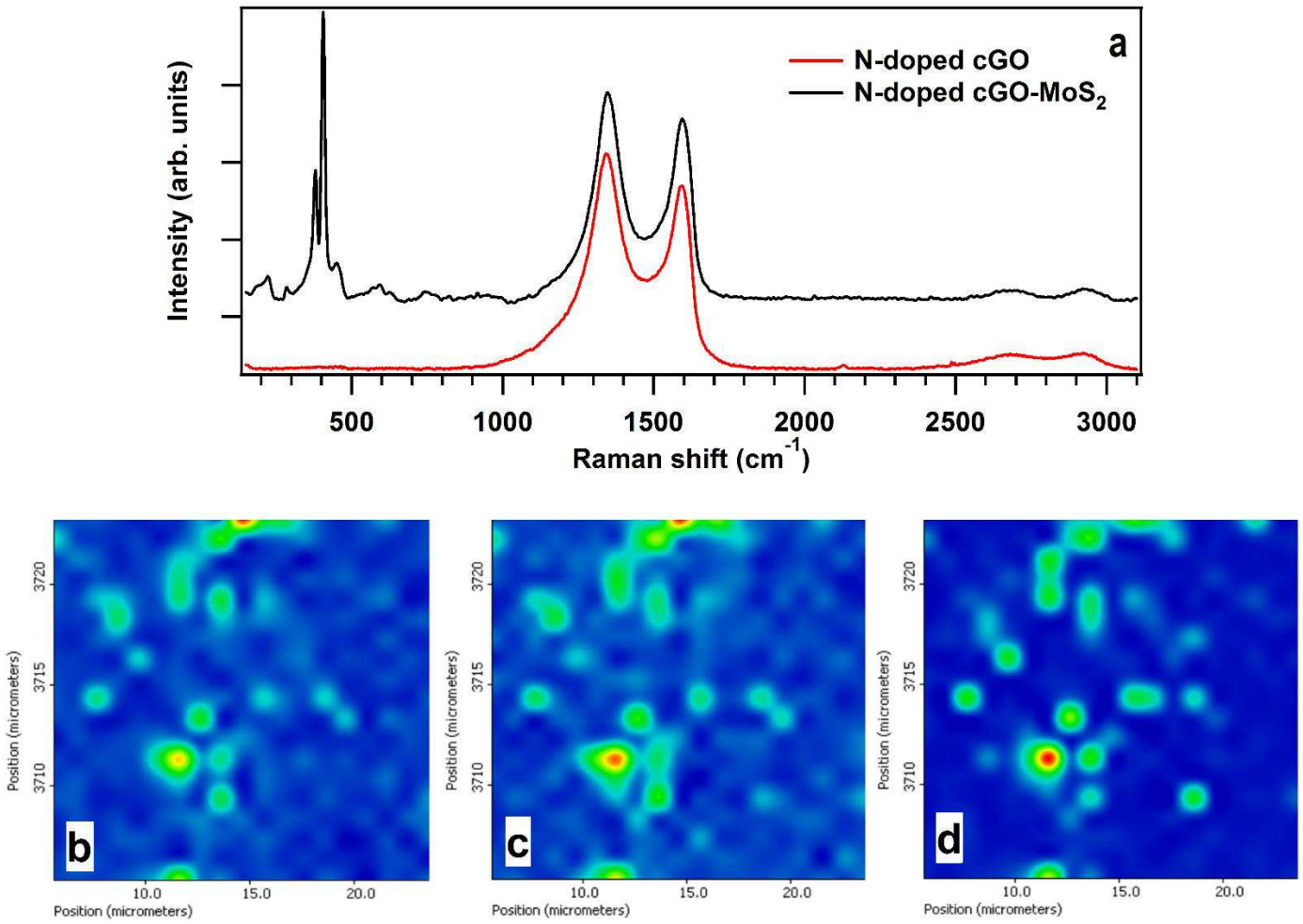

Figure 31: Raman spectrum of (a) N-cGO and of N-cGO/MoS_2; 2D plots of the XY Raman maps of the GO D band (1350 cm-1, b) and G band (1590 cm-1, c) and MoS_2 A_{1g} (405 cm-1, d) Raman intensity maps (18×18 µm) were acquired for the N-cGO/MoS_2 deposited on Si(100) wafer using a step of 1 µm.

Figure 31 reports the 2D XY maps of the GO D band (1355 cm-1) and G band (1600 cm-1) and MoS2 A1g (405 cm-1). The Raman intensity maps provide a direct evidence of the spatial arrangement of cGO and MoS2 components and we can infer that reduced GO and MoS2 NPs are located in the same zones, since the characteristic bands have the same intensity trend, indicating the formation of a nanohybrid material.

Conversely, UV-visible spectra (Figure 32) of the N-cGO/MoS_2 nanohybrids provide another confirmation of the bimodal growth of MoS_2 NPs. The spectrum of N-cGO/Mo_{S2} exhibits three characteristic absorption peaks: the peak centered at 975 nm evidences the presence of bulk-like MoS_2 and is the only peak observed in the UV-visible-NIR spectrum of solitary MoS_2 synthesized by aerosol methods.[77] The peaks at around 640 and 680 nm are related to the smaller MoS_2 NPs and is consistent with quantum size effects on this material, as previously reported for nanosized MoS_2.[77] With a view to the application of the N-cGO/MoS_2 nanohybrids as photocatalyst, the presence of these absorptions peaks in the visible range is remarkable due to the correspondence with the maximum of the solar emission spectrum. This also indicates an increase on the band gap of MoS_2 up to 1.8-2-2 eV, which makes it very appealing for water splitting applications.

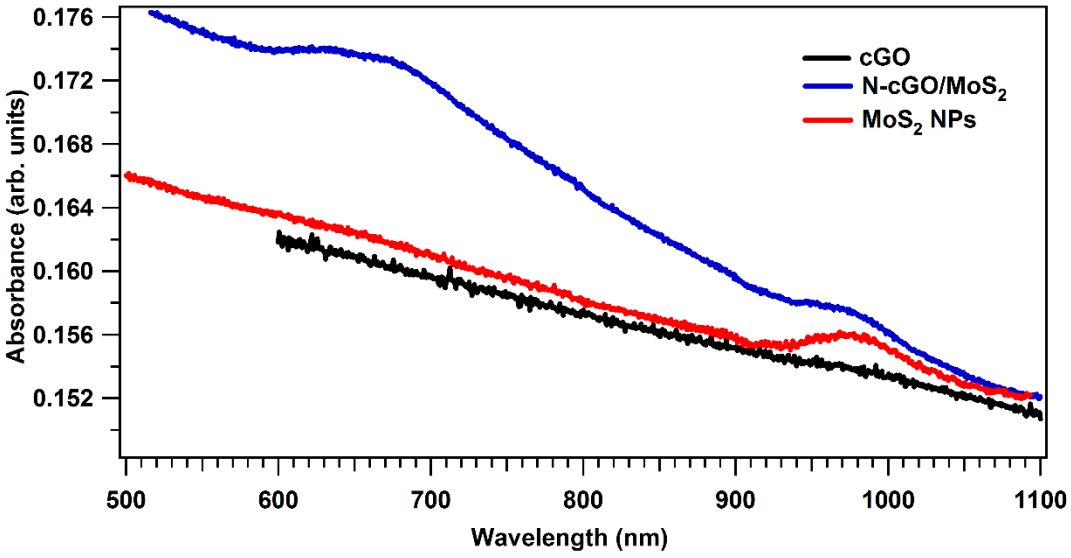

Figure 32: UV-visible spectra of cGO, MoS_2 NPs and N-cGO/MoS_2.

Photo-electrochemical characterization.

The photo-electrochemical catalytic behavior toward HER of the N-cGO/MoS_2 nanohybrids and of bare MoS_2 NPs obtained by aerosol processing without GO sheets were investigated. In all cases the Toray paper was used as support. The results obtained for the commercial MoS_2 on Toray paper and bare Toray paper are also presented as reference. Figure 33a shows the comparison of the polarization curves of the whole series. Bare MoS_2 NPs exhibit an overpotential for HER around 180 mV vs RHE, which is very similar to that of commercial MoS_2, and fully consistent with values previously reported in literature.[45,78,79] However, MoS_2 NPs prepared by the aerosol method exhibit higher current densities than commercial MoS_2 powders. This result can be attributed to the increase of active sites due to the small size of the NPs obtained by the aerosol method. The N-cGO/MoS_2 nanohybrids, however, show an improved HER activity as evidence by lower overpotential (~100 mV vs RHE) and significant higher current densities. This latter reaches in nanohybrids a value two times higher than in pure MoS_2 NPs at -250 mV vs RHE (94 mA $cm^{-2}mg_{Mo}^{-1}$ and 39 mA $cm^{-2}mg_{Mo}^{-1}$, respectively). The low overpotential of the nanohybrids is comparable with the lowest overpotentials for the electrochemical HER reported in literature for graphene/MoS_2 based materials. [5,6,12]

To obtain a further insight into HER activity of the different samples, Tafel plots were determined (Figure 33b). The resulting Tafel slope for bulk commercial MoS_2 is 122 mV/dec, indicating that hydrogen adsorption (Volmer step) is the rate-limiting step of HER.[80] Tafel slope is lower for the samples synthesized by aerosol method: 93 mV/dec and 94 mV/dec for N-cGO/MoS_2 nanohybrids and MoS_2 NPs, respectively. This indicates that the HER occurs through several reaction pathways.[80] Tafel slopes around 120mV/dec have been reported for MoS_2 grown on Toray paper[81] (120 mV/dec), for multi walled MoS_2 nanotubes grown on multi walled carbon nanotubes (CNT)[78] (109 mV/dec) and for MoS_2/CNT/graphene (100 mV/dec)[82]. On the other hand, a Tafel slope of ~41 mV/dec has been reported for ultrathin MoS_2 nanosheets grown on graphene.[5] Our higher slopes could be influenced by two factors: (i) charge transport limitations through the fibrous, porous network characteristic of Toray carbon paper used as substrate,[81] and (ii) the influence of the bigger MoS_2 NPs with a bulk-like structure

(as previously demonstrated by Raman and UV-visible spectroscopy) that compromises the conduction through MoS_2 inner layers.[78,83] However, the Tafel slope and the small overpotential of N-cGO/MoS_2 nanohybrids highlight the role of N-cGO in the enhancement of the activity of the MoS_2 NPs. This effect can be attributed to the improved electronic contact between the active MoS_2 NPs and the conductive graphene through the N-groups, as seen by XPS. Besides, UV-VIS and microscopy investigations indicate that N-cGO/MoS_2 nanohybrids present the smallest NPs, and therefore a larger number per mass of highly active edges, which are the main catalytic sites of MoS_2.[17]

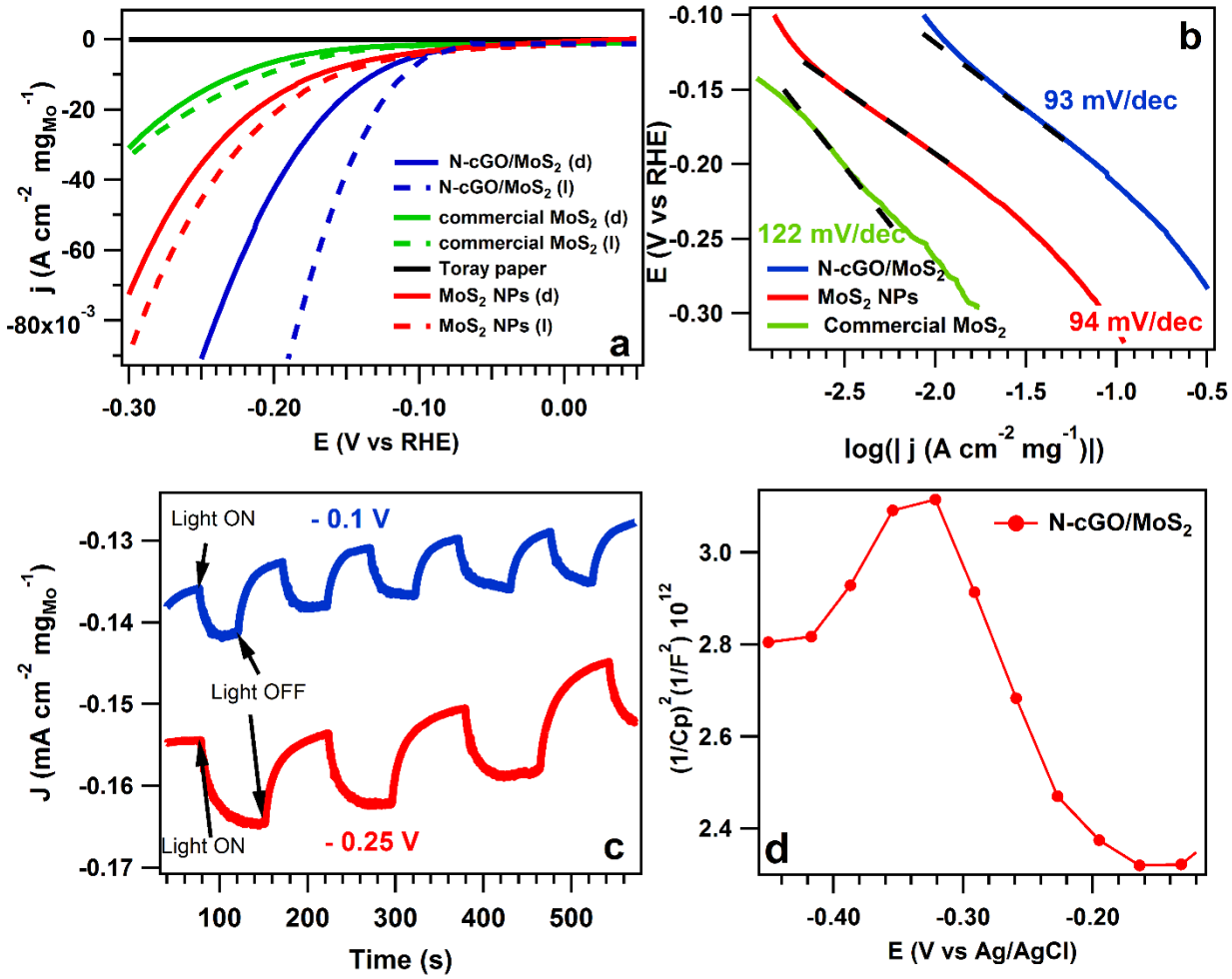

***Figure 33**: (**a**) Polarization curves (not iR corrected) in dark (d) and under illumination (l) for N-cGO/MoS_2, bare MoS_2 NPs obtained by the aerosol method, commercial MoS_2 (Sigma-Aldrich) and Toray paper in 0.5 M H_2SO_4 at room temperature; (**b**) Corresponding Tafel plots for N-cGO/MoS_2, MoS_2 NPs obtained by the aerosol method and commercial MoS_2 (Sigma-Aldrich); (**c**) J-t curves under light (ON) and dark (OFF) conditions at -0.1 V and -0.25 V vs RHE and room temperature for N-cGO/MoS_2; (**d**) Mott-Schottky plot at 1 kHz of the N-cGO/MoS_2 in dark.*

It is known that the N-doped graphene forms p-n nanojunctions with MoS_2 NPs, enhancing the charge separation.[6] For this reason, we investigated if light could further enhance the electrocatalytic activity of the N-cGO/MoS_2 nanohybrids toward HER. Figure 4c reports the j-t curves obtained at -0.1 V and -0.25 V vs RHE under light and dark conditions. Under illumination, the sample shows a percentage increase of 5 and 7 %-in the current density, whereas the relative increase of bare MoS_2 NPs is only of 1 % (Figure 34), at -0.1 V and -0.25 V, respectively.

Moreover, under illumination the onset potential slightly shifts to a higher value (~ -75 mV vs RHE, Figure 33a), which is somewhat lower than the one obtained by Meng et al.[6] (~ +50 mV vs RHE). Such difference can be traced back to the contribution of bigger MoS_2 NPs, as mentioned above. The better performance under illumination therefore is not simply due to the semiconductive character of MoS_2 alone, but it is connected to the presence of doped graphene oxide. Actually as previously reported[6] a p-n nanojunction is formed between the two materials, which has the effect of helping the charge separation thus boosting photoelectrochemical activity. In fact, MoS_2 NPs and N-cGO show respectively positive (p-type behavior) and negative (n-type behavior) slope for the Mott-Schottky plots (Figure 35). When coupled in the MoS_2/N-cGO nanohybrids, the formation of p-n nanojunctions is confirmed as indicated by the characteristic "inverted V-shape" of the Mott-Schottky plot (Figure 33d).

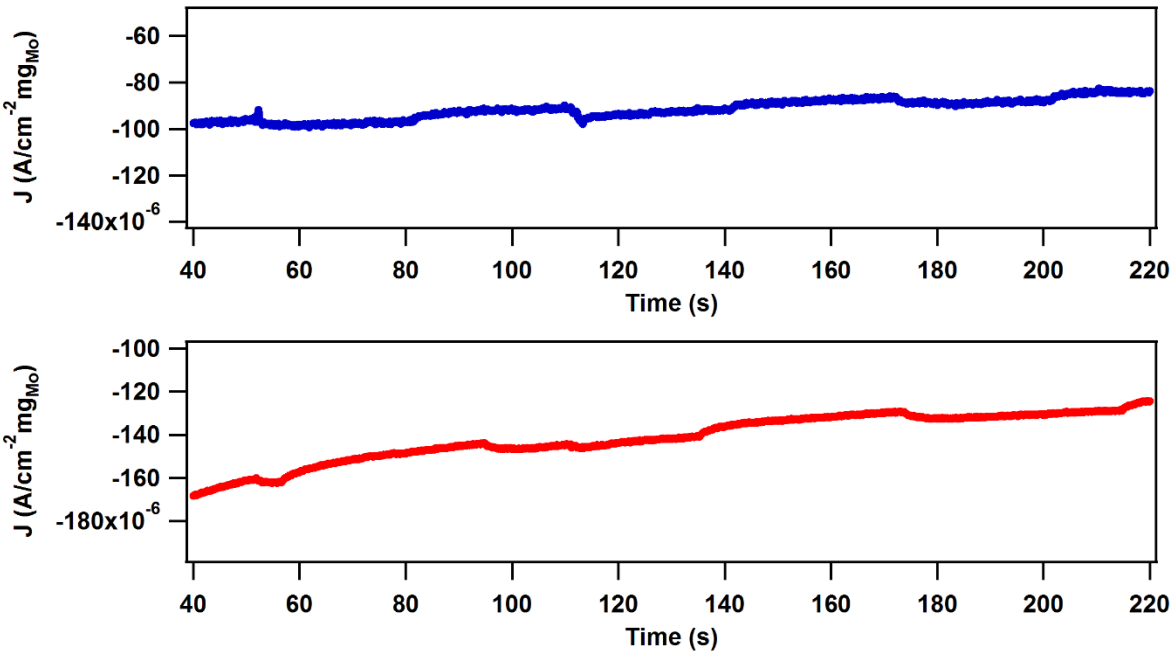

Figure 34: J-t curves under light (ON) and dark (OFF) conditions at -0.1 V (top) and -0.25 V (bottom) vs RHE and room temperature for MoS_2 NPs.

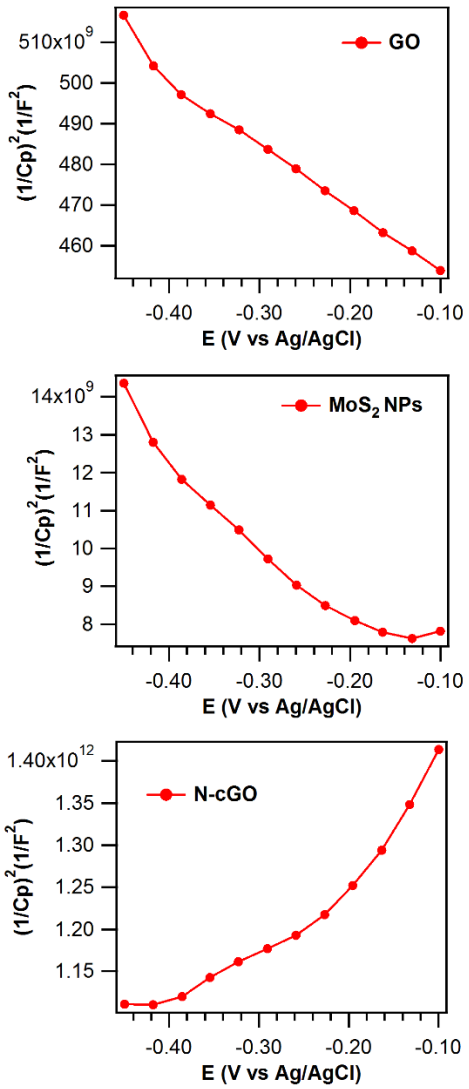

Figure 35: Mott-Schottky plot at 1 kHz of (a) GO, (b) MoS_2 NPs and (c)N-cGO in dark. In order to extract the values of the plots we have used a simplified standard Rs-(RC) circuit. More in detail: impedance spectroscopy was performed in the frequency range 100-0.1 KHz (ten points per decade in logarithmic scale), using an amplitude of 5 mV and single sine wave type. We investigate a potential range between -0.45 V and +0.3 (vs Ag/AgCl).

5.5 Conclusion

The present chapter fully demonstrates the huge potential of the aerosol processing applied to the synthesis of complex multicomponent systems. Actually, simply by adding additional components in the precursor solution we prepared in a simple and fast way, nanostructured graphene based materials with increasing level of complexity.

For the first time we were able to prepare by aerosol, doped materials without the need for long processing time or the use of toxic gases. Not only, since during aerosol processing graphene sheets heavily bend and wrinkle, it is possible to avoid the restacking of graphene sheets and to combine specific electronic properties induced by doping with the enhanced reactivity of surface sites induced by high local curvature. Therefore, by following this general one pot aerosol route, we demonstrate that it is possible to realize nanocomposites characterized by specific interaction between the single components. Such strategy is exemplified by N-cGO/MoS_2 nanohybrids: the rational assembly of their single constituents has allowed improving the performance in the electrochemical generation of hydrogen, which under illumination shows an increase in the current density 7 times higher with respect to simple MoS_2 NPs. This can be traced back to the formation of p-n nanojunctions between N-doped graphene and MoS_2 and to a better dispersion and smaller size distribution of catalyst NPs.

This hybrid system can actually be considered a multifunctional catalyst since it is based on the strong interaction between two moieties (creation of a p-n nanojunction between N-cGO and MoS_2) within a unique catalytic reaction (photoinduced hydrogen evolution reaction). The in situ hydrogen production is an important reaction in the field of tandem catalysis, because H_2 could be immediately employed in a successive reaction after the in situ production, therefore a more complex synthesis can become safer and more sustainable. As discussed in this chapter, the aerosol process permitted to obtain multicomponent catalyst in one pot synthesis. Therefore, properly modifying the precursors solution and the synthesis parameters, it is in principle possible to introduce in these N-cGO/MoS_2 nanohybrids another catalytic site. The high dispersion of NPs over crumpled graphene sheets, as demonstrated in this work, is an advantage in order to have a uniform dispersion of a new catalytic site in the composite material. For example, if we introduce an active site for hydrogenation reactions (i.e. Pd, Pt, Ni, Fe NPs) we pave the way to the possibility of exploit the in situ produced H_2 for the catalysis of hydrogenation reactions. From a more general point of view, in this chapter we highlighted the huge potentiality of aerosol processes for the multiscale design (from micro to atomic scale) of multifunctional materials that could be employed in the field of catalysis. Considering the synthesis of N-cGO-MoS_2 nanohybrids, at the atomic scale, we introduced a dopant (N) in the graphene structure. At the nano scale, we obtained a fine dispersion of MoS_2 NPs, useful for maximizing the number of active sites (edges). At the micro scale, we avoided the restacking of graphene sheets thanks to the crumpling process.

References

[1] R. Backov, *Soft Matter* **2006**, *2*, 452–464
[2] C. Boissiere, D. Grosso, A. Chaumonnot, L. Nicole, C. Sanchez, *Adv. Mater.* **2011**, *23*, 599–623.
[3] B. J. Kwon, J.-Y. Kim, S.-M. Choi, S. An, J. *Nanotechnology* **2014**, *25*, 085701.
[4] G. Xie, K. Zhang, B. Guo, Q. Liu, L. Fang, J. R. Gong, *Adv. Mater.* **2013**, *25*, 3820–3839.
[5] Y. Li, H. Wang, L. Xie, Y. Liang, G. Hong, H. Dai, *J. Am. Chem. Soc.* **2011**, 7296–7299.
[6] F. Meng, J. Li, S. K. Cushing, M. Zhi, N. Wu, *J. Am. Chem. Soc.* **2013**, *135*, 130628121322008.
[7] X.-K. Kong, C.-L. Chen, Q.-W. Chen, *Chem. Soc. Rev.* **2014**, *43*, 2841–2857.
[8] L. Zhang, J. Niu, M. Li, Z. Xia, *J. Phys. Chem. C* **2014**.
[9] J. Jin, F. Pan, L. Jiang, X. Fu, Liang, A. Wei, Z. Zhang, J. G. Sun, S.Lubrication, Physics, C.; *et al. ACS Nano* **2014**.
[10] H. Liu, Y. Liu, D. Zhu, *J. Mater. Chem.* **2011**, *21*, 3335– 3345.
[11] H. Wang, T. Maiyalagan, X. Xin Wang, *ACS Catal.*, **2012**, *2*, 781–794.
[12] D. Geng, S. Yang, Y. Zhang, J. Yang, J. Liu, R. Li, T.-K. Sham, X. Sun, S. Ye, S. Knights, *Appl. Surf. Sci.*, **2011**, *257*, 9193-9198.
[13] Y. Shao, S. Zhang, M. H. Engelhard, G.Li, G. Shao, Y. Wang, J. Liu, I. A. Aksay, Y. Lin, *J. Mater. Chem.* **2010**, *20*, 7491–7496.
[14] L. Liao, J.Zhu, X.Bian, L. Zhu, M. D. Scanlon, H. H. Girault, B. Liu, *Adv. Funct. Mater.* **2013**, *23,* 5326-5333.
[15] S. Yang, L. Zhi, K. Tang, X. Feng, J.Maier, K. Müllen, *Adv. Funct. Mater.* **2012***, 22*, 3634-3640.
[16] J. K. Nørskov, T. Bligaard, A. Logadottir, J. R.Kitchin, J. G. Chen, S. Pandelov, U. Stimming *J. Electrochem. Soc.* **2005**, *152*, J23-J26.
[17] J. Greeley, T.F. Jaramillo, J. Bonde, I. Chorkendorff, J.K. Nørskov, *Nat. Mater.* **2006,** *5*, 909-913.
[18] Y. Li, H. Wang, L. Xie, Y. Liang, G. Hong, H. Dai, *J. Am. Chem. Soc.* **2011**, *133,* 7296-7299.
[19] Z. H. Deng, L. Li, W. Ding, K. Xiong, Z. D. Wei, *Chem. Commun.* **2015**, *51*, 1893-1896.
[20] T. F. Jaramillo, K. P. Jørgensen, J. Bonde, J. H. Nielsen, S. Horch, Ib. Chorkendorff, *Science* **2007**, *317*, 100-102.
[21] A. K. Geim, I. V.Grigorieva, *Nature* **2013**, *499*, 419-425.
[22] A. G. Marquez, P. Horcajada, D.Grosso, G. Ferey, C. Serre, C. Sanchez, C. Boissiere *Chem. Commun.,* **2013**, 49, 3848—3850.
[23] A. K. Geim, K. S. Novoselov, *Nat. Mater.* **2007**, *6*, 183–191.
[24] S. Stankovich, D. A.Dikin, G. H. B.Dommett, K. M.Kohlhaas, E. J.Zimney, E. A.Stach, R. D.Piner, S. T.Nguyen, R. S. Ruoff, *Nature* **2006**, *442*, 282–286.
[25] V. C. Sanchez, A. Jachak, R. H. Hurt, A. B. Kane, *Chem. Res. Toxicol.* **2012**, *25*, 15–34.
[26] P. Wick, A. E. Louw-Gaume, M. Kucki, H. F. Krug, K. Kostarelos, B. Fadeel, K. Dawson. A. Salvati, E.Vázquez, L. Ballerini, *et al. Angew. Chemie Int. Ed.* **2014**, 2–7.
[27] S. Agnoli, G. Granozzi, *Surf. Sci.* **2013**, *609*, 1–5.
[28] S.Park, R. S. Ruoff, *Nat. Nanotechnol.* **2009**, *4*, 217–224.
[29] A. Lerf, H. He, M. Forster, J. Klinowski, *J. Phys. Chem. B* **1998**, *102*, 4477–4482.
[30] D. R. Dreyer, S. Park, C. W.Bielawski, R. S. Ruoff, *Chem. Soc. Rev.* **2010**, *39*, 228–240.
[31] X. Ma, M. Zachariah, C. Zangmeister, *Nano Lett.* **2011**, *12*, 486–489.
[32] Q. Wu, Y. Wu, Y. Hao, J. Geng, M. Charlton, S. Chen, Y. Ren, H. Ji, H. Li, D. W. Boukhvalov, R. D. Piner, C. W. Bielawski, R. S. Ruoff, *Chem. Commun. (Camb).* **2013**, *49*, 677–679.
[33] Y. Chen, F. Guo, A. Jachak, S.-P. Kim, D. Datta, J. Liu, I. Kulaots, C. Vaslet, H. D. Jang, J.Huang, A. Kane, V. B. Shenoy, R. H. Hurt, *Nano Lett.* **2012**, *12*, 1996–2002.
[34] S. Mao, Z. Wen, T. Huang, Y. Hou, Chen, J. *Energy Environ. Sci.* **2014**, *7*, 609.
[35] M. S. Spector, E. Naranjo, S. Chiruvolu, J. A. Zasadzinski, *The American Physical Society* **1994**, *73(21),2867(4)*.
[36] W. Wang, Y.Jiang, P.Biswas, *J. Phys. Chem. Lett.* **2012**, *3*, 3228–3233.
[37] J. Luo, H. D. Jang, T. Sun, L. Xiao, Z. He, A. P.Katsoulidis, M. G. Kanatzidis, J. M. Gibson, J. Huang, *ACS Nano* **2011**, *5*, 8943–8949.

[38] D. Wei, Y. Liu, Y. Wang, H. Zhang, L. Huang, G.Yu, *Nano Lett.* **2009**, *9*, 1752–1758.
[39] S. Yang, L. Zhi, K. Tang, X. Feng,. *Adv. Funct. Mat.* **2012**, *22*, 3634–3640.
[40] D. Deng, X.Pan, L.Yu, Y.Cui, Y.Jiang, J.Qi, W.-X. Li, Q.Fu, X.Ma, Q.Xue, Q. Fu, X. Ma, Q. Xue, G. Sun, X. Bao, *Chem. Mater.* **2011**, *23*, 1188–1193.
[41] L. Qu, Y. Liu, J. Baek, L. Dai, *ACS Nano* **2010**, *4*, 1321–1326.
[42] L. A. Kibler, *ChemPhysChem*, **2006**, 7, 985−991.
[43] S. Helveg, J. Lauritsen, E. Laegsgaard, I. Stensgaard, J. Norskov, B. Clausen, H. Topsoe, F. Besenbacher, *Phys. Rev. Lett.* **2000**, *84*, 951–954.
[44] P. Lazar, M**.** Otyepka, *Chem.–Eur. J.* **2017**, 23(20), 4863-4869.
[45] Z. Chen, D. Cummins, B. N. Reinecke, E. Clark, M. K. Sunkara, T. F. Jaramillo, *Nano Lett*. **2011**, 11, 4168−4175.
[46] T. Wang, L. Liu, Z. Zhu, P. Papakonstantinou, J. Hu, H. Liu, M. Li, *Energy Environ. Sci.* **2013**, 6, 625−633.
[47] D. S. Kong, H. T.; Wang, J. J Cha, M.Pasta, K. J. Koski, J. Yao, Y.Cui, *Nano Lett.* **2013**, 13, 1341−1347.
[48] T. F. Jaramillo, J. Bonde, J.; Zhang, B.-L. Ooi, K.Andersson, J.Ulstrup, I. Chorkendorff, *J. Phys. Chem. C* **2008**, 112, 17492−17498.
[49] A. Laursen, S. Kegnæs, *Energy Environ. Sci.* **2012**, *5*, 5577.
[50] Y.Li, H.Wang, L.Xie, Y. Liang, G.Hong, H. Dai, *J. Am. Chem. Soc.* **2011**, 7296–7299.
[51] A. J. Smith , Y.-H. Chang , K. Raidongia , T.-Y. Chen , L.-J. Li , J. Huang, *Adv. Energy Mater.* **2014**, 1400398
[52] X. Zong, Y. Na, F. Wen, G. Ma, J. Yang, D. Wang, Y. Ma, M. Wang, L. Sun, C. Li, *Chem. Commun. (Camb).* **2009**, 4536–4538.
[53] S. Skrabalak, K. Suslick, *Mater. Synth.* **2008**, 1–7.
[54] Y. Chen, F. Guo, A. Jachak, S.P. Kim, D. Datta, J. Liu, K. Iulaots, C. Vaslet, H.D. Jang, J. Huang, A. Kane, V.B. Shenoy, R. Hurt, *Nano Lett.* **2012**, *12*, 1996-2002.
[55] D. Parviz, S. D.Metzler, S.Das, F.Irin, M.J.Green, *Small* **2015**, DOI: 10.1002/smll.201403466.
[56] S. Mao, G. Lu, J. Chen, *Nanoscale* **2015**, *7*, 6924-6943.
[57] A. Bagri, C. Mattevi, M. Acik, Y. J. Chabal, M. Chhowalla, V. B. Shenoy, *Nat. Chem.* **2010**, *2*, 581-587.
[58] M. Favaro, S. Agnoli, M. Cattelan, A. Moretto, C. Durante, S. Leonardi, J. Kunze-Liebhäuser, O. Schneider, A. Gennaro, G. Granozzi, *Carbon* **2014**, *77*, 405-415.
[59] D.Usachov, O.Vilkov, A.Grüneis, D.Haberer, A.Fedorov, V. K.Adamchuk, A. B.Preobrajenski, P. Dudin, A.Barinov, M.Oehzelt, C. D. Laubschat, V.Vyalikh, *Nano Lett.* **2011**, *11*, 5401-5407.
[60] C. Mattevi, G. Eda, S. Agnoli, S. Miller, K. A. Mkhoyan, O.Celik, D Mastrogiovanni, G. Granozzi, E.Grafunkel, M. Chhowalla, *Adv. Funct. Mater.* **2009**, *19*, 2577-2583.
[61] M. Favaro, S. Agnoli, C.Di Valentin, C.Mattevi, M.Cattelan, L. Artiglia, E. Magnano, F.Bondino, S.Nappini, G. Granozzi, *Carbon,* **2013**, *68*, 319-329.
[62] J.-A. Yan, M. Y. Chou, *Phys. Rev. B,* **2010**, *82*, 125403.
[63] T. Susi, M. Kaukonen, P. Havu, M. P. Ljungberg, P. Ayalaand, E. I. Kauppinen, *Beilstein J., Nanotechnol.* **2014**, *5*, 121-132.
[64] M. Favaro, L. Ferrighi, G. Fazio, L. Colazzo, C. Di Valentin, C. Durante, F. Sedona, A. Gennaro, S. Agnoli, G. Granozzi, *ACS Catal.* **2015**, *5*, 129-144.
[65] T. A. Patterson, J. C. Carver, D. E. Leyden, D. M. A, Hercules, *J. Phys. Chem.* **1976**, *80*, 1700-1708.
[66] T. Liang, W. G. Sawyer, S. S. Perry, S. B. Sinnott, S. R. Phillpot, *J. Phys. Chem. C* **2011**, *115*, 10606-10616.
[67] J. Qi, L. Jiang, Q. Jiang, S. Wang, G. Sun, *J. Phys. Chem. C* **2010**, *114*, 18159-18166.
[68] J. Kibsgaard, Chen, Z. B. N. Reinecke, T. F. Jaramillo, *Nat. Mater*. **2012**, *11*, 936-941.
[69] S. X. Min, G. Q. Lu, *J. Phys. Chem. C*. **2012**, *16*, 25415-25424.
[70] M. Chhowalla, G. A. J. Amaratunga, *Nature* **407**, 164-167.
[71] W. Zhou, Z. Yin, Y. Du, X. Huang, Z. Zeng, Z. Fan, H. Liu, J. Wang, H. Zhang, *Small* **2013**, *9*, 140–147.
[72] D. N. Dunn, L. E. Seitzman, I. L. Singer, *J. Mater. Res*. **1998**, 13, 3001-3007.
[73] D. A. Dikin, S. Stankovich, E. J. Zimney, R. D.Piner, G. H. B. Dommett, G. Evmenenko, S. T. Nguyen, R. S. Ruoff, *Nature* **2007**, *448*, 457-460.

[74] Frey, G. L. Tenne, R. Matthews, M. J. Dresselhaus, M. S. Dresselhaus, G. *Phys. Rev. B* **1999**, *60*, 2883.
[75] D. Yang, A. Velamakanni, G.Bozoklu, S.Park, M.Stoller, R. D.Piner, S. Stankovich, I. Jung, D. A.Field, C. A. Ventrice, R. S. Rouff, *Carbon* **2009**, *47*, 145-152.
[76] H. Li, Q. Zhang, C. C. R. Yap, B. K. Tay, T. H. T Edwin, A. Olivier, D. Baillargeat, *Adv. Funct. Mater.* **2012**, *22*, 1385-1390.
[77] T. R. Thurston, J. P. Wilcoxon *J. Phys. Chem. B* **1999**, *103*, 11-17.
[78] A. B.Laursen, S. Kegnæs, S. Dahl, I. Chorkendorff, *Energy Environ. Sci.* **2012**, *5*, 5577-5591.
[79] D. Voiry, S. Malehi, R. Silva, T. Fujita, M. Chen, T. Asefa, V. B. Shenoy, G. Eda, M. Chhowalla, *Nano Lett.* **2013**, *13*, 6222-6227.
[80] J. D. Benck, T. R. Hellstern, J. Kibsgaard, P. Chakthranont, T. Jaramillo, *ACS Catal.* **2014**, *4*, 3957-3971.
[81] J. Bonde, P. G. Moses, T. F. Jaramillo, J. K. Nørskov, I. Chorkendorff, *Faraday Discuss.* **2008**, *140*, 219-231.
[82] D.H. Youn, S. Han, J. Y Kim, J. Y. Kim, H.Park, S. H Choi, J. S. Lee, *ACS Nano* **2014**, *8*, 5164-5173.
[83] H. Vrubel, D. Merki, H. X. Hu, *Energy Environ. Sci.* **2012**, *5*, 6136-6144.

Chapter 6

Conclusion

6. Conclusion

In this thesis, we have investigated the synthesis and characterization from the micro- through the nano- to the atomic scale of different nanostructured heterogeneous catalysts that can be applied in the field of energy conversion and chemical synthesis. In our studies, we have tried to emphasize the fundamental role that is played by materials design, and the great impact that a rationally driven synthesis can have on the ultimate performances. The chemical nature and the morphology of the catalysts have been deeply investigated together with their functional properties (i.e. chemical reactivity) in order to establish rigorous structure-activity relationships. This fundamental knowledge represents the cornerstone for the development of novel materials to be applied in specific applications. To do this, we have employed a large set of tools offered by Materials Science, exploring advanced synthesis methods and *operando* and *in-situ* characterization techniques.

In the chapters of this thesis, we have investigated four different case studies, which exemplify different aspects of materials design and that involve different length scales.

In Chapter 2, we have focused our attention of the design at the atomic scale of spinel oxide structures that were used as redox catalysts for the production of pure H_2 through CLR of ethanol. We have investigated the correlation between the reducibility of Fe/Co mixed spinels and the nature and site occupancy of the cations in their structures. In CLR processes, the reducibility of the redox catalysts plays a fundamental role in the overall catalytic activity. We combined the investigations by means of *operando* (Quick-EXAFS) and *ex-situ* techniques, to study the influence of cation sites occupancy on the redox properties of the materials. These structural data were combined with the analysis of the reaction products in order to identify which are the most chemically active cations inside the spinel structure and which parameters control the chemical activity toward ethanol decomposition (1^{st} step of CLR). These experiments have highlighted the influence of both coordination and chemical nature of the cations on the catalytic properties. In particular, we found that the cations in tetrahedral sites of the spinel structure show a higher reducibility with respect to octahedral ones, independently from their chemical nature. To the best of our knowledge, this is the first study in which it was possible to assess the role of chemical nature (Co vs Fe), geometrical site (tetrahedral vs octahedral site) and crystal phase (spinel vs wüstite) on multioxide redox chemistry. This lays the basis for a rational design of spinel oxide based materials with specific chemical and functional properties. In fact, the precise understanding of how some specific structural features at the atomic scale control the chemical reactivity represents an exceptional stepping stone to develop advanced catalysts for the selective conversion of alcohols, alternative solid state oxygen storage systems, and several applied materials that exploit the redox properties of oxides.

In Chapter 3, we have focused our attention on the design at the micro-, nano- and atomic-scale of nanostructured catalysts based on Pd nanoparticles supported on CeO_2, which have been tested for the selective methanol decomposition to syngas. The multiscale design of the materials passed through the synthesis of a variety of CeO_2 powders with different shapes (nanorods with different aspect ratio, nanocubes) and their decoration with Pd NPs. The ceria nanostructures were characterized by a variable size, (from few nanometers in small nanorods to hundreds of nanometers in the case of long rods), but exposing surfaces with well-defined atomic structures ((100) oriented facets). By a careful comparison of the performances of the catalysts and of their changes in working conditions, we deduced that the most important factors are the reducibility of ceria and the synergies that can be established by extremely small Pd nanoparticles and the defective substrate (i.e. oxygen vacancies concentration). The synthesis parameters of the ceria nanostructures played a key-role in their reducibility: the lower the synthesis temperature, the higher the reducibility and the oxygen vacancies concentration. Moreover, we demonstrated that on highly defective ceria nanostructures, the Pd NPs experienced a stronger interaction with the support. This favored the stabilization of “cationic” Pd species that,

in synergy with reduced ceria surface, showed improved catalytic performances. As a future perspective, the integration of this kind of catalysts in more complex multifunctional materials for the *in situ* production of syngas is quite appealing. In fact, in Chapter 4, we exploited this study is in order to design a core@shell material potentially applicable in the field of *tandem* catalysis.

In Chapter 4, we have demonstrated how to build a complex multivariate catalytic system with great promises for synergistic and cascade catalysis. We have started from the synthesis of a Manganese based MOF characterized by a controlled microporosity. This system was exploited as the initial platform for the creation of series of nanoreactors, simply by introducing different types of metal cations inside the MOF cavities. This has been possible thanks to the presence of flexible dipyrazoles linkers able to coordinate a wide gamut of "soft" metal cations (post synthetic metallation). The result is the formation of a crystalline material with size selected cavities, each containing an open metal site. To demonstrate the potential of such system, we have validated the use of the Rh(I) metallated MOF as a catalyst for the hydroformylation of styrene with syngas obtaining extremely good results in terms of activity, selectivity, and recyclability. This demonstrates that precisely designed MOFs represent an excellent materials platform for the heterogeneizazion of a large variety homogenous catalysts.

We then proceed further on this route by realizing more complex architectures and we exploited the previously studied Pd/CeO_2 catalysts as support for the manganese MOF. The final objective was to create in a controlled way core@shell nanoparticles where the core is represented by the Pd/CeO_2 nanocubes that have demonstrated to be quite effective in the decomposition of methanol to syngas and the shell is constituted by the Rh metallated manganese MOF, which on the other hand is extremely active for hydroformylation reactions.

By exploiting the layer-by-layer method, we were eventually able to synthesize this very complex multivariate system that contains two nanocatalysts in a precise structural arrangement. The rationale that has guided the synthesis of this system was the development of a hierarchical model system characterized by geometrically homogeneous and structurally defined units that could be used for a model system for the study of tandem catalysis processes.

As a matter of fact, the Pd/CeO_2@Rh-MnMOF tandem catalyst, given the atomic and nanoscale control of its single components could allow to investigate by a reductionist approach highly complicated cascade and synergistic reactions (e.g. synthesis of propanale by reaction of ethylene with syngas *in situ* produced by methanol decomposition). The ability to obtain a clean interface between the core and the shell, whose thickness can be controlled at the level of the single atomic layer, offers a convenient tool to investigate in a systematic way the concentration effects induced by the porous nature of the shell, and to understand the role of the distance between different catalytic centers, on the overall catalytic activity.

In Chapter 5, we have investigate a rather fascinating method for the preparation of nanostructured composite materials: the aerosol process. The most notable aspect of this technique is that each aerosol droplet can be considered as a microreactor that can be exploited for preparing single or multiple units, whose structure can be tuned from the nano to the micron scale. By modifying the chemical composition of the precursor solution/suspension, which will be atomized, it is possible to introduced different building blocks, chemical modifiers and structure directing agents. During the time of flight of the microdroplets inside a furnace with controlled atmosphere, all the chemical species present inside the microdroplet can react/decompose and spatially organize due to self-assembly or capillary forces and the final product can be collected at the exit of the furnace. In our case study, we have synthesized hybrid materials based on crumpled heteroatom doped graphene oxide (i.e. N-cGO) decorated with MoS_2 nanoparticles and we tested their catalytic activity in the electro and photoelectrochemical hydrogen production. This hybrid material can be considered a highly complex

multifunctional catalyst since it is based on the electronic interaction between two moieties that explicate different functions in a synergistic way within a unique catalytic cycle. In fact, N-cGO and MoS_2 combined together can form of a p-n nanojunction and singularly the N-cGO is responsible for charge collection and improving electron transport, whereas MoS_2 is a catalyst for the HER. These materials have a direct application in the field of energy conversion. Moreover, the hydrogen generation is also an important reaction in the field of tandem catalysis. H_2 could be immediately employed in a successive reaction after the *in situ* production, reducing the complexity of a process and improving its safety and sustainability. In our particular case, the sustainability of this process is highlighted also by the role of the solar light (reduction of the overpotential necessary to start the hydrogen evolution) and by the absence of noble metals in the nanohybrid catalyst. From a general point of view, the structure of this hybrid could be considered a rather general model for the synthesis of other functional materials based on the combination of two-dimensional nanosheets and nanoparticles.

Concluding, making an excursus through different case studies, we have highlighted the importance of the materials design at different length scale with the aim of improving significantly the efficiency and performances of heterogeneous catalysts. Moreover, our work underlines the still untapped potential of hierarchical multivariate systems in catalytic applications. The big challenges in this field are connected on the one hand to the preparation of controlled composite materials, which must be constituted by different building blocks synergistically connected to carry our specific functions, on the other hand to the comprehension of the changes of these materials in working conditions, which is the key for the ultimate understanding of the mechanisms at the basis of their exceptional reactivity.

In this context, the present thesis suggests that the aerosol process is a quite interesting synthesis strategy since it allows to prepare in a simple way in high yield, even very complex composite materials. Very few other techniques allow such a good control at different length scales of materials structure and composition.

Moreover, our work demonstrates that the combination of standard materials such as nanoparticles with metal organic frameworks can be used a versatile platform for developing these multivariate systems, although it is necessary a very precise control of the interfacial and structural properties of the overall system. MOFs in particular represent a treasure trove for the materials scientist who wants to tackle the great challenge of tandem catalysis since their inner cavities can be considered as incredibly sophisticated nanoreactors where both the physical dimension and chemical nature are tailored toward a specific application. Quite interestingly, MOFs are endowed with an ordered and crystalline nature that make them very appealing for fundamental studies. This aspect is closely intertwined with the necessity to make a substantial advancement in the comprehension of chemical process in materials bearing multiple catalytic centers. In fact, the fields of tandem, cascade and synergistic catalysis are still based on a high level of empiricism. Therefore, it is necessary to develop proper model systems and advanced investigations techniques able to tackle this high level of complexity. In this sense as exemplified in this work, the use of advanced *operando* and *in situ* techniques capable to operate in catalytic relevant conditions is of pivotal importance.

There is still a long way to go, but the advanced tools provided by materials science both in the synthesis and characterization of materials, partially showed in this thesis, have finally reached a maturity and technical advancement that may pave the way toward the rational design of complex multivariate systems able to perform quite complex functions. This may be a groundbreaking result, being a key enabling technology with a large impact in several fields such as the already mentioned tandem catalysis but also active self-regulating sensors, and stimuli responsive materials.

List of acronyms and abbreviations	
2D	Two-Dimensional
3D	Three-Dimensional
bcc	Body Centered Cubic
BE	Binding Energy
BET	Brunauer–Emmett–Teller
CFSE	Crystal Field Stabilization Energy
c-GO	Crumpled Graphene Oxide
CLR	Chemical Loop Reforming
CMG	Chemically Modified Graphene
CNPDs	Commercial Nanopowders
CVD	Chemical Vapor Deposition
DFT	Density Functional Theory
DRIFTS	Diffuse Reflectance Infrared Fourier Transform Spectroscopy
EC	Electrochemical
EDX	Energy Dispersive X-Ray Analysis
EISA	Evaporation Induced Self Assembly
EXAFS	Extended X-Ray Absorption Fine Structure
fcc	Face Centered Cubic
FT	Fourier Transformation
FWHM	Full Width at Half Maximum
G	Graphene
GC	Gas Chromatography
GIXRD	Grazing Incidence X-Ray Diffraction
GO	Graphene Oxide
HER	Hydrogen Evolution Reaction
HR	High Resolution
LbL	Layer By Layer
LCF	Linear Combination Fitting
LEED	Low Energy Electron Diffraction
LNRS	Long Nano Rods
LS	Linear Sweep
MOF	Metal Organic Framework
NCs	Nano Cubes
NEXAFS	Near Edge X-Ray Absorption Fine Structure
N-GO	Nitrogen Doped Graphene Oxide
NPs	Nano Particles

NRs	Nano Rods
OER	Oxygen Evolution Reaction
OPSE	Octahedral Preference Stabilization Energy
ORR	Oxygen Reduction Reaction
OSC	Oxygen Storage Capacity
PE	Pass Energy
PSC	Post-Synthetic Crystallization
PSM	Post-Synthetic Metalation
P-XRD	Powder X-Ray Diffraction
RT	Room Temperature
SBUs	Secondary Building Units
SEM	Scanning Electron Microscopy
SNRs	Small Nano Rods
SSA	Specific Surface Area
STEM	Scanning Transmission Electron Microscopy
STM	Scanning Tunneling Microscopy
TEM	Transmission Electron Microscopy
TGA	Thermogravimetric Analysis
TMD	Transition Metal Dichalcogenide
TPD	Temperature Programmed Desorption
UHV	Ultra-High Vacuum
WAXRD	Wide Angle X-Ray Diffraction
XAS	X-Ray Absorption Spectroscopy
XAFS	X-Ray Absorption Fine Structure
XANES	X-Ray Absorption Near Edge Structure
XPS	X-Ray Photoemission Spectroscopy
XRD	X-Ray Diffraction

List of publications

1. M. Favaro, **F. Carraro**, M. Cattelan, L. Colazzo, C. Durante, M. Sambi, A. Gennaro, S. Agnoli, G. Granozzi, Multiple doping in graphene oxide foams and quantum dots: new switchable systems for oxygen reduction and water remediation. ***J. Mater. Chem. A***, **2015**, **3**, 14334-14347.

2. **F. Carraro**, L. Calvillo, M. Cattelan, M. Favaro, M. Righetto, S. Nappini, I. Píš, V. Celorrio, D. J. Fermín, A. Martucci, S. Agnoli, G. Granozzi, Fast One-Pot Synthesis of MoS_2/Crumpled Graphene p–n Nanonjunctions for Enhanced Photoelectrochemical Hydrogen Production. ***ACS Appl. Mater. Interfaces***, **2015**, 7 (46), 25685–25692.

3. E. Pizzolato, S. Scaramuzza, **F. Carraro**, A. Sartori, S. Agnoli, V. Amendola, M. Bonchio, A. Sartorel. Water oxidation electrocatalysis with iron oxide nanoparticles prepared via laser ablation. ***J. Energy Chem.***, **2016,** 25, 2, 246–250.

4. D. Mazzier, **F. Carraro**, M. Crisma, M. Rancan, C. Toniolo and A. Moretto. A terminally protected dipeptide: from crystal structure and self-assembly, through co-assembly with carbon-based materials, to a ternary catalyst for reduction chemistry in water. ***Soft Matter***, **2016**, 12, 238-245.

5. V. Amendola, S. Scaramuzza, **F. Carraro**, E. Cattaruzza, Formation of alloy nanoparticles by laser ablation of Au/Fe multilayer films in liquid environment. ***J. Colloid and Interface Sci.***, **2017**, 489, 18-27.

6. **F. Carraro**, O. Vozniuk, L. Calvillo, L. Nodari, C. La Fontaine, F. Cavani, S. Agnoli, In operando XAS investigation of reduction and oxidation processes in cobalt and iron mixed spinels during the chemical loop reforming of ethanol, ***J. Mater. Chem. A, 2017,*** *5, 20808-20817.*

7. **F. Carraro,** K. Chapman, Z. Chen et al., Catalysis in MOFs: general discussion, ***Faraday Discuss*.,** **2017**,201, 369 - 394.

8. R. Parin, A. Martucci, M. Sturaro, S. Bortolin, M. Bersani, **F. Carraro**, D. Del Col, Dropwise condensation over nano-structured aluminum surfaces, **Revised version submitted,** ***ACS Appl. Mater. Interfaces***.

9. P. Sekar, L. Calvillo, C. Tubaro, M. Baron, A. Pokle, **F. Carraro**, A. Martucci and S. Agnoli, Cobalt Spinel Nanocubes on N-doped Graphene: a Synergistic Hybrid Electrocatalyst for the Highly Selective Reduction of Carbon Dioxide to Formic Acid, ***ACS Catal.,*** **2017,** 7 (11), 7695–7703.

10. A. Privitera, M. Righetto, M. De Bastiani, **F. Carraro**, M. Rancan, L. Armelao, G. Granozzi, R. Bozio, L. Franco, Hybrid Organic/Inorganic Perovskites-Polymer Nanocomposites: Towards the Enhancement of Structural and Electrical Properties*, **J. Phys. Chem. Letters*****,* **2017,** 8 (24), 5981–5986.

Updated at December 2017.

List of oral/poster presentations

1. Graphene 2016, Genova, 19-22 April 2016. **Oral presentation**: "Fast one-pot synthesis of MoS_2/CrumpledGraphene p-n nanojunction for enhanced photoelectrochemical hydrogen production".
2. Congresso Nazionale di Chimica Inorganica, 14-17 September 2016, Padova. **Oral presentation**: "Towards a deeper understanding of reduction and oxidation of spinel oxides: an *in situ* study".
3. Faraday Discussion: New Directions in Porous Crystalline Materials, 05-07 June 2017, Edinburgh (UK). **Poster presentation**: "Layer-by-layer growth of MnMOF for the design of hierarchical tandem catalysts".
4. Composites of Metal and Covalent Organic Frameworks: Fundamental Design & Applications, 12-14 September 2017, Granada (Spain). **Oral Presentation**: "Layer-by-layer growth of MOFs for the design of hierarchical tandem catalysts".
5. Materials, Characterization, and Catalysis Workshop, 15-17 January 2018, Zurich (Swizterland). **Poster Presentation**: "Layer-by-layer growth of MOFs for the design of hierarchical tandem catalysts".

List of Collaborations

- Prof. Fabrizio Cavani research group, **University of Bologna**, Dept. of Industrial Chemistry
- Prof. David Fermin research group, **University of Bristol**, School of Chemistry
- Prof. Christian Doonan research group, **University of Adelaide**, Dept. of Chemistry
- Prof. Maria Cristina Paganini research group, **University of Torino**, Dept. of Chemistry
- Prof. Alex Martucci research group, **University of Padova**, Dept. of Materials Engineering
- Prof. Stefano Paganelli research group, **University of Venezia**, Dept. of Molecular Science and Nanosystems
- Prof. Carla Marega research group, **University of Padova**, Dept. of Chemistry
- Dr. Francesc X. Llabrés i Xamena research group, **University of Valencia**, Dept. of Chemical Technology
- Dr. Luca Nodari, **ICMATE,** CNR Padova

Acknowledgments

Ringrazio prima di tutto la mia famiglia, che mi ha sostenuto e mi ha permesso di arrivare fino alla fine di questo percorso di studi. Senza di loro non potrei essere arrivato fino a quest'ultima pagina. Ringrazio poi Irene, che mi ha sopportato/supportato durante questi anni di studi, nonostante tutti i momenti in cui la mia testa rimaneva troppo tempo in laboratorio.

Ringrazio il mio supervisore, Prof. Stefano Agnoli, per tutto quello che mi ha insegnato e per tutto l'aiuto che mi ha dato in questi anni di dottorato. Questa tesi e tutti gli altri lavori pubblicati non sarebbero stati possibili senza i suoi insegnamenti e il suo aiuto.

Ringrazio tutto il gruppo di Scienza delle Superfici e Catalisi, dai professori ai laureandi, ognuno ha contribuito ad aiutarmi in questi anni ed ognuno mi ha insegnato qualcosa. Grazie al Prof. Granozzi per i preziosi consigli e per il sostegno alla mia carriera ed allo sviluppo di tutto il gruppo. Grazie Laura, Mattia, Marco e Luca. Siete stati dei fantastici colleghi e amici.

Thanks to all the researchers with whom I was lucky enough to collaborate during my PhD. Especially, I wanted to thanks Prof. Christian Doonan for giving me the precious opportunity to work in his laboratories.

Grazie a Marcello, Alberto e Dario, compagni di sofferenze e di ricerca da tanti anni. Grazie anche a tutti i miei amici fuori dall'università, che hanno dovuto sorbirsi tutti i miei "no devo scrivere la tesi/l'articolo/etc".

Grazie.